UNIVERSITY OF BIRMINGHAM

DEVELOPMENT AND OPTIMIZATION OF SMALL-SCALE RADIAL INFLOW TURBINE FOR WASTE HEAT RECOVERY WITH ORGANIC RANKINE CYCLE

By

Kiyarash Rahbar
MEng. (Mechanical Engineering)

Thesis submitted in Partial Fulfilment of Requirements for the Degree of

DOCTOR OF PHILOSOPHY

School of Mechanical Engineering
The University of Birmingham
Edgbaston, Birmingham, UK
January 2016

به نام پدرم که ایستادگی و شهامت آموخت

برای مادرم که آغوشش امن ترین پناهم بود

به صداقت خواهرم که پیوسته همراهم بود

و ...

به چشمان یار که معنای دوست داشتن بود

کیا - پاییز ۹۴

ACKNOWLEDGEMENTS

This work would not have been possible without the guidance and expertise of **Dr. Raya Al-Dadah**. I am truly grateful for her mentoring and trust during the whole period of this project. I wish to thank her for the numerous moments spent working together on the practical and theoretical issues as well as for countless valuable discussions. I appreciate her endless support, advice and especially the clear-cut reviewing of my thesis and the scientific papers.

I would also like to express my deep gratitude to **Dr. Saad Mahmoud** who provided me with constructive advices along this work and shared his valuable experience in the crucial stages of my candidature. His interest and encouragement was profoundly beneficial in development and progress of this research.

Special thanks goes to **Mr. Simon Rowan,** senior laboratory technician, for his help, availability and technical advice in constructing the experimental facility and manufacturing the turbine but above all for his friendship during these years. Last but not least, thanks to all my friends and colleagues especially Nima who has been like a brother and Yavar during all these years.

Kiyarash Rahbar
January 2016

LIST OF PUBLICATIONS

Journal Publications:

1- Rahbar, K., S. Mahmoud, R. K. Al-Dadah and N. Moazami (2015). "Parametric analysis and optimization of a small-scale radial turbine for Organic Rankine Cycle." Elsevier, *Energy* **83**(0): 696-711.

2- Rahbar, K., S. Mahmoud, R. K. Al-Dadah and N. Moazami (2015). "Modelling and optimization of organic Rankine cycle based on a small-scale radial inflow turbine." Elsevier, *Energy Conversion and Management* **91**(0): 186-198.

3- Rahbar, K., S. Mahmoud and R. K. Al-Dadah (2014). "Mean-line modeling and CFD analysis of a miniature radial turbine for distributed power generation systems*." Oxford university press, *International Journal of Low-Carbon Technologies,* doi: 10.1093/ijlct/ctu028.

4- Rahbar, K., S. Mahmoud, R. K. Al-Dadah, N. Moazami and A. Bahr Ennil (2015). "Preliminary mean-line design and optimization of a radial turbo-expander for waste heat recovery using organic Rankine cycle." Elsevier, *Energy Procedia* **75**: 860-866.

5- Bahr Ennil, A., S. Mahmoud, R. K. Al-Dadah, A. Al-Jubori and K. Rahbar (2015). "Prediction of Losses in Small Scale Axial Air Turbine Based on CFD Modelling." Elsevier, *Energy Procedia* **75**: 3271-3276.

6- Rahbar, K., S. Mahmoud, R. K. Al-Dadah and N. Moazami. Organic Rankine cycle: A review of applications, working fluids and expansion machines. (Submitted to the Journal of *Applied thermal engineerin*g, Elsevier – under first revision)

7- Rahbar, K., S. Mahmoud, R. K. Al-Dadah and N. Moazami. Organic Ranline cycle: Investigating the effect of expander efficiency on the modeling and optimization of organic Rankine cycle for waste heat recovery applications. (Submitted to the Journal of *Applied Energy*, Elsevier – under review)

---

* Award winning paper for the best article published in the International Journal of Low-Carbon Technologies in 2015. (http://www.oxfordjournals.com/our_journals/ijlct/ijlctbestarticles.html)

Conference Publications:

1- Rahbar, K., S. Mahmoud, R. K. Al-Dadah and N. Moazami (2015). "Integrated modelling and multi-objective optimization of organic Rankine cycle based on radial inflow turbine." 60th ASME Turbo Expo 2015: Turbine Technical Conference and Exposition, Montreal, Quebec, Canada, June 15–19, 2015. Paper No. GT2015-42835.

2- Rahbar, K., S. Mahmoud and R. K. Al-Dadah (2015). "Optimized efficiency maps and new correlation for performance prediction of ORC based on radial turbine for small-scale applications." In the 3rd international seminar on ORC power systems, ASME ORC 2015, 12-14 October 2015, Brussels, Belgium.

3- Rahbar, K., S. Mahmoud, R. K. Al-Dadah, N. Moazami and A. Bahr Ennil (2015). "Preliminary mean-line design and optimization of a radial turbo-expander for waste heat recovery using organic Rankine cycle." In the 7th International Conference on Applied Energy (ICAE), 28-31 March 2015, Abu Dhabi, UAE.

4- Rahbar, K., S. Mahmoud, R. K. Al-Dadah and A. Elsayed (2013). "Modelling of a miniature radial turbine for distributed power generation systems." In the 5th International Conference on Applied Energy (ICAE), 1-4 July 2013, Pretoria, South Africa.

5- Bahr Ennil, A., S. Mahmoud, R. K. Al-Dadah, A. Al-Jubori and K. Rahbar (2015). "Prediction of Losses in Small Scale Axial Air Turbine Based on CFD Modelling." In the 7th International Conference on Applied Energy (ICAE), 28-31 March 2015, Abu Dhabi, UAE.

6- Rahbar, K., S. Mahmoud, R. K. Al-Dadah and N. Moazami. One-dimensional and three-dimensional numerical optimization and comparison of single-stage supersonic and dual-stage transonic radial inflow turbines for the ORC. (Submitted to the proceedings of the ASME 2016 Power and Energy Conference in Charlotte, North Carolina, USA – under review)

ABSTRACT

Expander is the critical component of the organic Rankine cycle (ORC) and its performance has significant effect on the overall cycle efficiency. This thesis is an investigation of different strategies for efficient development and optimization of radial-inflow turbines (RIT) for small-scale ORC systems with power capacity of less than $5kW_E$. A novel methodology for modelling, optimization and experimental study of the small-scale RITs was proposed that encompassed the one-dimensional mean-line modelling and optimization, three-dimensional CFD analysis and optimization and experimental testing. Such methodology proved to be effective as it allows systematic investigation of the key input parameters on the turbine performance and multi-level optimization to reliably find the optimum turbine geometry that led to maximum performance. Initially, the proposed methodology was employed to develop a small-scale compressed air RIT for validation purposes. The results showed that it is possible to effectively improve the turbine performance while employing both mean-line and CFD approaches. The experimental study of the compressed air RIT revealed that the CFD model can with good accuracy predict the turbine performance and such model can be used as benchmarking model for analysing small-scale RITs. Extending the proposed approach to RITs for ORC systems that operate with organic fluids revealed that they had strong real-gas behaviour and necessitated the real-gas formulation to accurately predict their behaviour. Deficiencies of the constant turbine efficiency assumption that was commonly used in majority of the literature studies were highlighted by showing the errors that such assumption caused during the cycle analysis and fluid selection. In addition, a novel approach for integrated modelling of organic RIT with the ORC coupled with the genetic algorithm optimization technique was developed that not only alleviated the errors during fluid selection and cycle analysis but also optimized the ORC performance based on a wide range of cycle and turbine

input design parameters. To alleviate the formation of shack waves and supersonic losses at high expansion ratios (up to ten) as well as improving the performance of the ORC, a novel dual-stage transonic RIT was developed and optimized for maximum isentropic efficiency. Such turbine showed considerably higher cycle thermal efficiency when compared with the single stage supersonic RIT. Moreover, the optimized dual-stage transonic RIT obtained by the mean-line optimization was further optimized using 3-D CFD optimization using design of experiment, Meta-model and genetic algorithm. Such optimization proved to be very efficient as it substantially improved the turbine isentropic efficiency of both stages by about 10%. CFD results for the optimized dual-stage transonic turbine at the design operating point showed the turbine isentropic efficiency of 87.12%, ORC thermal efficiency of 13.19% and net power output of 2.436kW. Such results were considerably higher than the reported values for other types of expanders in the literature for the same range of power capacity and highlighted the potential and effectiveness of the combined mean-line and CFD optimization approaches developed in this thesis to further improve the ORC performance based on the RITs.

TABLE OF CONTENTS

List of Figures

List of Tables

NOMENCLATURE

Symbols

A	Area (m^2)
b	Blade height (m)
BK	Blockage factor (-)
C	Absolute flow velocity (m/s)
C_{nozzle}	Nozzle chord length (m)
C_p	Specific heat capacity at constant pressure (J/kg-K)
d	Diameter (m)
d_{hyd}	Hydraulic diameter (m)
d_s	Specific diameter (-)
ER	Expansion ratio (-)
f	Friction coefficient (-)
f_{curve}	Turbine friction factor (-)
h	Enthalpy (J/kg)
Δh_{actual}	Actual specific enthalpy drop (J/kg)
Δh_{ideal}	Ideal specific enthalpy drop (J/kg)
i	Incidence angle (degree)
k	Loss Coefficient (-)
l	Length (m)
l_{hyd}	Hydraulic length (m)
$\dot{m}$	Mass flow rate (kg/s)
Ma	Mach number (-)
N_s	Specific speed (-)
$O_{throat,nozzle}$	Nozzle throat width (m)
P	Pressure (Pa)
Q	Volume flow rate (m^3/s)
R	Gas constant (J/kg-K)
RR	Relative roughness (m)
Re	Reynolds number (-)
r	Radius (m)
r_c	Mean radius of curvature (m)
S	Entropy (J/kg-K)
S_{nozzle}	Nozzle blade pitch (m)
SC	Swirl coefficient (-)
SF	Shape factor (-)
SP	Sizing parameter (-)
T	Temperature (K)
t	Blade thickness (m)
$\Delta T_{superheating}$	Degree of superheating (K)

U	Rotor blade velocity (m/s)
VR	Volumetric expansion ratio
W	Relative flow velocity (m/s), Work output (W)
x	Quality (-)
Z	Blade number (-), Compressibility factor (-)
Greek letters	
α	Absolute flow angle with respect to radial (degree)
β	Relative flow angle with respect to radial (degree)
γ	Specific heat capacity ratio (-)
ε	Clearance (m)
η	Efficiency (-)
μ	Dynamic viscosity (Pa-s)
υ	Isentropic velocity ratio (-)
ξ	Absolute meridional velocity ratio
ρ	Density (kg/m^3)
σ	Solidity (-)
φ	Flow coefficient (-)
ψ	Loading coefficient (-)
ω	Rotational velocity (RPM)
Subscripts	
1-5	Stations across turbine
6-7	Stations across the cycle
b	Back plate
c	Curvature
cr	Critical
cyc	Cycle
E	Electrical
eva	Evaporator
ex	Expander
f	Friction
hub	Rotor exit hub
hyd	Hydraulic
m	Meridional direction
mech	Mechanical
nbp	Normal boiling point
r	Radial
rel	Relative
rms	Root mean square
s	Isentropic
Sonic	Speed of sound
vol	Volute
x	Axial

Stage	Turbine inlet to turbine outlet
t	Total, stagnation
th	Thermal
tip	Rotor exit tip
ts	Total to static
tt	Total to total
wf	Working fluid
θ	Tangential direction
Superscripts	
‾	Average
Acronyms	
ALT	Atmospheric lifetime
CFD	Computational fluid dynamics
CHP	Combine heat and power
CPC	Compound parabolic collector
CPG	Centralized power generation
DOE	Design of experiments
DPG	Distributed power generation
DUI	Datum universal interface
EES	Engineering equation solver
EoS	Equation of state
FEA	Finite element analysis
GA	Genetic algorithm
GWP	Global warming potential
HTF	Heat transfer fluid
ICE	Internal combustion engine
ODP	Ozone depletion potential
OF	Objective function
ORC	Organic Rankine cycle
OSF	Optimal space filling
OTEC	Ocean thermal energy conversion
PS	Pressure surface
RANS	Reynolds-averaged Navier-Stokes
RIT	Radial inflow turbine
RPM	Revolutions per minute
RS	Response surface
RSS	Root Sum Square
RTD	Resistance temperature detector
SRC	Steam Rankine cycle
SS	Suction surface
SST	Shear stress transport
WHR	Waste heat recovery

CHAPTER 1

INTRODUCTION

1.1. Background

Nowadays energy is a key factor in the global economy and is considered as a crucial input for all industrial and production processes. The effectiveness of energy generation and consumption processes has remarkable impacts on our society and environment. Following the international energy agency (IEA) report (International Energy Agency 2014), extending the current trend of energy consumption and energy efficiency to 2050 yields a growth of 70% and 60% in the global energy demands and emissions respectively compared to 2011. The associated emissions result in a long-term global average temperature rise of 6°C by 2050 which can result in potentially devastating consequences such as climate change, energy security and unsustainable future. IEA (2014) suggested an effective scenario called "2DS" which offers a vision for a sustainable energy system that reduces carbon dioxide (CO_2) emissions to maintain the global temperature rise within 2°C by 2050. The "2DS" scenario offers drastic actions to industry, energy sector key players and policy makers to substantially improve the energy efficiency of systems in order to limit increases in the energy demand by 25% and cut emissions by 50% during the next 40 years. This strategy creates a framework that can simultaneously deliver secure, affordable and environmentally sustainable energy systems and shifting the

energy landscape as a whole. Such scenario requires necessary actions in all aspects as there is no single technology, energy source or policy that can be solely employed to decarbonize the energy systems in line with the "2DS". In contrast, it demands a mix of actions including utilization of renewables such solar, wind and geothermal energies, smart transmission and distribution of electricity, electrification of transportation sector and enhanced international and regional cooperation (International Energy Agency 2014). In essence, the future sustainable energy systems are expected to be smarter, renewable oriented, integrated, well-regulated and more distributed.

Improvements in energy efficiency have significant contribution to the "2DS" scenario. For example, power in the traditional electrical grid (or centralized power generation) followed one way from the generation station to the load. The traditional grid uses the highest possible voltage level to transmit and distribute large quantities of power. During this transport there are associated losses that accounts for 12% of power and 30% of delivered electricity cost as reported by (World Energy Council 2013). In addition, there are implicit costs in terms of carbon emissions in which the fuel that is consumed to generate electricity is not fully consumed by the end user. Therefore, it is necessary to minimize these losses in order to increase the energy efficiency of the system. Moreover, centralized power generation (CPG) requires large capital investment cost for electrification of remote areas where the infrastructure requires the electricity but at low quantities. Moreover, CPG suffers from costly investment of about 3,500 billion dollars for OECD counties for upgrading the transmission and distribution network (Pepermans *et al.* 2005), high cost of electricity deregulation and control devices and harmful environmental impacts due to the use of fossil fuels.

In this regard, distributed (on-site) power generation (DPG) is a promising alternative that overcomes all the deficiencies of the CPG. Distributed power generation is an independent

electric source connected directly to the distribution network or to the customer site with the power ratings shown in Table 1-1 (Ackermann *et al.* 2001). DPG is becoming a new trend in the world's ever-increasing demand for energy as it exhibits unique advantages such as reduced transmission and distribution losses, emergency backup power in the case of power outage for hospitals, telecommunications centres and data storage centres, lower damages and economic losses in the case of natural disasters, environmentally friendlier than CPG, versatility for suppling the electricity demand in remote areas (i.e. sub-Saharan Africa) and security and reliability due to its compatibility with wide range of fuels . In fact DPG can utilise any source of energy including solar, geothermal or waste heat.

Table 1-1 Power rating of the DPG systems (Ackermann *et al.* 2001)

Category	**Power rating**
Distributed micro power generation	1Watt to 5KW
Distributed small power generation	5KW to 5MW
Distributed medium power generation	5MW to 50MW
Distributed large power generation	50MW to 300MW

About 50% of the world's energy consumption is wasted as heat due to the limitations of energy conversion processes (Siemens power generation division 2014). This waste heat can be from variety of sources such as industrial and household waste heat, gas and steam turbines exhaust heat, internal combustion engines exhaust heat, solar radiation and geothermal and biomass heats. Adopting waste heat recovery (WHR) with DPG systems has a great potential in increasing the system efficiency while reducing the fuel consumption, lowering the CO_2 emissions, reducing demand on the primary fuel because more power can be generated with the same amount of fuel and thus enhancing sustainability by increasing the power cycle conversion efficiency (Siemens power generation division 2014). This efficiency gain can be achieved through the implementation of the best available technologies. Compared to the steam Rankine cycle's need for superheating device, Kalina cycle's complex systems structure, Tilateral's

flash cycle's difficult two-phase expansion, supercritical CO_2 cycle's high operating pressure and thermoelectric generator's expensive material and low efficiency, organic Rankine cycle (ORC) has the favourable characteristics of simple structure, high reliability, small size, low cost and easy maintenance (Bao *et al.* 2013). ORC technology proved to be one of the most reliable and efficient solutions that utilizes the waste heat of the above-mentioned thermal heat sources for supplying the electricity demand through the DPG systems. In other words, ORC units utilise the otherwise wasted energies and convert them into useful power in the range of few kW_E to tens of MW_E. The ORC is similar to the steam Rankine cycle (SRC) but instead of water it utilizes organic compounds such as hydrocarbons and/or refrigerants that boil at low temperature and pressure. This facilitates the ultimate versatility of the ORC to capture almost any low to medium temperature (from 60°C up to 350°C) heat sources to generate power. Compared to SRC, the ORC exhibits unique advantages such as small size, low capital and maintenance cost, simplicity, high reliability and low environmental impacts when combined with renewables. Due to this, the ORC technology has been deployed at fast pace during the past few years across the globe and experienced remarkable advances due to the extensive academic research.

Several studies have been conducted in the literature about the ORC which can be mainly categorized as thermodynamic modelling of the ORC, optimization of the ORC overall performance metrics such as thermal and exergy efficiencies and selection of appropriate working fluid for a specific type of low-grade heat source such as geothermal heat (Madhawa Hettiarachchi *et al.* 2007, Saleh *et al.* 2007, Guo *et al.* 2011, Shengjun *et al.* 2011, Tempesti *et al.* 2012), solar radiation (Tchanche *et al.* 2009, Wang *et al.* 2009, Delgado-Torres *et al.* 2010, Rayegan *et al.* 2011), biomass heat (Al-Sulaiman *et al.* 2011, Liu *et al.* 2011, Qiu *et al.* 2012), ocean thermal energy (Sun *et al.* 2012), waste heat of micro gas turbines (Invernizzi *et al.* 2007,

Muñoz de Escalona *et al.* 2012, Clemente *et al.* 2013, Mago *et al.* 2013), waste heat of internal combustion engines (Dolz *et al.* 2012, Katsanos *et al.* 2012, Wang *et al.* 2012, Sprouse Iii *et al.* 2013) and waste heat of SRC (Rashidi *et al.* 2011, Liu *et al.* 2012). In contrast, there has been relatively little published work regarding the development and optimization of the expanders used in the ORC and in all the above studies constant expander efficiency was considered during the analyses. The expander is a critical component in a relatively efficient ORC system and has significant effect on the overall cycle performance (Bao *et al.* 2013). Despite the few studies that considered the modelling and experimental study of the ORC based on volumetric scroll or screw expanders (Lemort *et al.* 2009, Quoilin *et al.* 2010, Twomey *et al.* 2013, Zhang *et al.* 2014), very limited published studies are reported that investigate the performance of volumetric expanders (i.e. turbines) for the ORC. Even, these volumetric expanders were not designed specifically for the cycle thermodynamic operating conditions and working fluids properties but were modified version of existing compressors and exhibited low isentropic efficiencies in the range of upto 75%. Compared to the volumetric (scroll and screw) expanders, radial inflow turbine (RIT) offers the advantages of high efficiency, mature manufacturability, light weight, small number of moving parts and high power to weight ratio (Qiu *et al.* 2011, Bao *et al.* 2013). There exists a knowledge gap regarding the development and optimization of small-scale RITs with isnetropic efficienes higher than volumetric expanders that can be used with low-power capcity ORC systems and neccesiates the need for substantial academic research in this field. Figure 1-1 is useful in understanding the content of this section.

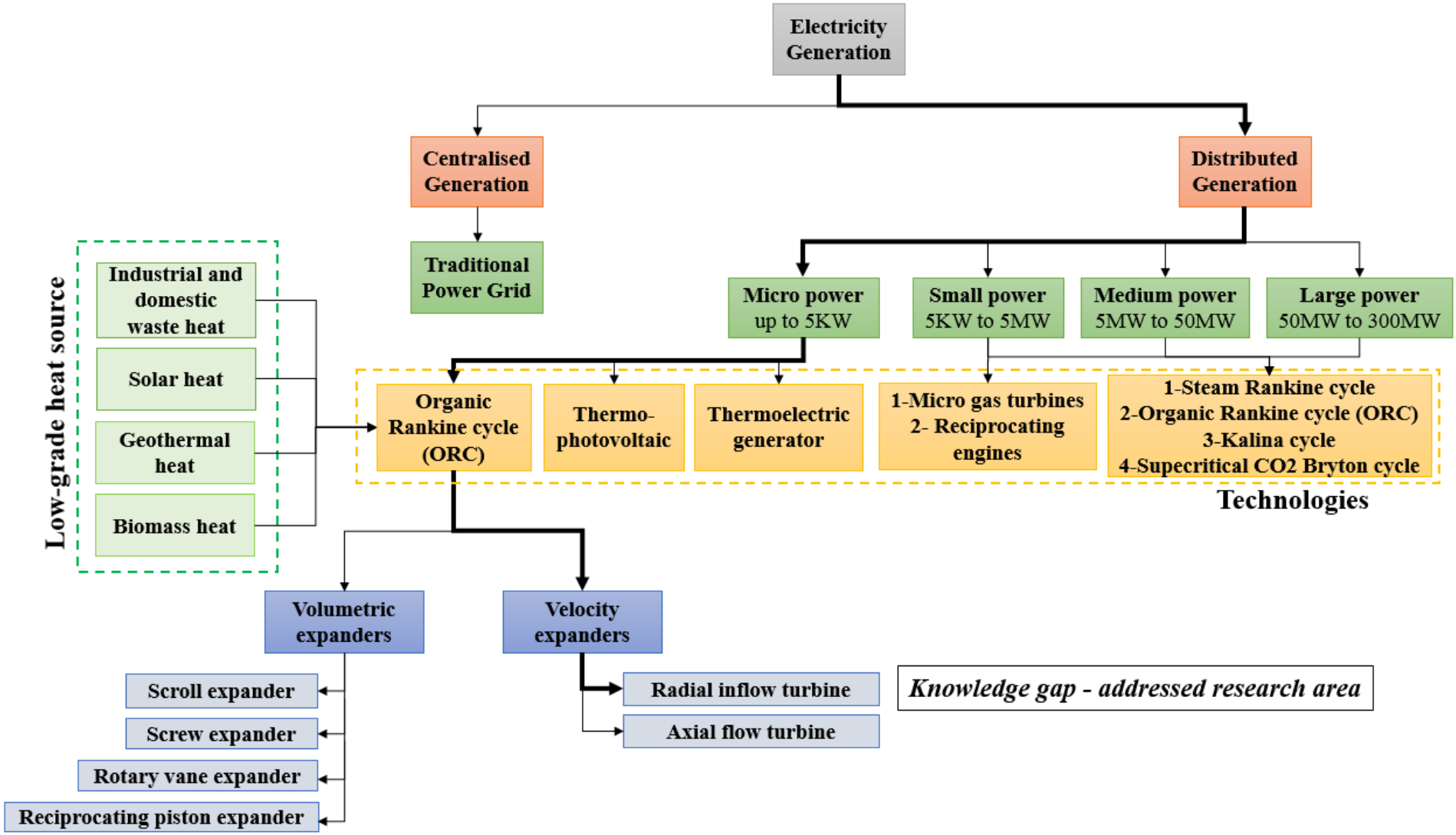

Figure 1-1 Classification of the electricity generation systems and technologies and identification of the knowledge gap

1.2. Objectives and scope

As shown in section 1.1 while they are critical component of the ORC, RITs have received relatively little attention from the ORC community. Together ORC and RIT when utilizing low-to-medium grade waste heat sources offer a sustainable solution for energy efficiency improvements with great potential in various applications. The present research aims at investigation of different strategies for development and optimization of highly efficient small-scale RIT as the expander of small-scale ORC systems with the power capacities of less than $5kW_E$ and has the following objectives:

- Developing and validating a generalized methodology for design and performance prediction of small-scale RITs for DPG applications encompassing detailed one-dimensional modelling followed by the aerodynamic analysis using computational fluid dynamics (CFD) and structural analysis using finite element analysis (FEA). Then conducting the experimental studies for validating the proposed methodology.
- Extending the developed one-dimensional simulation code for design and performance prediction of organic RITs for the ORC based on real-gas formulation and intergrating an optimization algorithm for maximizing the RIT performance. Moreover, integrating the one-dimensional modelling of RIT with modelling of the ORC to replace the constant efficiency assumption that is used in majority of the literature studies for more realistic cycle analysis.
- Establishing new correlations for performance and size prediction of ORC RIT using the developed simulation code that can be integrated with the ORC general analysis code for accurate efficiency prediction of the RIT without the need for performing complete RIT design procedure.

- Developing a novel dual-stage transonic organic RIT that can both obtain high expansion requirement of the ORC while maintaining high turbine isentropic efficiency by limiting the flow regime to transonic level.
- Performing three-dimensional CFD optimization of the dual-stage transonic organic RIT to further improve the performance (i.e. isentropic efficiency) and then conducting the CFD simulations to obtain the turbine performance maps for a wide range off-design operating conditions. Eventually, obtaining the ORC performance based on the turbine off-design simulation results that will be useful for component selection, cost analysis and integration of the ORC system with a topping cycle (cascading).

1.3. Thesis outline

This thesis has been organized in seven chapters. Comprehensive literature review of the ORC including background, applications, working fluid selection and expander design and testing are reviewed in chapter two. Design methodology of the RIT starting from simple one-dimensional modelling to complex three-dimensional CFD and FE analyses are described in chapter three. The solid modelling, manufacturing and experimental study of the developed RIT together with the explanation of the instrumentations, calibration and uncertainty analyses and validation of the methodology will be presented in chapter four. The established methodology in chapter three and four will serve as the basis for further analysis in chapter five where the one-dimensional simulation code is advanced further to facilitate design, optimization and integrated modelling of RIT with ORC suitable for organic fluids with real gas formulation. Using such procedure new correlations for performance and size prediction of organic RIT are presented in chapter five as well. In chapter six the detailed three-dimensional CFD optimization of the dual-stage RIT is presented together with the creation of the turbine performance maps as well as estimation of the ORC performance under such operating

conditions. Finally, summary of the most remarkable results identified in the preceding chapters and recommendations for future developments of the current work will be presented in chapter seven.

CHAPTER 2

ORGANIC RANKINE CYCLE- LITERATURE REVIEW

2.1. Introduction

The ever-increasing demand for energy, scarcity of traditional energy sources and severe environmental issues are, perhaps, the biggest global challenges that need immediate actions. In this regard, harnessing the renewable energies and waste heat recovery are considered as potential solutions that can effectively address these issues. Organic Rankine Cycle (ORC) is proved to be reliable technology that can efficiently convert these low to medium-grade heat sources into useful power. This chapter summarizes a comprehensive literature review including the background for the ORC's history, configurations, applications, working fluids and expansion devices.

2.2. ORC background

Organic Rankine cycle (ORC) is analogous to the steam Rankine cycle (SRC) as it contains all the main components of the SRC such as evaporator, expansion device, condenser and pump with the only difference that the water is replaced by an organic compound (i.e. hydrocarbons, refrigerants, ethers and siloxanes). In fact the ORC technology is rather old perhaps as old as the SRC. The first patented concept of an engine using ether as the working fluid is dated back to 1826 (Galloway *et al.* 1836). Substantial efforts were invested during the first half of the 20th century to develop the ORC technology for power generation mainly by exploiting the solar and geothermal energies (Shuman 1907, Tabor *et al.* 1963, Pytilinski 1978, Curran 1981). As a consequence of the oil crisis and the environmental issues during the 70s and 80s, the development of the ORC systems occurred at a faster pace in various aspects such as novel configurations like cascaded cycle (Bronicki 1972), alternative organic fluids such as zeotropic mixtures (Wang *et al.* 2009), and innovative applications such as the use of ORC in vehicles (Dolz *et al.* 2012). Such trend continued at a fast-pace until today.

2.3. ORC configurations

As discussed in section 2.2 the ORC layout is very similar to the SRC, though, it is considerably simpler as there is no need for the water-steam drum to be connected to the boiler and one single heat exchanger is capable to facilitate all three phases of the heating process as preheating, vaporization and superheating (Quoilin 2011). Figure 2-1 shows a schematic of the simple organic Rankine cycle. The flow process across the ORC components is described as following:

- 1-2: The high pressure vapour organic fluid is directed to the expander in which its thermal energy is converted into the mechanical energy of shaft as it expands to lower pressure.
- 2-3: The vapour is then condensed in the condenser using a cooling medium (air or water) in a constant pressure process.
- 3-4: The low pressure organic fluid is pressurized with a pump.
- 4-1: The organic fluid is vaporized in the evaporator using a low-grade waste heat source in a constant pressure process and a new cycle begins.

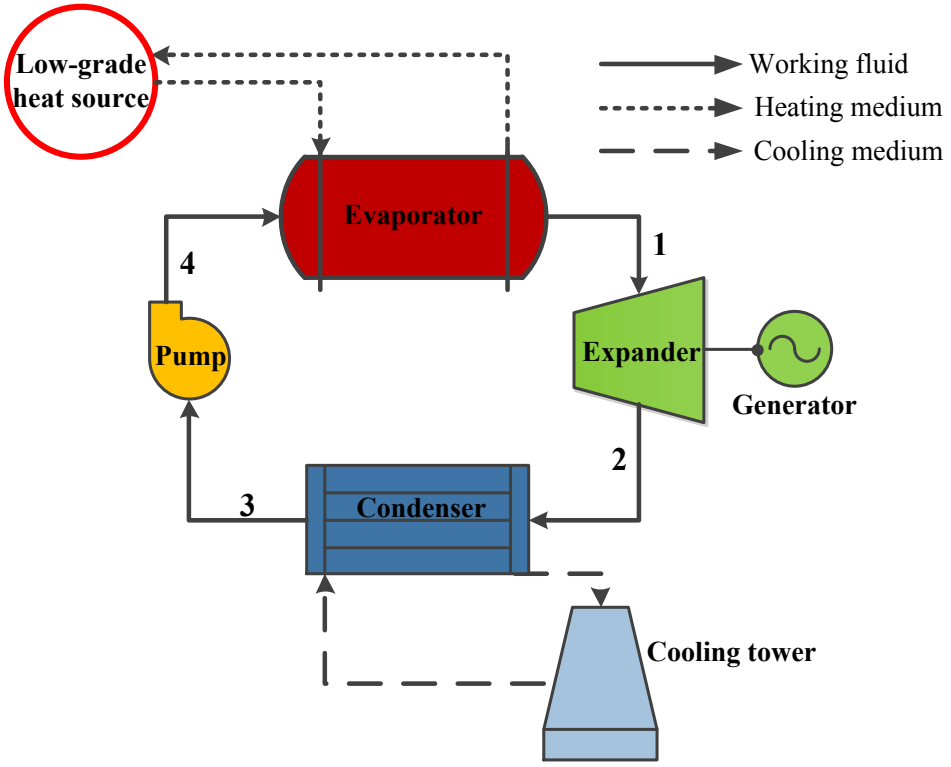

Figure 2-1 Schematic of the simple ORC layout

The corresponding temperature-entropy diagram of the simple organic Rankine cycle is shown in Figure 2-2.

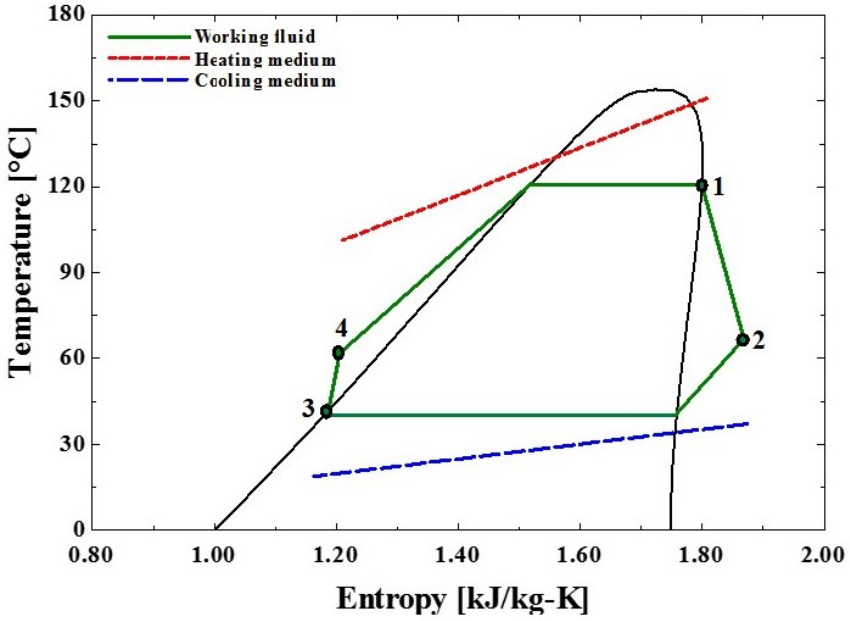

Figure 2-2 Temperature-entropy diagram of the simple ORC

If the turbine exit temperature is considerably high, the thermal efficiency of the simple organic Rankine cycle can be augmented by adding a recuperator (an internal heat exchanger) between the turbine exit and condenser inlet (Wang *et al.* 2011). The recuperator can exploit the residual heat after the turbine for pre-heating the working fluid before it enters the evaporator. In other words, for the recuperated organic Rankine cycle shown in Figure 2-3 the average temperature of heat transfer to the cycle is higher than the simple ORC while the average temperature of heat transfer to the environment is lower than the simple ORC and such differences yield in higher cycle thermal efficiency (Saleh *et al.* 2007).

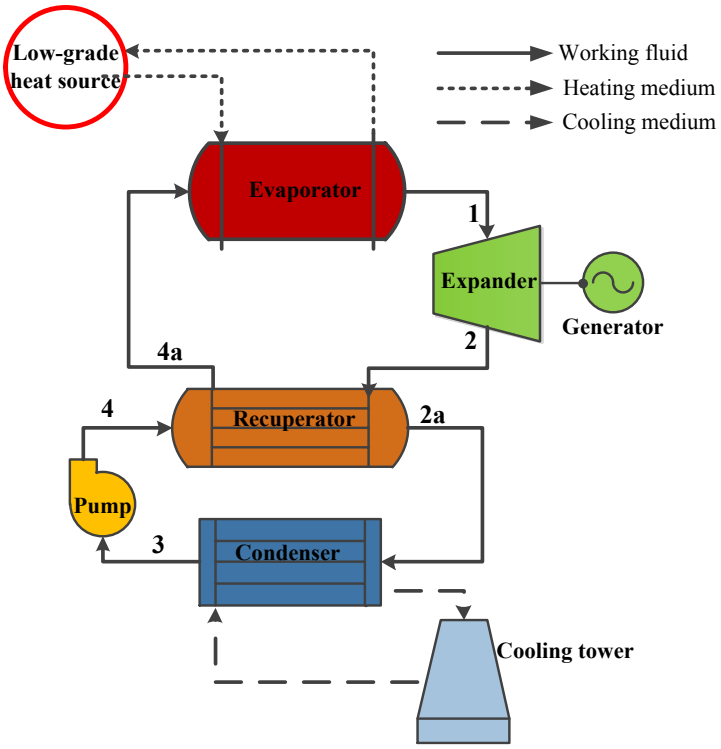

Figure 2-3 Schematic of the recuperated ORC layout

The corresponding temperature-entropy diagram of the recuperated organic Rankine cycle is shown in Figure 2-4. Comparing Figure 2-2 and 2.4 shows the advantage of using the recuperator but with higher complexity and at higher initial capital cost.

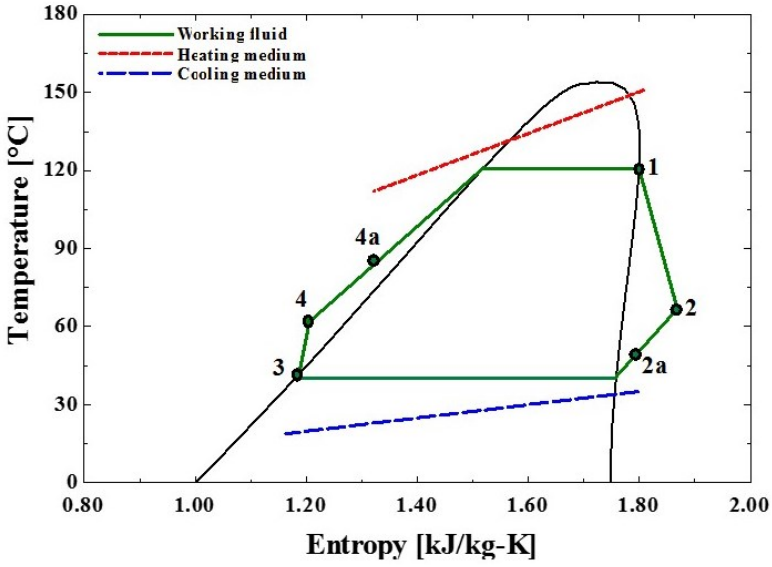

Figure 2-4 Temperature-entropy diagram of the recuperated ORC

2.4. Organic working fluid selection

The choice of working fluid is a crucial factor in the ORC system design and performance. Thermo-physical properties of working fluids have major impacts on the system efficiency, economic viability, components' size, system stability, expander's performance, safety and environmental issues (Schuster *et al.* 2009, Stoppato 2012, Bao *et al.* 2013). The selection of the working fluid is critical to achieve high cycle thermal efficiency as well as maximizing the heat extraction from the hot stream. Organic fluids are often heavy compounds with large molecular weights and low boiling temperature and pressure. They are characterized based on their slope of saturation vapour diagram as dry, isentropic and wet fluids with positive, zero and negative slopes respectively as presented in Figure 2-5. With the lower operating temperatures of the ORC, dry and isentropic fluids are favourable compared to the wet fluids such as water because of their superheated condition after expansion. This eliminates the need for the superheating equipment and the potential damages caused by the impingement of liquid droplets onto the components in the fluid path. These characteristics can significantly reduce the evaporator size and the expander maintenance hence will reduce the capital and running cost of the system.

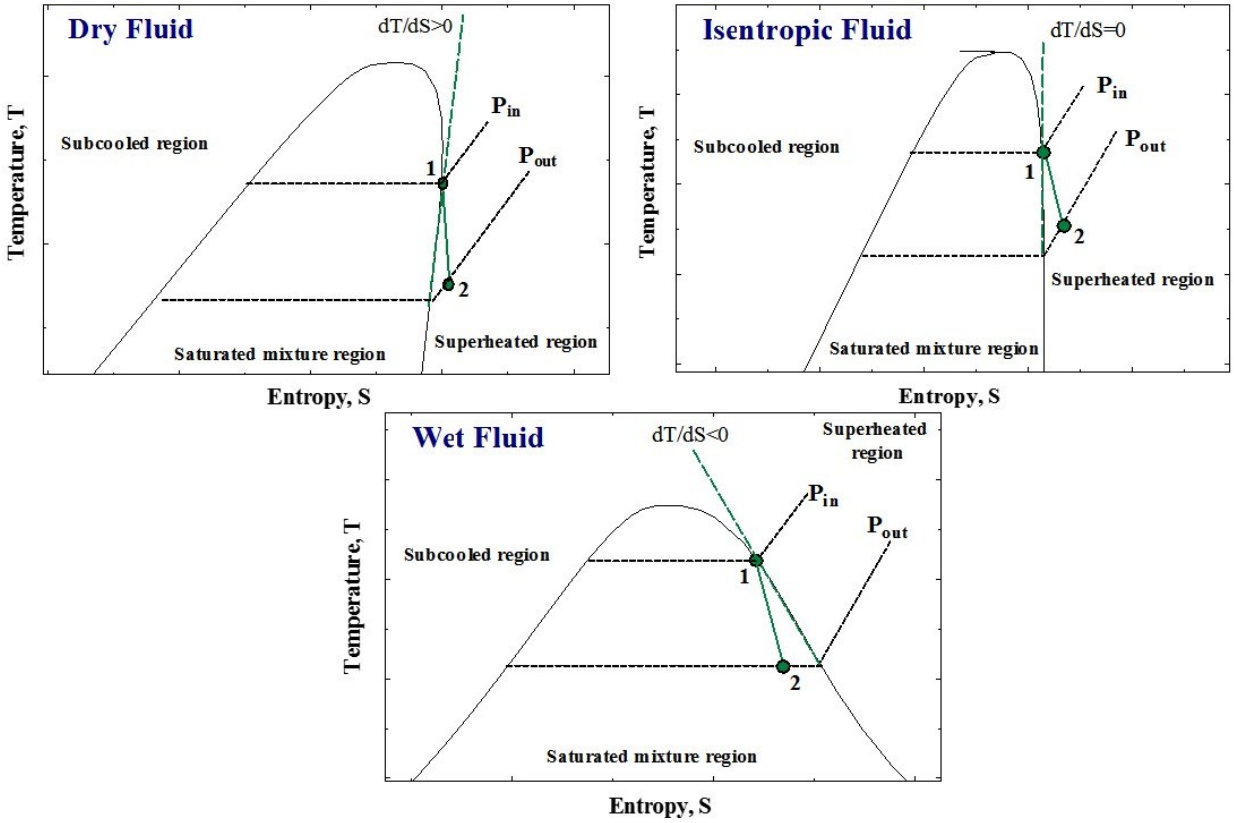

Figure 2-5 Temperature-entropy diagram of dry, isentropic and wet fluids

Apart from this, other important thermo-physical properties that should be considered in the selection of the organic working fluid are discussed below.

- **Latent heat of vaporization:** With the low-grade waste heat sources used in the ORC systems, organic fluids with lower latent heat of vaporization are preferable as this allows generating larger flow rates of vapour with the same quantity of heat (Bao *et al.* 2013).

- **Specific volume:** Having low specific volume (large vapour density) is perhaps one of the most important advantages of the organic fluids. Fluids with low specific volume yield smaller volume flow rates and consequently results in smaller heat exchanger and expander sizes and hence reduce the size and cost remarkably. Figure 2.6 shows the vapour specific

volume of some common organic fluids as well as water and highlights the advantage of organic fluids.

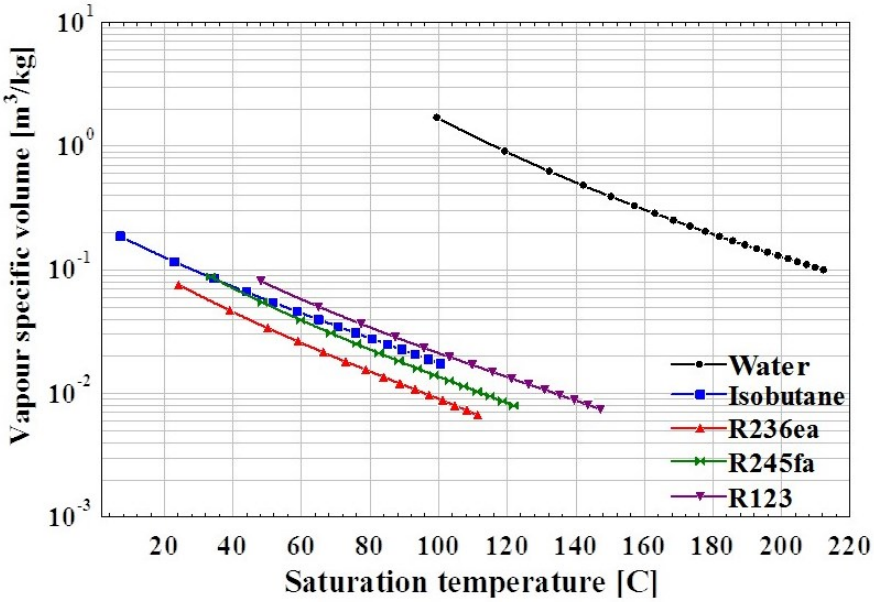

Figure 2-6 Saturated vapour specific volume vs. saturated temperature for some common refrigerants as well as water

- **Critical temperature:** A cycle configuration of good efficiency is obtained from the fluids with a high critical temperature (Invernizzi *et al.* 2007).
- **Thermal stability:** Under high working temperature and pressure, there is a possibility for the organic fluids to decompose leading to corrosion and ignition. Therefore, it is necessary for them to maintain their thermal stability under elevated temperatures.
- **Environmental impacts:** The selection of working fluid should follow the current and possibly future environment protection standards and regulations by having zero Ozone Depletion Potential (ODP), minimal Global Warming Potential (GWP) and low Atmospheric Lifetime (ALT).

- **Safety:** For the operators' health and safety issues, it is preferable to use non-toxic and non-flammable organic fluids to protect the personnel in the case of fluid leakage from the system.
- **Specific heat:** Liquid specific heat should be low so that it can decrease the power consumption by the pump and increase the net power output (Bao *et al.* 2013).
- **Material compatibility:** The organic fluids should have non-corrosive and non-eroding characteristics to most of common engineering materials that are used for manufacturing the ORC components such as heat exchangers, expanders, seals and gaskets and connecting pipes.
- **Viscosity:** A low viscosity both in liquid and vapour phases is beneficial in order to reduce the heat exchangers and pipes frictional losses.
- **Cost and availability:** Due to the international protocols obligating the phase-out of some common organic fluids and also newly proposed legislations such as F-gas regulation, a market search is necessary regarding to the availability and cost-effectiveness of candidate fluid prior to its selection.

However, there is no single optimal organic fluid that can satisfy all the above requirements simultaneously and there is always trade-off between various criteria based on their priority for each individual application. Numerous studies are reported in the literature investigating various procedures and methods for the selection of suitable organic working fluid.

Hung (2001) studied five different working fluids and compared them based on the distribution of irreversibility in different component of the ORC. It was concluded that efficient

operation of the ORC depends on two key factors namely the operating conditions and thermodynamic properties of fluids. Among the investigated fluids, *p*-Xylene showed the lowest irreversibility and proved to be suitable for recovering a high temperature waste heat. Saleh *et al.* (2007) carried out a screening process of 31 pure organic compounds including dry, isentropic and wet fluids such as alkanes, fluorinated alkanes, ethers and fluorinated ethers. They assessed the cycle thermal efficiencies of all these fluids for both simple ORC and recuperated ORC and both subcritical and supercritical cycle configurations. They concluded that the highest thermal efficiencies are obtained by dry fluids with high boiling temperatures in a recuperated ORC where n-pentane showed the highest thermal efficiency of 13%. Drescher *et al.* (2007) developed a software for finding a thermodynamically suitable working fluid for the ORC by examining more than 700 compounds and adopting a new plant design by avoiding the pinch point at the start of vaporization. The maximum cycle thermal efficiencies were reported for the family of alkyl-benzenes. Tchanche *et al.* (2009) investigated the selection of suitable fluids for low-temperature solar ORC by studying the properties of 20 organic fluids and comparing them in terms of thermal efficiency, volume flow rate, expansion ratio, toxicity and flammability. They showed that none of the investigated fluids have all the desirable characteristics and decision making should be based on a compromise between the advantages and drawbacks of each fluid. They concluded that for the mentioned application R134a has the most favourable characteristics followed by R152a, R290, butane and isobutane. Branchini *et al.* (2013) conducted a systematic study of the ORC by calculating its performance based on six different thermodynamic parameters including cycle efficiency, specific work, recovery efficiency and heat exchangers size parameter using three aromatics, three siloxanes, two refrigerants and three hydrocarbons as the working fluids. Their study provided a useful guideline for selecting the most appropriate fluid and ORC configuration based on the defined

operating parameters and application. Larsen *et al.* (2014) used multiple regression models to find the optimum cycle thermal efficiency and then classified the best working fluids for a wide heat source temperature range. From the results refrigerants and alkanes (dry fluids) were dominant among the optimum fluids.

2.5. Comparison with steam Rankine cycle (SRC)

Steam Rankine cycle is probably one of the most mature and reliable technologies for converting large-scale thermal energy (such fossil-fired power plants) into useful power using water as the working fluid. Water itself is characterized as a favourable fluid with good thermal stability, low viscosity, cheap, abundant, efficient energy carrier (high latent and specific heats), non-toxic and non-flammable with no environmental impacts (Tchanche *et al.* 2009). However, water is considered as a wet fluid with a negative slope of saturation curve as shown in Figure 2-5. This is the key difference between water and most of the commonly used organic fluids that are either dry or isentropic as depicted in Figure 2-7. Due to this characteristic of water, superheating (up to 500°C or 600°C) is necessary in the SRC to avoid the condensation during the expansion and the consequent damage to the expander. Moreover, at such high temperatures of the SRC, inadequate turbine insulation could cause uneven or rapid temperature changes in turbine shells, thus resulting in interference and damage to packing seal teeth (Li *et al.* 2011). In contrast, the use of dry and isentropic fluids and low to medium temperature levels (up to 350°C) in the ORC reduces the need of superheating equipment and complex insulation. For water the entropy change between the saturated liquid and vapour lines is much larger than the organic compounds as shown in Figure 2-7. Such feature results in high irreversibility in the evaporator for the SRS and consequently smaller exergy efficiency compared to the ORC. However, the large latent heat of water is advantageous compared to organic fluids as for the

same amount of thermal heat, lower water mass flow rate is required and consequently the pump power consumption is reduced compared to the ORC.

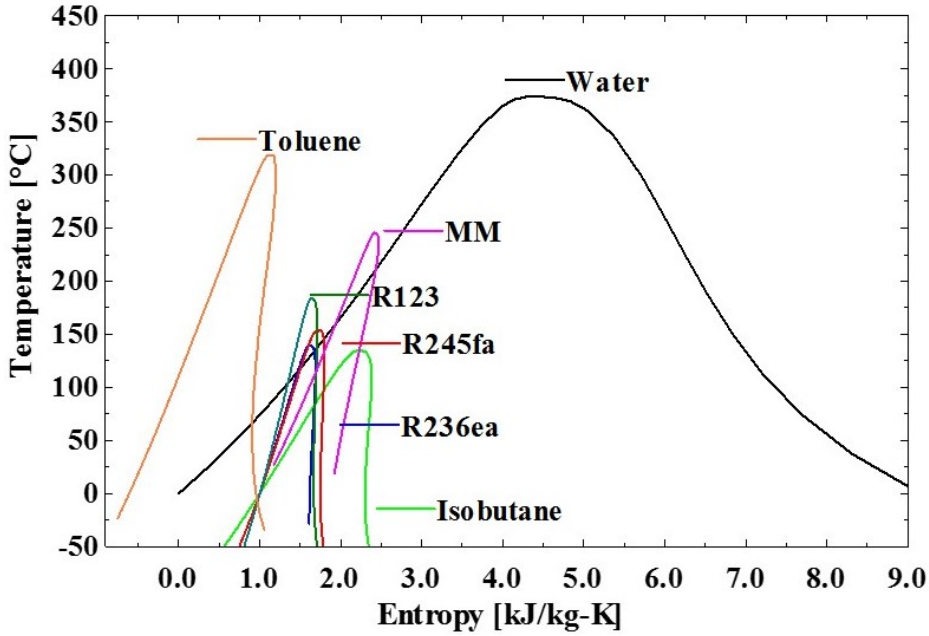

Figure 2-7 Temperature-entropy diagram of water and some common organic working fluids

Moreover, SRC often operates below the atmospheric pressure in order to enhance the thermal efficiency. The inevitable result of sub-atmospheric condensation is the infiltration of non-condensable gases into the system thus requiring the addition of de-aeration equipment or de-aerating feed-water heater (McMahan 2006). In contrast, with the availability of a wide range of organic fluids it is possible to select those with high condensation pressure and facilitate above-atmospheric condensation with no or little maintenance. Furthermore, with the characteristics of water (low density and large enthalpy drop), the expander design for SRC is often complex and costly with multi-stage (more than three) architecture and with extraction points between each stage to increase the cycle efficiency and remove the non-condensable gases. In contrast, with the characteristics of organic fluids (large density and small enthalpy drop), the ORC expander design is simpler with one or two stages and lower peripheral

velocities that reduce the structural stresses. Table 2-1 summarizes the advantages and drawbacks of the SRC and ORC when employed for low to medium grade waste heat recovery.

It can be concluded that, for high temperature applications (above 400°C) and for the CPG systems, the SRC is a more suitable technology considering its cost and complexity (Tchanche *et al.* 2011). But for the low to medium temperature heat sources (solar heat, geothermal heat, industrial and domestic waste heat) and for the DPG applications that require minimum on-site control, maintenance and cost, the ORC is a more viable option and is considered as the core technology that was studied in the present thesis.

Table 2-1 Comparison of ORC with SRC – summery

Steam Rankine Cycle (SRC)	Organic Rankine Cycle (ORC)
Advantages	
1. Working fluid is plentiful and cheap 2. Lower mass flow rate and consequently smaller pump consumption	1. Versatility in terms of heat sources (solar, geothermal and industrial waste heat) 2. Small size due to high fluid density 3. Alleviation of safety concerns due to low pressure and temperature of organic fluids 4. Low capital and maintenance cost due to the superheated condition after expansion and safe operation of expander 5. Higher condensing pressure and no need for vacuum equipment 6. Simpler expander design (one or two stages) 7.Low temperature heat recovery once-through boiler
Drawbacks	
1. Uneconomically low thermal efficiency when exhaust steam temperature drops below 370°C 2. Bulky equipment due to high specific volume of steam (Figure 2-6) 3. High capital cost, safety concerns and complex system due to requirements of high temperature and pressure (500°C and 60bar) 4. High maintenance cost due to erosion and corrosion of blades caused by steam droplets 5. Complex multi-stage and bulky expander design 6. Mandatory air removal in a condensing mode with sub-atmospheric pressure	1. Higher mass flow rates and larger pump power consumption 2. Lower efficiency at higher temperatures (above 450°C, (Quoilin 2011))

2.6. ORC applications

2.6.1. Biomass combined heat and power (CHP)

Biomass is the world's fourth largest energy source providing about 10% of the world's energy demand (IEA 2008). Biomass is widely available from several industrial and agricultural processes such as furniture industry or agricultural and forest residues. Biomass has great potential in providing combined heat and power (CHP) simultaneously. Biomass can be transformed into heat using combustion and the heat can be converted to electricity using the ORC. Such systems has received growing attention especially for the DPG systems with low power capacity (Tchanche *et al.* 2011). Most of the ORC biomass systems are binary cycles as shown in Figure 2-8.

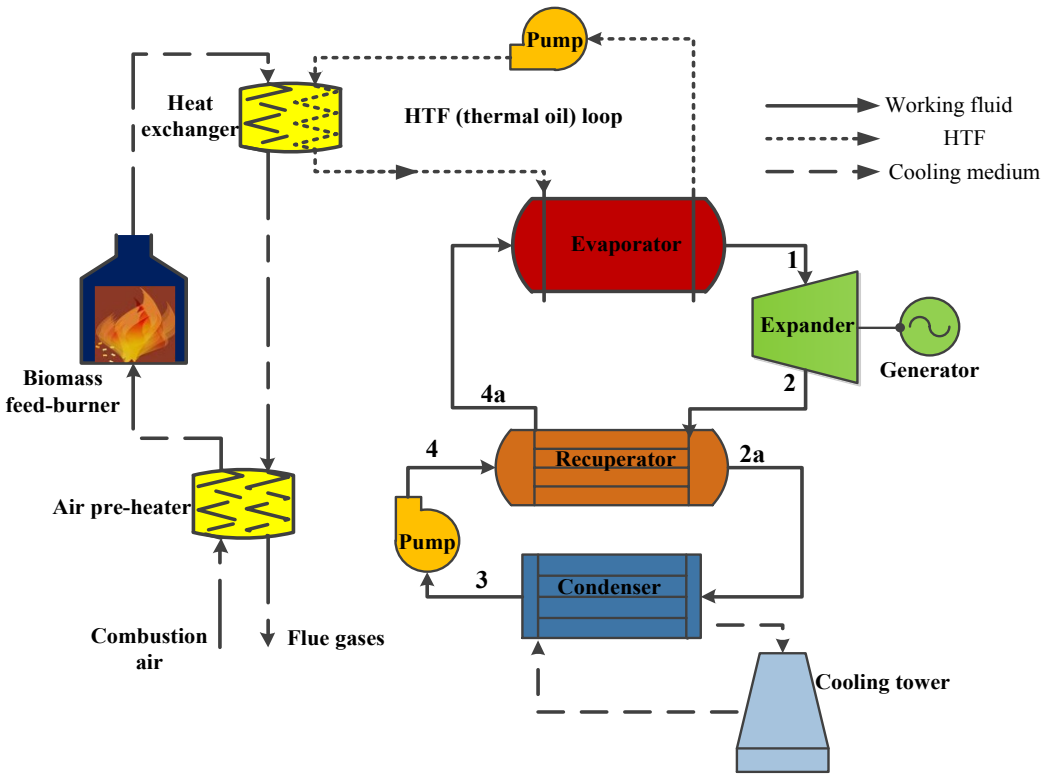

Figure 2-8 Schematic of a biomass CHP ORC system

The heat form the biomass feed-burner is transferred via the flue gases to the heat transfer fluid (thermal oil). Then the hot thermal oil is directed to the ORC evaporator to vaporize the organic working fluid. The use of intermediate heating medium (thermal oil) has some advantages such as low pressure in the evaporator, insensitivity to the load changes, simple and safe control and operation (Tchanche *et al.* 2011).

Liu *et al.* (2011) studied the thermodynamic modeling of a $2kW_E$ biomass-fired CHP system with the simple ORC using three fluids as HFE7000, HFE7100 and n-pentane. They showed that both superheating and sub-cooling are detrimental to the ORC thermal efficiency. The reported overall CHP efficiency is in the order of 80% with the electrical efficiency in the range of 7.5% to 13.5%. They concluded that the ORC efficiency is dependent on several factors including the modeling conditions, working fluids, hot water temperature in the biomass boiler and the amount and quality of heating supplied by the CHP system. Qiu *et al.* (2012) conducted an experimental study of a biomass-fired micro-CHP system based on the recuperated ORC for domestic applications using a $50kW_{th}$ biomass-pellet burner. They used vane type rotary air motor as the expander and HFE7000 as the working fluid and obtained 0.861kW of electricity and CHP efficiency of 78.69% and electrical efficiency of 1.41%. They suggested that the cooling water temperature (46°C) at the exit of the condenser is suitable for domestic washing and underfloor heating. Prando *et al.* (2015) assessed the energy performance of a biomass boiler coupled with the ORC operating with MDM (octamethyltrisiloxane) working fluid under the real operating conditions and identified the potential improvements. They reported that a decrease of 10°C in the district heating network temperature can improve the electric efficiency of the ORC generator by one percent. They also concluded that this temperature reduction reduced the associated losses in the boiler including exhaust latent thermal loss which accounted for 9% of the boiler input power.

2.6.2. Solar power cycles

Solar energy is one of the most promising renewables as it is non-exhaustible, pollution-free and exploitable in most parts of the world. The sun releases 4×10^{26} W of energy, but the radiation strikes the earth surface at approximately 8×10^{16} (Rabl 1985). The amount of energy released by sun in one hour (430×10^{20}J) was found to be more than the world's energy consumption in 2001 (410 x 10^{20}J) (Lewis *et al.* 2006). Energy from the sun can be utilized in electricity generation directly through PV cells or indirectly through solar thermal power systems. Solar thermal power generation using concentrating collectors is a mature technology. Collectors capture the sun radiation and concentrate it on either a focal line or focal point depending on the type of the collector. This radiant heat is used to heat up the heat transfer fluid that passes through the collectors. ORC is a reliable technology for utilizing such low-grade heat especially in small-scale systems for electricity generation. Figure 2-9 shows the schematic of the solar ORC power cycle.

Delgado-Torres *et al.* (2010) analyzed the energy required by the ORC for a solar driven reverse osmosis desalination. They assessed the performance of twelve organic compounds such as R134a, R227ea, propane and R245ca and four different models of commercially available stationary solar collectors including flat plate, compound parabolic and evacuated tube collectors. They considered both indirect vapor generation using water as the heat transfer fluid and direct vapor generation inside the collectors. The reported results showed that dry fluids require smaller unit aperture area than wet fluids except for ammonia. The minimum solar collector aperture unit area of 10-11 m^2/kW was obtained with evacuated tube collector in direct vapor generation method and with solar irradiance of 1000W/m^2.

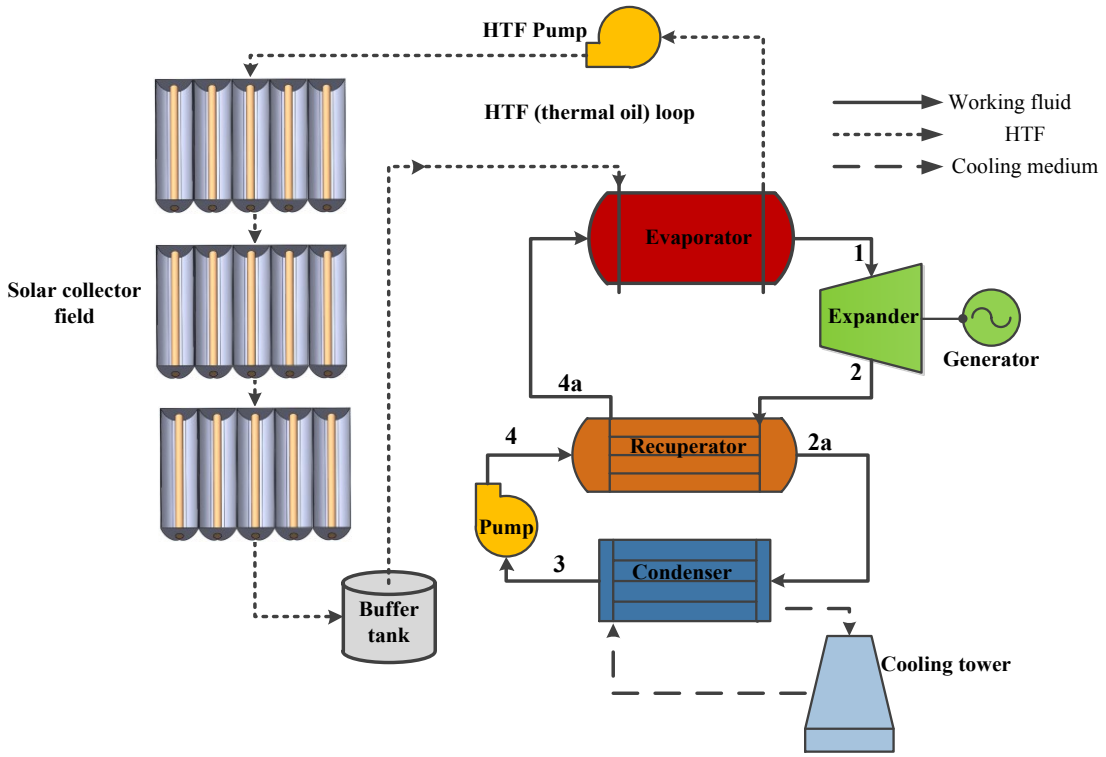

Figure 2-9 Schematic of a solar ORC power cycle

Pei *et al.* (2010) performed the modeling of an innovative solar thermal electricity generation system with regenerative ORC, low concentration ratio compound parabolic collector (CPC) and R123 as the working fluid. They identified the advantages of such system in terms of reduced heat transfer irreversibility and use of phase change thermal storage material. Results showed that the regenerative ORC has electrical efficiency of 8.6% for the irradiance of 750W/m^2 and 4.9% for the non-regenerative ORC. Antonelli *et al.* (2014) studied a thermal power plant equipped with volumetric expander and CPC. Both the expander and collector were analytically investigated in this study in terms of power output, isentropic efficiency, specific fluid consumption, sun incidence angle and fluid temperature. The analysis pointed out the dominant effect of the working fluid saturation temperature on the thermal efficiency, expander performance and power absorbed by the axillaries. They also concluded that at temperatures

between 110°C to 120°C the concentration ratio should be limited to 1.75 to 2.25 for high performance. Wang *et al.* (2014) carried out off-design analysis of a solar-powered ORC using CPC and R245fa as the working fluid. They studied the system's performance with the change in environment temperature, thermal oil mass flow rate and vapor flow rate in the CPC over a whole day and in different months. The results indicated that a decrease in the environment temperature and thermal oil mass flow rate can improve the performance with the maximum exergy efficiency in December and maximum power in June or September.

2.6.3. Geothermal binary power cycles

The geothermal energy (earth's heat) that is naturally embedded in the deep layers of the earth is a renewable form of energy. It is estimated that the energy stored at depth of 3km from the earth surface is as high as $43{,}000{,}000\times 10^{18}$J (DiPippo 2005). This energy can be exploited by drilling deep wells and transferring the hot brine trapped in the sub-layers to the surface via the production well. Depending on the geographical location the brine temperature varies. However, the average geothermal gradient near the Earth's surface is about 300K/km (Tchanche *et al.* 2011). The hot brine can transfer its heat to an organic fluid in the evaporator of the ORC and returns to the injection well at low temperature. Figure 2-10 shows schematic of a geothermal ORC binary power cycle.

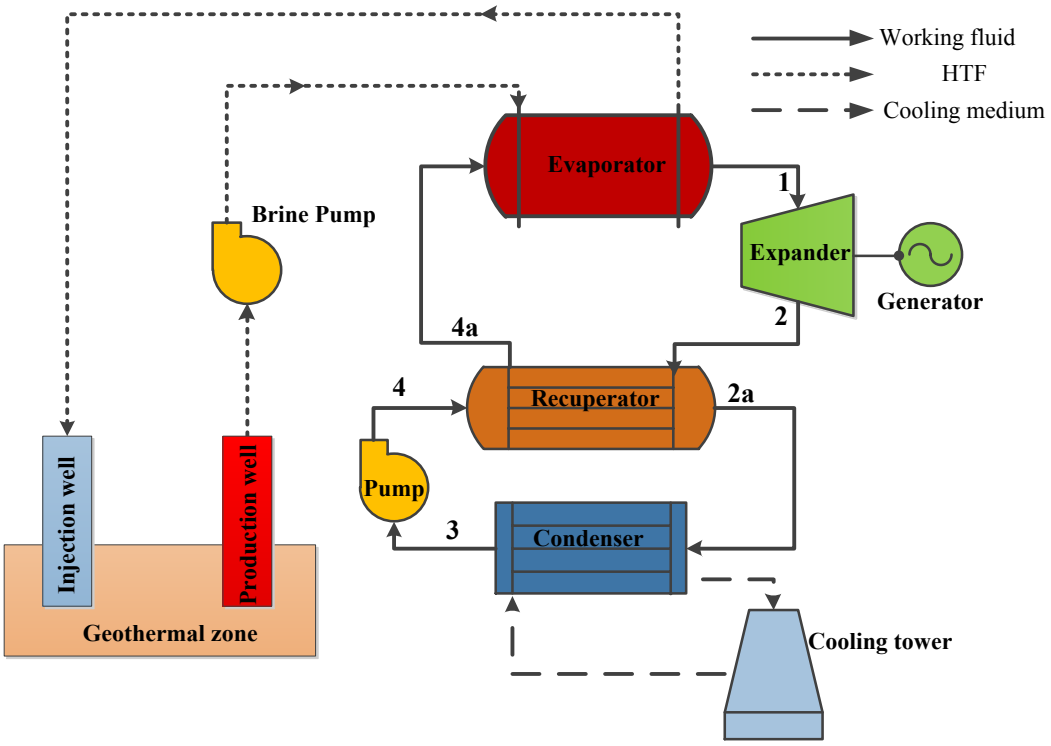

Figure 2-10 Schematic of a geothermal ORC binary power cycle

Madhawa Hettiarachchi *et al.* (2007) proposed a cost-effective design criterion as the ratio of total heat exchanger area to net power output for the ORC driven by geothermal heat. They optimized the proposed objective function (OF) for four organic fluids using steepest descent method. It was shown that the choice of working fluid can greatly affect the OF and for some fluids the difference was more than twice. The minimum OF was achieved by the ammonia while R123 and n-pentane showed higher cycle thermal efficiency. Liu *et al.* (2013) carried out thermodynamic investigation of the ORC with a wet cooling system using five hydrocarbons driven by geothermal heat in the temperature range of 100°C to 150°C and reinjection temperature of 70°C. The results indicated that the optimal condensation temperature for maximum power output is around 29.6°C when the cooling water inlet temperature is about 20°C. Isobutane showed the highest power output at inlet temperatures

greater than 120°C followed by butane. Zhai *et al.* (2014) carried out fluid screening for the geothermal ORC system including both hydrocarbons and hydrofluorinecarbon working fluids. They built a thermodynamic model for optimizing the power output based on the evaporating temperature. Results indicated that the heat source temperature should vary from 110°C to 130°C. Cammarata *et al.* (2014) performed thermodynamic analysis of the ORC for a geothermal primary source using flow-chart numerical tool based on a lumped parameters approach and highlighted the potential of numerical tools in predicting the cycle performance. The results were presented for isopentane and isobutane in the form of temperature –entropy diagram to quantify effectiveness and benefits of the investigated scenarios.

2.6.4. Internal combustion engines (ICE) waste heat recovery

On average, two thirds of the fuel energy consumed by an ICE is wasted through the exhaust gases and the cooling liquid (Glavatskaya *et al.* 2012). A typical spark ignition ICE with a thermal efficiency ranging from 15% to 32%, releases 1.7 to 45kW of heat through the radiation (at a temperature close to 80-100°C) and 4.6-120kW via the exhaust gas (400-900°C) (El Chammas *et al.* 2005). This waste heat from the engine (mainly from exhaust gas and cooling circuit) is large enough to allow efficient heat recovery with the ORC technology (if the exhaust temperature is higher than 450°C, SRC may be a better choice). The electricity generated from the on-board ORC can be used for supplying auxiliary units such as the air conditioning or recharging the batteries. One of the main issues with the on-board ORC in ICEs is the strong transient behaviour of the system which requires complex controlling schemes in order to maintain acceptable efficiency and performance levels. Figure 2-11 shows the position and flow diagram of an on-board ORC for ICE WHR.

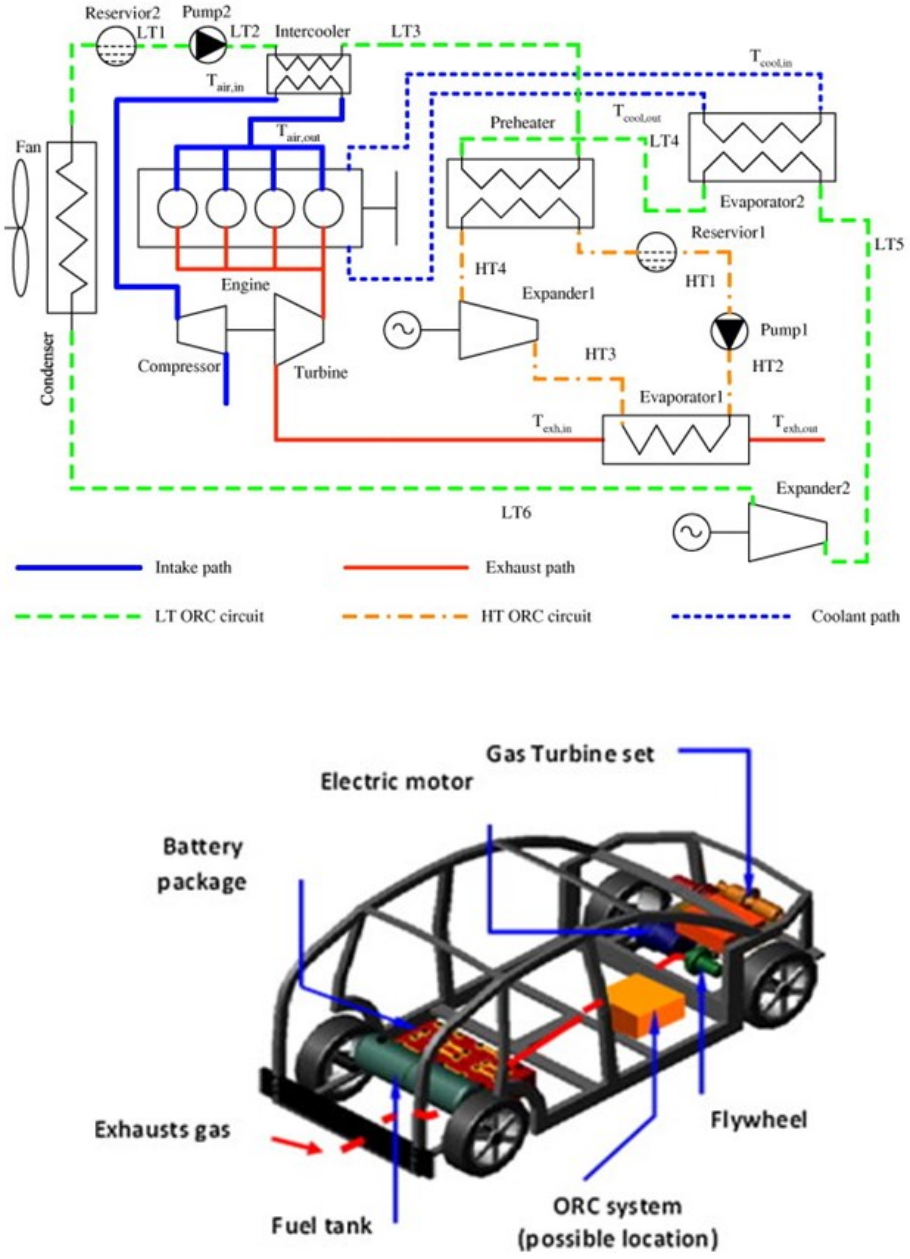

Figure 2-11 (Top) schematic flow diagram of on-board ORC system combined with a light-duty diesel engine (Zhang *et al.* 2013), (Bottom) possible location of ORC in the vehicle (Capata *et al.* 2014)

Endo *et al.* (2007) developed a Rankine cycle system for a hybrid vehicle with automatic control based on the engine load variation. The results showed that the thermal efficiency was increased from 28.9% to 32.7% at 100km/h constant vehicle speed and with maximum power output of 2.5kW. Wang *et al.* (2011) analysed the performance of nine different working fluids

based on ICE transient operating conditions. A model was built in Matlab coupled with REFPROP to compare the performance of investigated fluids. They showed that due to the large variance in the engine exhaust gas operating conditions, definition of the suitable operating range that can maximize utilization of waste heat is crucial. Results indicated that R11, R141b, R113 and R123 exhibit better performance while R245fa and R245ca were shown to be more suitable for this application as they are environmentally friendlier compared to others. Dolz *et al.* (2012) studied two bottoming cycles as SRC and ORC for waste heat recovery of a heavy-duty diesel engine. The amount of waste energy from the diesel engine was evaluated and the two configurations were compared in terms of minimum external irreversibility, complexity, efficiency and power. Zhang *et al.* (2013) conducted the performance analysis of a light-duty diesel engine bottoming with a dual loop ORC for WHR of the engine exhaust using R245fa and R134a. The reported results showed that the output power increases from 14% to 16% in the peak effective thermal efficiency region and from 38% to 43% in the small load region when the engine is equipped with ORC system. Capata *et al.* (2014) studied the feasibility of an on-board ORC WHR system suitable for all types of thermally propelled vehicles especially for ICEs and automotive application. They concluded that the patented system have benefits in terms of reducing the fuel consumption and emissions as the extra power produced by the ORC can be used for vehicle auxiliaries, though, the system size and weight remained unresolved challenges.

2.6.5. Gas and steam power cycle exhaust heat recovery

It is a common practice in the large-scale power plants to recover the exhaust heat from gas turbines in a Bryton cycle to produce steam for driving SRC system. Usually the exhaust gas from the gas turbine is in the range of 500-600°C which makes the SRC a more attractive option for WHR (Table 2-1). However, with emergence of micro-gas turbines during the 90s

as remote power units and with power capacity of less than 500kW and exhaust temperature of less than 400°C, significant attention has been paid to the WHR of micro-gas turbines with the ORC for small-scale applications in order to increase the overall thermal efficiency. Figure 2-12 shows the schematic of a gas (micro-gas) turbine with a bottoming ORC power system.

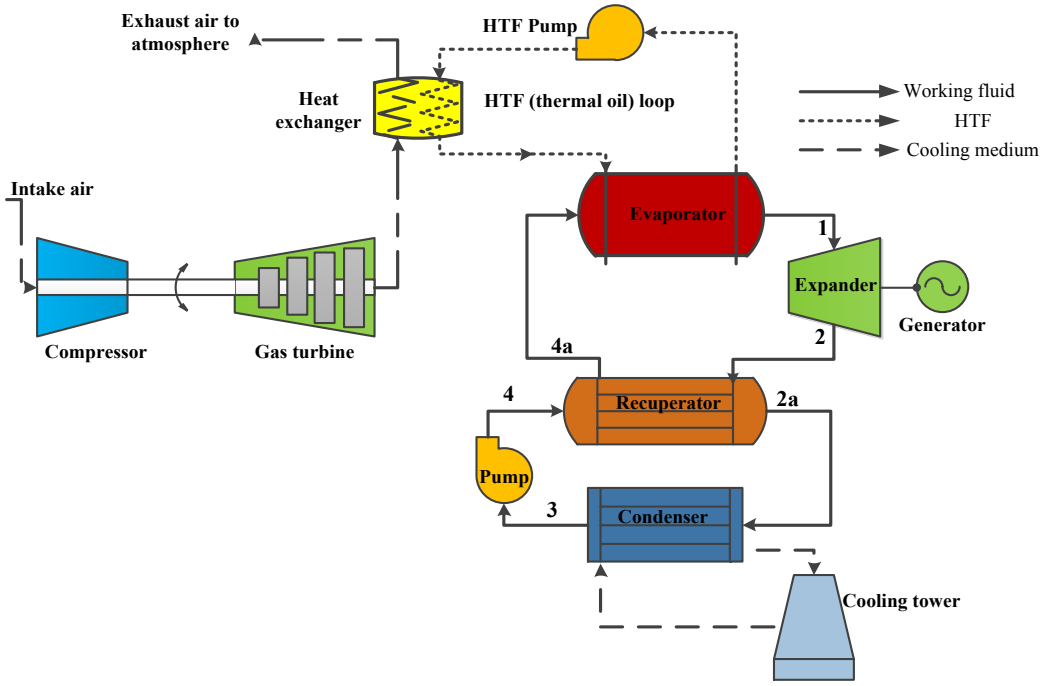

Figure 2-12 Schematic of gas (micro-gas) turbine with the bottoming ORC power system

Invernizzi *et al.* (2007) investigated the feasibility of enhancing the performance of a 100kW$_E$ micro-gas turbine with a bottoming ORC by examining the performance of sixteen different organic fluids. Thermodynamic analysis showed that the combined configuration can increase the net electric power output by 33.3% which was equal to 40% increase in the electrical efficiency when using MM (hexamethyldisiloxane) as the working fluid. Munoz de Escalona *et al.* (2012) analysed the rated and part-load performance of five commercial gas turbines (whether intercooled or recuperated) with a bottoming ORC system using eight organic fluids including MM, R245fa, isopentane and toluene. They examined various control strategies

to capture as much heat as possible from the gas turbine exhaust with the aim of maximizing the overall efficiency. It was observed that keeping vapour flow rate in the ORC system at a constant value produces the maximum power at any operating condition including the part-load. Khaljani *et al.* (2015) carried out thermodynamic, exergo-economic and environmental assessment of a gas turbine with a bottoming ORC with a single-pressure heat recovery steam generator using R123 as the working fluid. The results indicated that the maximum exergy destruction rate occurred in the gas turbine combustion chamber. It was also shown that, increasing the pressure ratio across the compressor and improving the gas turbine efficiency improve the system's performance but at the higher investment cost.

Rashidi *et al.* (2011) conducted parametric optimization of a SRC with a bottoming ORC (ammonia as the working fluid) and two feed water heaters using artificial neural network and artificial bees colony as the optimization schemes. Thermal and exergy efficiencies and specific power output were considered as the objective functions. The results indicated that the maximum values of the specific power and thermal and exergy efficiencies for ammonia are significantly greater than those for water. Liu *et al.* (2012) investigated the waste heat recovery from a conventional SRC with the ORC and examined nine potential organic fluids such as R134a, R245fa, R365mfc and R1234yf for this purpose. They evaluated the performance of all fluids in terms of cycle overall efficiency at various steam turbine exit pressure and cooling air temperature and for both simple and recuperated ORC systems. The reported results indicate that if the bottoming ORC is recuperated the results can be improved and among the investigated fluids benzene showed the best performance with the combined cycle efficiency of 33.35%.

2.6.6. Ocean thermal energy conversion (OTEC) with ORC

Oceans cover more than 70% of the Earth' surface and are the world's largest solar energy collector and storage system. Oceans' energy could be used as a plentiful and inexhaustible renewable energy. Ocean thermal energy conversion (OTEC) is a technology that extracts power from the oceans natural thermal gradient. In other word, the untapped solar energy that is trapped in the upper ocean water layers can be converted into electricity through a thermodynamic cycle. Since the water temperature at depth of about 50m from the sea level is between 20-29°C, the ORC is an effective solution for converting this low-grade heat into power. In such system, the ocean's surface warm water is used as a heating medium to vaporize the organic fluid in the evaporator. Then the cold ocean's water from deeper layers is used as a cooling medium to condense the organic fluid. Figure 2-13 shows the schematic of the closed OTEC system employing ORC for power generation.

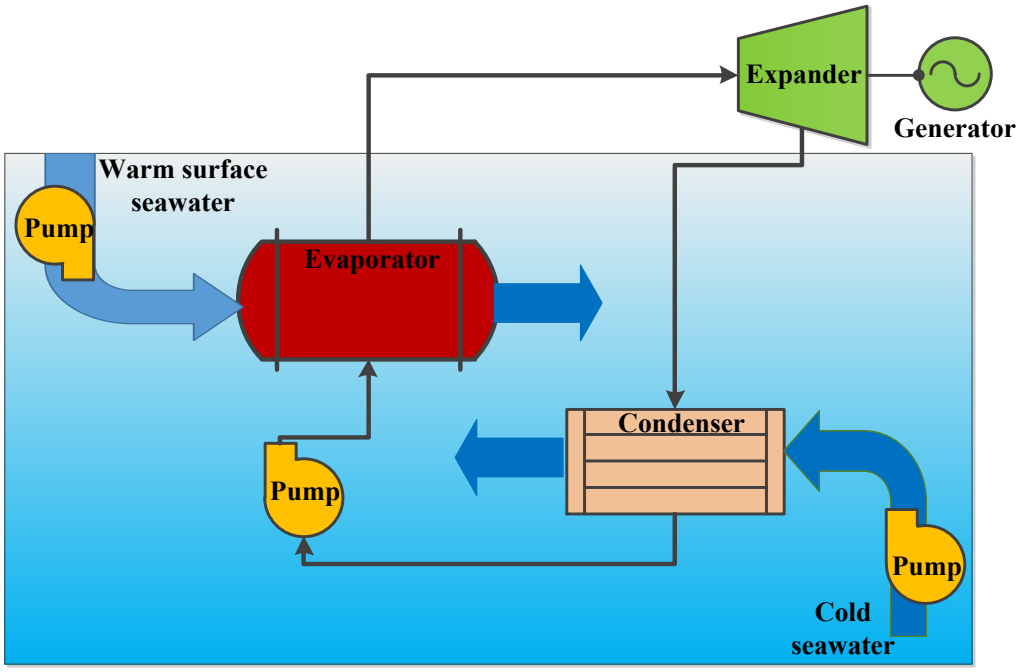

Figure 2-13 Schematic of a closed OTEC ORC system

Wang *et al.* (2010) verified the feasibility of utilizing OTEC combined with solar energy for electricity generation. They studied the effect of turbine inlet temperature and pressure, condenser exit temperature and turbine exit quality on the system efficiency for both dry (i.e. R113, R114, R123) and wet fluids (i.e. R11, R152a, R500). The reported results showed that wet fluids with very steep saturated vapor T-S diagram exhibited better overall performance compared to the dry fluids. Sun *et al.* (2012) carried out the optimization of exergy efficiency for the ORC used in the OTEC system with ammonia and R134a as the working fluids. The system net power output was achieved based on the ORC characteristics which were mainly dependant on the warm seawater temperature, warm seawater mass flow rate and evaporator and condenser temperatures. Reported results showed that ammonia is a better choice if maximizing the net power output is the priority. Furthermore, it was suggested that in small-scales, the selection of heat exchangers size should correspond to the choking point for the maximum net power output. Jung *et al.* (2014) studied the feasibility of the combined OTEC systems which uses the latent heat from the exhaust of a SRC instead of ocean warm surface water. They suggested that such system is advantageous as the OTEC heat source can always be kept at 32 °C. Selection of working fluid, thermodynamic analysis and the impact on the topping SRC when providing steam to the ORC were the main outcomes of this study. Results showed that, this system can improve the condenser vacuum, reduce the pump power consumption and reduce the temperature of discharge side.

Due to the excessive pressure levels and safety concerns of the supercritical ORC systems, majority of the studies explained in this chapter considered the subcritical ORC configuration either with the simple or recuperated layout (Figure 2-1 and 2.3). Therefore, for a subcritical ORC system the maximum evaporation temperature is dictated by the critical temperature of the organic working fluid. The ORC evaporation temperature is classified into three categories

and for each category the most promising fluids are listed based on the above literature survey as shown in Figure 2-14.

Fluid	$T_{critical}$ (°C)
R134a	101.1
R245fa	154.1
R152a	113.3
R236fa	124.9
R227ea	102.8
R143a	72.7
R236ea	139.3
Isobutane	144.9
Ammonia	132.3

Fluid	$T_{critical}$ (°C)
R123	183.7
R245ca	174.6
N-butane	152
HFE7000	164.5
HFE7100	195.3
N-pentane	196.5
Isopentane	187.2
MM	245.5
Ethanol	241.6

Fluid	$T_{critical}$ (°C)
Benzene	288.9
Toluene	318.6
MDM	290.9
MD4M	380.1
D4	313.3
Cyclohexane	280.5

Figure 2-14 List of the best fluids obtained from the literature survey and categorized based on heat source temperature and fluid's critical temperature

2.7. Expansion devices

Expansion machines are the core of the ORC systems and play a critical role in determining the cycle efficiency. In order to improve the cycle efficiency, the selection of expanders is of considerable importance to the development of the ORC systems (Qiu *et al.* 2011). The choice of the expansion machines strongly depends on the cycle operating conditions, type of working fluid and the range of net power output. In general, expansion machines can be categorized into two types as the volumetric type (i.e. scroll, screw, reciprocating piston and rotary vane expanders) and velocity type (i.e. axial flow and radial inflow turbines).

2.7.1. Scroll expander

Scroll compressors have been extensively used in the air-conditioning and refrigeration industry over the past few decades with the total production of 100 million since 2006 (Song *et al.* 2015). Currently, the majority of scroll expanders that are utilized in the low-grade WHR with the ORC are the modified versions of the scroll compressors that are not designed specifically for the ORC operating conditions. This deficiency has led to remarkable performance deviation between the experimental and theoretical results due to major loss factors such as under and over expansion, friction losses, internal leakage, flow pressure drop and heat losses (Lemort *et al.* 2012).

Scroll expanders are categorized into three main types as hermetic refrigeration compressor, automotive air-conditioning compressor and open drive air compressor which are depicted in Figure 2-15 (Song *et al.* 2015). In general, scroll expander combines two spiral wraps in which one is fixed and the other rotates. When the orbiting direction of the moving wrap coincides with the fixed wrap the space in between the two decreases and they work as a compressor. If the rotating direction is reversed, the volume in between the two wraps increases and they work as an expander. In other words, the expansion is generated by the increase in the volume between the two wraps (built-in volume ratio). Figure 2-16 details the working principle of the scroll expander.

Saitoh *et al.* (2007) carried out the experimental study of a low-temperature solar ORC with scroll expander, CPC and R113 as the working fluid. They assessed the performance of the ORC using both hot water and actual solar radiation as the heating medium. Results of the former case showed that the ORC and scroll expander efficiencies of 12% and 63% were achieved respectively.

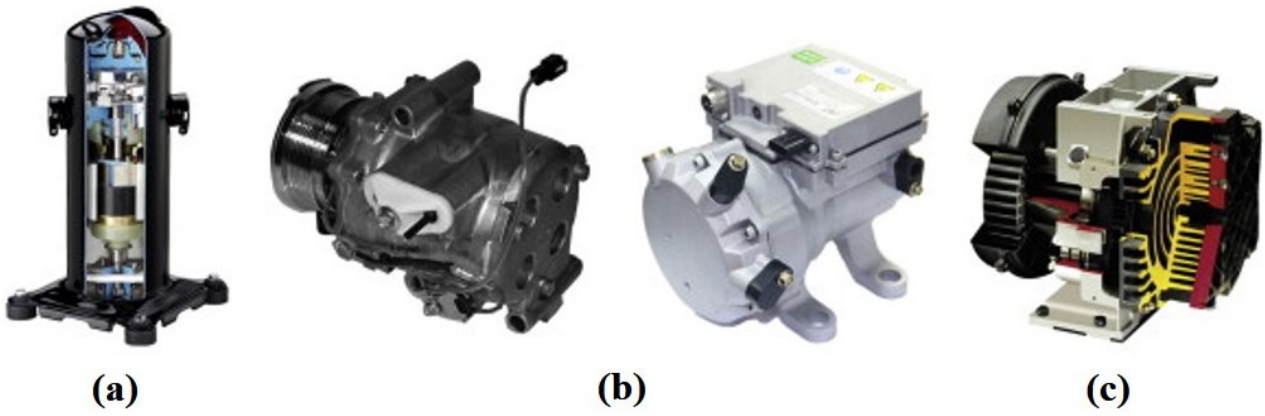

Figure 2-15 Various expander types, (a) hermetic refrigeration compressor, (b) automotive air-conditioning compressor, (c) open drive air compressor (Song *et al.* 2015).

Under actual solar radiation, the ORC and scroll expander efficiencies were reported as 11% and 65% respectively while the total power generation efficiency based on the solar radiation at the aperture of the CPC was reported as 7%. Quoilin *et al.* (2010) proposed a semi-empirical model for the ORC based on the hermitic scroll expander and R123 as the working fluid. The model was validated against experimental results with fair agreement. The experimental results showed two main drawbacks for the expander as significant leakage of R123 to environment and low volumetric performance. The maximum reported cycle and scroll expander efficiencies were 7.4% and 68% respectively.

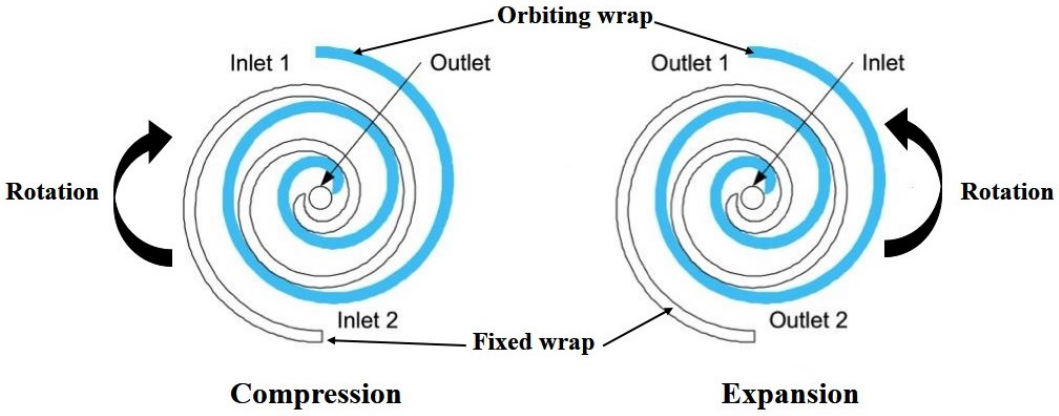

Figure 2-16 Working principle of the scroll compressor and expander

Twomey *et al.* (2013) performed the dynamic modelling of scroll expander with R134a as the working fluid for a small-scale solar ORC in which the model parameters were calibrated experimentally. The validation of scroll expander model showed agreement within ±10% of shaft power and ±5% of rotational speed. For 50m^2 of collector area, the ORC and scroll expander efficiencies were reported as 3.47% and 59% with the total power of 676W. They suggested that the produced power can be consumed during the peak load by utilization of a solar storage.

2.7.2. Screw expander

Screw expanders have been used as expansion devices in ORC plants, especially for geothermal and waste heat applications (Bao *et al.* 2013). Screw expander consists of a pair of meshing helical rotors, a male and a female rotor, contained in a casing which surrounds them with clearances in the order of 50μm (Qiu *et al.* 2011) where such tight clearance significantly increases the cost of the manufacturing. The expansion process in screw expanders has three phases in which at first the inlet high pressure working fluid enter the space between the two rotors and commences the rotation (intake) then the tooth-spacing volume starts to increase due to the pressure of the fluid and creates power as the two meshing rotors rotate (expansion) and finally when the tooth-spacing volume is connected to the outlet the exhaust begins until the tooth-spacing volume reaches zero (exhaust). Figure 2-17 details the working principle of the screw expander.

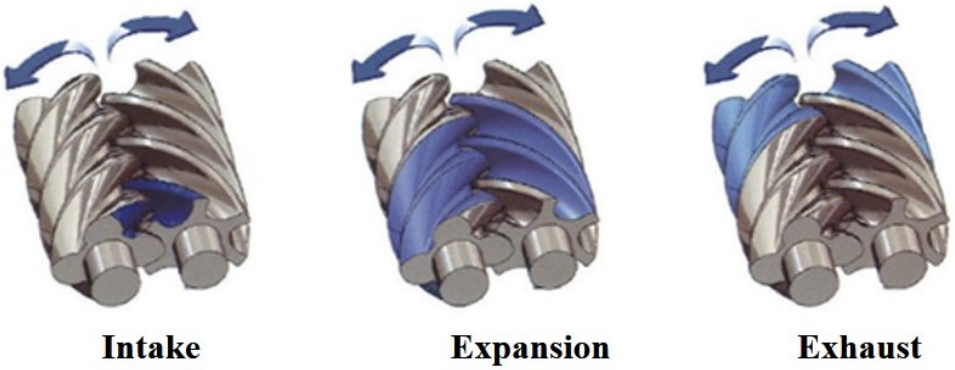

Figure 2-17 Working principle of the screw expander (Zhejiang Turbine Import & Export Trade Co. 2011)

Leibowitz *et al.* (2006) carried out development and experimental study of a cost effective ORC system with twin screw expander and R124 as working fluid with power ranging from 20kW$_E$ to 25kW$_E$. They performed the modelling of two screw expanders as symmetric and "N" types and considered the effect of wet expansion on their performance. The results of demonstration unit estimated a total cost in the range of $1,500 to $2,000/kW$_E$, depending on size. Wang *et al.* (2011) tested a single screw expander to verify its performance under various operating conditions such as different intake flow, different humidity, constant torque, and constant rotational speed, though, they used air as the working fluid. The reported results showed a total power of 5kW with the inlet pressure of 600kPa, rotational speed of 2850rpm and the maximum total efficiency of 32.5%. They suggested that single screw expanders has good part load characteristics but with poor expander efficiencies in the range of 20% to 30% which was mainly due to the lubrication problems. Ziviani *et al.* (2014) carried out a detailed geometry-based modelling of screw expander for waste heat recovery with the ORC. They developed a rotation-dependent function that describes the geometry of the screw rotors and the engaging surfaces, heat losses, oil-flooded mixing and leakage paths and also validated it with the published studies.

2.7.3. Reciprocating piston expander

Reciprocating piston expanders are complex devices that require accurate inlet and exhaust valve timing with excessive frictional losses due to the large number of moving parts. However, they have been widely used in the majority of ICEs WHR with ORC since a wet expansion can be tolerated with this kind of expander. Figure 2-18 details the working principle of the reciprocating piston expander.

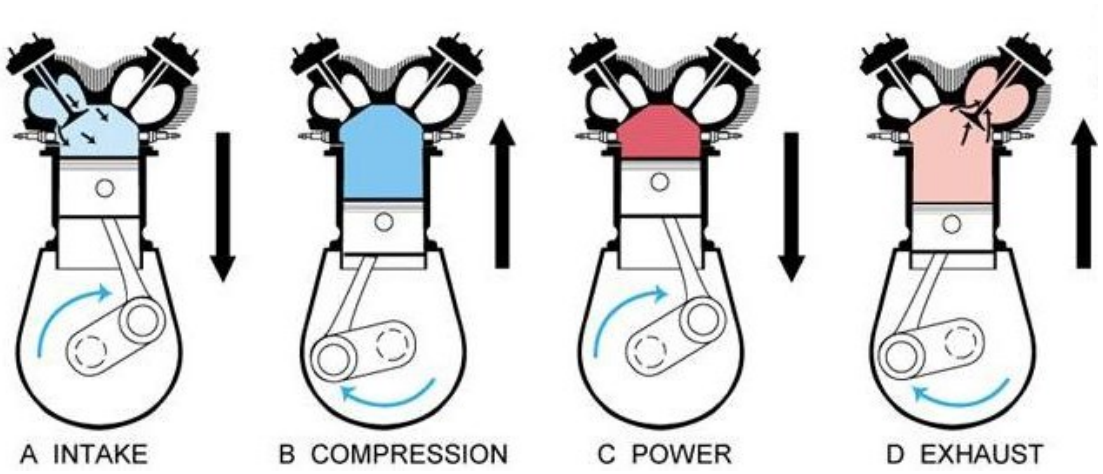

Figure 2-18 Working principle of reciprocating piston expander (Bloch *et al.* 2006)

Glavatskaya *et al.* (2012) proposed a steady-state semi-empirical model of the reciprocating piston expander considering the ambient and mechanical losses and internal leakage. The model was validated with manufacturer's data with a maximum deviation of 4.7%. The reported results showed that the maximum expander isentropic efficiency and volumetric efficiency are 70% and 60% respectively. Clemente *et al.* (2013) carried out the preliminary design of piston expander with the ORC using R245fa and n-pentane as the working fluids. It was shown that the maximum expander efficiency does not exceed 65% due to the low shaft speed.

2.7.4. Rotary vane expander

Rotary vane expander is originally air motor designed to use compressed air to drive rotors (Qiu *et al.* 2011). An air motor converts the energy of compressed air into mechanical energy. With significant modification of air motors (to prevent leakage in the case of organic fluids) they can operate in reverse to act as an expander. Figure 2-19 shows a schematic and exploded geometry of a typical rotary vane expander. The expansion process is obtained, when the chamber spaces between the cylinder wall and the sliding vanes slotted into the rotor increase as the rotor turns clockwise within the eccentric cylinder housing (Qiu *et al.* 2011). The organic fluid enters the vane expander form chamber "A" and commences the rotation. The trapped vapour is expanded as volume of the chamber increases until the leading vane of the chamber passes the outlet port (Qiu *et al.* 2011).

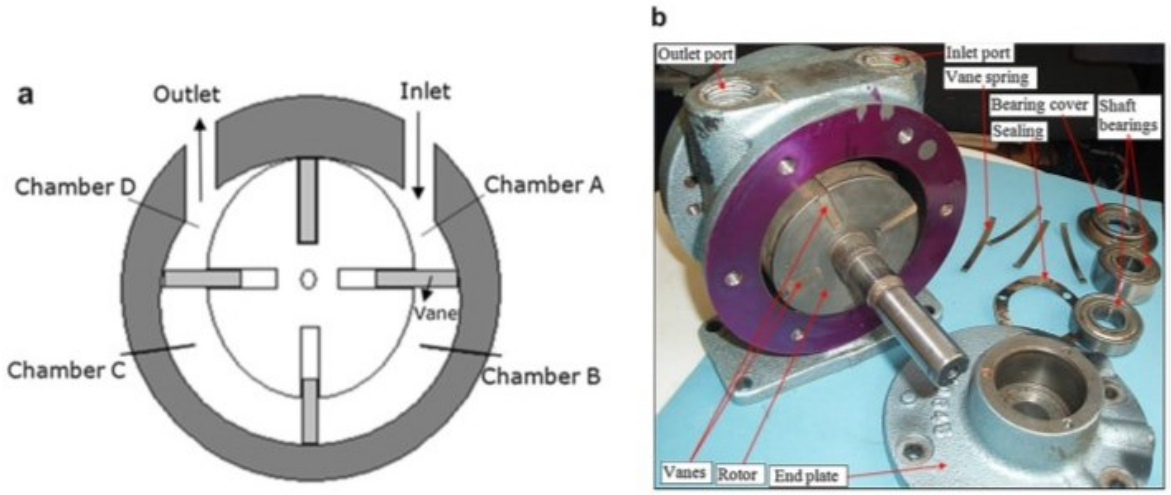

Figure 2-19 Working principle of rotary vane expander (Qiu *et al.* 2011)

Musthafah *et al.* (2010) conducted thermodynamic analysis of the expansion profiles of rotary vane expander used in the ORC with three working fluids as R245fa, ammonia and CO_2 (supercritical). The reported results for expansion profiles showed a similarity at different hot side temperatures. They used this feature to introduce a variable mechanism for expansion

profile fitting in the rotary vane expander. Qiu *et al.* (2012) carried out the experimental investigation of a biomass-fired ORC with rotary vane expander using HFE7000 and HFE7100 as the working fluids. The total electrical efficiency of 1.41% and net power of 861W were achieved under the investigated operating conditions with maximum expander efficiency of 55.45%. Cipollone *et al.* (2014) investigated the performance of the rotary vane expander experimentally with R236fa as the working fluid. The experiments were conducted both at design and off-design operating conditions with the maximum cycle efficiency and power of 7.6% and 1.5kW respectively.

2.7.5. Turbo-expanders (axial flow and radial inflow turbines)

Turbines are devices that convert kinetic energy of a continuously flowing fluid to the mechanical energy of shaft by the dynamic action of a set of moving blades. Turbines are classified as axial flow and radial inflow based on their flow path as shown in Figure 2-20. The obvious difference between the two is that in the radial inflow turbine (RIT) there is significant change in the mean radius between the turbine inlet and exit while for axial flow there is only a minimal change in the mean radius, if any. Such radius change in the RIT produces lossless Coriolis force that creates additional specific power than an equivalent axial turbine. Due to this, RIT requires smaller and/or fewer stages compared to the axial flow turbine which reduces the cost and enhance the compactness. Hence, RIT is particularly attractive for small-scale units with low flow rates but higher expansion ratios (higher specific power output), whereas axial flow turbines are suitable for high power capacities (more than 500kW_E) with large mass flow rates and low expansion ratios.

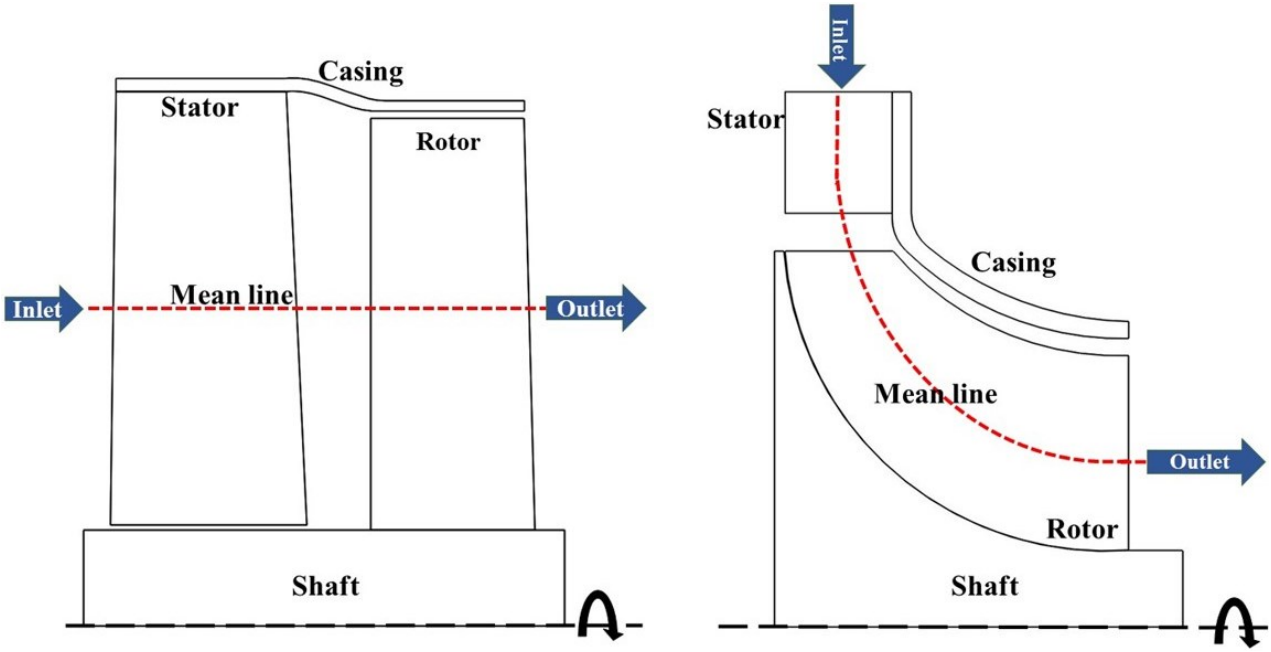

Figure 2-20 Schematic diagram of axial flow (left) and radial inflow (right) turbines

Apart from this, in small-scale units RIT exhibits additional unique advantages over axial configuration as following:

- RIT is manufactured as a one-piece casting or forged whereas an axial rotor often demands separate blades and disk (Moustapha *et al.* 2003).
- One-piece casting of RIT creates higher stiffness and robustness with enhanced rotor-dynamic stability and reduced overall production cost.
- RIT is less sensitive to the blade profile tolerance issues and requires far fewer blades per row which can offer a significant cost advantage, particularly in smaller sized units (Aungier 2006).
- RIT allows for optimum performance over a wider spectrum of off-design conditions by controlling the flow through variable geometry nozzles and smoothing effects of external variations inherent in the ORC applications (Marcuccilli *et al.* 2007).

- For small-scale units where maintaining the blade profile accuracy level required for high efficiency, axial flow turbines may be impractical or prohibitively expensive, RIT is an appealing candidate (Aungier 2006).
- Downsizing the axial flow turbine for small-scale units require the blades to be made very small and numerous, so that the wetted area and hence the frictional losses increase, as do blade blockage effects (Whitfield *et al.* 1990).
- The running clearance necessary between the rotor tip and casing becomes a great fraction of the blade height for small-scale axial turbine and tip clearance loss can become severe, whereas, this issue is relaxed in small-scale RIT due to its geometry.
- Axial turbine generates significant axial force which increases thrust bearing losses and expenses while this is minimal for the RIT (Hoffren *et al.* 2002).

These unique features make the RIT an appealing contender expander for the small-scale compact ORC systems in contrast to the axial turbine which is more suitable for the large-scale systems. Moreover, compared to the volumetric expanders discussed in sections 2.7.1 to 2.7.4, design, modelling and experimental study of the RIT specifically for small-scale ORC systems are scarce in the literature. Marcuccilli *et al.* (2010) conducted an extensive investigation of different working fluids to select the most promising fluid in terms of cycle thermal efficiency for a geothermal binary power cycle and to estimate the most suitable fluid for the RIT operation. The fluids were ranked based on a performance factor which was defined as the ratio of the cycle thermal efficiency to the square of the turbine diameter and such value was assumed to give the best compromise between the performance and size. The turbine diameter was calculated from isentropic enthalpy drop and volume flow rate using a proprietary formula (not shown in the paper). The reported results showed that propylene has the best performance factor

of 0.748 with the turbine total power of 5000kW$_E$ and diameter of 410mm operating at the inlet temperature of 150°C. Sauret *et al.* (2011) performed thermodynamic modelling of the simple ORC for a geothermal binary power system using five different organic fluids. Then for the most promising cycle conditions the one-dimensional modelling of the RIT rotor was conducted in a separate module un-coupled with the ORC model. The maximum power of 332kW achieved by R143a and with turbine expansion ratio varied from 3.3 to 6.9. Reported results showed that maximum turbine isentropic efficiency of 78.5% was achieved by R143a with the turbine inlet total temperature and pressure of 140°C and 60bars respectively and rotor inlet diameter of 140mm rotating at 24000rpm. Pei *et al.* (2011) designed a small-scale ORC with R123 and RIT with the nominal power of 3.3kW$_E$. Modelling results showed turbine isentropic efficiency of 71% operating at turbine inlet temperature and pressure of 100°C and 7.86bar respectively. The reported rotational speed and expansion ratio were 60000rpm and 7.145 respectively. They carried out experimental study of the proposed system to examine the turbine heat transfer and power conversion in the ORC. Their experimental results showed a total heat loss of 34W (based on convection and radiation) and maximum cycle thermal and turbine isentropic efficiencies of 6.8% and 65% respectively with a shaft power of 1.36 kW. Fiaschi *et al.* (2012) built a model for preliminary thermo-fluid dynamic design of a 50kW$_E$ RIT for the ORC and investigated the performance of six organic fluids. The model operated with twelve design inputs including thermodynamic and geometry ratio parameters. In order to achieve acceptable performance inputs were computer-aided adjusted by the operator. The maximum turbine isentropic efficiency of 83% was achieved by R134a with the turbine inlet total temperature and pressure of 147°C and 38bars respectively and with the rotor inlet diameter of 48mm rotating at 54000rpm. Kang (2012) designed an ORC system with nominal power of 30kW$_E$ based on the RIT using R245fa as the working fluid. The cycle analysis was conducted

separately and the operating conditions were used for designing the RIT. Modelling results showed that the maximum turbine efficiency of 75% was achieved at the turbine inlet temperature and pressure of 80°C and 7.32bar respectively. The reported rotor inlet diameter, rotational speed and expansion ratio were 125mm, 20000rpm and 4.11 respectively. The three-dimensional geometry of the turbine was designed based on the geometrical similarity with a compressed air turbine and built in-house. The experimental results of the designed RIT and ORC system showed maximum cycle and turbine efficiencies of 5.55% and 78.7% respectively with the maximum power of 32.7kW_E. Clemente *et al.* (2013) carried out preliminary design of RIT's stator and rotor for a bottoming ORC system operating with R245fa, isopentane and isobutane working fluids. The turbine thermodynamic design parameters were achieved from a separate cycle analysis and then used in the RIT design procedure. The maximum power of 26.3 kW_E with turbine isentropic efficiency of 77% was achieved by isopentane at the turbine inlet temperature and pressure of 180°C and 30.2bar respectively. The reported rotor inlet diameter, rotational speed and expansion ratio for isopentane were 65.8mm, 70000rpm and 19.95 respectively. Wong *et al.* (2013) investigated the re-design and retrofit of an off-the-shelf RIT from turbocharger of a small petrol-driven vehicle for use as the expander in a 1kW_E ORC system. The turbine was selected based on the properties of R245fa working fluid operating at 97°C and 17 bars respectively and with the specific speed of 0.6. One-dimensional modelling of the selected turbine was conducted in order to investigate its off-design performance at various rotational speed, mass flow rate and expansion ratios with the maximum turbine efficiency of 77%. The selected turbine was tested with compressed air at room temperature to evaluate the leakage and lubrication requirements and identify the necessary modifications to the selected turbocharger turbine in terms of seals, casing and bearings.

Based on the literature review discussed in section 2.7, comparison of various expanders used in the ORC system is summarized in Table 2-2 including their nominal power range, rotational speed, advantages and drawbacks. Except for the higher rotational speed of the RIT, it has superior advantages compared to the other volumetric expanders in terms of efficiency, compactness and simplicity and can be a promising expander for small-scale ORC systems. Moreover, summary of laboratory-scale experimental research that investigated the performance of various expanders with the ORC is presented in Table 2-3. The selected organic working fluid, tested operating conditions and the best achieved performance in terms of the expander isentropic efficiency, cycle thermal efficiency and power output are shown in this table. It is clear that, majority of the experimental studies are conducted using the volumetric expanders especially scroll expander with isentropic efficiency in the range of 60% to 70%, power capacity of about 2kW and expansion ratios of less than 5. However, RIT showed better performances with turbine isentropic efficiency in the range of 65% to 85%, power capacity in the range of 1.5 to 30kW and expansion ratios of up to 7. In the power range of less than $1kW_E$, scroll expanders are probably the best choice, though, for the power capacity of between 1 to $5kW_E$, RIT shows competing performance in terms of efficiency and has great potential as a candidate expander. Therefore, there is a need for extensive research on the efficient development of such turbines to further improve the performance of small-scale ORC in the power range of up to 5kWE.

Table 2-2 Comparison of various ORC expanders

Type	Capacity range (kW_E)	Rotational speed	Advantages	Drawbacks
Scroll expander	1-10	<6000	1. Light weight 2. Low rotational speed 3. No inlet and exhaust valves which reduce noise	1. Low power capacity 2. Significant lubrication to operate without wear 3. Most kinetically complex geometry compared to other volumetric expanders 4. Under and over expansion losses if there is mismatch between ORC and expander nominal volume ratios 5. Friction, suction and internal leakage losses
Screw expander	15-200	<6000	1. Tolerate two-phase flow 2. Low rotational speed	1. Lubrication requirement 2. Difficult manufacturing with tight tolerances 3. Critical sealing requirements 4. High cost 5. Limited internal built-in volume ratio due to length of rotor 6. Swept volume limited by the maximum rotor diameter
Reciprocating piston expander	20-100	-	1. Tolerate two-phase flow 2. Higher pressure ratio compared to other volumetric expanders 3. Mature manufacturability	1. Large number of moving parts with high friction and wearing 2. Heavy weight 3. Torque impulse 4. Requires precise timing for inlet and exhaust valves 5. Critical balancing requirements
Rotary vane expander	1-10	<6000	1. Tolerate two-phase flow 2. Stable torque 3. Simple structure	1. Lubrication requirement 2. Low capacity 3. Critical sealing requirements to prevent leakage
Radial inflow turbine	<500	8000-65000	1. High efficiency 2. Light weight 3. Compact layout 4. Mature manufacturability 5. High power to weight ratio 6. Small number of moving parts 7. Stability	1. High rotational speed 2. High Mach number (possibility of local choking)

Table 2-3 Summary of experimental studies of ORC with various expanders

Reference	Expander type	Working fluid & tested operating conditions	Maximum obtained performance
(Zanelli *et al.* 1994)	Scroll	**R134a**; ω=2400-3600rpm; *ER*=2.4-4; T_{eva}=170°C; P_{eva}=6.4bar	η_{exp}=65%; $Power_{mech}$=1-3.5kW
(Kane *et al.* 2003)	Scroll	**R123, R134a**; ω=3000rpm; *ER*=2.3; T_{eva}=120-150°C;	η_{exp}=68%; $Power_E$=7.32kW$_E$; $\eta_{cyc,th}$=13.67%
(Ingley *et al.* 2005)	Scroll	**Ammonia**; ω=2000rpm	η_{exp}=18.2%; $Power_{mech}$=0.209kW
(Peterson *et al.* 2008)	Scroll	**R123**; ω=1400rpm; *ER*=4.57; T_{eva}=174°C; P_{eva}=6.4bar	η_{exp}=49.9%;$Power_{mech}$=0.256kW; $\eta_{cyc,th}$=7.2%
(Saitoh *et al.* 2007)	Scroll	**R113**; ω=1800rpm; T_{eva}=136°C; P_{eva}=9.4bar	η_{exp}=63%; $Power_{mech}$=0.45kW; $\eta_{cyc,th}$=12%
(Lemort *et al.* 2009)	Scroll	**R123**; ω=2660rpm; ; *ER*=5.2; T_{eva}=143°C; P_{eva}=10bar	η_{exp}=68%; $Power_{mech}$=1.8kW
(Manolakos *et al.* 2007)	Scroll	**R134a**; ω=3900rpm; T_{eva}=70°C	η_{exp}=65%; $Power_{mech}$=2.05kW; $\eta_{cyc,th}$=7.8%
(Bracco *et al.* 2013)	Scroll	**R245fa**; ω=3000-4500rpm; *ER*=5-6.5; T_{eva}=90-150°C;	η_{exp}=73%; $Power_{mech}$=1.5kW; $\eta_{cyc,th}$=8%
(Schuster 2011)	Screw	**R245fa**; ω=2300rpm; *ER*=2.65-4.84; T_{eva}=125°C; P_{eva}=10-18bar	η_{exp}=60%; $Power_E$=2.5kW$_E$
(Brasz JJ *et al.* 2000)	Screw	**R113**; ω=3600rpm; *ER*=2.85; P_{eva}=12.9bar	η_{exp}=70%; $Power_{mech}$=20kW
(Qiu *et al.* 2012)	Rotary vane	**HFE7000**; ω=856rpm; *ER*=2; T_{eva}=118°C; P_{eva}=6.7bar	η_{exp}=55.45%;$Power_E$=0.85kW$_E$; $\eta_{cyc,th}$=3.89%
(Cipollone *et al.* 2014)	Rotary vane	**R236fa;** ω=1554rpm; *ER*=3.46; T_{eva}=120°C; P_{eva}=12.7bar	$Power_E$=1.47kW$_E$; $\eta_{cyc,th}$=7.6%
(Zhang *et al.* 2007)	Reciprocating piston	**CO_2**; ω=306rpm; *ER*=2.34; P_{eva}=7.8bar	η_{exp}=62%
(Yamamoto *et al.* 2001)	Radial inflow turbine	**R123**; ω=35000rpm; T_{eva}=75°C; P_{eva}=3.5bar	η_{exp}=48%; $Power_{mech}$=0.15kW
(Kang 2012)	Radial inflow turbine	**R245fa**; ω=20000rpm; *ER*=4.11; T_{eva}=80°C; P_{eva}=7.32bar	η_{exp}=78.7%;$Power_{mech}$=32.7kW; $\eta_{cyc,th}$=5.22%
(Yagoub *et al.* 2006)	Radial inflow turbine	**HFE301**; ω=60000rpm; *ER*=1.1; T_{eva}=70°C; P_{eva}=1.3bar	η_{exp}=85%; $Power_{mech}$=1.5kW; $\eta_{cyc,th}$=7.5%
(Nguyen *et al.* 2001)	Radial inflow turbine	**n-pentane**; ω=65000rpm; *ER*=3.45; T_{eva}=81°C; P_{eva}=3.8bar	η_{exp}=49.8%; $Power_E$=1.44kW$_E$; $\eta_{cyc,th}$=4.3%
(Pei *et al.* 2011)	Radial inflow turbine	**R123**; ω=60000rpm; *ER*=7.14; T_{eva}=100°C; P_{eva}=7.86bar	η_{exp}=65%; $Power_E$=1.36kW$_E$; $\eta_{cyc,th}$=6.8%
(Li *et al.* 2012)	Radial inflow turbine	**R123**; ω=40000rpm; *ER*=6.3; T_{eva}=80°C	η_{exp}=68%; $Power_E$=2.4kW$_E$; $\eta_{cyc,th}$=7.4%
(Inoue *et al.* 2007)	Radial inflow turbine	**TFE**; ω=25000rpm; *ER*=4.8; T_{eva}=77°C	η_{exp}=85%; $Power_E$=13.5kW$_E$; $\eta_{cyc,th}$=6.7%

2.8. Summary and conclusions

From the literature survey the following conclusions can be drawn:

- Majority of conducted ORC studies were mainly devoted to the selection of suitable working fluid for various applications or thermodynamic modelling and optimization of the ORC global performance metrics. But much fewer studies were conducted about the expander design, optimization and experimental testing.

- Among the available experimental researches on the ORC expanders, majority of them used volumetric expanders (especially scroll) in which the machine were retrofitted and modified from the currently built devices (i.e. existing compressors) and not specifically designed based on the selected working fluid's thermo-physical properties and the imposed cycle thermodynamic operating conditions. In addition, very limited literature is available regarding the analytical modelling and optimization of the RIT for small-scale ORC systems with the power range of up to $5kW_E$.

- In all the ORC modelling studies discussed in chapter two, a constant arbitrary expander efficiency was considered for a wide range of operating conditions and for various working fluids ignoring the possibility that the expander was capable of achieving these efficiencies in practice or not. This does not necessarily yield accurate results (as will be shown in this thesis) where each fluid may exhibit different performance under different operating conditions.

- The few available experimental researches that used RIT (Table 2-3) are limited to a single-stage configuration with expansion ratios limited to about seven or less. The reason being that increasing the expansion ratio beyond this limit increases the Mach number at the rotor inlet and creates shock waves with significant

supersonic losses. However, from thermodynamics point of view it is desirable to increase the pressure difference in the ORC (between evaporator and condenser shown in Figure 2-2) in order to increase the cycle thermal efficiency.

- In all of the studies that carried out modelling of the RIT for ORC (Marcuccilli *et al.* 2010, Pei *et al.* 2011, Sauret *et al.* 2011, Fiaschi *et al.* 2012, Kang 2012, Clemente *et al.* 2013), the designer adjusted the turbine design parameters iteratively in order to achieve desirable results and if unacceptable the process was repeated. However, this procedure has several deficiencies as it does not necessarily assure that the optimum combination of the turbine design parameter is achieved for the maximum turbine performance and it is extremely reliant upon the designer experience. Moreover, it does not consider a broad range for the input parameters which increases the possibility of overlooking the best solution. In addition, the results should be manually checked by the designer to ensure that the application and geometrical constraints are satisfied.

CHAPTER 3

METHODOLOGY FOR DEVELOPING RADIAL INFLOW TURBINE (RIT)

3.1. Introduction

This chapter proposed a complete methodology for developing small-scale RIT for DPG applications. The one-dimensional (mean-line) modelling, three-dimensional CFD and FE analyses of a compressed air small-scale RIT will be described in details. The proposed approach will serve as the basis to be further extended for developing highly efficient organic RITs for small-scale ORC systems in the following chapters.

3.2. Dimensional analysis and turbine selection

Turbomachines require a set of non-dimensional parameters that can readily describe the machine's overall performance for assessment, selection and comparison. The data obtained from experimental study of various types of turbomachines are reduced to a manageable number of non-dimensional parameters using dimensional analysis (similitude). This approach is advantageous as it enables the data to be presented in a useful and concise manner and to assess the performance of a range of geometrically

similar machines and to scale existing designs to different sizes (Whitfield *et al.* 1990). Following (Whitfield *et al.* 1990), the basic parameters that influence the behaviour of a turbomachine are collected in the form of a functional relation shown by Equation 3-1 .

$$f\left(d_4, \omega, \dot{m}, P_{t,1}, T_{t,1}, P_{t,5}, T_{t,5}, R, \gamma, \mu\right) = 0 \qquad \text{Equation 3-1}$$

Where d_4 is the rotor inlet diameter, ω is the rotational speed, $\dot{m}$ is the mass flow rate, $P_{t,1}$ and $T_{t,1}$ are the turbine inlet total pressure and temperature, $P_{t,5}$ and $T_{t,5}$ are the turbine exit total pressure and temperature, R is the gas constant, γ is the specific heat capacity ratio and μ is the dynamic viscosity. Application of dimensional analysis reduces the full dimensional parameters to a smaller non-dimensional group as depicted by Equation 3-2.

$$\eta_{ts} = f\left(ER_{ts}, \frac{\dot{m}\sqrt{\frac{RT_t}{\gamma}}}{P_t \pi \frac{d^2}{4}}, \frac{\omega d_4 \pi}{60\sqrt{RT_t\gamma}}, Re, \gamma\right) \qquad \text{Equation 3-2}$$

With the assumption of single working fluid passing through the turbine and fully developed turbulent flow regime, Equation 3-2 is simplified into more common forms as shown below:

$$\eta_{ts} = f(\varphi, \psi, Ma) \qquad \text{Equation 3-3}$$

$$\eta_{ts} = f(N_s, d_s, Ma) \qquad \text{Equation 3-4}$$

$$\eta_{ts} = f(\varphi, \upsilon, Ma) \qquad \text{Equation 3-5}$$

Where φ, ψ, N_s, d_s and υ are the flow and loading coefficients, specific speed, specific diameter and isentropic velocity ratio respectively defined as following:

$$\varphi = \frac{C_{m5}}{U_4} \qquad \text{Equation 3-6}$$

$$\psi = \frac{\Delta h_{actual}}{U_4^2} \qquad \text{Equation 3-7}$$

$$N_s = \frac{\omega\sqrt{Q_5}}{\Delta h_{ideal}^{0.75}} \quad \text{Equation 3-8}$$

$$d_s = \frac{d_4 \Delta h_{ideal}^{0.75}}{\sqrt{Q_5}} \quad \text{Equation 3-9}$$

$$\upsilon = \frac{U_4}{\sqrt{2\Delta h_{ideal}}} \quad \text{Equation 3-10}$$

Several authors (Wood 1963, Balje 1981, Japikse *et al.* 1994) developed various turbine performance correlation charts for different configurations (axial, radial and mixed flow) based on various non-dimensional parameters as shown in Figure 3-1. The selection of turbine is often commenced based on the application's operating conditions and constraints such as rotational speed, mass flow rate and power. Knowing such inputs allows determination of two non-dimensional parameters using Equations Equation 3-6 to 3-10. The intersection of these two non-dimensional values determines the optimum turbine configuration as illustrated in Figure 3-1. In this chapter the defined operating conditions for a small-scale laboratory-based turbine are such that the value of non-dimensional parameters will be laying on the optimum operating region of RITs (as will be shown in the following sections). Hence, this configuration was selected throughout this thesis also due its advantages discussed in chapter two.

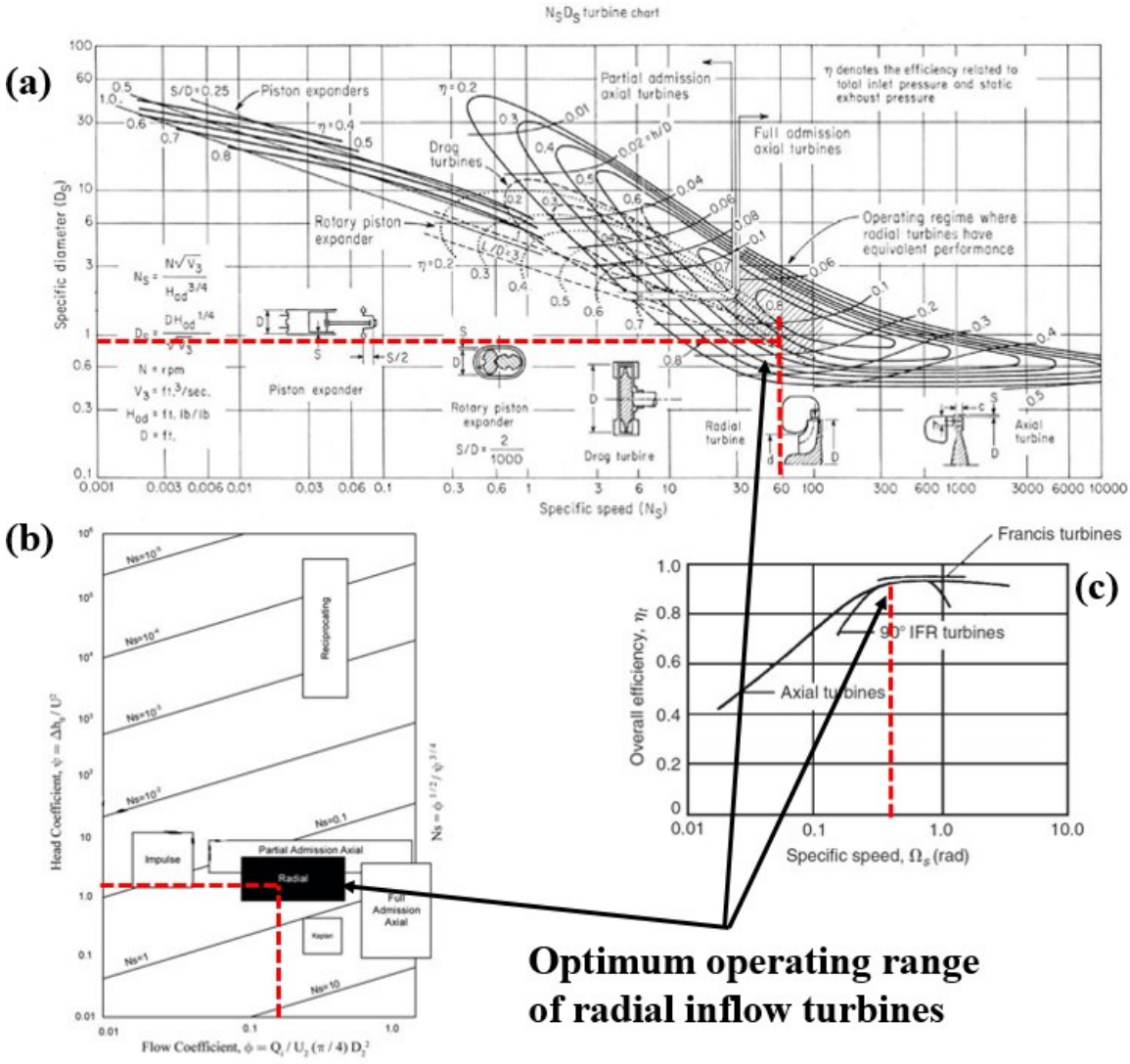

Figure 3-1 Optimal operating range of radial inflow turbines based on various non-dimensional parameters (a) (Balje 1981) (b) (Japikse *et al.* 1994) (c) (Wood 1963)

3.3. Radial inflow turbine (RIT) architecture

The RIT consists of four key components as volute (casing), nozzle, rotor and diffuser as illustrated in Figure 3-2. The incoming fluid is accelerated and distributed uniformly around the periphery of the turbine via volute (1-2). Further acceleration and increase in the tangential component of velocity is achieved by nozzle ring (2-3) before it enters the rotor. The empty space between the nozzle and rotor (3-4) allows for the nozzle outlet wakes to mix out (Moustapha *et al.* 2003).

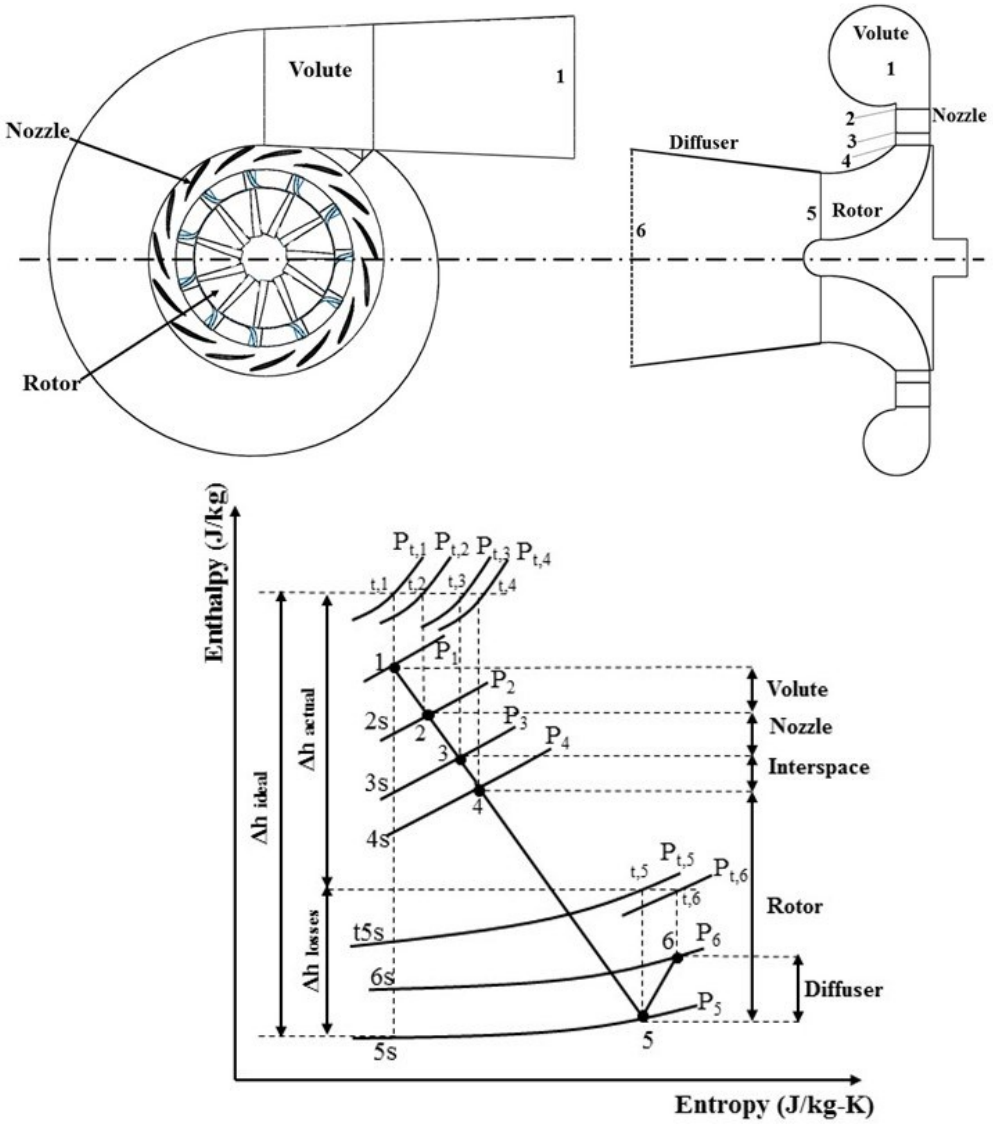

Figure 3-2 Schematic of radial inflow turbine components, (top left) front view, (top right) meridional view, (bottom) enthalpy-entropy diagram of turbine stage expansion

Then the kinetic energy of the fluid is converted into mechanical energy of shaft as it expands through the rotor (4-5). If the kinetic energy of exhaust is significant (with N_s as high as 0.7) a diffuser can be employed to recover the otherwise wasted energy (5-6). The corresponding enthalpy-entropy diagram detailing the expansion process across the stage is also shown in Figure 3-2.

3.4. Development methodology overview

This section provides an overview of the design process of the RIT, starting from the preliminary specification of the turbine performance to the detailed aerodynamic simulations and completing with manufacturing and prototype testing. Figure 3-3 shows the flow chart of the proposed methodology indicating the necessary steps needed to be carried out to achieve the desired outcomes. With the known operating conditions obtained from the cycle analysis or application, the initial stage is the mean-line (one-dimensional) modelling and optimization. Mean-line modelling determines the overall geometrical parameters of the RIT at a set of key stations (Figure 3-2) together with an estimate of the turbine potential performance based on the specified input parameters. Since the mean-line modelling involves the exploration of a very large design space, it is also possible to conduct the mean-line optimization of the turbine performance metrics (i.e. efficiency and power) using analytical optimization schemes such as evolutionary algorithms. In addition, mean-line modelling is capable of predicting the complete performance maps for a wide range of off-design operating conditions. Then for the candidate design suggested by the mean-line modelling, the full three-dimensional blade geometry is defined using the key geometry parameters transferred from the mean-line phase to a CAD package. Although it is fast, the simple one-dimensional (mean-line) model cannot thoroughly capture the complex behaviour of the RIT as the flow is strongly three-dimensional, viscous and turbulent with transonic and supersonic flow regime in most cases. Hence, it is required to evaluate the aerodynamics of the created blade geometry in more details using inviscid or viscose (RANS equations) CFD simulations and if necessary modify the geometry to improve the performance.

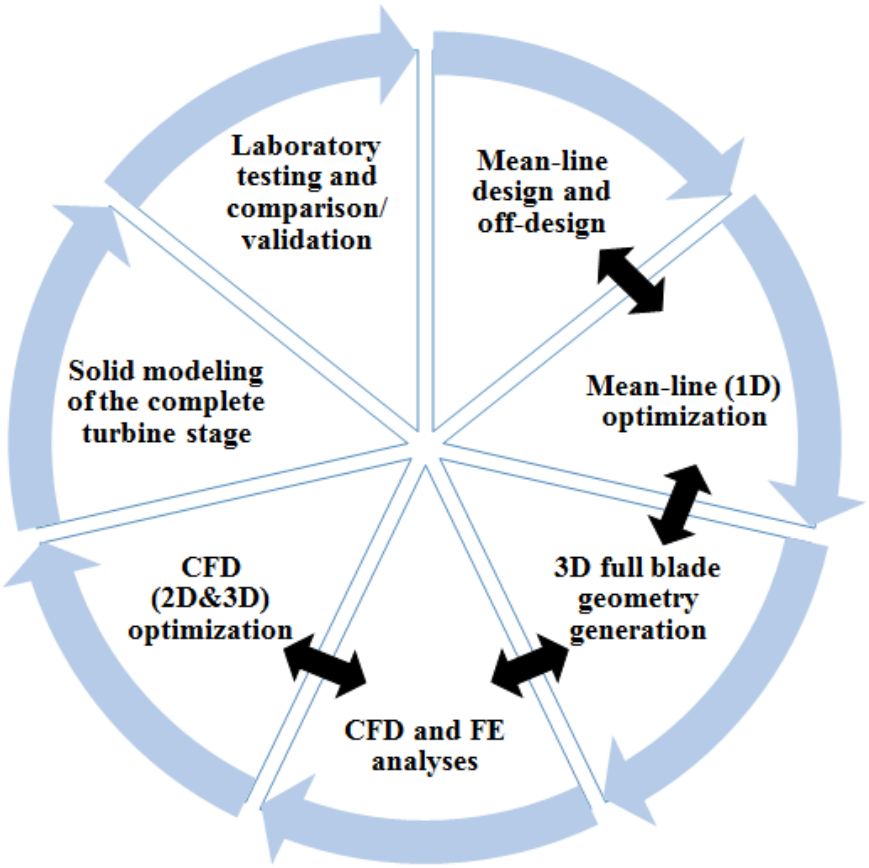

Figure 3-3 Overview of the methodology (adopted and modified from (Japikse *et al.* 1994))

At the same time, it is necessary to evaluate the mechanical integrity of the three-dimensional blade using finite element analysis (FEA) and assess the blade stress and displacement due to the fluid pressure and centrifugal forces. Similar to the mean-line stage, it is possible to conduct the three-dimensional CFD and FEA optimization of the blade in order to further improve its performance. If the results of mean-line or CFD are not acceptable or not satisfying the constraints, the data should be transferred back and forth between the necessary steps (shown by black arrows) until desired outcomes are achieved. When the blade geometries (both nozzle and rotor) are fully satisfactory, it is required to carry out solid modelling and drafting of the complete assembly together with the design and selection of the complementary components such as shaft, bearings and seals. The complete assembly needs to be manufactured for laboratory testing and the

mean-line and/or CFD results should be compared and/or validated with the experiments for necessary modifications or improvements. With such novel approach, the initial large design space is gradually narrowed down and will converge to the final optimum design as it is shown in Figure 3-4.

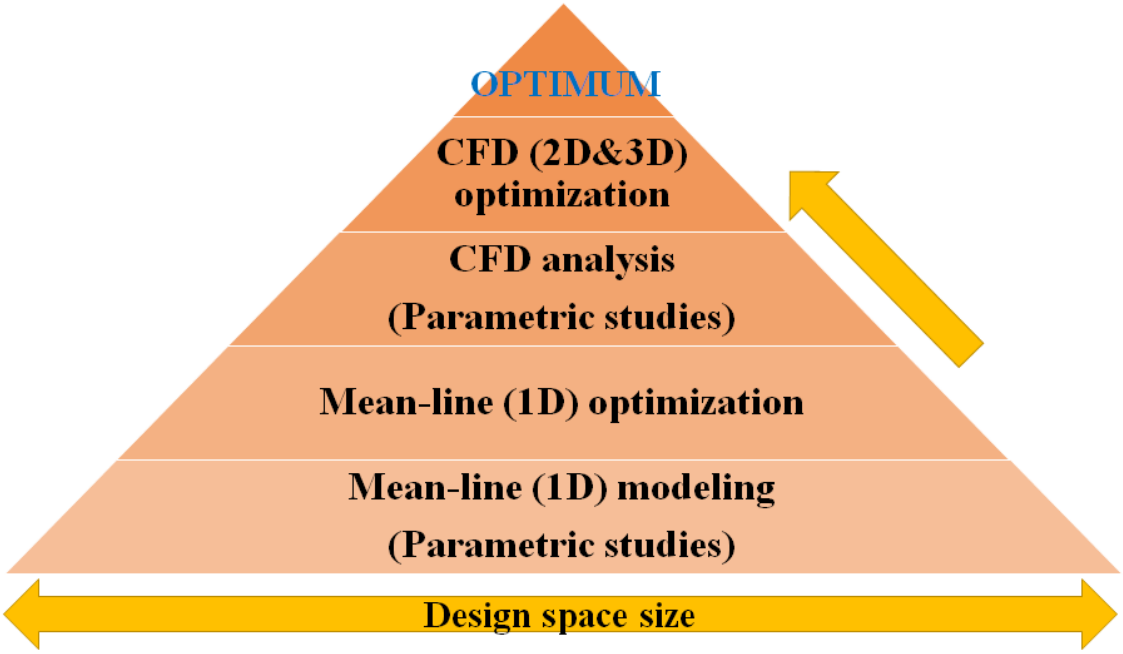

Figure 3-4 Schematic of multi-level design and optimization of RIT

3.5. Mean-line (one-dimensional) modelling and performance estimation

3.5.1. Overview of the mean-line procedure

Mean-line modelling is based on a one-dimensional assumption that the fluid's properties are constant on a plane normal to its direction of motion and thus vary only in one direction that follows the geometry of blades on the mean streamline and such line represents the average of the passage conditions (Whitfield *et al.* 1990). Mean-line modelling determines the flow dynamic properties and geometric parameters (such as rotor inlet and exit velocity triangles, rotor inlet tip and exit radii and blade heights) at key stations throughout the stage. Euler turbomachinery equation and fluid dynamics

principles such as conservation of mass, momentum and energy are the basic equations that build the model together with the inclusion of aerodynamic losses and blockage. Mean-line modelling is a highly iterative process since it requires comprehensive studies of many different configurations by exploring a large design space created by variation of a large group of input parameters. Inputs to the mean-line model include the operating conditions (turbine inlet total temperature and pressure, mass flow rate and expansion ratio), non-dimensional parameters (velocity ratio, specific speed, loading coefficient) and geometry ratios (ratio of rotor exit hub to tip radii) that are either provided as an input file or an output from another code (i.e. cycle analysis program). With the provided inputs and the initial guess of the turbine isentropic efficiency, the preliminary design of the rotor is carried out.

Based on the calculated velocity triangles and basic geometry of the rotor, the overall characteristics for the remaining components such as the nozzle, volute and diffuser are determined. Using these results and the loss correlations, the model determines a more accurate prediction of the turbine stage efficiency. This value is then used as the initial guess for the turbine isentropic efficiency and the process is repeated until convergence is achieved to the specified tolerance. For high expansion ratios that can lead to a choked nozzle and/or rotor throat, the mean-line code includes an additional subroutine to address this effect. Figure 3-5 outlines the flowchart of the mean-line model detailing the overall procedure. The mean-line model is implemented into the engineering equation solver (EES) software (Klein 2013). This allows the use of its extensive and reliable built-in functions to determine the transport and thermodynamic properties for both ideal and real gases throughout the model and use its powerful iterative sparse-matrix solving technique. In this chapter only modelling of the rotor and nozzle based on ideal-gas relationships (using air as the working fluid) is described. Extending the proposed

approach in this chapter to include the modelling of volute as well as real-gas formulation of organic fluids is explained in details in chapter five.

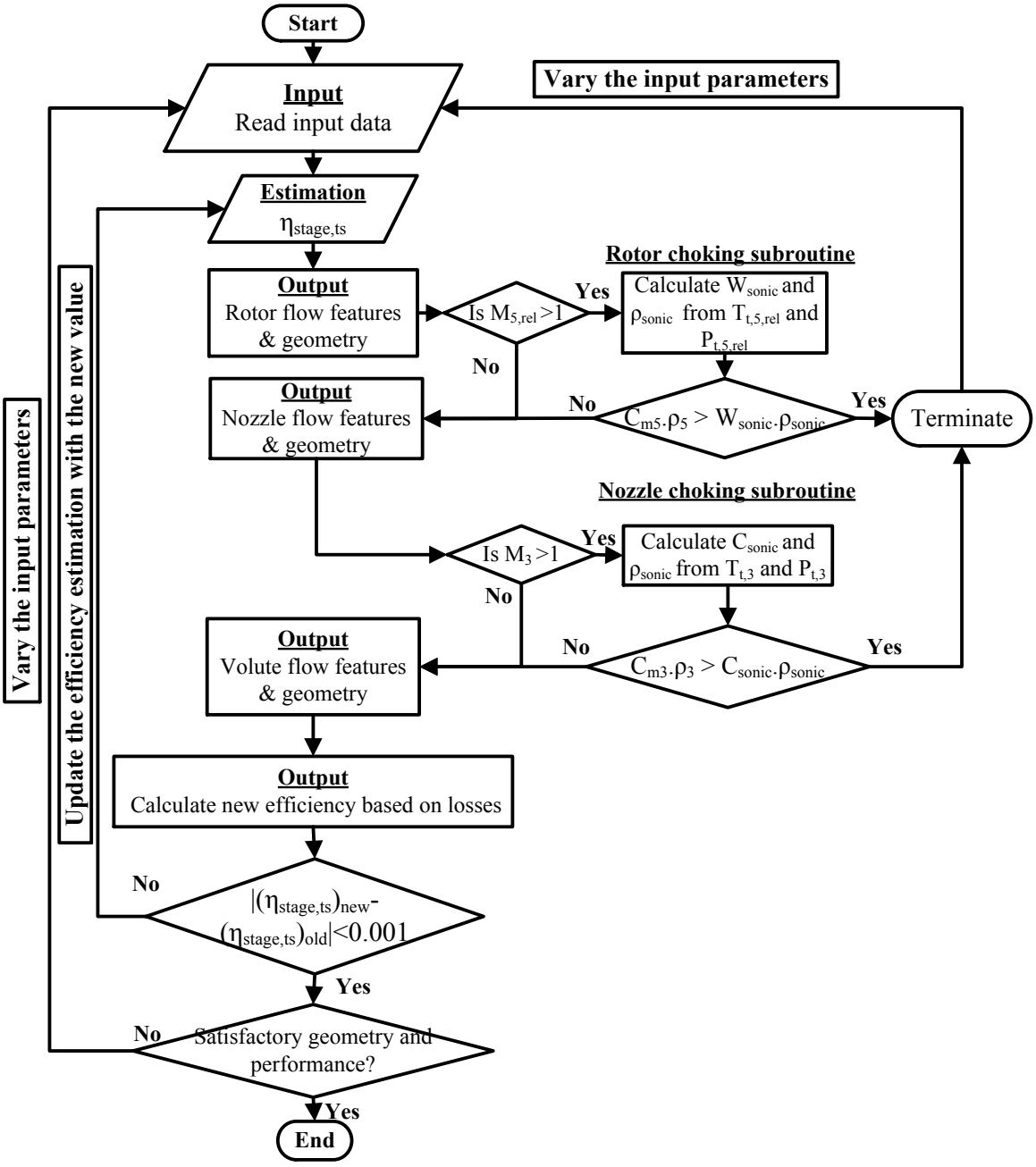

Figure 3-5 Flowchart of the mean-line model adopted from (Rahbar *et al.* 2015 [a])

3.5.2. Rotor modelling

The choice of non-dimensional parameters for rotor modelling is arbitrary and depends on the availability of performance correlation charts and experience, however, the set of N_s-D_s or set of φ-ψ or solely ν are often used. In this chapter isentropic velocity ratio (ν) is employed as it combines stage expansion ratio and rotational speed. Another advantage of utilizing ν is that plotting the turbine efficiency against ν is almost independent of the rotational speed (Whitfield *et al.* 1990). Such non-dimensional parameter together with other turbine inputs (Table 3-1) establish the rotor principal geometry and velocity triangles at inlet and exit as shown in Figure 3-6. The velocity ratio shown by Equation 3-10 can be described with ideal-gas laws using Equation 3-11.

$$\nu = \frac{U_4}{C_s} = \frac{U_4}{\sqrt{2C_P T_{t,1}\left(1 - \left(\frac{P_5}{P_{t,1}}\right)^{\frac{\gamma-1}{\gamma}}\right)}} \qquad \text{Equation 3-11}$$

Where C_s (spouting velocity) is the velocity that has an associated kinetic energy equal to the isentropic enthalpy drop from turbine inlet total pressure to the final exhaust pressure (Dixon *et al.* 2010). With the known turbine input parameters (Table 3-1) spouting velocity (C_s) can be immediately determined leading to determination of the rotor wheel inlet velocity (U_4) with the pre-set velocity ratio value. Consequently, the rotor inlet radius (r_4), actual specific enthalpy drop (Δh_{actual}) and power will be obtained as below:

$$r_4 = \frac{U_4}{\omega} \qquad \text{Equation 3-12}$$

$$\Delta h_{actual} = 0.5 C_s^2 \eta_{stage,ts} \qquad \text{Equation 3-13}$$

$$Power = \dot{m} \Delta h_{actual} \qquad \text{Equation 3-14}$$

Where the stage total-to-static efficiency ($\eta_{stage,ts}$) will be iterated based on the loss models as will be discussed in the following sections.

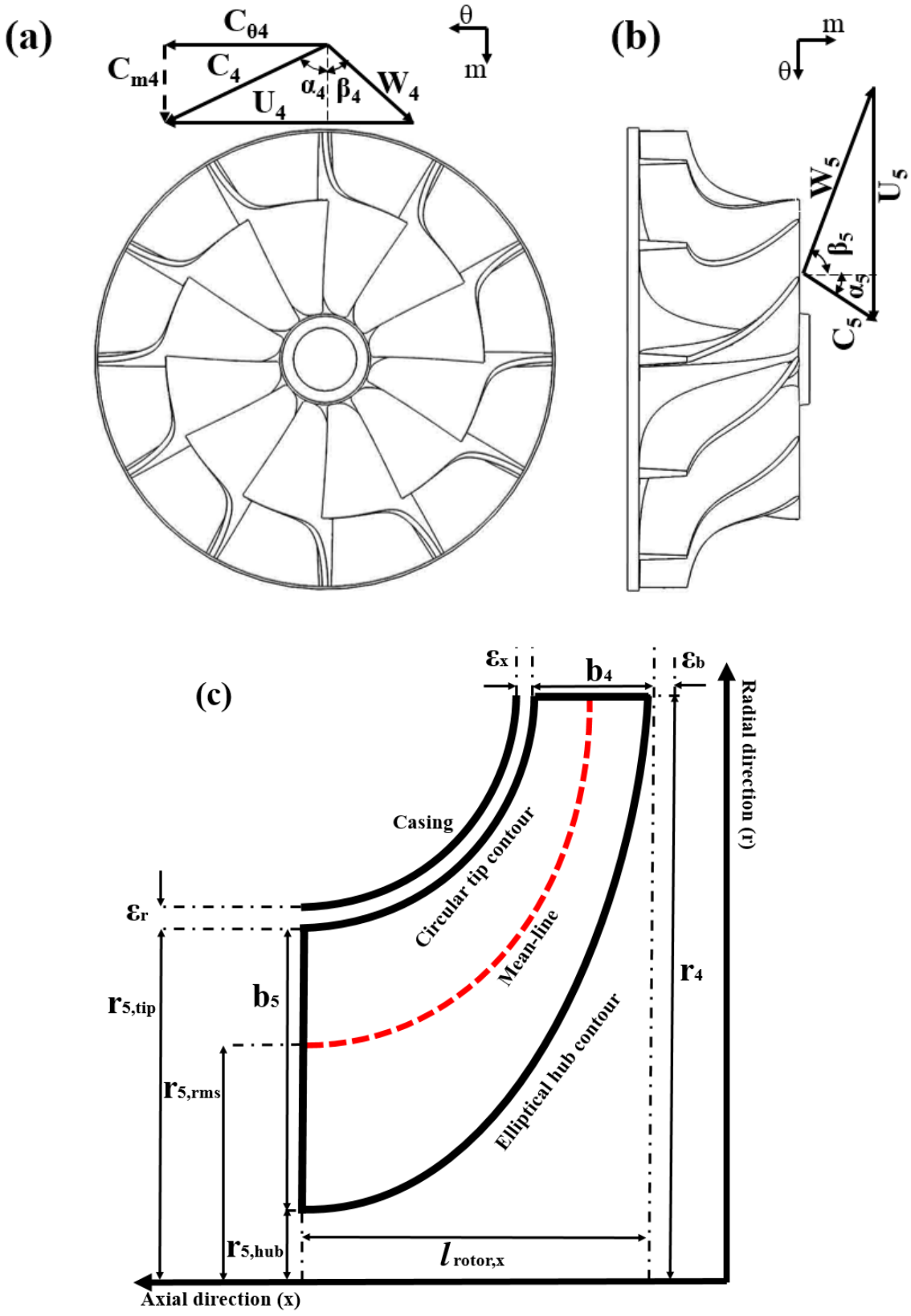

Figure 3-6 Rotor inlet and exit velocity triangles (a, b), meridional view of the turbine rotor with notion of principal dimensions (c)

With the known r_4 the rotor exit hub and tip radii ($r_{5,hub}$, $r_{5,tip}$) can be found with the input geometry ratios shown in Table 3-1 and based on them the rotor exit flow area (A_5) and $r_{5,rms}$ are calculated accordingly.

$$A_5 = \pi(r_{5,tip}^2 - r_{5,hub}^2)(1 - \mathrm{BK}) \quad \text{Equation 3-15}$$

$$r_{5,rms} = \sqrt{\frac{A_5}{2\pi} + r_{5,hub}^2} \quad \text{Equation 3-16}$$

Where BK is the blockage factor due to the effect of boundary layer growth at the rotor exit with the value of 0.1 as suggested in (Baines 2003). With the adiabatic assumption ($T_{t,1} = T_{t,4}$), total thermodynamic properties at the rotor inlet and exit are obtained as following (Moustapha *et al.* 2003, Aungier 2006):

$$P_{t,4} = P_{t,1} - \left(\rho_{t,1} C_s^2 \frac{1 - \eta_{stage,ts}}{8}\right) = P_{t,1} - \left(\rho_{t,1} \Delta h_{actual} \frac{1 - \eta_{stage,ts}}{4\eta_{stage,ts}}\right) \quad \text{Equation 3-17}$$

$$T_{t,5} = T_{t,1}\left(1 - \eta_{stage,ts}\left(1 - \left(\frac{1}{ER_{ts}}\right)^{\frac{\gamma-1}{\gamma}}\right)\right) \quad \text{Equation 3-18}$$

Equation 3-17 is used as an initial estimate of the losses in the nozzle (and volute if applicable). After the first iteration when the geometry of nozzle (and volute) is known, the nozzle (and volute) loss will be used instead. Euler turbomachinery equation (Equation 3-19) was used for calculating the velocity triangles both at the inlet and outlet of rotor blades.

$$\Delta h_{actual} = U_4 C_{\theta,4} - U_5 C_{\theta,5} = \frac{1}{2}\left[\left(U_4^2 - U_5^2\right) - \left(W_4^2 - W_5^2\right) + \left(C_4^2 - C_5^2\right)\right] \quad \text{Equation 3-19}$$

Equation 3-19 shows the advantage of RIT over the axial flow turbine where for the latter the term (U_4^2-U_5^2) has no contribution to the specific power as U is approximately constant from inlet to exit (Figure 2-20). In contrast, due to the significant radius change in the RIT this term has considerable contribution to the overall specific power (specific

enthalpy drop) that underlines its dominance specifically for compact units. As suggested in (Whitfield *et al.* 1990, Moustapha *et al.* 2003, Aungier 2006) the rotor exit swirl angle (α_5) is often considered to be zero in order to reduce the rotor exit kinetic loss and then Equation 3-19 can be readily solved for $C_{\theta,4}$. Subsequently, solution for the velocity triangles are obtained with the known rotor inlet absolute flow angle (α_4) given in Table 3-1 and the trigonometric rules. Afterwards, static thermodynamic properties at the rotor inlet and exit as well as rotor inlet width (b_4) are obtained as following:

$$T_4 = T_{t,4} - \frac{C_4^2}{2C_p} \qquad \text{Equation 3-20}$$

$$P_4 = P_{t,4}\left(\frac{T_4}{T_{t,4}}\right)^{\frac{\gamma}{\gamma-1}} \qquad \text{Equation 3-21}$$

$$T_5 = T_{t,5} - \frac{C_5^2}{2C_p} \qquad \text{Equation 3-22}$$

$$P_5 = P_{t,5}\left(\frac{T_5}{T_{t,5}}\right)^{\frac{\gamma}{\gamma-1}} \qquad \text{Equation 3-23}$$

$$b_4 = \frac{\dot{m}RT_4}{2\pi r_4 C_{m,4} P_4} \qquad \text{Equation 3-24}$$

It should be mentioned that it is sometimes required to add a positive swirl ($\alpha_5 > 0$) in order to compromise between the passage loss and exit kinetic loss. Also in some cases a negative exit swirl ($\alpha_5 < 0$) is required for increasing the power output (Equation 3-19). These cases should be treated differently and their solving method is based on an iterative algorithm shown in Figure 3-7 and is implemented into the mean-line code. With this procedure the velocity triangles and static thermodynamic properties can be determined accurately with any value of α_5 (i.e. positive, zero or negative).

The rotor axial length ($l_{rotor,x}$) and the number of rotor blades (Z_{rotor}) are determined from (Aungier 2006) and (Glassman *et al.* 1976) correlations respectively.

$$l_{rotor,x} = 1.5\left(r_{5,tip} - r_{5,hub}\right) \quad \text{Equation 3-25}$$

$$Z_{rotor} = \frac{\pi}{30}(110 - \alpha_4)\tan\alpha_4 \quad \text{Equation 3-26}$$

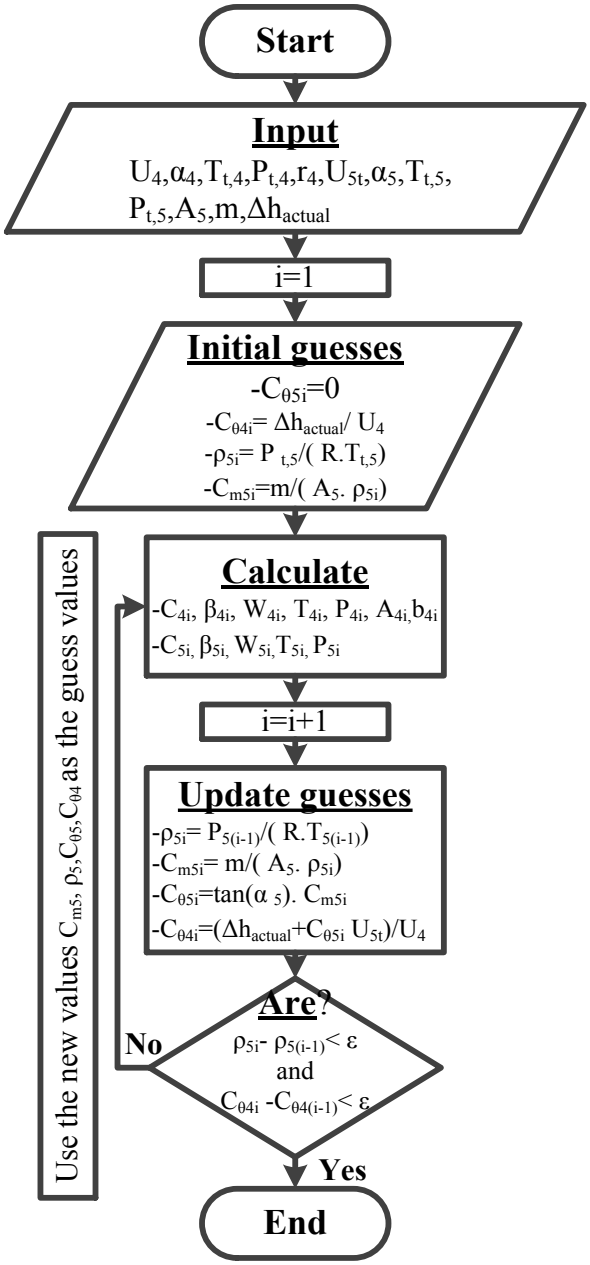

Figure 3-7 Algorithm for calculating velocity triangles and static thermodynamic properties for any α_5

3.5.3. Nozzle modelling

For nozzle modelling a constant blade height equal to the rotor inlet blade height is assumed (b_3=b_4) along the length of nozzle vanes while the nozzle exit absolute flow angle is also set to be the same as the rotor inlet absolute flow angle (α_3= α_4) as shown in Figure 3-8. With the assumption of isentropic expansion in the volute (casing) and interspace (Benson 1970), the thermodynamic properties and absolute velocities (C_2, C_3) both at the inlet and exit are obtained iteratively using conservation of mass and angular momentum, thermodynamic properties at turbine and rotor inlets ($P_{t,1}$, $T_{t,1}$, $Pt_{,4}$, $T_{t,4}$), Equation 3-27 (Watanabe *et al.* 1971) and 3.28.

$$r_3 = r_4 + 2b_4 \cos \alpha_4 \qquad \text{Equation 3-27}$$

$$C_{\theta,3} = \frac{C_{\theta,4} r_4}{r_3} \qquad \text{Equation 3-28}$$

The nozzle inlet to exit radii ratio (r_2/r_3) and nozzle solidity (σ) (ratio of nozzle chord length to nozzle pitch) are set to 1.25 and 1.35 respectively as suggested in (Glassman *et al.* 1976). Consequently the nozzle chord length (C_{nozzle}), nozzle pitch (S_{nozzle}) and number of nozzle blades (Z_{nozzle}) are determined as following:

$$C_{nozzle} = \sqrt{\left| r_2^2 + r_3^2 - \sqrt{\left| (r_2^2 + r_3^2)^2 - \left(\frac{r_2^2 + r_3^2}{\cos\left(\frac{\alpha_2 + \alpha_3}{2}\right)} \right)^2 \right|} \right|} \qquad \text{Equation 3-29}$$

$$S_{nozzle} = \frac{C_{nozzle}}{\sigma} \qquad \text{Equation 3-30}$$

$$Z_{nozzle} = \frac{2\pi r_3}{S_{nozzle}} \qquad \text{Equation 3-31}$$

Safeguard has been implemented in the mean-line code to limit the upper boundary of the thirty blades for the nozzle. Accordingly the nozzle throat opening (O_{throat}) and

nozzle total throat area ($A_{throat,total}$) are determined as below ignoring the nozzle vanes trailing edge thickness.

$$O_{throat} = S_{nozzle} \cos \alpha_3 \quad \text{Equation 3-32}$$

$$A_{throat,total} = O_{throat} b_3 Z_{nozzle} \quad \text{Equation 3-33}$$

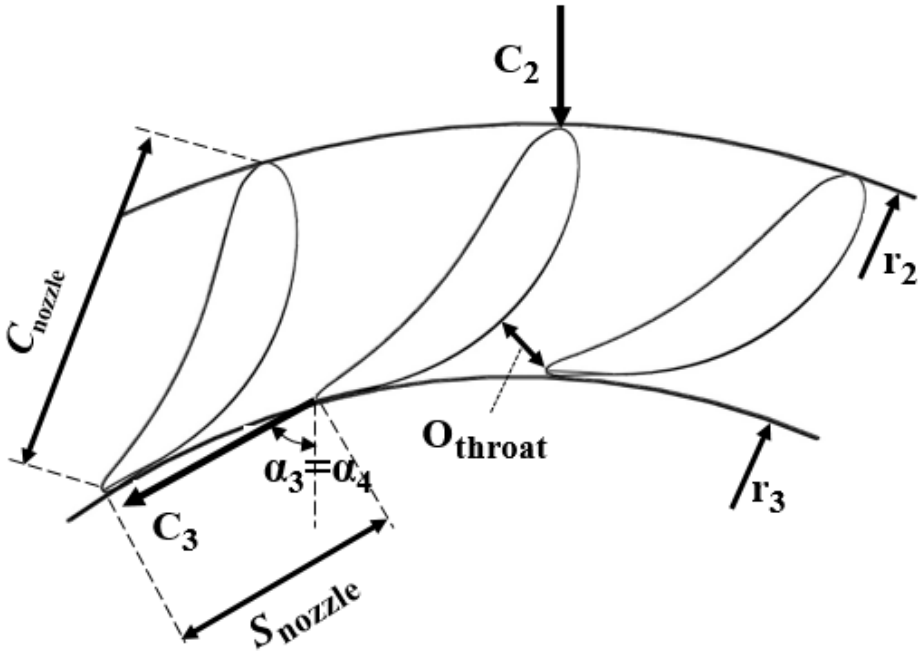

Figure 3-8 Schematic of the nozzle ring with corresponding geometry and velocity vectors

3.5.4. Performance estimation with loss models

The turbine stage total-to-static isentropic efficiency for real and ideal gases is defined by Equation 3-34 and 3-35 respectively (with no diffuser).

$$\eta_{stage,ts} = \frac{\Delta h_{actual}}{\Delta h_{ideal}} = \frac{\Delta h_{actual}}{\Delta h_{actual} + \sum \Delta h_{losses}} = \frac{h_{t,4} - h_{t,5}}{h_{t,4} - h_{5s}} \quad \text{Equation 3-34}$$

$$\eta_{stage,ts} = \frac{1 - \frac{T_{t,5}}{T_{t,4}}}{1 - (\frac{P_5}{P_{t,4}})^{\frac{\gamma-1}{\gamma}}} \quad \text{Equation 3-35}$$

In the present mean-line model, performance estimation of the turbine is obtained iteratively using the loss models as was shown in Figure 3-5. The losses are considered as total enthalpy drop and consist of incidence, friction, secondary, tip clearance, exit

kinetic, windage and nozzle friction losses. With the calculated turbine losses, the new estimate of the turbine stage total-to-static efficiency is obtained and the model employs the new value as the initial guess and the process is repeated until convergence is achieved to the specified tolerance.

3.5.4.1. Incidence loss

Incidence loss is the enthalpy drop due to the flow disturbance at the rotor blade inlet when the rotor flow angle is different form the optimum angle (incidence angle) and is calculated using Equation 3-36 (Suhrmann *et al.* 2010).

$$\Delta h_{incidence} = \frac{W_{\theta,4}^2}{2} \qquad \text{Equation 3-36}$$

Where $W_{\theta,4}$ is the relative tangential (circumferential) flow velocity at the rotor inlet.

3.5.4.2. Friction loss

The friction loss generated due to the shear forces between the flow and rotor blade's solid surface (dependant on the surface roughness) is determined from Equation 3-37 (Suhrmann *et al.* 2010) .

$$\Delta h_{friction} = f_{curve}\left(\frac{W_4 + \left(\frac{W_{5,tip} + W_{5,hub}}{2}\right)}{2}\right)^2 \frac{l_{hyd}}{d_{hyd}} \qquad \text{Equation 3-37}$$

Where f_{curve} is the friction factor that is modified to account for the curvature effects of RIT and is calculated by Equation 3-38 (Musgrave 1980).

$$f_{curve} = f\left(1 + 0.075\overline{Re}^{0.25}\sqrt{\frac{d_{hyd}}{2r_c}}\right)\left(\overline{Re}\left(\frac{d_4}{2r_c}\right)^2\right)^{0.05} \qquad \text{Equation 3-38}$$

Where f is the friction factor and is obtained by Equation 3-39 (Churchill 1977).

$$f = 8\left(\left(\frac{8}{\overline{Re}}\right)^{12} + \left(\left(2.457ln\left(\frac{1}{\left(\frac{7}{\overline{Re}}\right)^{0.9} + 0.27RR}\right)\right)^{16} + \left(\frac{37530}{\overline{Re}}\right)^{16}\right)^{-1.5}\right)^{\frac{1}{12}} \quad \text{Equation 3-39}$$

RR is the wall relative roughness with the value of 0.0002m suggested by (Suhrmann *et al.* 2010) and is assumed to be constant throughout this chapter. $\overline{Re}$ is the averaged Reynolds number between the rotor inlet and exit and is determined by Equation 3-40

$$\overline{Re} = \frac{\frac{U_4 b_4 \rho_4}{\mu_4} + \frac{U_5 b_6 \rho_5}{\mu_5}}{2} \quad \text{Equation 3-40}$$

The rotor hydraulic length (l_{hyd}) and hydraulic diameter (d_{hyd}) are obtained using Equation 3-41 and 3-42 respectively (Glassman *et al.* 1976, Moustapha *et al.* 2003).

$$l_{hyd} = \frac{\pi}{2}\left(\sqrt{\frac{\left(r_4 - r_{5,tip} + \frac{b_4}{2}\right)^2 + \left(\frac{b_5}{2}\right)^2}{2}}\right) \quad \text{Equation 3-41}$$

$$d_{hyd} = 0.5\left(\frac{4\pi r_4 b_4}{2\pi r_4 + Z_{rotor} b_4} + \frac{2\pi(r_{5,tip}^2 - r_{5,hub}^2)}{\pi(b_5) + Z_{rotor}(b_5)}\right) \quad \text{Equation 3-42}$$

The rotor mean radius of curvature (r_c) which represents the curvature of the mean-line is obtained based on the geometry of the rotor blade hub and tip contours (circular and elliptical respectively) and by averaging the radius of the mean-line at the rotor inlet and exit that led to Equation 3-43.

$$r_c = r_4 - r_{5,tip} + \frac{b_4 + b_5}{2} \quad \text{Equation 3-43}$$

3.5.4.3. Secondary loss

Local flow circulations imposed on the main flow (secondary flows) almost inevitably occur in the RIT due to the simultaneous radius change in the meridional plane and strong pressure gradient in the blade-to-blade plane. The associated secondary loss is calculated with Equation 3-44 (Rodgers *et al.* 1987).

$$\Delta h_{secondary} = \frac{C_4^2 d_4}{Z_{rotor} r_c} \quad \text{Equation 3-44}$$

3.5.4.4. Tip clearance loss

Due to the necessary running clearance (gap) between the rotor tip and casing (Figure 3-6) some of the flow is leaked through the gap from the pressure surface to the suction surface without utilizing its kinetic energy to create mechanical work. The clearance loss is obtained by Equation 3-45 (Baines 2003).

$$\Delta h_{tip\ clearance} = \frac{U_4^3 Z_{rotor}}{8\pi}\left(0.4\varepsilon_x C_x + 0.75\varepsilon_r C_r - 0.3\sqrt{\varepsilon_x \varepsilon_r C_x C_r}\right) \quad \text{Equation 3-45}$$

$$C_x = \frac{1 - \left(\frac{r_{5,tip}}{r_4}\right)}{C_{m,4} b_4} \quad \text{Equation 3-46}$$

$$C_r = \left(\frac{r_{5,tip}}{r_4}\right)\frac{l_{rotor,x} - b_4}{C_{m,5} r_5 b_5} \quad \text{Equation 3-47}$$

Where ε_x and ε_r are the axial and radial tip clearances and are considered to be equal throughout this thesis.

$$\varepsilon_x = \varepsilon_r = \varepsilon_b = 0.04(b_5) \quad \text{Equation 3-48}$$

3.5.4.5. Exit kinetic loss

Exit kinetic loss is the enthalpy drop due to the wasted kinetic energy of exhaust which has not been completely converted into the shaft mechanical work (utilization of diffuser can reduce such loss). Equation 3-49 is used to determine the exit kinetic loss.

$$\Delta h_{exit} = \frac{C_5^2}{2}$$ Equation 3-49

3.5.4.6. Windage loss

The only external loss that is usually considered in the modelling of RIT is the windage (disc friction) loss due to the fluid leakage between the back face of the rotor disc and the stationary turbine back plate (Whitfield *et al.* 1990) shown in Figure 3-6. Equation 3-50 depicts the windage loss.

$$\Delta h_{windage} = \frac{k_f \bar{\rho} U_4^3 r_4^2}{4\dot{m}}$$ Equation 3-50

Where $\bar{\rho}$ is the average density between the rotor inlet and exit, ε_b is the rotor back plate clearance obtained by Equation 3-48 and k_f is calculated as below (Whitfield *et al.* 1990).

$$k_f = 3.7 \frac{\left(\frac{\varepsilon_b}{r_4}\right)^{0.1}}{Re^{0.5}} \quad for\ Re < 10^5$$ Equation 3-51

$$k_f = 0.102 \frac{\left(\frac{\varepsilon_b}{r_4}\right)^{0.1}}{Re^{0.2}} \quad for\ Re > 10^5$$ Equation 3-52

3.5.4.7. Nozzle friction loss

Nozzle friction loss is found by Equation 3-53 (Whitfield *et al.* 1990) where $\bar{C}$ is the average of the nozzle inlet and exit absolute velocities and f is obtained by Equation 3-39.

$$\Delta h_{friction,nozzle} = 4f\bar{C}^2 \frac{l_{hyd,nozzle}}{d_{hyd,nozzle}}$$ Equation 3-53

$$l_{hyd,nozzle} = r_2 - r_3$$ Equation 3-54

$$d_{hyd,nozzle} = 0.5\left(\frac{8\pi r_2 b_3 \cos\alpha_2}{4\pi r_2 + \frac{4\pi r_2 b_3}{\sigma}} + \frac{8\pi r_3 b_3 \cos\alpha_3}{4\pi r_3 + \frac{4\pi r_3 b_3}{\sigma}}\right)$$ Equation 3-55

Further details regarding the developed mean-line code in EES is provided in Appendix (B).

3.5.5. Parametric studies and selection of the candidate turbine

The developed mean-line code was employed to perform parametric studies in order to investigate the effect of input variables on the turbine critical performance parameters (i.e. power and efficiency) and turbine size (i.e. rotor inlet diameter). Such parametric studies are based on simultaneous variation of two input parameters in a defined range (with other inputs kept constant) and plotting their effects on the performance parameters mentioned above. Such plots are then examined to determine the values of these two parameters that give the best performance. Such values will be fixed in the next run where two other variables will be changed and this process will be repeated until the best values will be identified for all the input parameters. The mean-line code input parameters and their variation ranges are shown in Table 3-1. The results of the parametric studies are presented in Figure 3-9 to 3.13.

Table 3-1 Mean-line code input parameters and their range

Parameter	Unit	Range	Selected value
Operating parameters			
Inlet total temperature ($T_{t,1}$)	K	323 - 473	323
Inlet total pressure ($P_{t,1}$)	kPa	150 - 400	200
Expansion ratio (ER_{ts})	(-)	1.5 - 3	2
Mass flow rate ($\dot{m}$)	kg/s	0.03 - 0.1	0.09
Turbine design parameters			
Velocity ratio (v_{ts})	(-)	0.6 - 0.9	0.68
Rotational speed (ω)	rpm	40000 - 60000	55000
Rotor inlet absolute flow angle (α_4)	degree	60 - 80	78.6
Rotor exit absolute flow angle (α_5)	degree	-10 - 10	0
Rotor exit hub to inlet radii ratio ($r_{5,hub}/r_4$)	(-)	0.15 - 0.45	0.2
Rotor exit tip to inlet radii ratio ($r_{5,tip}/r_4$)	(-)	0.5 - 0.8	0.55

Power, stage total-to-static efficiency and rotor diameter were plotted versus inlet total pressure ($P_{t,1}$) at various inlet total temperature ($T_{t,1}$) as shown in Figure 3-9. It is clear from Figure 3-9(a) and (c) that the effect of $T_{t,1}$ is more significant on the power output and the rotor inlet diameter than $P_{t,1}$.

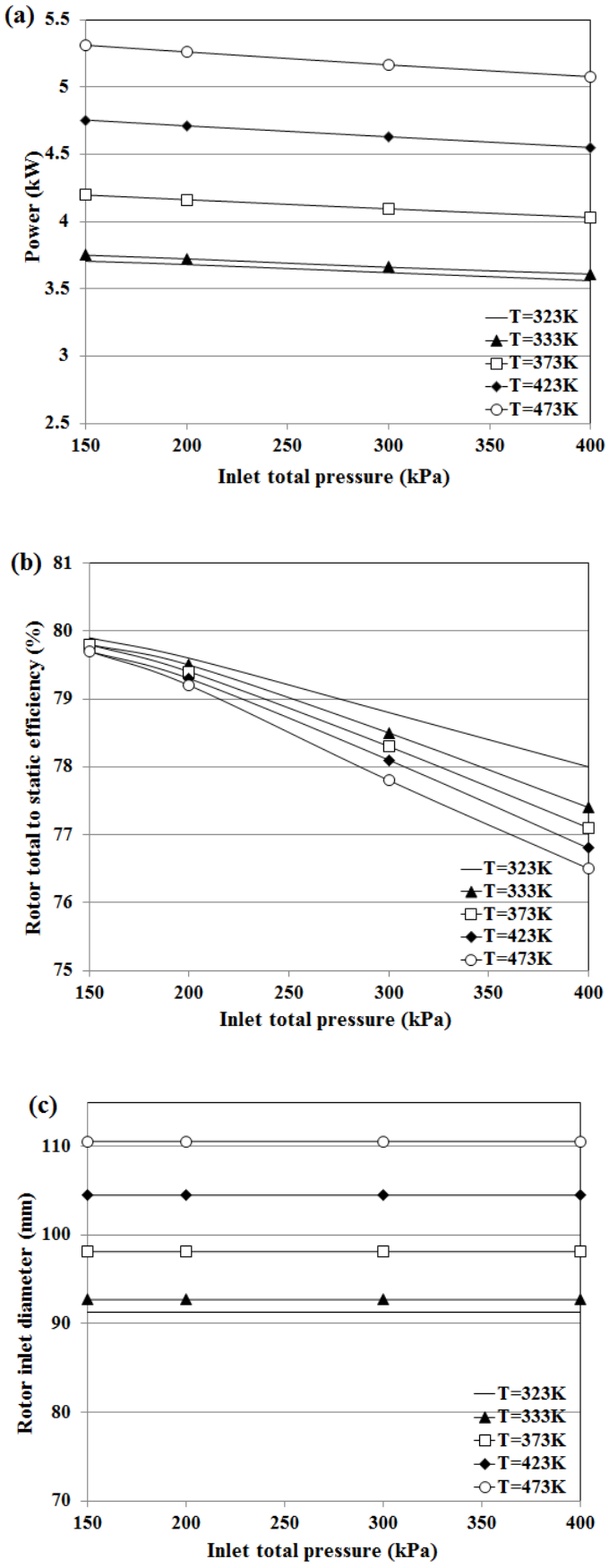

Figure 3-9 Effect of inlet total pressure and temperature on the power, size and efficiency

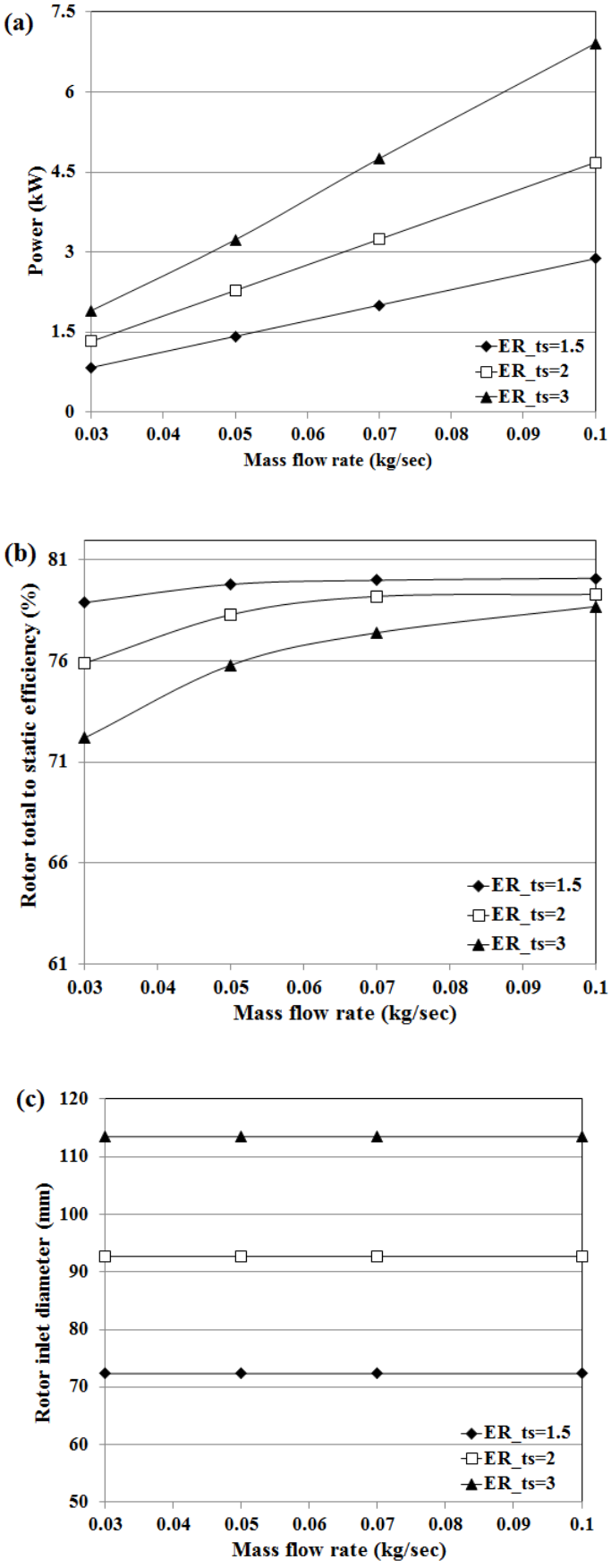

Figure 3-10 Effect of mass flow rate and expansion ratio on the power, size and efficiency

In contrast, Figure 3-9(b) shows that the effect of $T_{t,1}$ is limited as increasing $T_{t,1}$ from 323K to 473K reduces stage efficiency only by 1.5%, while, increasing $P_{t,1}$ from 150kPa to 400kPa is more considerable as it reduces stage efficiency by 3.5% . Figure 3-10 shows that power and efficiency are increasing as the mass flow rate increases. This is directly related to the relation between mass flow rate and power as shown in Equation 3-14 with constant enthalpy drop. Moreover, at higher mass flow rates the temperature drop across the turbine is increasing leading to higher efficiency levels with constant expansion ratio (ER_{ts}) as illustrated by Equation 3-18. However, rotor inlet diameter is independent of mass flow rate variation. It is only for the stage total-to-static efficiency and at lowest ER_{ts} of 1.5 that the effect of increasing the flow rate is limited. As depicted in Figure 3-10(a) power is increasing as the ER_{ts} increases because of the larger actual enthalpy drop across the turbine, however, higher ER_{ts} of 3 will have the adverse effect of reducing the stage total-to-static efficiency (Figure 3-10(b)) and increasing the rotor diameter (Figure 3-10(c)). This is due to the fact that at larger d_4 the wetted blade surface in contact with the fluid increases considerably resulting in larger friction loss and hence reduces the efficiency. It is evident from Figure 3-11 that there exists an optimum condition that yields highest power and efficiency at the velocity ratio (v) of about 0.7. Such behaviour is one of the main characteristics of RIT and the results in Figures Figure 3-11(a) and (b) are in accordance with (Meitner *et al.* 1983, Whitfield *et al.* 1990, Dixon *et al.* 2010). Moreover, these results illustrate that both power and efficiency are a strong function of v as increasing v from 0.6 to 0.9 reduces both efficiency and power by about 33% and 37.5% respectively. In contrast, efficiency and power are a weak function of rotational speed (ω) since the lines of constant ω fall in a narrow region and for preliminary turbine design they can be approximated as a single line.

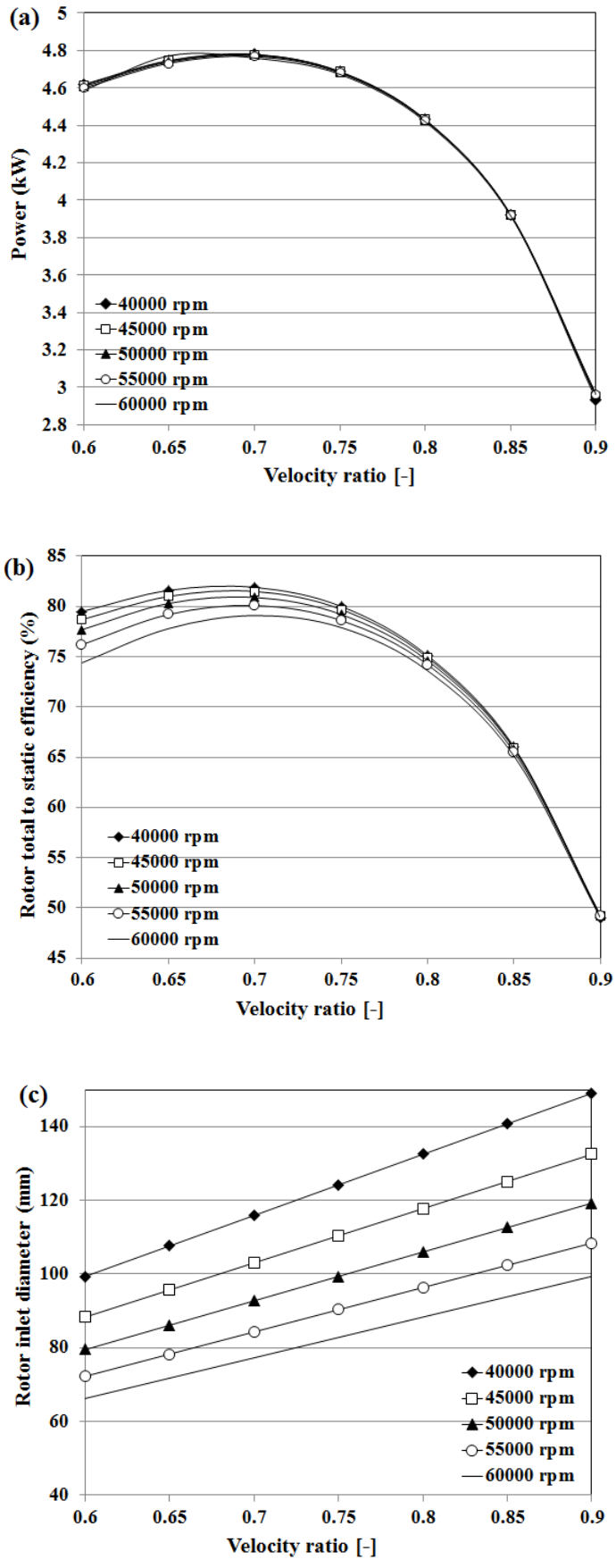

Figure 3-11 Effect of velocity ratio and rotational speed on the power, size and efficiency

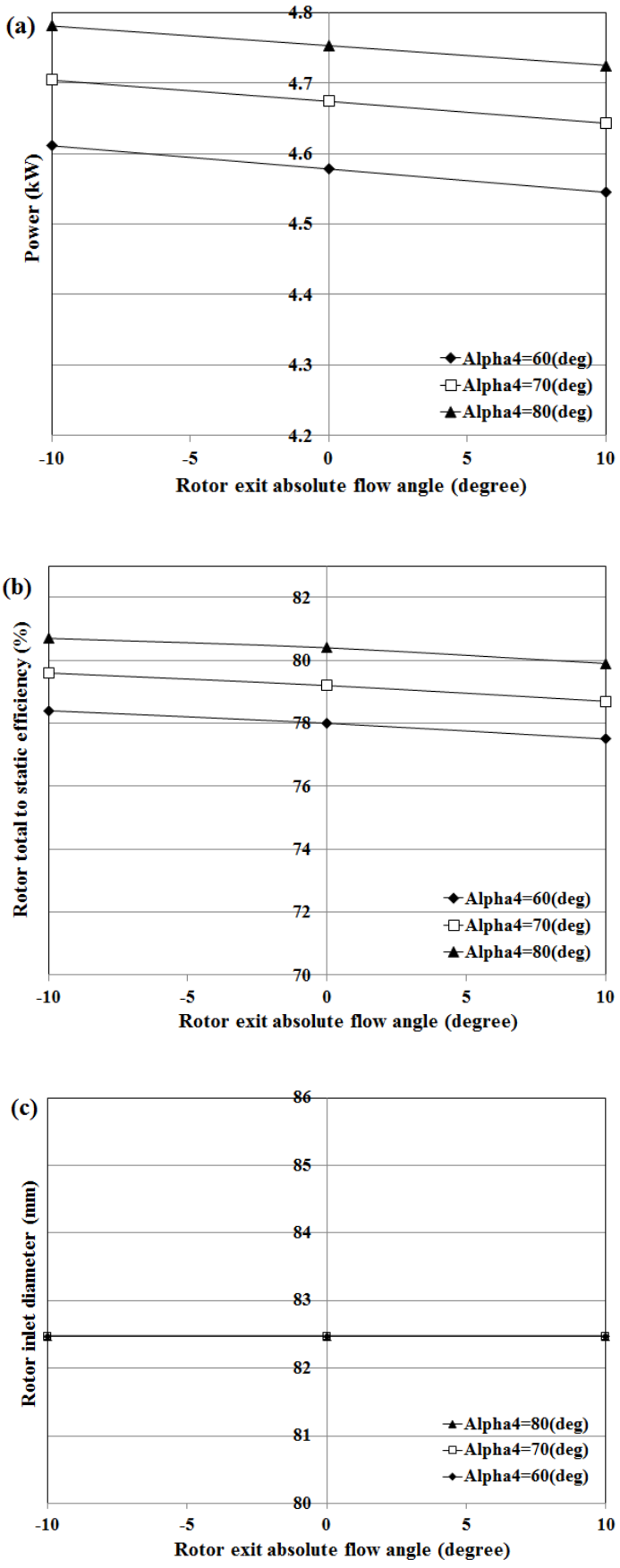

Figure 3-12 Effect of rotor inlet and exit absolute flow angles on the power, size and efficiency

Such feature is one of the main reasons for selecting v as the non-dimensional design parameter in this chapter. Figure 3-11(c) shows that the effects of these parameters on the rotor inlet diameter is significant and as the RPM increases, the rotor diameter decreases while as the velocity ratio increases, the rotor inlet diameter increases. Figure 3-12 shows that the effect of varying the rotor inlet absolute flow angle (α_4) is more significant than the rotor exit absolute flow angle (α_5) while the rotor diameter being completely independent of these variations.

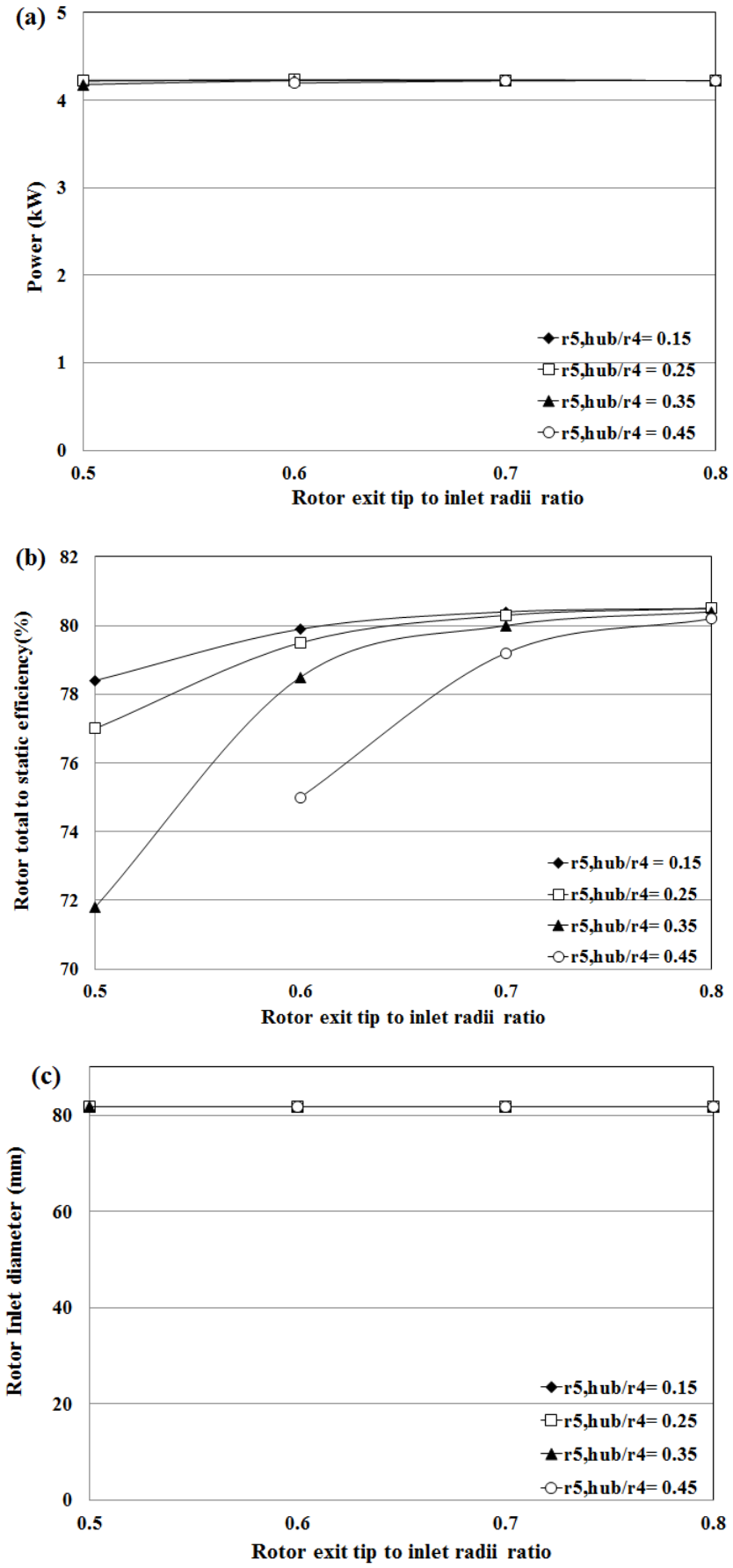

Figure 3-13 Effect of rotor radii ratio on the power, size and efficiency

Increasing α_4 results in larger absolute circumferential velocity at rotor inlet ($C_{\theta,4}$) as shown in Figure 3-6 and based on Equation 3-19 it enhances the actual enthalpy drop and consequently power and efficiency (with fixed expansion ratio and isentropic enthalpy drop). Figure 3-13 presents the variation of the rotor radii ratios and it is only the stage efficiency that is noticeably affected by such variation. With fixed $r_{5,hub}/r_4$ ratio, increasing $r_{5,tip}/r_4$ results in larger flow area at rotor exit (A_5) based on Equation 3-15 and according to the conservation of mass, the exit flow absolute velocity (C_5) is reduced resulting in smaller exit kinetic losses and consequently increases the efficiency. However, at the same time increasing $r_{5,tip}/r_4$, increases the secondary losses (Equation 3-44) and the combination of these two effects offset the increase in efficiency curve at high $r_{5,tip}/r_4$ values. Based on the above parametric studies the best values for all of the investigated input parameters are selected and summarized in Table 3-1. Table 3-2 shows the mean-line modelling results obtained by running the code using the selected values of Table 3-1. As can be seen from the performance parameter results the values of the N_s, d_s, φ and ψ are in the favouring operating region of the RIT based on Figure 3-1 and underlines the rationale selection of this configuration of turbomachinery in this chapter.

Although this approach is effective for systematic investigation of the key input parameters, it strongly depends on the experience and doesn't necessarily assure that the optimum combination of the inputs is achieved. Moreover, outputs are required to be manually checked against the application and geometrical constraints. These deficiencies have been addressed in chapter five in which the mean-line code has been integrated with an optimization method to perform true analytical optimization of the performance subjected to various constraints.

Table 3-2 Mean-line modelling results

Parameter	Unit	Value
Thermodynamic properties		
Rotor inlet total pressure ($P_{t,4}$)	kPa	194.12
Rotor inlet total temperature ($T_{t,4}$)	K	323
Rotor inlet static pressure (P_4)	kPa	152.38
Rotor inlet static temperature (T_4)	K	301.4
Rotor exit total pressure ($P_{t,5}$)	kPa	102.21
Rotor exit total temperature ($T_{t,5}$)	K	275.9
Rotor exit static pressure (P_5)	kPa	100
Rotor exit static temperature (T_5)	K	274.2
Geometry parameters		
Rotor inlet diameter (d_4)	m	0.080634
Rotor inlet blade height (b_4)	m	0.004979
Rotor exit tip diameter ($d_{5,tip}$)	m	0.04435
Rotor exit hub diameter ($d_{5,hub}$)	m	0.01613
Rotor exit area (A_5)	m^2	0.001206
Rotor axial length ($l_{rotor,x}$)	m	0.02117
Rotor blade number (Z_{rotor})	-	16
Nozzle inlet diameter (d_2)	m	0.10564
Nozzle exit diameter (d_3)	m	0.0845
Nozzle pitch (S_{nozzle})	m	0.01015
Nozzle total throat area ($A_{throat,total}$)	m^2	0.000249
Flow velocities and angles		
Rotor inlet wheel velocity (U_4)	m/s	232.21
Rotor inlet relative flow angle (β_4)	degree	-39.61
Rotor inlet absolute velocity (C_4)	m/s	199.1
Rotor inlet Mach number (Ma_4)	-	0.5985
Rotor inlet relative Mach number ($Ma_{4,rel}$)	-	0.1432
Rotor inlet relative velocity (W_4)	m/s	-49.82
Rotor exit relative flow angle at hub ($\beta_{5,hub}$)	degree	-38.35
Rotor exit relative flow angle at RMS ($\beta_{5,RMS}$)	degree	-60.62
Rotor exit relative flow angle at tip ($\beta_{5,tip}$)	degree	-67.04
Rotor exit absolute velocity (C_5)	m/s	58.7
Rotor exit relative velocity at RMS ($W_{5,RMS}$)	m/s	-140.6
Rotor exit relative Mach number ($Ma_{5,rel,RMS}$)	-	0.417
Performance parameters		
Specific speed (N_s)	-	0.409
Specific diameter (d_s)	-	5.297
Flow coefficient (φ)	-	0.2528
Loading coefficient (ψ)	-	0.8791
Power	kW	4.152
Total-to-static efficiency ($\eta_{stage,ts}$)	%	81.3

3.6. Detailed three-dimensional analysis (CFD & FEA)

3.6.1. Overview of the detailed design procedure

The actual flow field in the RIT is in fact strongly three-dimensional, viscose and turbulent with inevitable secondary flow regions. In addition to that, the transonic or supersonic flow regimes (with shock waves), tip clearance effects and interactions of adjacent nozzle and rotor blade rows make the flow behaviour even more complex. Although it is fast and simple, mean-line (one-dimensional) modelling cannot capture all the aforementioned features and it is required to evaluate the aerodynamics of the turbine passage in greater details using computational fluid dynamic (CFD). CFD is the process by which a variety of numerical mathematical techniques are applied in order to solve the equations (usually RANS equations) that govern the flow field aerodynamics (Japikse *et al.* 1994). If carefully validated, CFD is a very strong tool that facilitates the investigation of the flow in turbine passage accurately to directly address those undesirable features by improving the blade geometry. Moreover, CFD reduces the time and expenses associated with prototype manufacturing and testing. Figure 3.14 outlines the schematic diagram of the detailed CFD and FEA procedures that will be carried out in this chapter. The key geometric characteristics (i.e. inlet tip diameter, inlet blade height, exit tip and hub radii and exit blade angles) of the candidate turbine stage shown in Table 3-2 are used as input for three-dimensional geometry generation of the nozzle and rotor blades using ASNSY^{R15} BladeGen software. Next the grid will be created via structured hexagonal elements using ANSYS^{R15} TurboGrid software. The selected boundary conditions from the mean-line modelling such as inlet total pressure and temperature, expansion ratio and rotational speed are used to perform the CFD analysis using commercial ANSYS^{R15} CFX software.

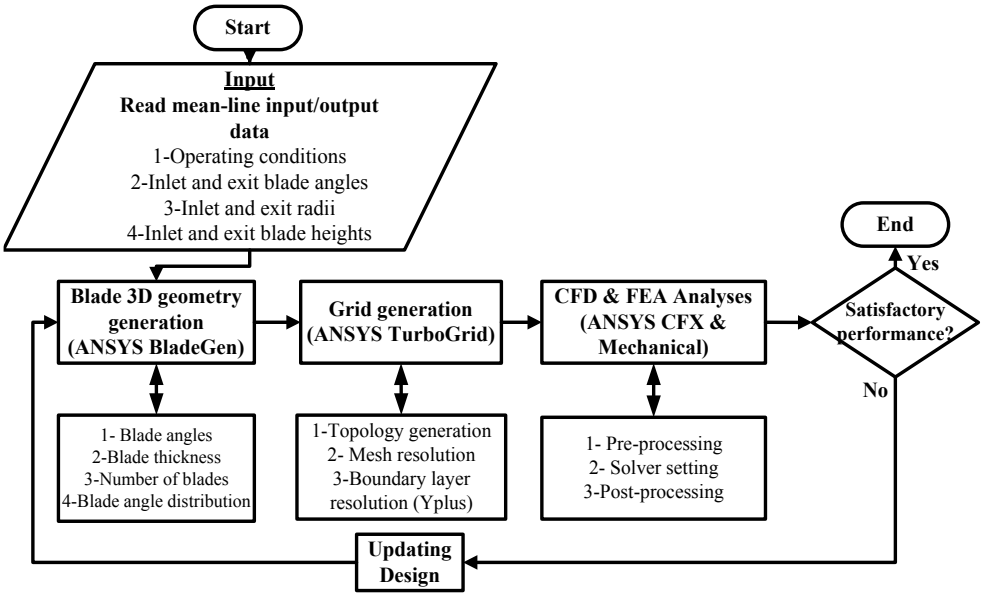

Figure 3-14 Schematic diagram of the detailed phase (CFD & FEA)

The obtained fluid pressure distribution across the blade surface area together with the blade rotational speed are imported from the ANSYS^{R15} CFX to ANSYS^{R15} Mechanical to conduct FEA and assess the mechanical integrity of rotor blade in terms of stress and displacement and if unsatisfactory, this procedure will be repeated by updating the blade geometry. It should be noted that the mean-line modelling still remains as a key part of the proposed approach since it can converge as closely as possible to an optimum configuration (Figure 3-4). If this stage is not accomplished effectively, long time may be spent by making trial CFD and FE analyses that are far from the optimum design. Hence, a combination of both approaches was utilized for effective design of the RIT.

3.6.2. 3-D CAD modelling of rotor and nozzle geometries

By employing the BladeGen software three-dimensional geometry of the nozzle and rotor blades are created using pressure/suction and angle/thickness modes respectively. Apart from the mean-line data (Table 3-2) that define the meridional blade profile, it is required to set the blade angle and thickness distribution between the rotor inlet and exit and the stagger and metal wedge angles and the throat area for the nozzle. Figure 3-15

presents the graphical user interface (GUI) of the initial nozzle and rotor blade geometries in the BladeGen software where the rotor hub and tip meridional contours are defined by Bezier-Bernstein polynomial and the blade angle and thickness distributions are defined by fourth and third order spline curves respectively.

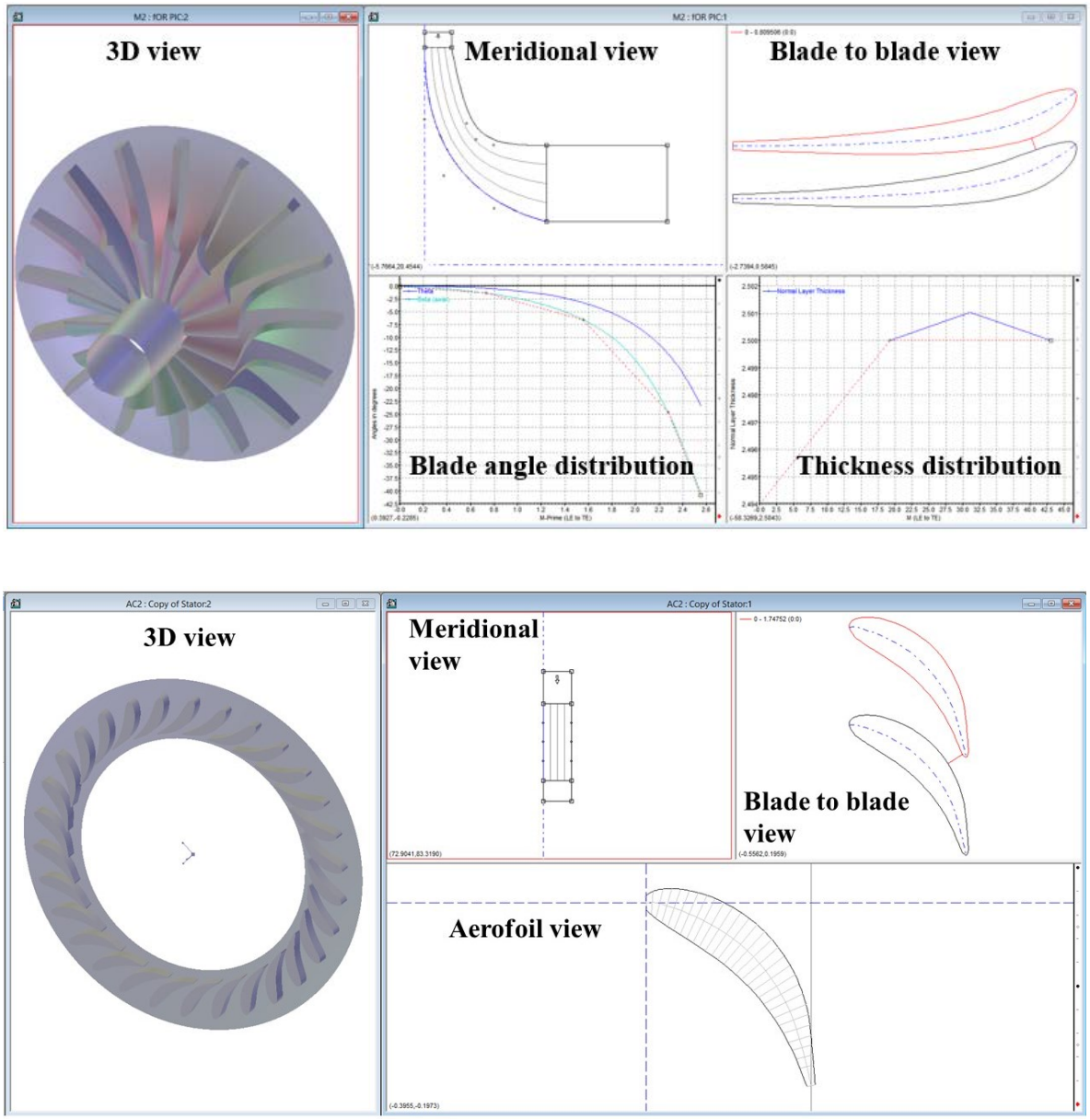

Figure 3-15 Screen shots of the BladeGen GUI. (Top) rotor, angle/thickness mode, (bottom) nozzle, pressure/suction mode

3.6.3. Computational fluid dynamics (CFD) analysis

3.6.3.1. CFD setup and turbulence modelling

The computational mesh was constructed automatically via structured hexagonal elements (mostly based on O-H grid). In depth grid independence study was carried out and described in the next section. The 3-D RANS equations were solved using the high resolution advection scheme with the shear stress transport (SST) turbulent flow model. The advantage of using SST turbulent flow model compared with others is the capability of automatic near-wall treatment for locating the first node away from the wall (Y^+) that captures the turbulence closure.

Inlet total temperature and pressure were set as the boundary conditions at the nozzle inlet (assuming negligible losses in the casing) while static pressure was set at the rotor outlet and it was assumed that the upstream flow approaches the nozzle in the perpendicular direction (radial axis). A mixing plane model (stage interface) was applied at the nozzle-rotor interface to provide communication across the stationary and rotating blade row domains. Such model performs a circumferentially averaging of the fluxes through bands on the interface. The CFD analyses were conducted for one rotor blade passage and two nozzle blade passages to obtain the pitch angle ratio of around unity and results are assumed to represent the complete nozzle and rotor wheels due to the periodicity. The nozzle domain has no tip clearance while the rotor domain includes a tip clearance of 0.56mm obtained from the mean-line modelling which according to (Dixon *et al.* 2010) is a suitable value that can be obtained by current manufacturing techniques. In addition, all the walls are assumed to be smooth, adiabatic with no-slip conditions.

The CFX solver convergence criterion was set to 10^{-5} for all the residuals (RMS) with the physical timescale of $0.5/\omega$ as suggested in the CFX user's manual and all the analyses were carried out at the steady state condition. The CFD analyses were conducted

on an Intel® CPU core i7 - 4790@ 3.60GHz with 32GB RAM. Figure 3-16 outlines the details of the computational fluid domains for the nozzle and rotor blades. As can be seen in this figure the inlet and exit fluid domains are extended about one and half axial chord length of nozzle and rotor respectively in order to improve the numerical stabilization of the solution as suggested in (de Souza *et al.* 2011).

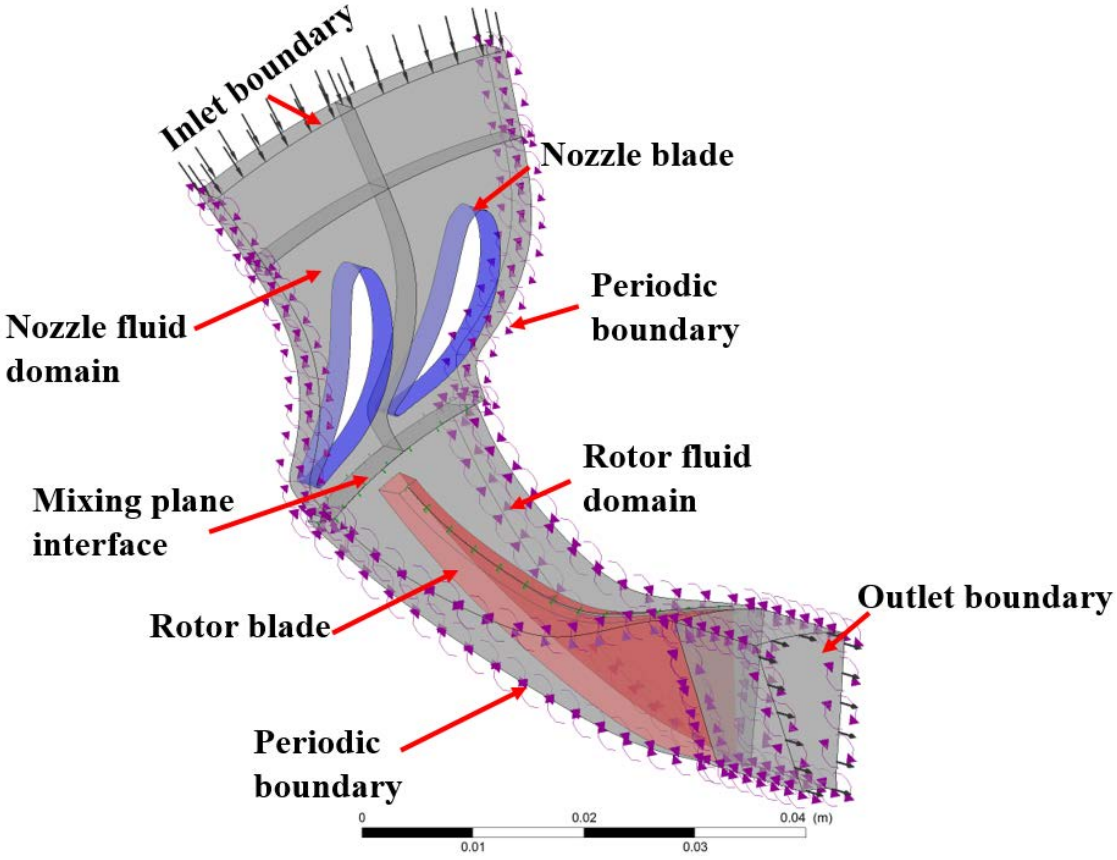

Figure 3-16 Computational fluid domains for nozzle and rotor

3.6.3.2. Grid sensitivity analysis

Grid independence study was carried out for the initial turbine stage that was created based on the mean-line modelling data and the specified grid size was fixed in following sections for further CFD analyses. Six main decision parameters were included in these studies with the main attention to the stage efficiency, Y^+ and CPU time. The mesh resolution was increased by adding more elements in the hub-to-tip and blade-to-blade

directions because the Y^+ variation depends on the first grid spacing to a wetted surface in those two directions. Y^+ itself is a dimensionless distance from the wall and determines the first node away from the wall (boundary layer mesh size) and is required to be around unity for the *K-ω* based SST turbulent flow model as suggested in CFX user's manual. Table 3-3 presents the results of such study.

Table 3-3 Grid sensitivity study results

	Number of elements		Stage total-to-static efficiency (%)	Power output (kW)	Mass flow rate (kg/s)	Y^+ [(b)]	Global imbalance [(c)] (%)	CPU time [(d)] (min)
	Nozzle[(a)]	Rotor						
1	20280	30384	80.727	4.6	0.0974	31.34	0.00015	4
2	97768	318356	81.48	4.366	0.0919	6.08	0.00265	12
3	247680	448972	81.95	4.356	0.0912	3.24	0.0716	22
4	400608	911378	82.15	4.366	0.0911	1.67	0.0314	38
5	597042	1848809	82.25	4.370	0.0911	0.9015	0.0092	74

[(a)] The number of nozzle elements is per passage.
[(b)] The Y^+ values are averaged throughout the nozzle and rotor blade passages.
[(c)] The global imbalance values are averaged throughout the nozzle and rotor blade passages.
[(d)] The CPU times are based on parallel run on 4 CPU cores.

As it is clear from Table 3-3 all the global imbalances are much less than 1% which confirms the proper convergence in the solver as suggested in the CFX solver theory guide. The larger the number of elements both in the rotor and nozzle passage the lower the Y^+ value and closer to the desired range. The stage efficiency varies with a difference of 0.75% between rows 1 and 2 and reduces to 0.1% between rows 4 and 5. The predicted power output and mass flow rate for various grid sizes did not vary significantly from rows 2 to 5. It is only for row 1 that the power is over-predicted by a maximum of 5.3% between rows 1 and 2 due to the over-prediction in mass flow rate by about 6.4%. Among the investigated grid resolutions, the values in rows 4 and 5 provided the least variation in efficiency, power and mass flow rate together with the Y^+ value that is in the suggested range. However, there exists noticeable difference between various grid resolutions CPU time that increases significantly as the Y^+ value decreases. Therefore, as a compromise

between the accuracy of the results, grid independence and the computational time, the grid size in the fourth row of Table 3-3 was selected for the rest of the CFD analyses followed in this chapter and it's shown in Figure 3-17.

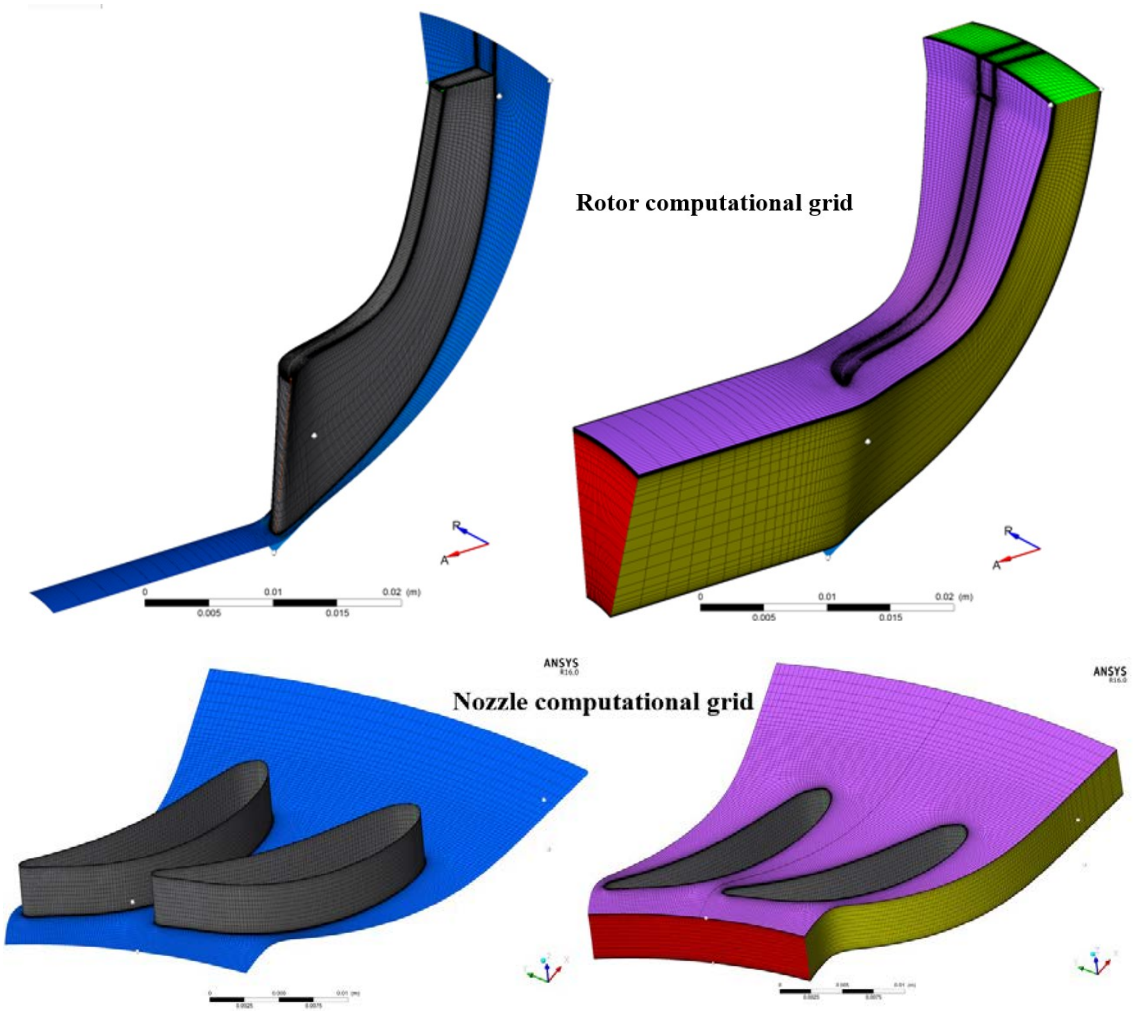

Figure 3-17 Selected grid size for the nozzle and rotor blade passages

3.6.3.3. Effect of blade angle distribution

In general, the principal focus of the aerodynamic evaluations was the bladed regions of the turbine, with the rotor having the highest priority. Therefore during the CFD analyses several iterations were tried for a series of rotor geometry variations including changes in the blade angle distributions, blade thickness, shape of the leading edge (LE) and the number of rotor blades. The various blade shapes were analysed and based on

their quantitative (efficiency and power) and qualitative (velocity vectors, secondary flows, entropy contours and blade loading) results, the most favourable configuration was selected and pursued for further analysis in the next chapter.

Four different blade profiles were investigated with the aim of achieving uniform flow with minimal secondary losses and least entropy generation rate (highest isentropic efficiency). Figure 3-18 shows these profiles in terms of blade angle distribution versus normalized meridional distance. Blade profile "A" has a very small turning angle in the large portion of the passage and very sharp turning around the exit, blade profile "B" has significant turning in the first part of passage and small turning at the exit, blade profile "C" has modest blade turning angle along the whole length of the passage while blade profile "D" is somewhat the combination of the blade profiles "A" and "C".

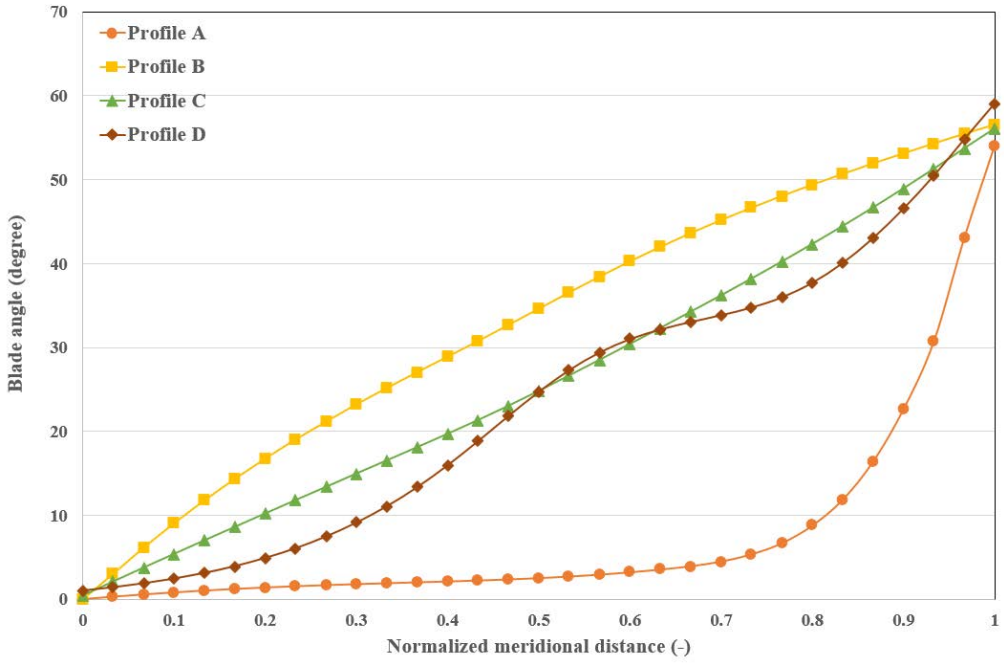

Figure 3-18 Blade angle distribution at half span for 4 different blade profiles

In this thesis most of the CFD qualitative results will be shown at three different blade spans as 5%(near the hub), 50% (mid span) and 90% (near the shroud) and depicted

in Figure 3-19. Moreover, the nozzle shape including angles and number of blades were kept constant during the CFD analyses.

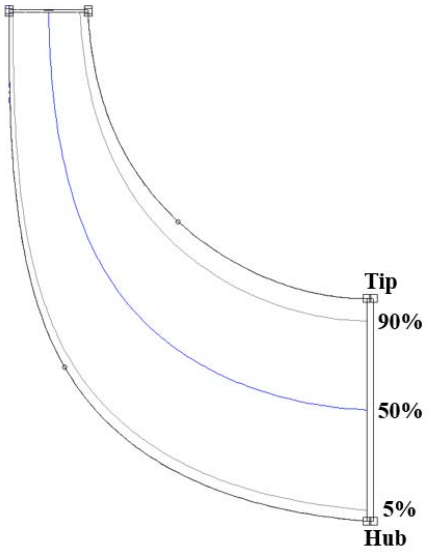

Figure 3-19 The position of the spans across the meridional channel for presentation of results

FiguresFigure 3-20 to 3.23 show the blade-to-blade velocity vectors at half span for the four different blade profiles that were investigated. All configurations have 16 rotor blades as suggested by Equation 3-26. As shown in Figure 3-21 there exist noticeable flow separation together with strong secondary flows on the pressure surface (PS) of profile "B" just downstream of the leading edge. Such flow characteristics also exist in the profile "C" as shown in Figure 3-22 but the intensity of the secondary flows (local flow circulation) has been reduced considerably and the flow expands smoothly after this region. The development of such secondary flows on the PS at the rotor inlet region of profile "D" was substantially reduced with a preferential flow pattern for the remainder of the passage as presented in Figure 3-23.

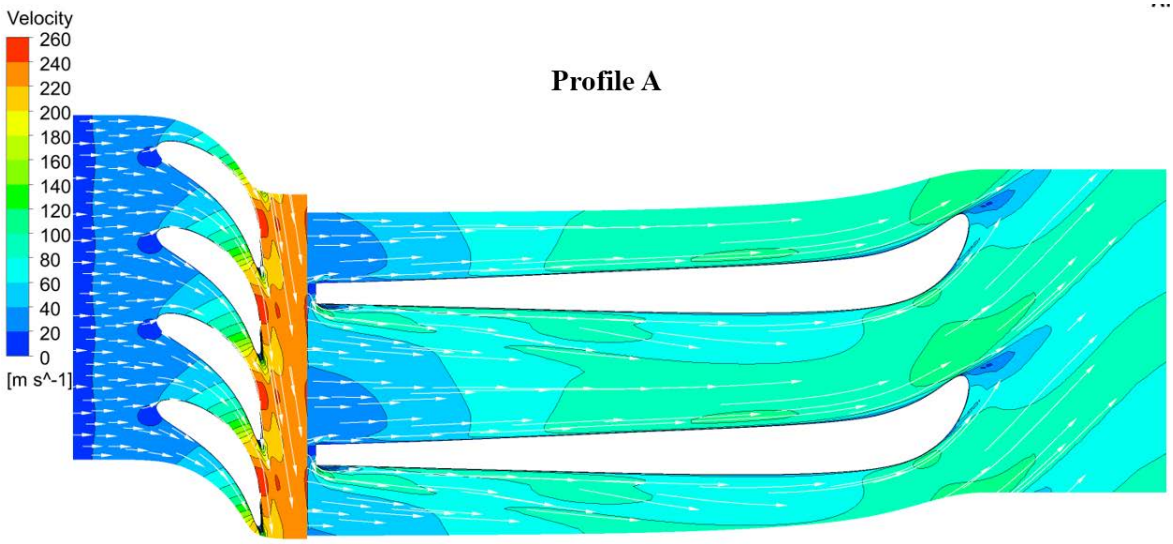

Figure 3-20 Velocity vectors at half span for the blade profile "A"

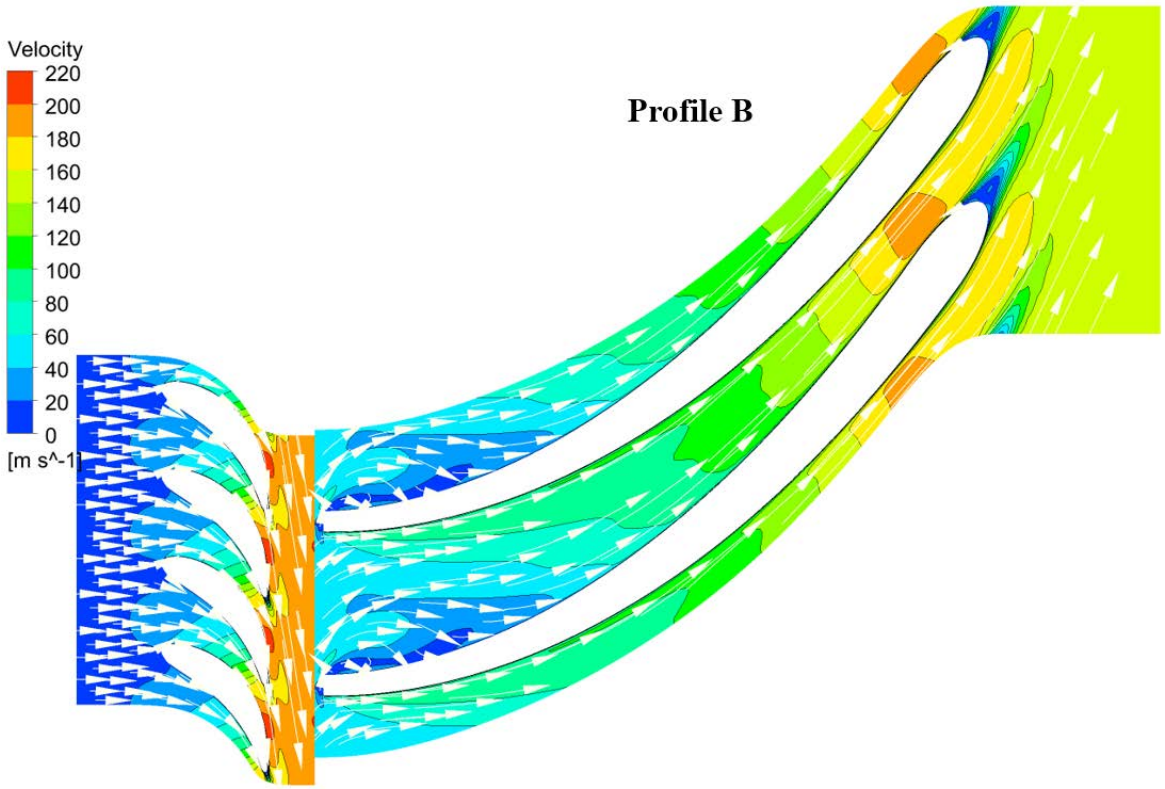

Figure 3-21 Velocity vectors at half span for the blade profile "B"

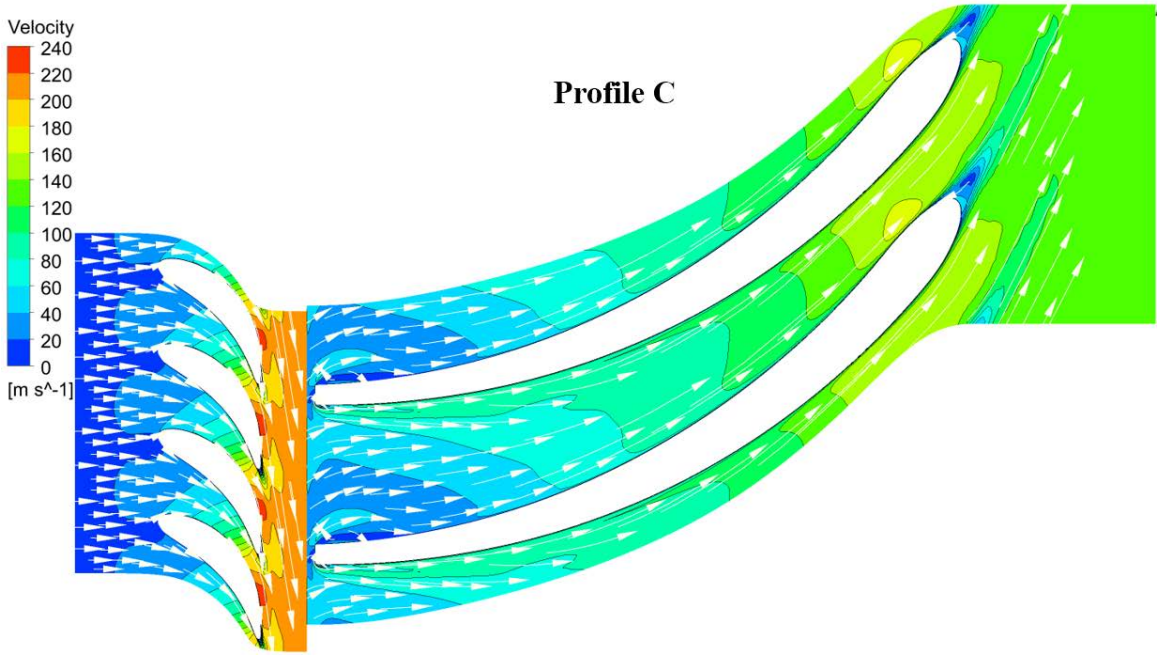

Figure 3-22 Velocity vectors at half span for the blade profile "C"

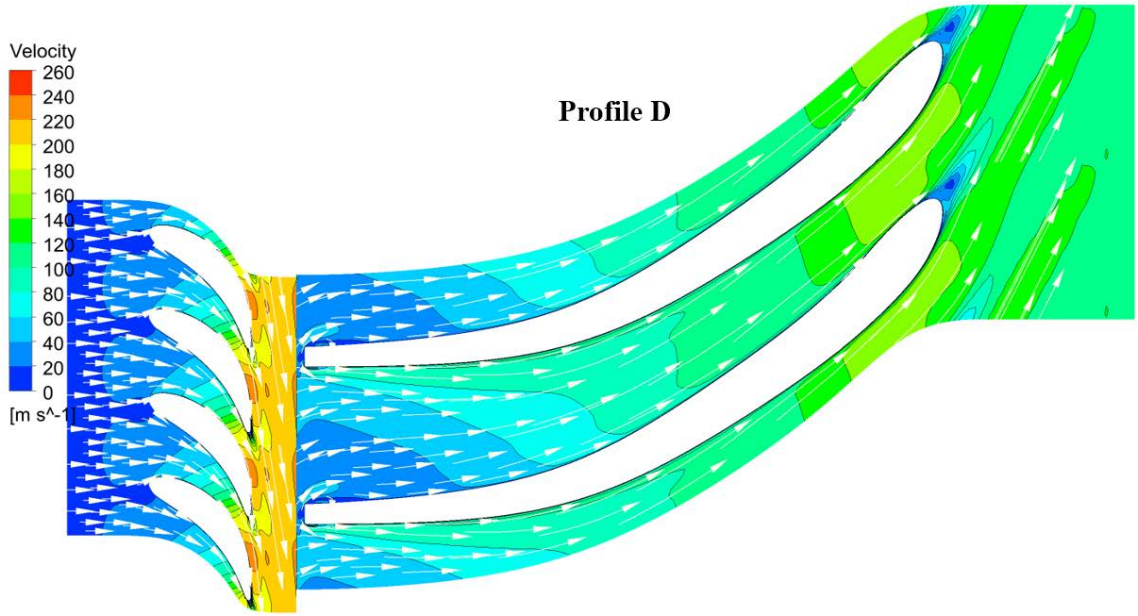

Figure 3-23 Velocity vectors at half span for the blade profile "D"

Although profile "A" seems appealing as there is no evidence of secondary flow formation (Figure 3-20), such profile was unable to accelerate the relative flow velocity (W_5) to high levels in most of the rotor passage with the maximum value of 86.03 m/s compared to the 121.7m/s, 116.32m/s and 111.6m/s for profiles "B", "C" and "D" respectively. On the other hand, the largest W_5 for profile "B" resulted in largest C_5 of 88.13m/s and hence the largest exit kinetic loss compared to 83.06m/s and 80.87m/s for profiles "C" and "D" respectively.

More importantly, due to the low flow velocity levels the viscous shear force became dominant in the passage of profile "A" and results in high level of entropy generation in large portion of the passage as it is shown by the entropy contour plot in Figure 3-24. Comparing the entropy distribution contour charts at half span for all four profiles depicted in Figure 3-24 to 3.27 revealed that the level of entropy distribution in profile "D" was the lowest. Such characteristic is the principal reason for the profile "D" to exhibit the highest efficiency of 83.33% compared to the other profiles as summarized in Table 3-4. Although profile "C" has competitive performance (82.57%), the subtle variation in the blade angle distribution of the blade profile "D" resulted in noticeable reduction in entropy generation as it is evident by comparing Figure 3-26 and 3.27. Moreover, the CFD predicted mass flow rate and power (Table 3-4) for the blade profile "D" are in very good agreement with the mean-line design values of 0.09kg/s and 4.152kW respectively. The slight over prediction/improvement in the predicted stage efficiency by CFD (83.33%) can be attributed to the subtle variation of the blade angle distribution in the light of earlier analyses of blade profiles "A" to "C" as well as excluding the windage loss (flow leakage from back plate of rotor) during the CFD analyses. Thus, the profile "D" was selected as the best configuration to further investigate the effect of thickness, leading edge (LE) shape and number of blades.

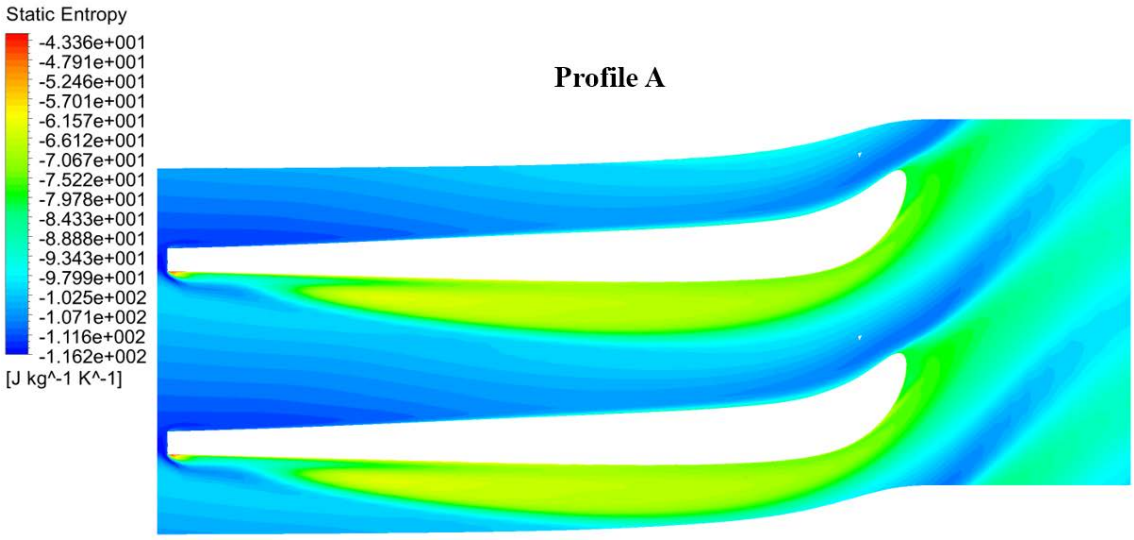

Figure 3-24 Contours of entropy distribution at half span for the blade profile "A"

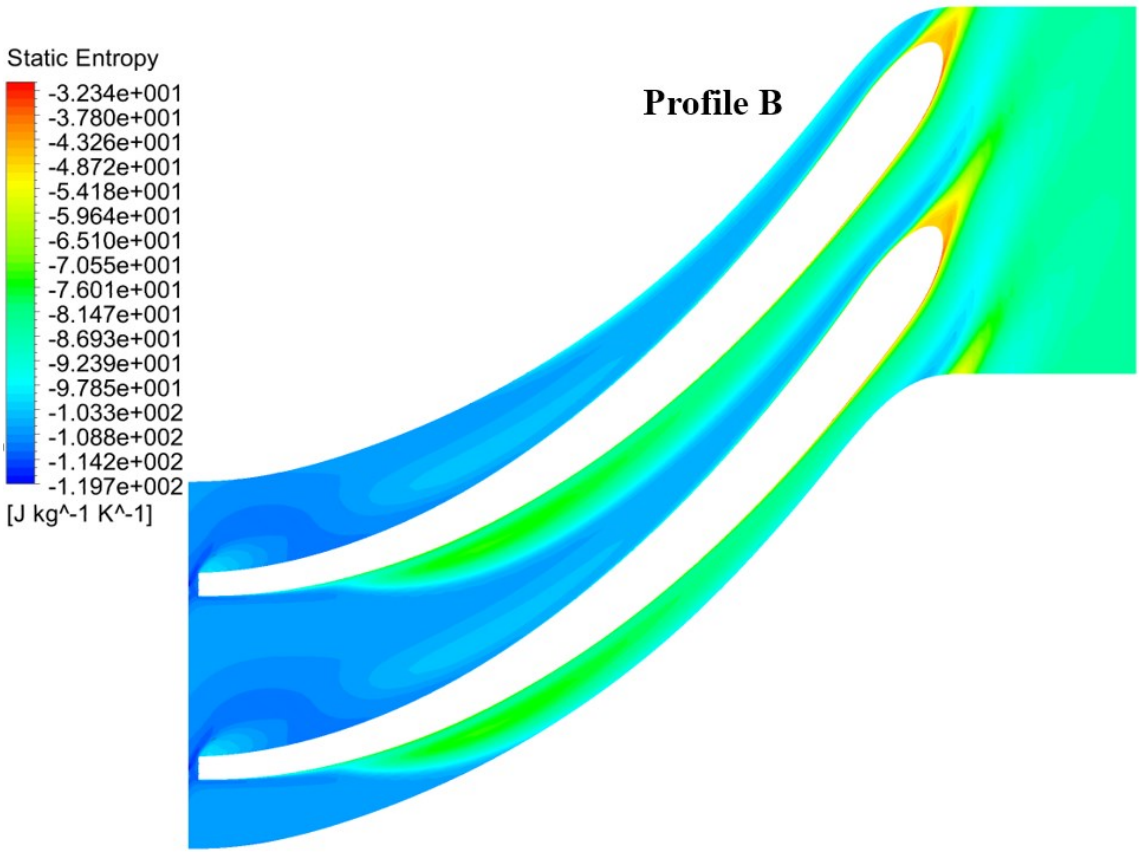

Figure 3-25 Contours of entropy distribution at half span for the blade profile "B"

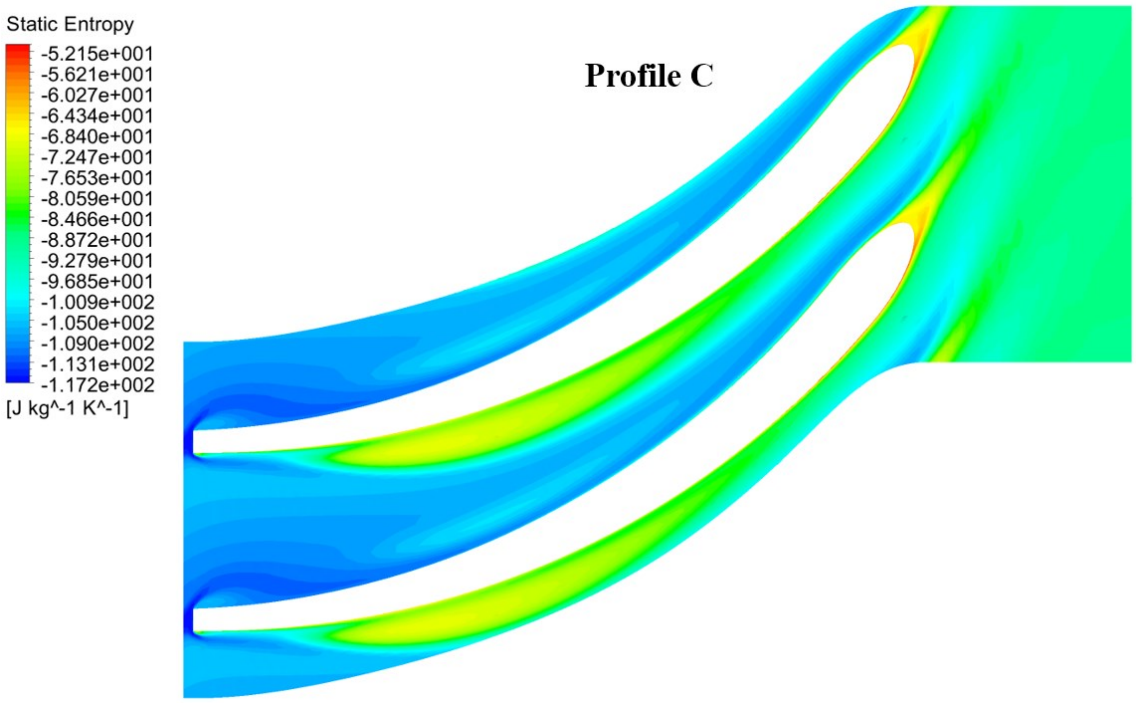

Figure 3-26 Contours of entropy distribution at half span for the blade profile "C"

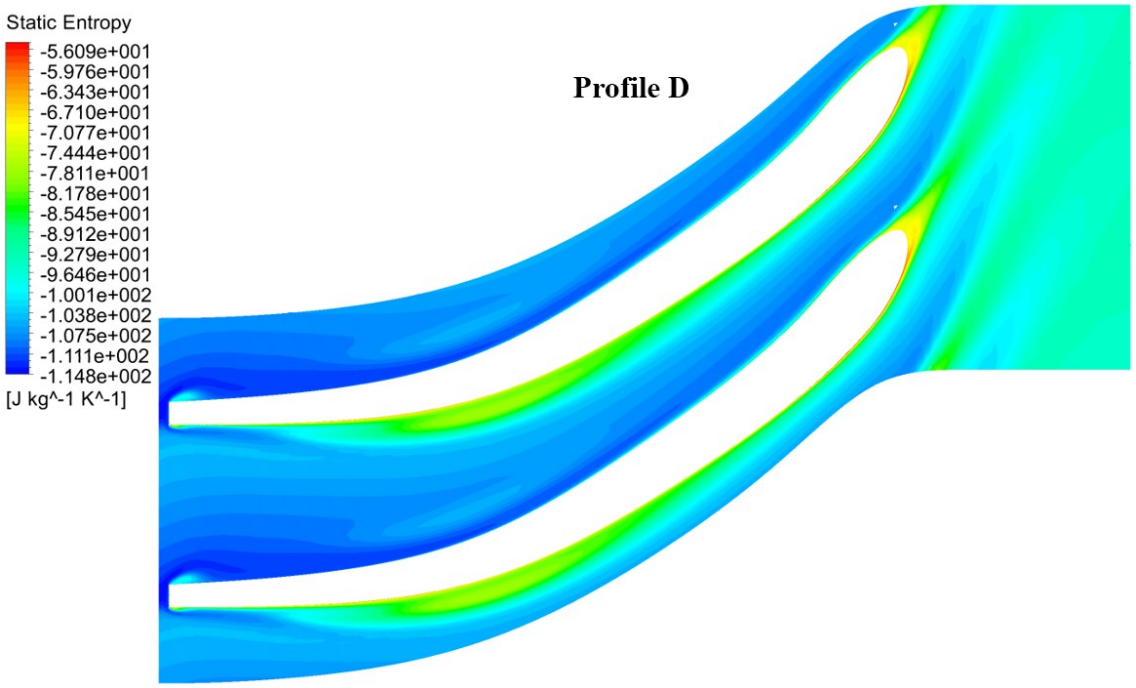

Figure 3-27 Contours of entropy distribution at half span for the blade profile "D"

Table 3-4 Summary of main performance parameters from CFD analyses of 4 investigated blade profiles

	Stage total-to-static efficiency (%)	Power (kW)	Mass flow rate (kg/s)
Profile A	82.15	4.366	0.0911
Profile B	78.58	3.675	0.0801
Profile C	82.57	4.092	0.085
Profile D	83.33	4.190	0.0863

3.6.3.4. Effect of blade thickness and leading edge (LE) profiles

Following the results in section 3.6.3.3, the profile "D" was selected in order to further investigate the effect of varying the thickness distribution from hub-to-tip and also the effect of the rotor LE shape. It should be noted that for all the CFD analyses in section 3.6.3.3, the thickness was kept constant with the value of about 2mm from hub-to-tip as illustrated in Figure 3-28 (a). From the aerodynamic point of view, the lower the thickness the better the performance (as will be shown in this section) subject to structural analysis that will be described in section 3.6.4. Therefore, for the modified case the rotor blade hub-to-tip thickness has been reduced linearly from about 2mm near the hub to about 1mm near the blade tip as depicted in Figure 3-28 (b). At the same time, the shape of the rotor blade LE has also changed from a square cut-off shape to a curved elliptical shape. Figure 3-29 shows the two modifications on the original profile "D" in the blade-to-blade view at half span. Conducting the CFD analysis for the modified profile "D" with the same CFD setup and mesh resolution as described in sections 3.6.3.1 and 3.6.3.2, resulted in stage efficiency, power and mass flow rate of 84.51%, 4.343kW and 0.0884kg/s respectively. Apparently the implemented modifications improved the turbine efficiency by about 1.18% while the power was increased by about 153W.

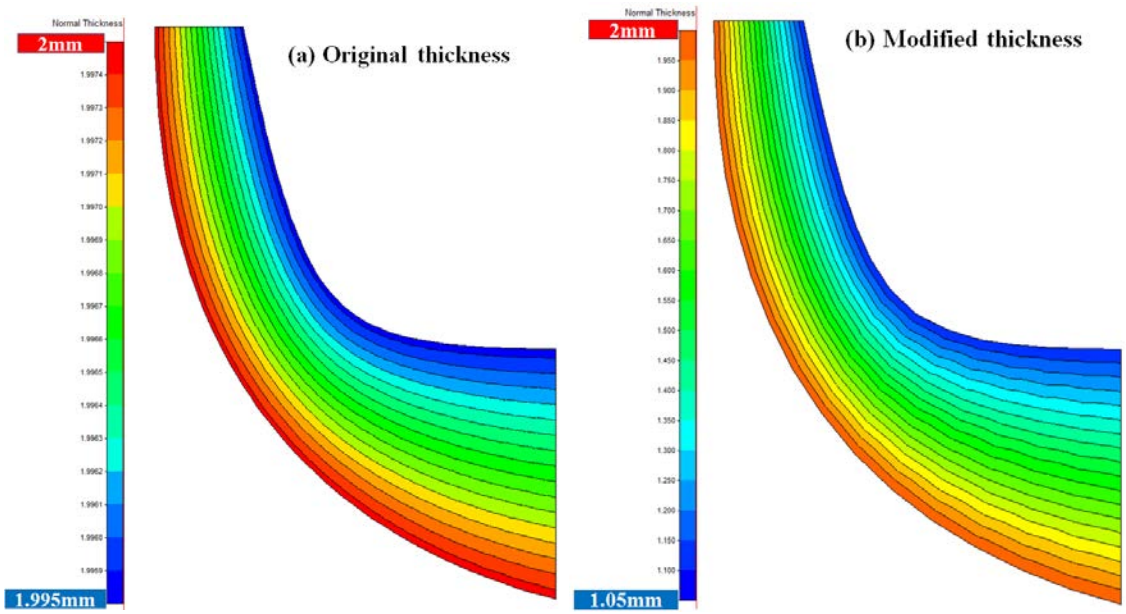

Figure 3-28 Variation of hub-to-tip blade thickness (a) Original thickness, (b) Modified thickness

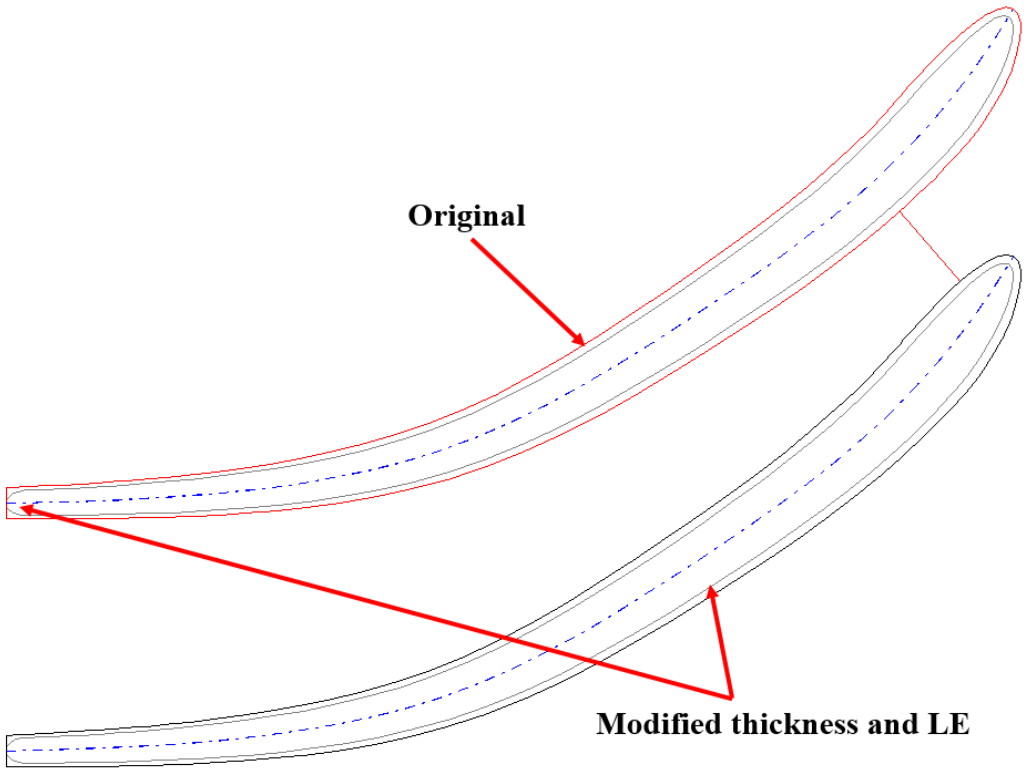

Figure 3-29 Blade-to-blade view of the original and modified thicknesses and LE shapes at half span

Such improvements can be attributed to two main factors. Firstly, due to the shape of the rotor leading edge for the original case there was flow blockage at the rotor inlet and consequently a recirculation zone (shown by red arrow in Figure 3-30) that occupied a small portion of the inlet passage as depicted by the velocity streamlines in Figure 3-30(a). However, the modified leading edge shape reduced the flow blockage and almost entirely eliminated the formation of the flow reversal as illustrated by Figure 3-30(b). Furthermore, the reduction in the blade thickness increased the effective flow area compared to the original case (considering the growth of the boundary layer blockage on the blade surfaces and end walls for both cases) and therefore slightly larger mass flow rate was predicted by the CFD for the modified case (0.0884kg/s) compared to the original case (0.0863kg/s). However, even with larger mass flow rate the average value of the absolute flow velocity at rotor outlet for the modified case (56.86m/s) was slightly lower than the original case (57.4m/s) as shown in Figure 3-31. This is due to the fact that with the growth of boundary layer in the original case where the effective flow area was reduced, the flow was required to move with higher velocity in order to conserve mass and hence led to larger exit kinetic loss. The accumulative effects of these two factors resulted in better performance for the modified thickness and it was selected for further CFD investigations in the next section.

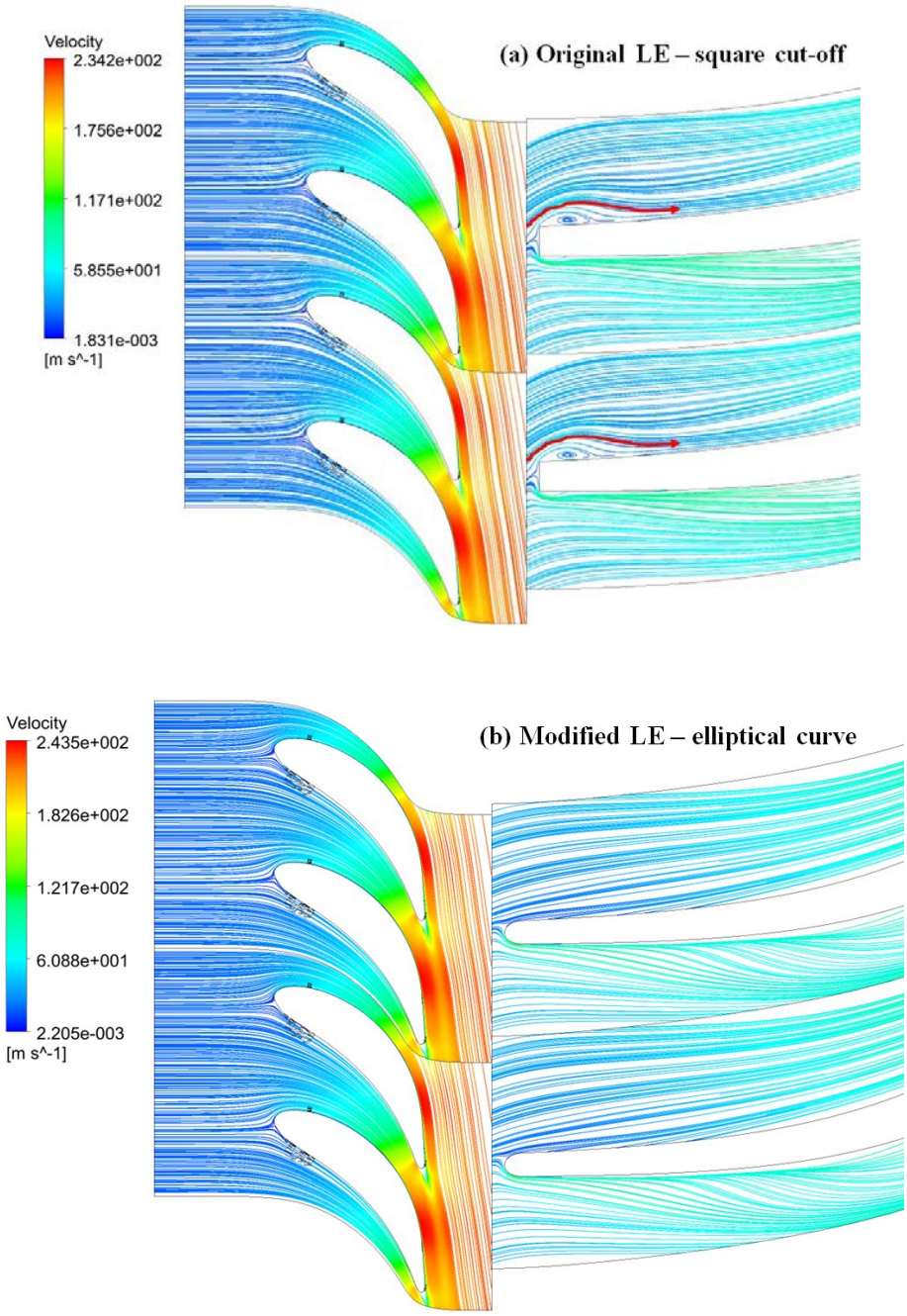

Figure 3-30 Velocity streamlines at half span (a) original LE – square cut-off (b) Modified LE – elliptical curve

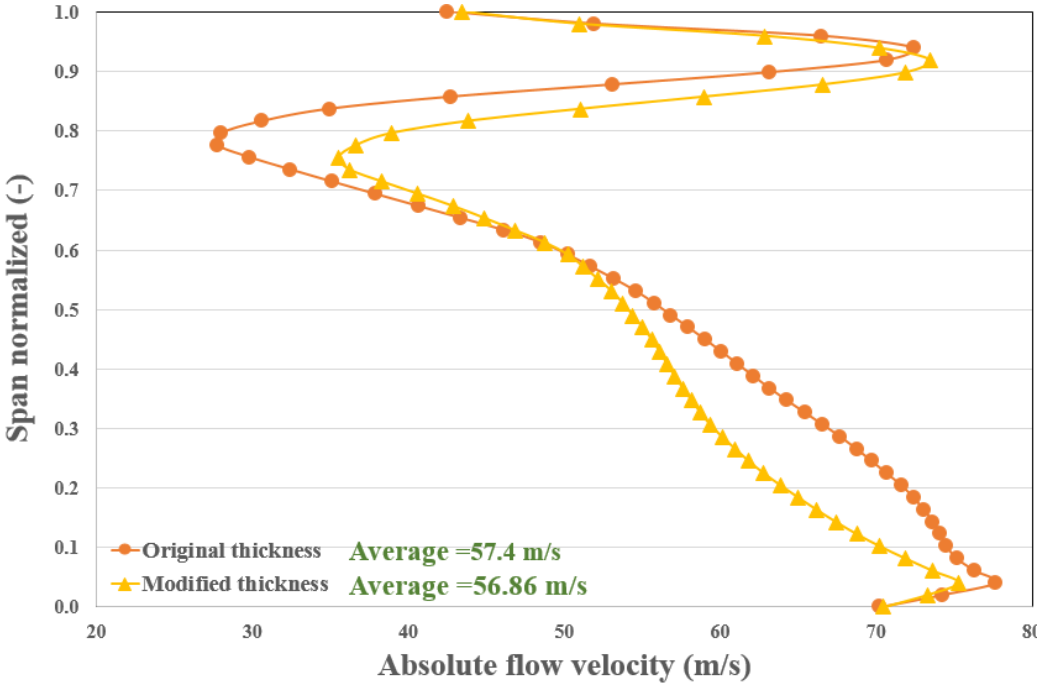

Figure 3-31 Absolute flow velocity at the rotor outlet for the original and modified profile "D"

3.6.3.5. Effect of rotor blade number

The minimum number of rotor blades is a critical parameter that affects the performance, blade loading and the rotating inertia of the turbine. Despite a number of empirical correlations such as the one shown in Equation 3-26, accurate estimation of the minimum number of rotor blades that leads to best performance can be reliably obtained with CFD analysis. The flow field behaviour, blade loading and the global performance parameters were examined for different number of rotor blades (Z_{rotor}) to select the appropriate value. Profile "D" with modified thickness and LE shape (section 3.6.3.4) was investigated with lower number of blades as Z_{rotor} =11, Z_{rotor} =13 and Z_{rotor} =15 compared to the original value of Z_{rotor}=16. Figure 3-32 to 3.35 show the blade loading and Mach number distribution contour plots at half span for rotor blade numbers 11, 13, 15 and 16 respectively. As it is evident from the results, there is an optimum number of blades with the maximum efficiency of 84.54% obtained with Z_{rotor}=15, though the results for the other cases were also competitive.

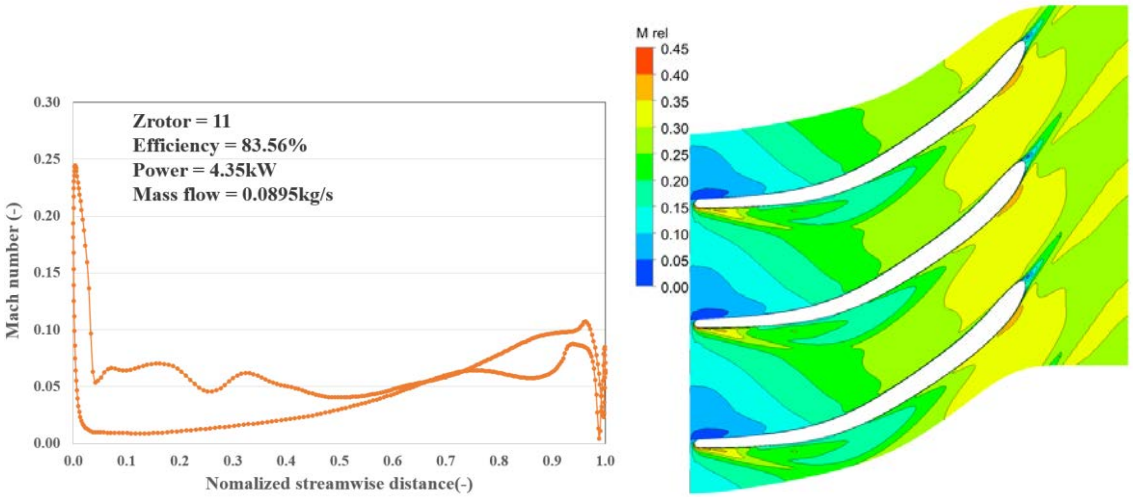

Figure 3-32 Blade loading (left) and Mach number (right) for Z_{rotor} =11

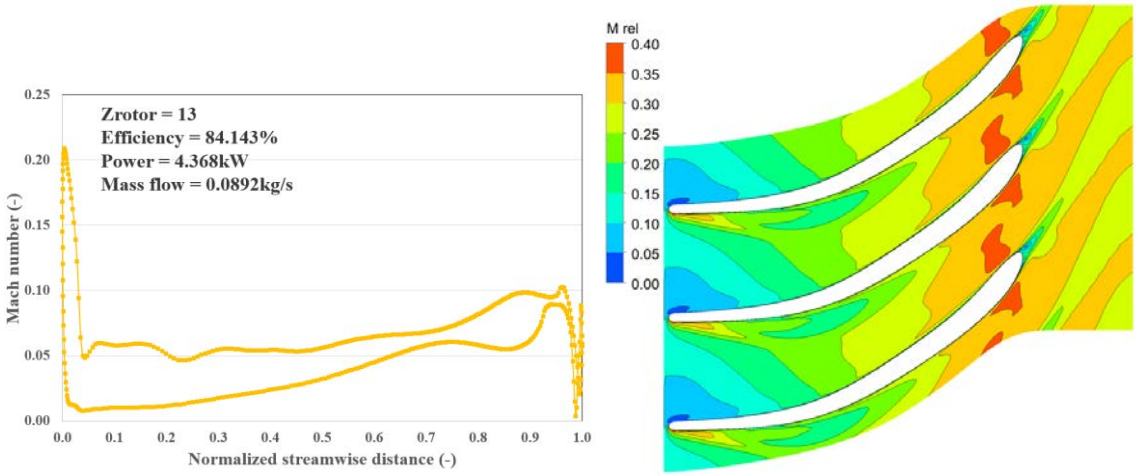

Figure 3-33 Blade loading (left) and Mach number (right) for Z_{rotor} =13

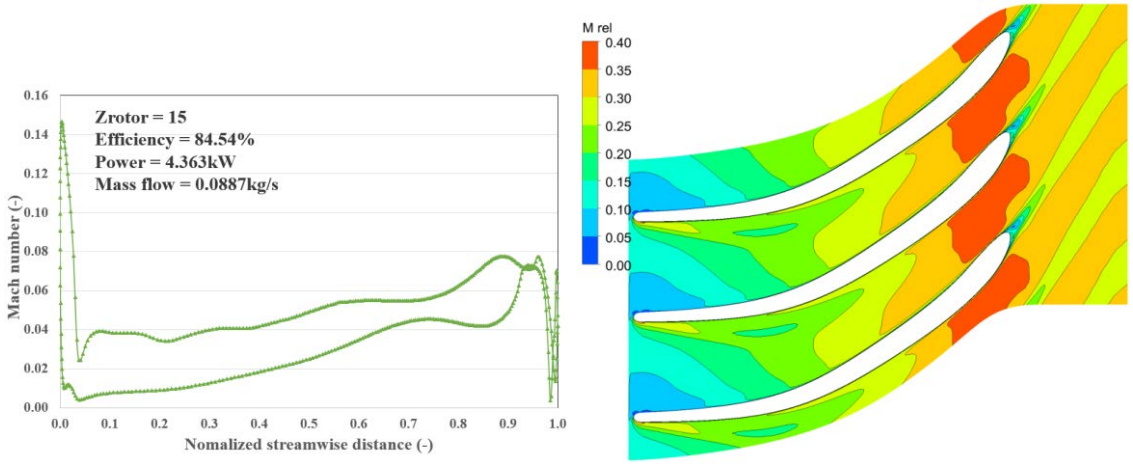

Figure 3-34 Blade loading (left) and Mach number (right) for Z_{rotor} =15

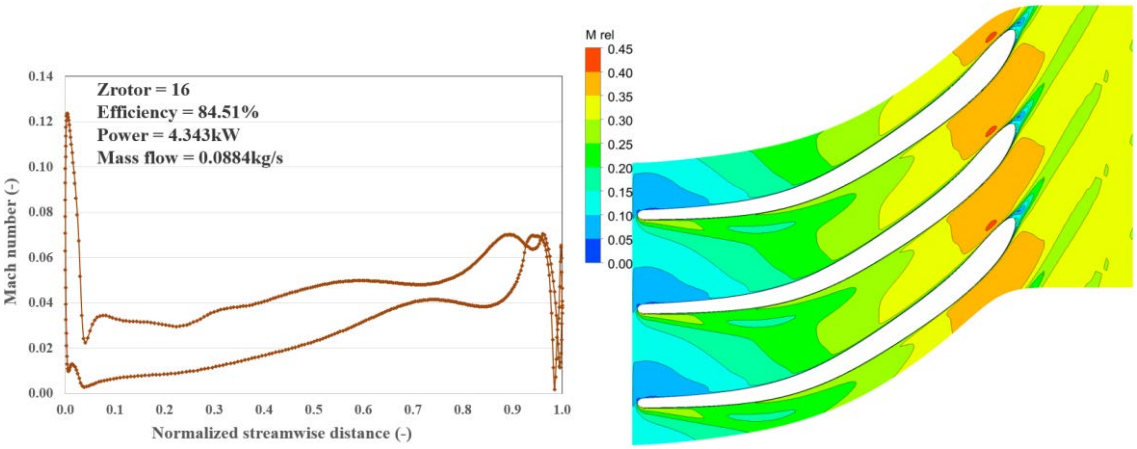

Figure 3-35 Blade loading (left) and Mach number (right) for Z_{rotor} =16

The case with Z_{rotor}=11 suffered from strong secondary flow and flow separation on the suction surface (SS) starting from downstream of the LE and propagating to about 65% of the stream-wise passage length. Such effect is clearly visible from the blade loading chart (Figure 3.32) with excessive diffusion levels and almost negative loading. For the other cases there is no evidence of negative loading. Since the aim of the rotor blade is to increase the relative Mach number as close as possible to the design value, both cases with Z_{rotor} =11 and 13 are unable to accelerate the flow relative velocity and therefore the relative Mach number to as high as 0.417 (Table 3-2) compared to Z_{rotor} =15 and 16. As can be seen from Figures Figure 3-34 and 3.35, a major part of the rotor passage near the trailing edge (TE) is occupied with Mach number contour of about 0.4 compared to the two other cases. Since the maximum efficiency is obtained by Z_{rotor}=15 and it provided smooth expansion on both SS and PS with uniform velocity vectors and even slightly larger power output compared to Z_{rotor} =16, such value was selected. Moreover, Z_{rotor} =15 assures that the number of rotor and nozzle blades are odd and even respectively in order to avoid the possible resonances due to the blades interaction. It is clear from the above results that, CFD analysis can be used to predict a more realistic

rotor design in terms of blade profiles, thickness distribution and number of blades. Therefore the blade profile "D" with the modified thickness and LE shape and Z_{rotor} =15 was selected as the final configuration from the aerodynamic evaluation and was used for further FEA, manufacturing and experimental testing explained in the next sections.

Complementary results in terms of pressure, Mach number and entropy distribution along the meridional channel of the case with Z_{rotor} =15 are shown in Figure 3-36. Clearly, there is smooth expansion in the nozzle and rotor across the meridional channel of the final geometry. Similarly, both the nozzle and rotor designs were sufficient to accelerate the flow velocity to the required design values. The entropy propagation is in accordance with the blade-to-blade plots. There exist slight rise in the entropy especially at the inlet portion of the rotor passage due to the formation of the weak flow reversal on the PS just downstream of rotor's LE.

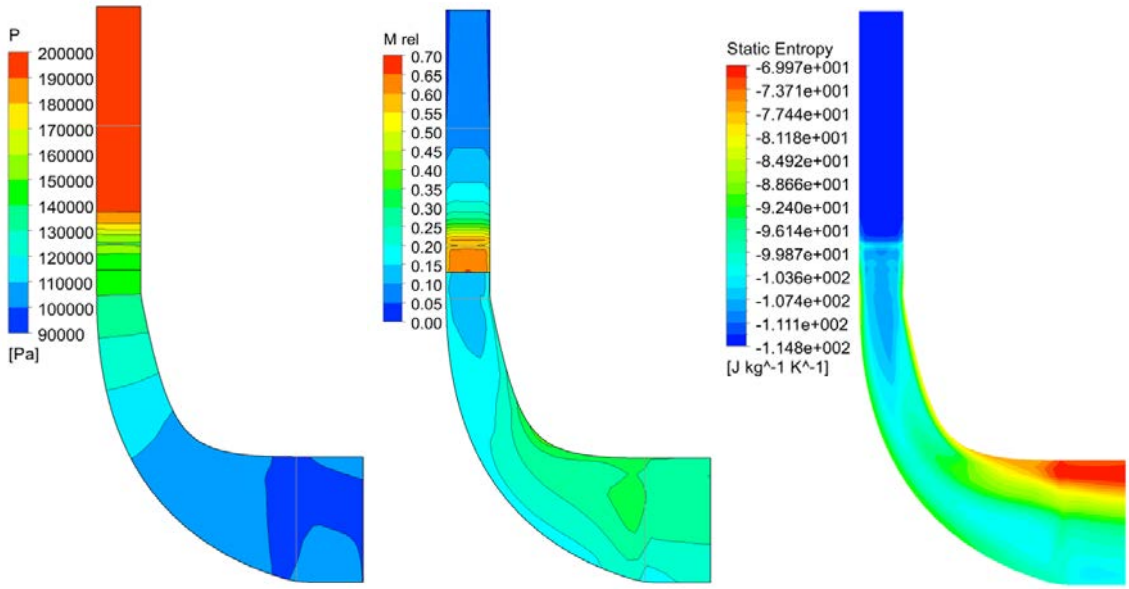

Figure 3-36 Meridional pressure (left), Mach number (middle) and entropy (right) distribution contour plots

However, the entropy increased significantly at the outlet region of the rotor near tip where the rotor tip leakage flow travelling away from the SS mixed out with the rotor TE wake and increased losses.

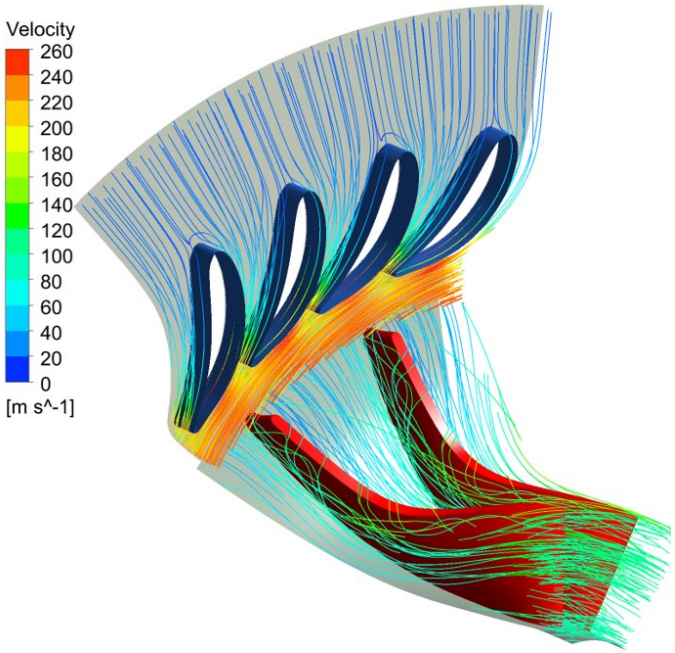

Figure 3-37 3-D velocity streamlines within nozzle and rotor passages

Figure 3-38 Final 3-D geometry of the rotor and nozzle

Figure 3-37 presents the 3-D velocity streamlines within the nozzle and rotor passages and illustrates the smooth velocity as well as the tip leakage flow. Additionally, Figure 3-38 illustrates the final 3-D geometry of the rotor and nozzle imported into a CAD package. For this final configuration the key results from the mean-line model were compared against the CFD results as summarized in Table 3-5 where the stage efficiency increased from 81.3% to 84.54% by improving the flow dynamics of the turbine. As can be seen from the Table 3-5, majority of the results are in close proximity when comparing the mean-line with CFD. This confirms that the developed mean-line model can fairly accurately predict the turbine performance and flow features of small-scale RITs and it can provide reliable results in the absence of CFD simulation.

Table 3-5 Comparison of the mean-line model and CFD results for the final rotor geometry

Parameter	Mean-line model	CFD
$T_{t,4}$ (K)	323	322.89
$P_{t,4}$ (kPa)	194.12	192.7
T_4 (K)	301.4	298.11
P_4 (kPa)	152.38	145.18
C_4 (m/s)	199.1	223.9
W_4 (m/s)	-49.82	-47.26
α_4 (degree)	78.6	78.906
β_4 (degree)	-39.61	-20.74
Ma_4 (-)	0.599	0.658
$T_{t,5}$ (K)	275.9	273.92
$P_{t,5}$ (kPa)	102.21	102.13
T_5 (K)	274.2	272.16
P_5 (kPa)	100	100
C_5 (m/s)	58.7	56.42
$W_{5,RMS}$ (m/s)	-140.6	102.64
α_5 (degree)	0	13.63
$\beta_{5,RMS}$ (degree)	-60.62	-57.55
$Ma_{5,rel}$ (-)	0.417	0.398
$\dot{m}$ (kg/s)	0.09	0.0887
Power (kW)	4.152	4.363
$\eta_{stage,ts}$ (%)	81.3	84.54

3.6.3.6. CFD analysis of the complete turbine stage

It was required to conduct the CFD analysis of the full nozzle and rotor wheels together with the casing. Due to the shape of the nozzle, an annular plenum with constant cross section (in contrast to volute) and sufficient volume was designed to transfer the fluid around the periphery of the nozzle.

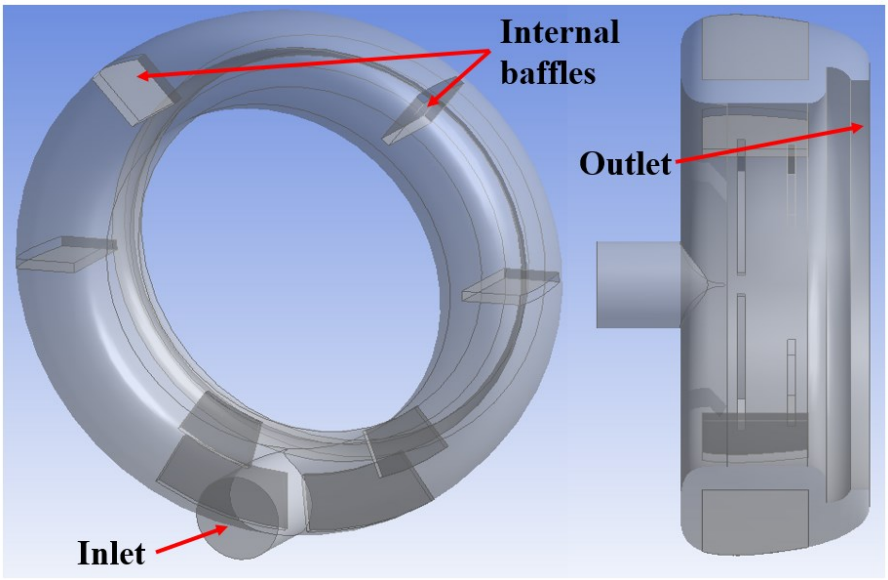

Figure 3-39 casing 1 with perpendicular inlet and internal baffles

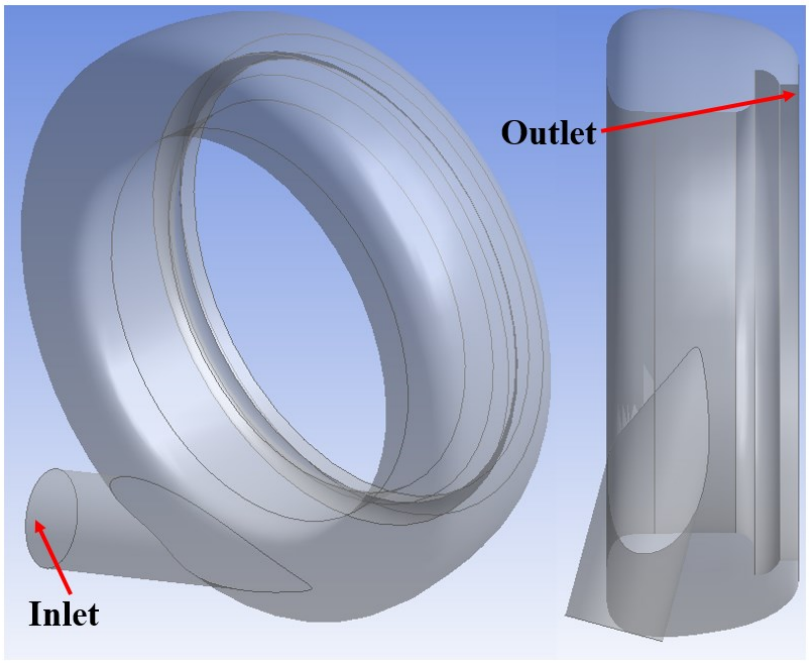

Figure 3-40 casing 2 with side inlet

The casing itself was supposed to provide the flow to the nozzle with minimal pressure loss, appropriate incidence angle and low gas velocity. Two configurations with same cross section and volume but with different arrangement of the inlet duct were analysed as shown in Figure 3-39 and 3.40. The former shows the casing with inlet pipe perpendicular to it and internal baffles while for the latter the inlet duct was located on the side of the casing. The mesh independence study for obtaining the minimal pressure variation from inlet to outlet resulted in total of 187145 and 186737 tetrahedron elements for casings 1 and 2 respectively as shown in Figure 3-41. The CFD setup for the nozzle and rotor domains followed the same procedure as explained in section 3.6.3.1 with the only difference that since all the complete rotor blades and nozzle vanes were simulated, the periodic boundary conditions were removed from the setup. The casing was considered as an additional stationary component with the specification of the inlet boundary conditions at its inlet instead of the nozzle inlet.

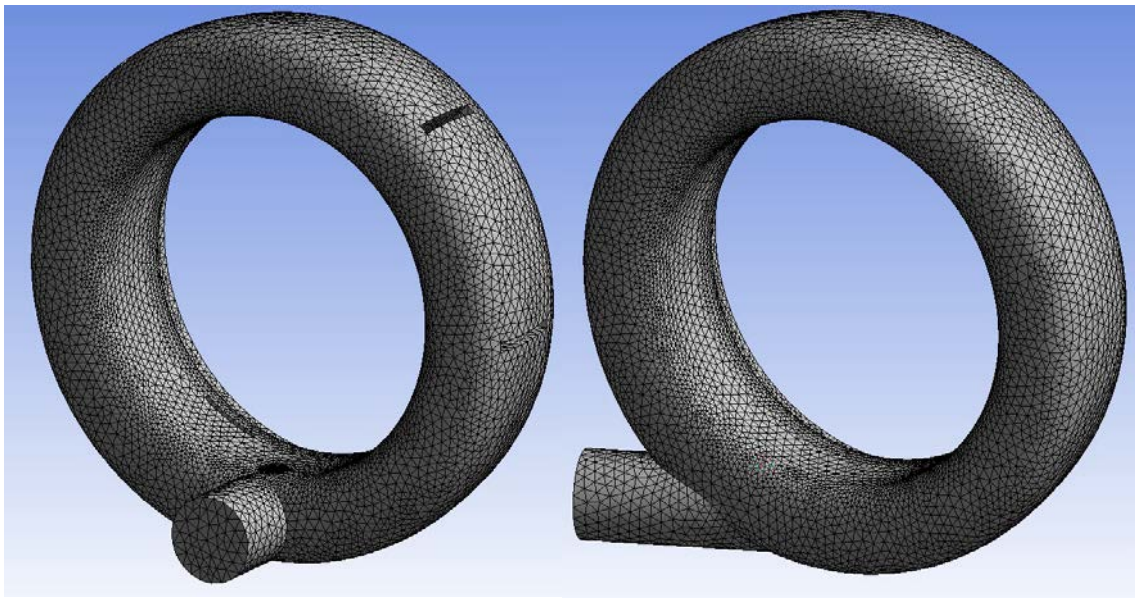

Figure 3-41 Mesh for casing 1 (left), casing 2 (right)

Moreover, an extra interface (general grid interface connection) was created between the casing outlet and nozzle inlet. Figure 3-42 and 3.43 illustrate the CFD setup of the complete turbine stage with casing 1 and 2 respectively. The simulations took about eight hours, four each case with parallel run on 4 CPU cores and the results are shown in Figure 3-44 to 3.46. Although, casing 2 provides a more uniform velocity streamlines within the casing, the level of velocity is much higher, 110 m/s, in casing 2 compared to casing 1 with velocity of about 60m/s.

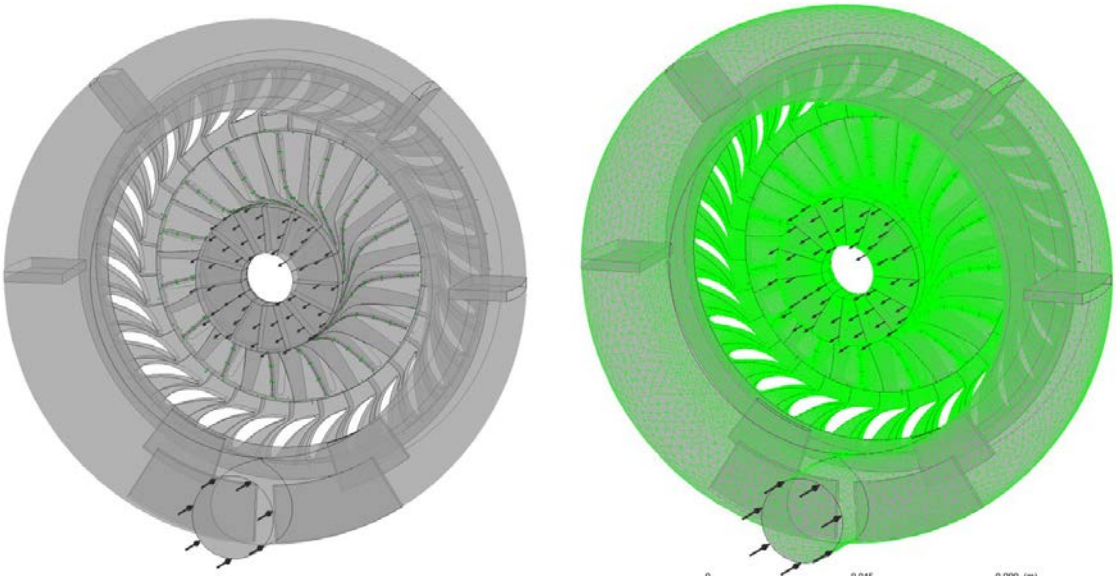

Figure 3-42 CFD setup of the complete turbine stage with casing 1

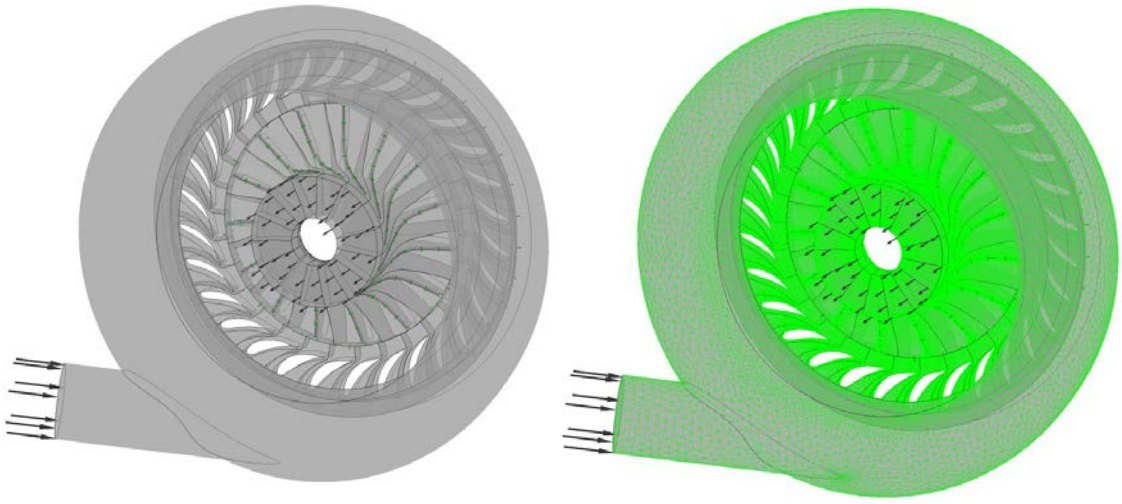

Figure 3-43 CFD setup of the complete turbine stage with casing 2

Moreover, there exist severe flow separation and negative loading in the nozzle blades of the simulation with casing 2 as can be seen in FiguresFigure 3-44 and 3.45. This is due to the fact that the nozzle design requires the flow to be in the perpendicular direction for optimum incidence but rather casing 2 provide the flow at an inclined angle. Comparing the nozzle blade loading for both casings (Figure 3-44) make such characteristic clearer as there is significant negative loading in the large portion of the nozzle passage from about 30% of the stream-wise distance to almost end of the nozzle passage for casing 2.

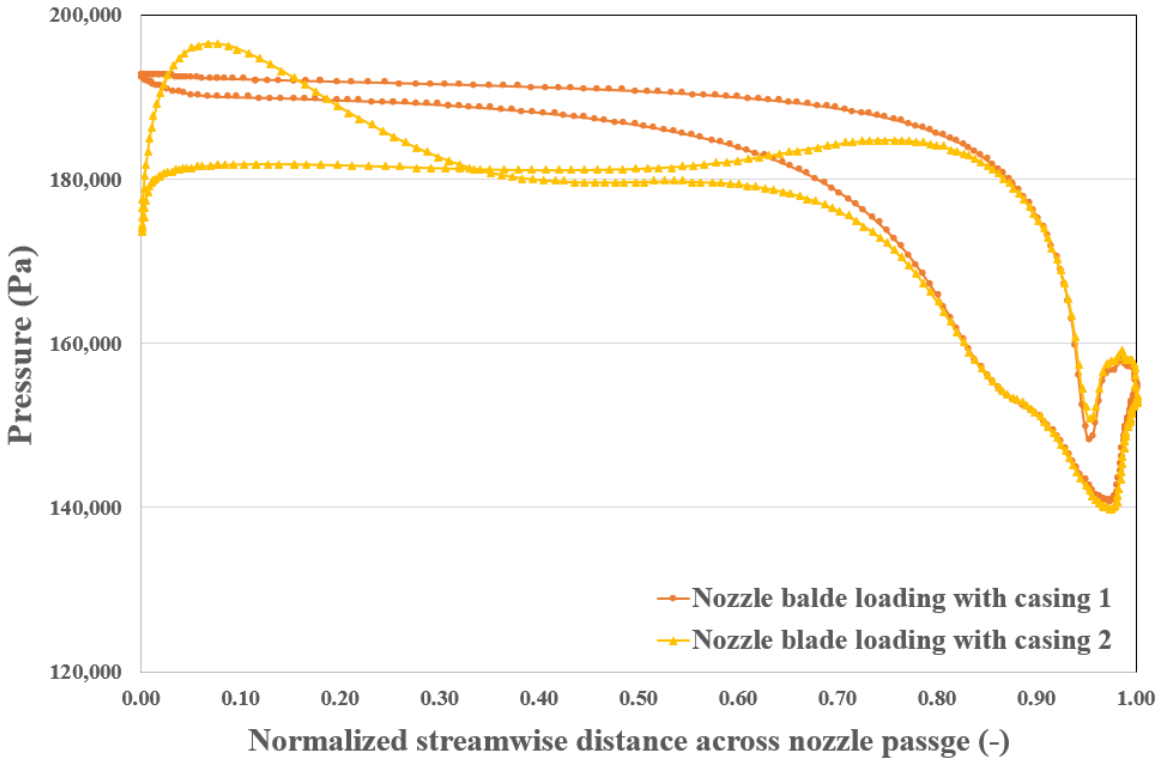

Figure 3-44 Nozzle blade loading obtained from the complete stage CFD analysis

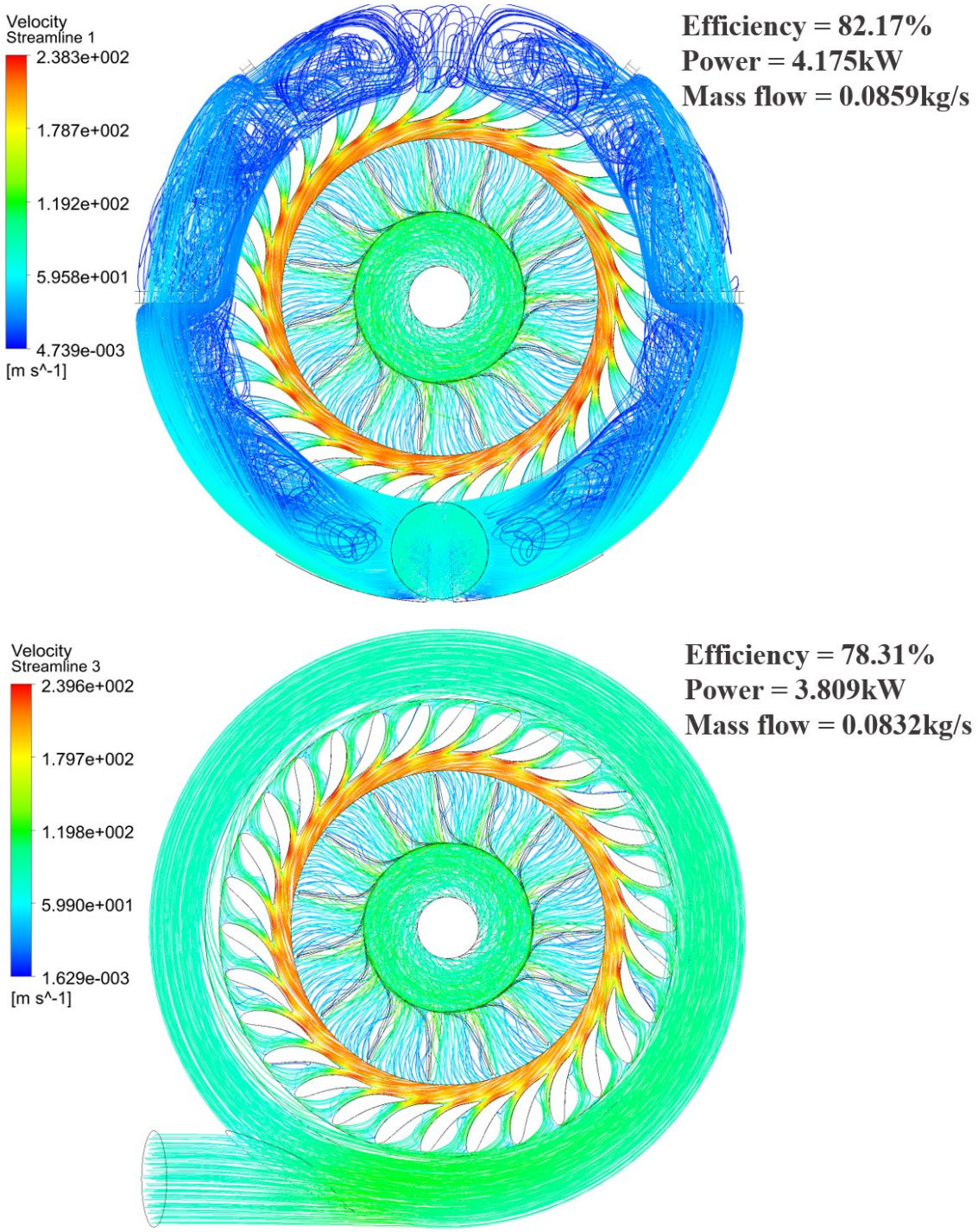

Figure 3-45 Velocity streamlines for complete turbine stage (top) with casing 1, (bottom) with casing 2

In contrast there is quite smooth and favourable expansion in the nozzle blades with casing 1 with no negative loading and also with optimum incidence as there is no pressure spikes at the nozzle inlet compared to the noticeable spikes for casing 2 (refer to Figure

3-44). Furthermore, it's apparent from the contours of entropy distribution at half span (Figure 3-46) that casing 1 exhibited much better performance as the level of entropy values is lower compared to casing 2. Such features resulted in 3.86% higher stage efficiency as well as 366W higher power for the simulation with casing 1 and such configuration was selected and perused in the next chapter.

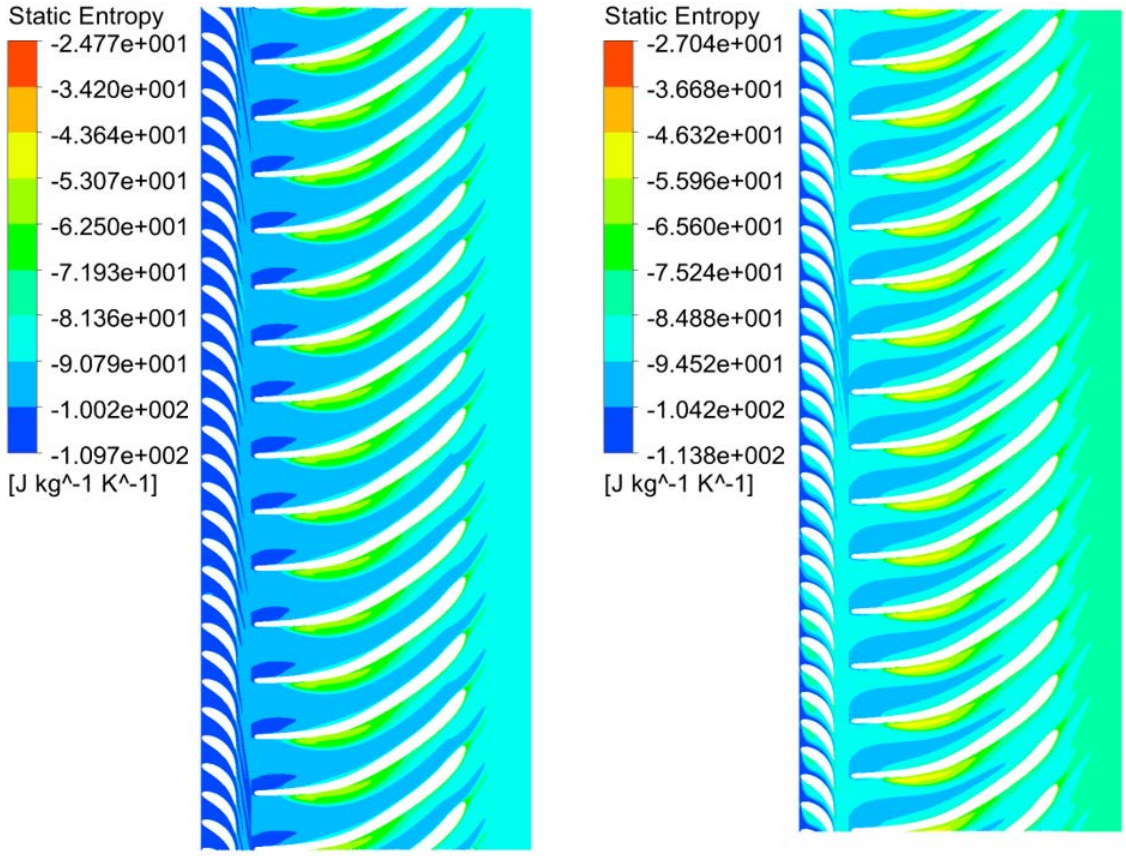

Figure 3-46 Contours of entropy distribution in blade-to-blade view at half span, (left) with Casing 1, (right) with Casing 2

3.6.4. Finite element analysis (FEA)

3.6.4.1. Material selection and properties

In order to carry out the FE analyses, the rotor material should be specified. It was decided to manufacture all the components using additive layer manufacturing technique (3-D printing) as will be discussed in chapter four. Objet FullCure720^{TM} is the standard original multi-purpose transparent material widely used in 3-D printers. The properties of

the aforementioned material are summarized in Table 3-6 and was used for the FEA. The maximum tolerable temperature for such material is about 50˚C before deformation as it is specified by the glass transition temperature.

Table 3-6 Material properties of Objet FullCure 720^{TM}

Parameter	Manufacturer values
Tensile strength (MPa)	60
Modulus of elasticity (MPa)	2870
Flexural strength (MPa)	76
Flexural modulus (MPa)	1718
Density (kg/m^3)	1185
Poisson's ratio (-)	0.27
Glass transition temperature (°C)	50

3.6.4.2. FEA modelling strategy, grid generation and setup

The final rotor blade 3-D geometry defined by the CFD studies in section 3.6.3 was investigated further to assess its mechanical integrity using FEA. The FE analyses involved investigation of the blade stress and displacement under both the fluid pressure on the blade surface and also centrifugal forces due to the rotational speed. Since the rotor is the critical component amongst all, FEA are merely conducted for this part. All the FEA simulations were performed with ANSYS^{R15} Mechanical, part of the ANSYS^{R15} workbench to ease the transfer of information between the CFD and FEA modules. The objet FullCure720^{TM} material properties (Table 3-6) were defined in ANSYS^{R15} Mechanical and assigned to the rotor blade. The rotor blade hub surface was specified as a fixed support (Figure 3-47) for both FEA due to the fluid pressure and due to the rotational speed. For the former, the blade surface was selected and the imported pressure from the CFD simulation was applied to it. For the latter the rotation axis was defined based on the rotor configuration and the design speed (55000rpm) and direction were assigned to it (Figure 3-47).

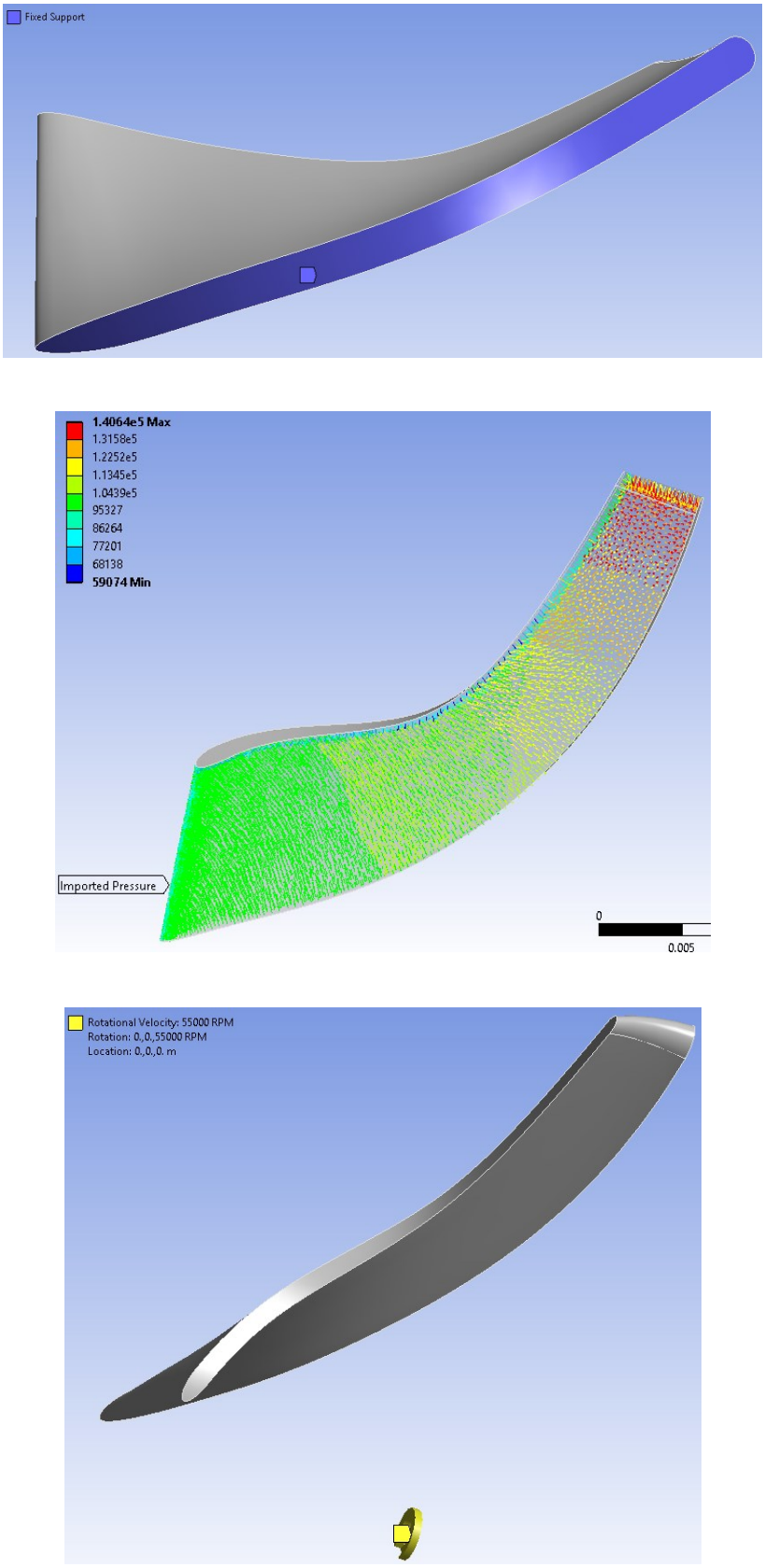

Figure 3-47 Specified boundary conditions for the FEA, (Top) fixed support, (middle) imported pressure from CFD simulation, (bottom) rotational speed and axis of rotation

The aim of all FEA simulations were to assure that the maximum stress and displacement were below the material tensile strength (60MPa) and the running clearance (0.56mm between rotor tip and casing) respectively. Therefore, equivalent von-Mises stress and total deformation were defined as the output of the FEA simulations.

3.6.4.3. Mesh sensitivity study and FEA results

Similar to the CFD analyses, mesh independence study was carried out using three different grid resolution while the rotor maximum stress and displacement were monitored and the results are summarized in Table 3-7. Tetrahedron mesh type was used to generate the grid in all cases as demonstrated in Figure 3-48.

Table 3-7 Mesh independence study results of FEA

	Number of elements	Maximum von-Mises stress (MPa)		Maximum displacement (mm)	
		Due to pressure	Due to rotation	Due to pressure	Due to rotation
1	4283	0.6309	23.57	0.02055	0.1895
2	14162	0.9819	22.01	0.01615	0.1944
3	50274	1.1104	25.11	0.015	0.1957

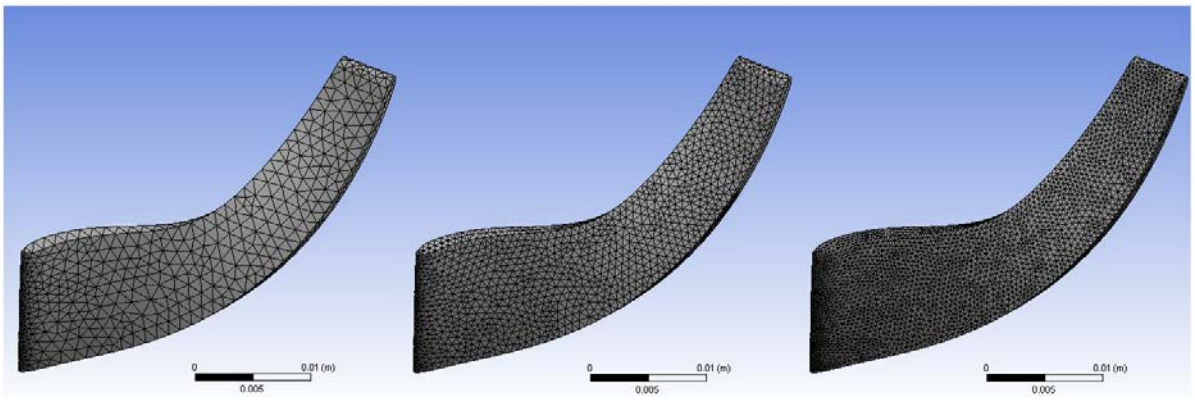

Figure 3-48 FEA tetrahedron mesh, (left) coarse mesh, (middle) medium mesh, (right) fine mesh

As it is evident from the results in Table 3-7 there exist considerable deviation between the maximum stress and maximum displacement due to pressure between rows 1 and 2 with the maximum deviation of 35.7% and 21.41% respectively. However,

increasing the number of elements from 14162 to 50274 (rows 2 and 3) reduces such variations to 11.57% and 7% respectively. On the other hand, the maximum stress due to the rotational speed increased from 22MPa to 25.11MPa. Therefore, the more conservative results from the mesh in row 3 was selected as the grid independence values. The contour plots for stress and displacement distribution due to both pressure and rotational speed based on the mesh resolution in row 3 of Table 3-7 are shown in Figure 3-49.

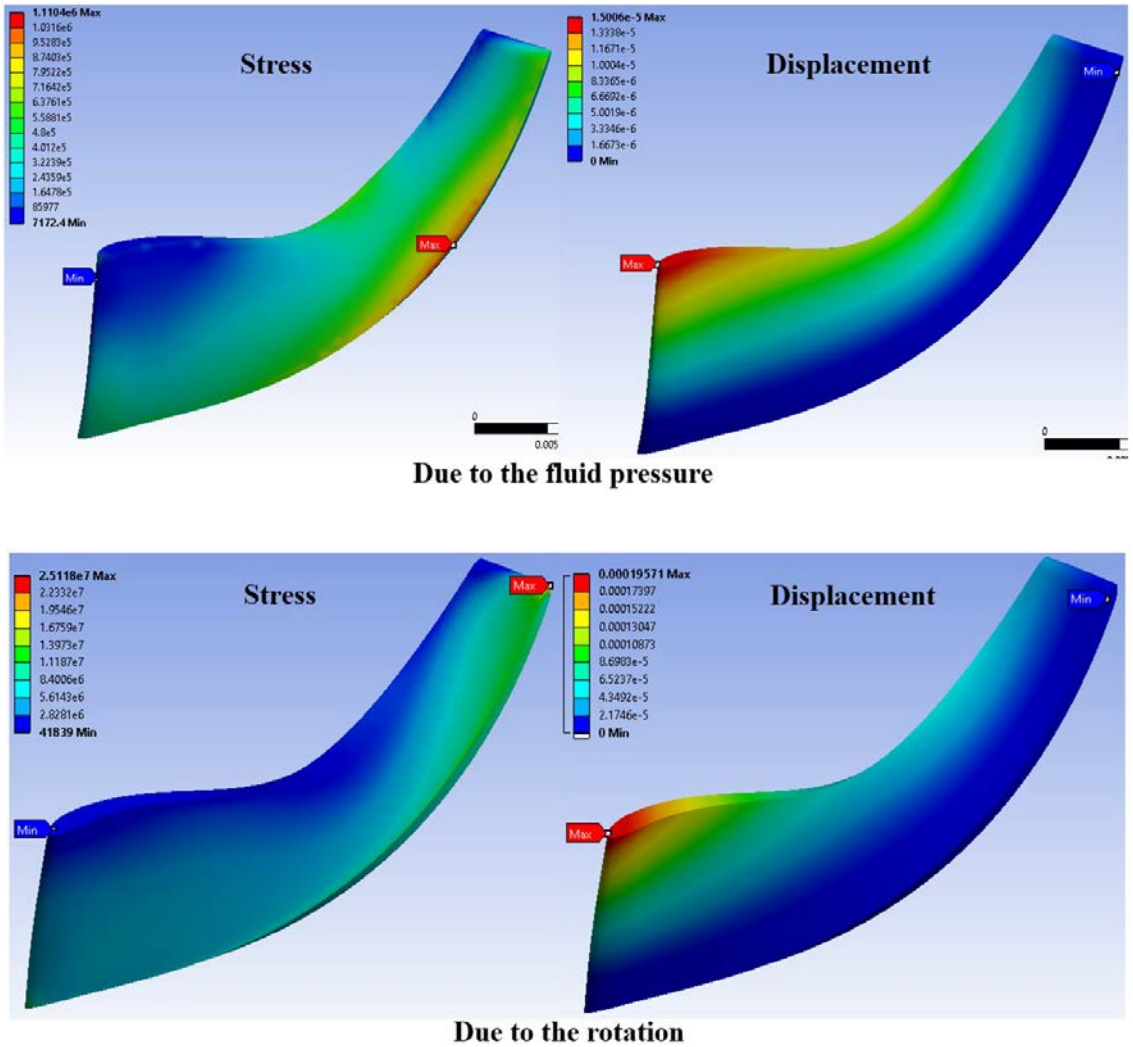

Figure 3-49 Stress and displacement distribution contour plots, (top) due to pressure, (bottom) due to rotation

It is evident that the maximum stress and displacement are all well below the material tensile strength and the running clearance and confirms the mechanical integrity

of the developed rotor. The maximum stress occurred in the blade root at hub for both pressure and rotational speed while the maximum displacement was at the blade exit tip for both cases. It should be noted that there still exist room for further reduction of the blade thickness and hence increase the isentropic efficiency (section 3.6.3.4) while keeping the maximum stress below the tensile limit, however, the minimum thickness was also limited by the manufacturing technique (as will be discussed in the next chapter) to 1mm. Therefore, the FE analysis was considered sufficient for the purpose of this chapter.

3.7. Summary and conclusions

This chapter proposed an effective methodology for developing RIT for small-scale applications. Such method encompasses the one-dimensional mean-line modelling, aerodynamic investigation using CFD simulations as well as FE analysis for assessing the mechanical integrity of the turbine blades. Mean-line modelling enables fast and fairly accurate estimation of the turbine performance as well as obtaining the key geometrical parameters of the RIT stage. Such unique feature allows investigating the effect of a large group of input parameters on the turbine performance and size in a very short time. The parametric studies showed that the turbine efficiency was affected by almost all of the investigated input parameters whereas the turbine power output was mostly affected by $T_{t,1}$, $\dot{m}$, ER_{ts}, v and α_4 and the turbine rotor inlet diameter was only affected by $T_{t,1}$, ER_{ts}, v and ω. The results of such parametric studies are substantially useful for selecting the best values for the turbine input parameters that led to high performance. Although effective, mean-line modelling cannot capture the complete behaviour of the flow within the RIT blade passages due to the three-dimensional and complex nature of such flow. Therefore, the candidate RIT configuration suggested by the mean-line modelling was required to be further investigated with the CFD analysis. The shape of the rotor blade in

terms of the blade angle and thickness distributions and the number of rotor blades was modified using the CFD analysis to reduce the entropy generation and losses and consequently increasing the efficiency. Such CFD simulations were effective as they improve the turbine isentropic efficiency from 81.3% obtained from mean-line modelling to 84.5% obtained by the CFD analysis. To ensure the mechanical integrity of the turbine rotor blade obtained with CFD simulations, FE analyses were performed. The results of the maximum stress and displacement showed that they were well below the limits and assured the safe operation of the developed RIT. The results in this chapter serve as the basis for further investigating the developed RIT by conducting experiments for validation purposes (as will be shown in the next chapter) and completing the methodology proposed in this chapter.

CHAPTER 4

MANUFACTURING AND EXPERIMENTAL TESTING OF THE DEVELOPED COMPRESSED AIR RIT

4.1. Introduction

The compressed air turbine developed in chapter three has great potential to be integrated with the compressed air energy storage (CAES) systems for generating electricity. CAES is a cost effective technology where the surplus of electrical energy is stored in the form of high-pressure air in underground or aboveground storage reservoirs by running a compressor. Then during peak demand this compressed air is released and expanded through a turbine to generate electricity (Safaei *et al.* 2013). Compare to the Brayton cycle, CAES can save up to two-third of the generated electricity by storing air and recovering it later in the process (Kokaew *et al.* 2013). This is due to the fact that turbine's output no longer needs to be used to drive the air compressor, the turbine can generate almost three times as much electricity as the same size turbine in a simple

Brayton cycle configuration (Lemofouet *et al.* 2006). Therefore, developing efficient compressed air turbines such as the one in chapter three is vital for CAES application and RIT can play an important role in increasing the efficiency of this energy conversion process.

Recalling the turbine development methodology proposed in chapter three (refer to Figure 3-3), it is the last two steps that remained and needs to be completed. Thus, in this chapter the CAD modelling, manufacturing technique and experimental testing of the RIT developed in chapter three will be described in details together with the explanation of the instrumentation, calibration and uncertainty analysis. Moreover, the accuracy of the CFD model will be assessed by comparing the experimental results with the corresponding CFD values and eventually the effectiveness of the proposed approach will be highlighted.

4.2. 3-D CAD solid modelling and manufacturing

4.2.1. CAD modelling

The nozzle ring and rotor wheel (Figure 3-38) together with the complementary components such as casing (Figure 3-39), shaft and bearing housing were imported into the SolidWorks CAD package to include the fillets at the rotor blade root as well as accommodating the bearings, retaining rings, O-rings and grooves within the casing. The casing itself was designed in two pieces in order to ease its manufacturing. Hybrid ceramic ball bearing with two rubber seals was selected to allow for high rotational speed as well as for sealing requirements. O-rings and their grooves were accommodated between any two flanges for the purpose of appropriate sealing. Moreover, in the light of earlier FEA of the complete turbine assembly (Figure 4-1) the thickness of casing was specified together with the inclusion of stiffening ribs to ensure the mechanical integrity of casing under the operating pressure. The complete turbine assembly is presented in

Figure 4-2 and 4-3. Further details can be found in the turbine detailed drawings in Appendix C.

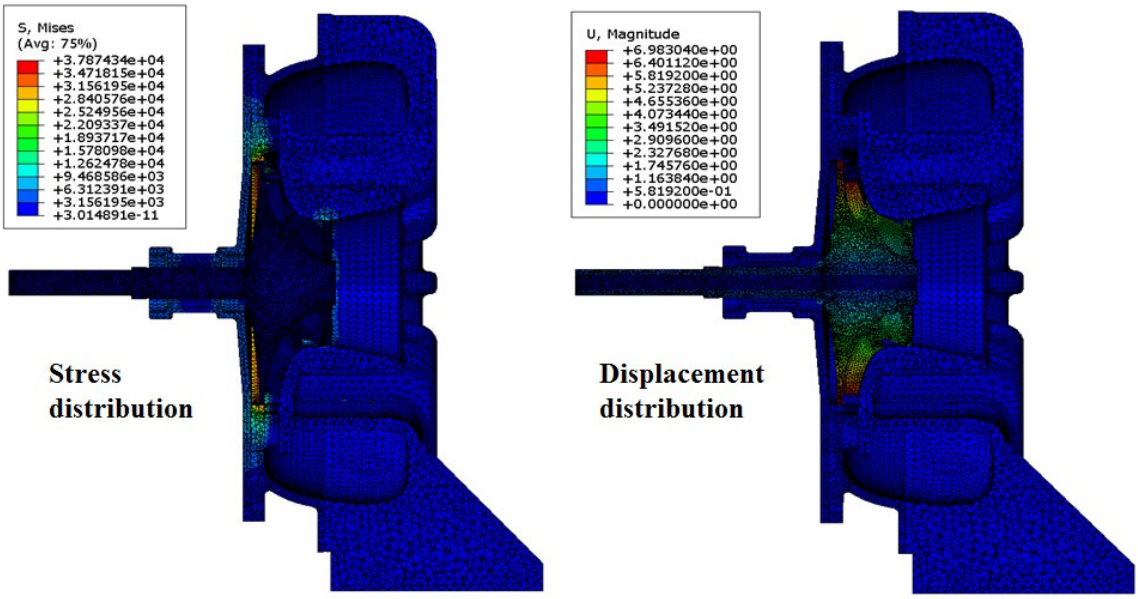

Figure 4-1 FEA of the complete turbine assembly

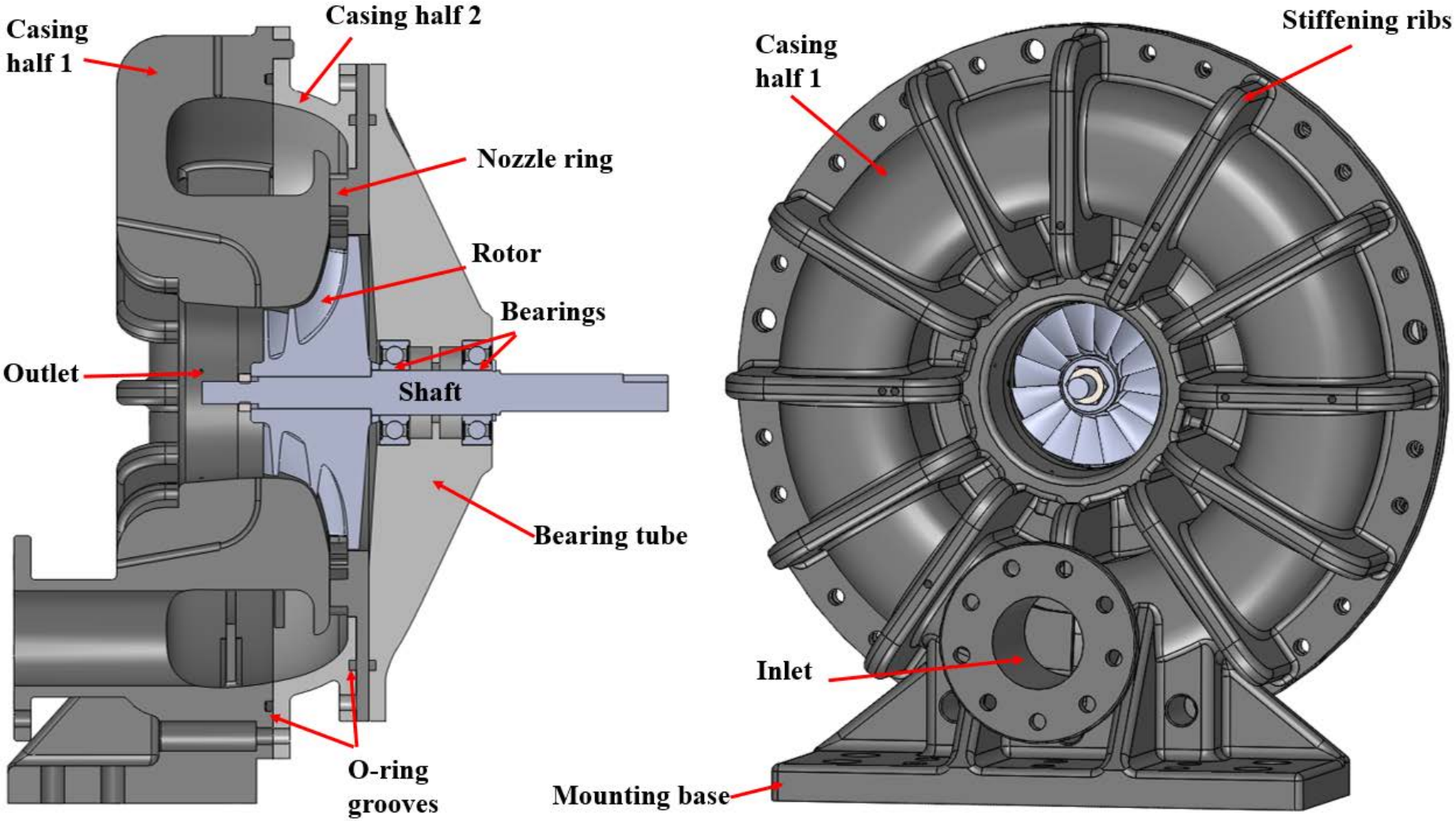

Figure 4-2 CAD model of the complete turbine assembly, (left) section view, (right) isometric view

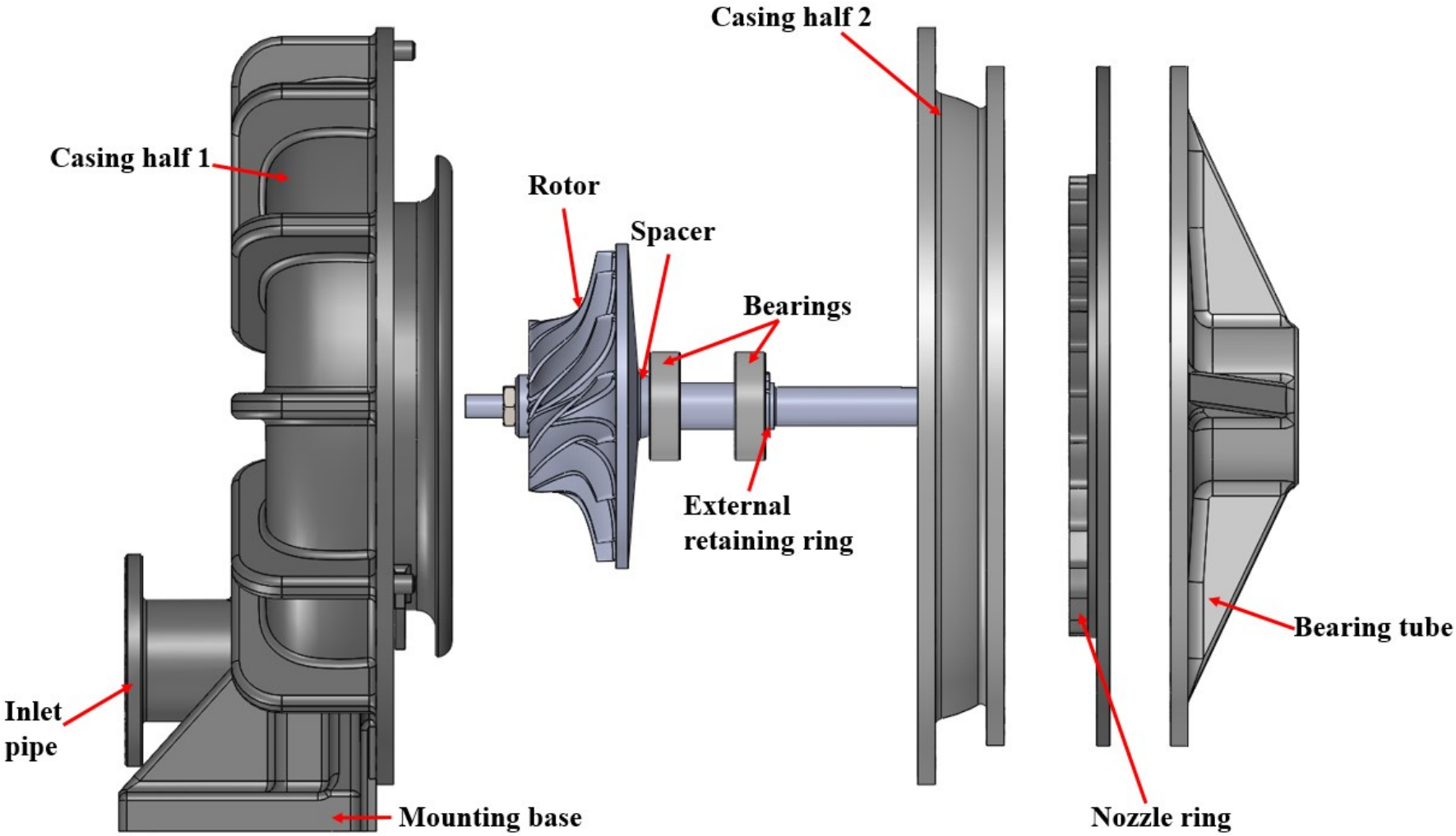

Figure 4-3 CAD model of the complete turbine assembly exploded view

4.2.2. Additive layer manufacturing

Rapid prototyping using additive layer manufacturing technique (3-D printing) is an emerging technology with substantial advancements in the past few years. This technology utilizes standard inkjet printing technology by creating the parts layer-by-layer (layer thickness of about 32microns) by depositing a liquid binder onto thin layers of powder. The printing head moves over a bed of powder upon which it prints the cross sectional data and distributes the power accurately and evenly across the build platform. The print head applies the cross sectional data for the next layer which binds itself to the previous layer and such procedure is repeated until the complete physical model is created. Such procedure is fast, efficient and economical for manufacturing of the parts that are not possible to be manufactured with conventional techniques (i.e. milling and turning) or are substantially expensive. All the components of RIT stage were manufactured in-house with the OBJET EDEN 250 3-D printer using objet FullCure 720 at the school of Mechanical Engineering, University of Birmingham except for the shaft that was machined from mild steel. Figure 4-4 illustrates all the manufactured parts.

4.3. Experimental testing

4.3.1. Description of experimental facility

Figure 4-5 presents schematic diagram of the experimental facility used in testing of the developed RIT. It consists of a compressed air tank supply, heater tape and control box, flow meter, turbine, instrumentations, torque meter, valves and data acquisition device. The compressed air from the supply tank is initially passed through a filter-regulator to both remove any condensate and dirt from the flow stream and also regulate the inlet pressure to the required level. Then the regulated air passed through a globe valve to accurately control the flow rate.

Figure 4-4 Manufactured turbine components with 3-D printing

A section of the piping system is wrapped with a 500W heater tape to enable variation of the air temperature at the turbine inlet. The heating rate of heater tape is controlled by a thermocouple at the turbine inlet based on the adjusted temperature of the control box. The heated air is then passed through the flow meter to measure the flow rate. A pressure gauge was fitted after the flow meter and close to the turbine inlet to determine the pressure at the turbine inlet. The heated air enters the turbine inlet duct where a Pitot-static tube and thermocouples are fitted for measuring inlet pressure and temperature. The air circulated around the casing, passed through nozzle and rotor and discharged from the turbine exit duct where one pressure transducer and several thermocouples are fitted for measuring the exit pressure and temperature. All the instruments are connected to data loggers which are connected to PC for recording data. The turbine shaft is connected with coupling to one end of the torque meter for measuring the rotational speed, torque and power. In order to apply load to the turbine shaft, the other end of torque meter is connected with coupling to a brushless DC generator which itself is connected to a variable resistance to facilitate variation of load. The data from torque metre is transferred to PC for recording. Figure 4-6 presents the fabricated test facility and its different components.

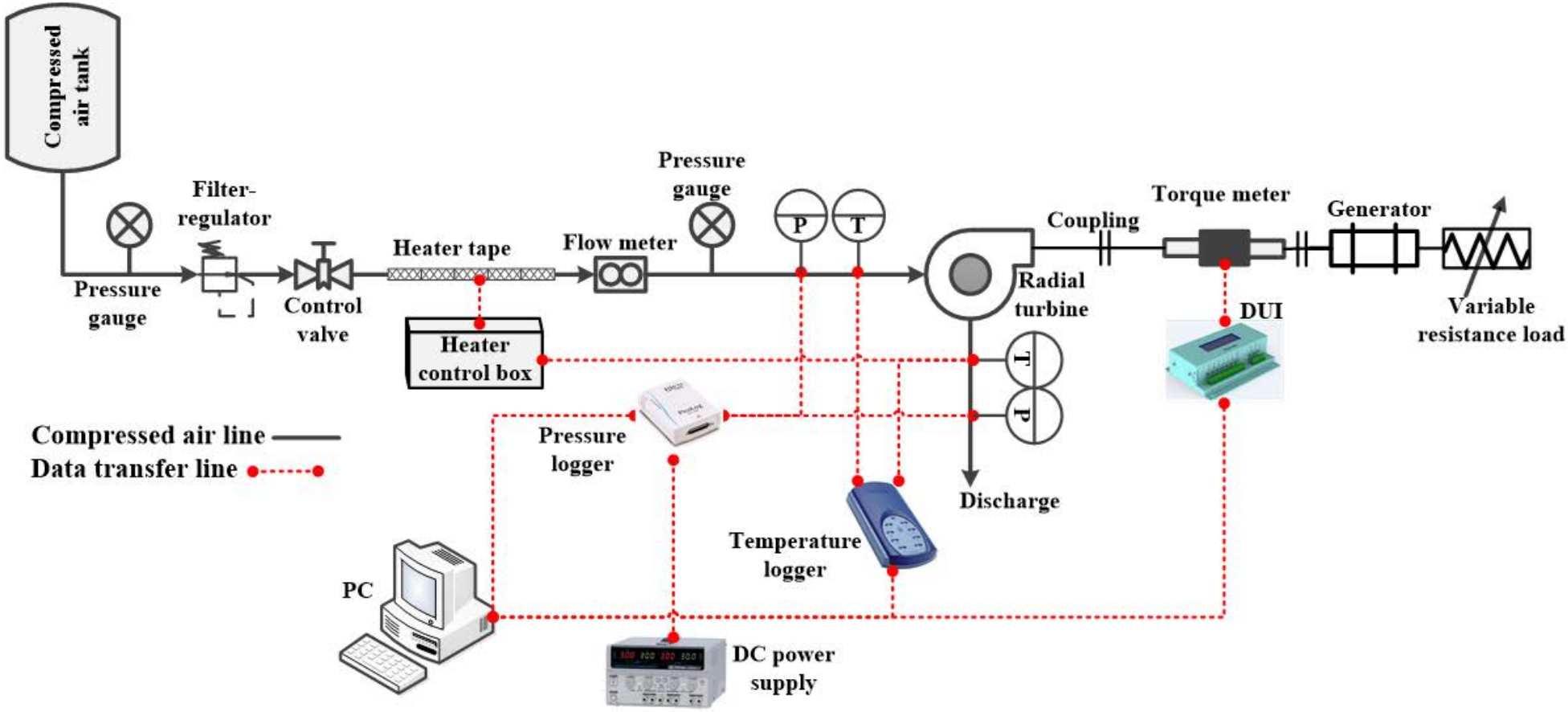

Figure 4-5 Schematic of the experimental compressed air RIT test facility

Figure 4-6 Fabricated experimental facility for testing the compressed air RIT

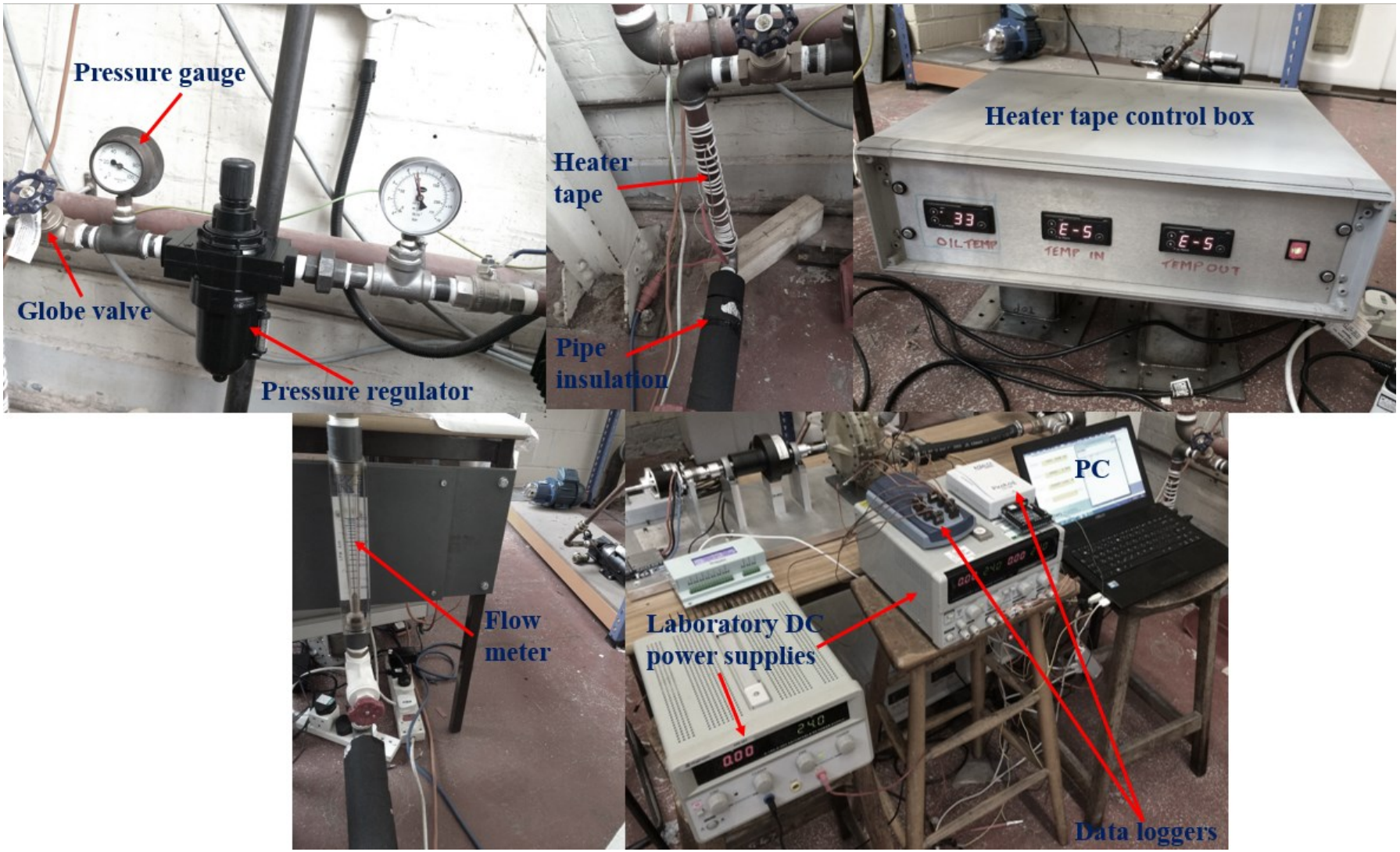

Figure 4-6 *(Continued)*

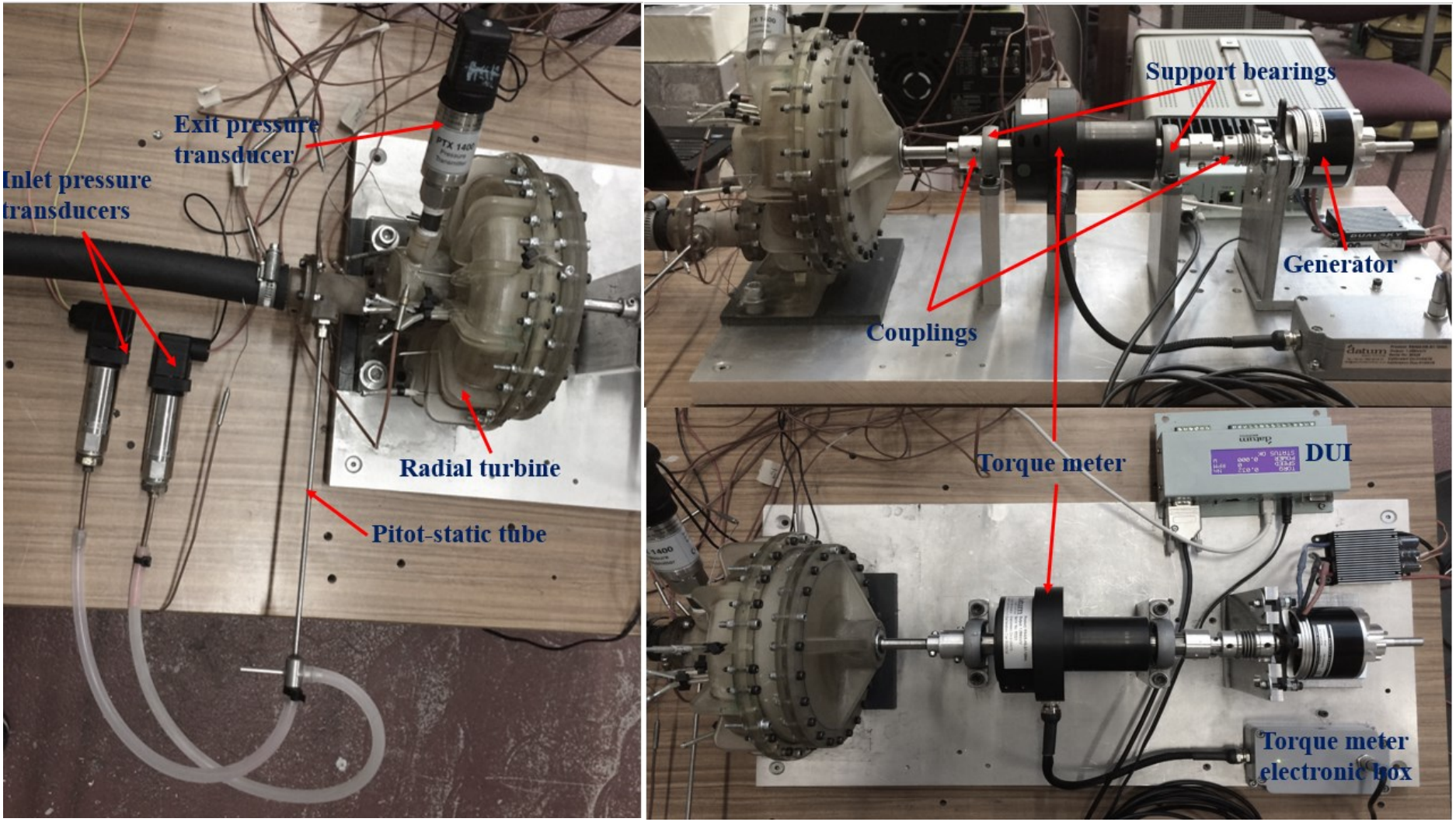

Figure 4-6 *(Continued)*

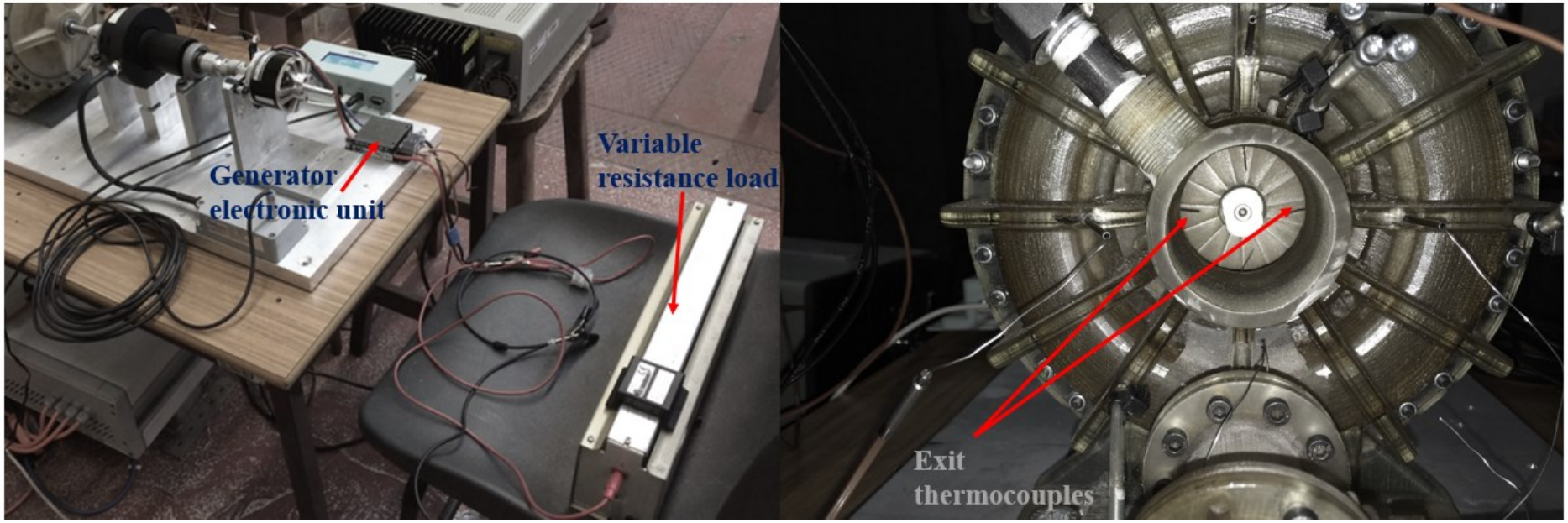

Figure 4-6 *(Continued)*

4.3.2. Instrumentation

The test facility was instrumented with measuring devices of temperature, static and total pressures, flow rate and torque to enable evaluating the turbine power and efficiency under a range of operating conditions.

4.3.2.1. Thermocouples

Three thermocouples were installed at the turbine inlet pipe while four equi-spaced thermocouples were located circumferentially around the turbine exit pipe close to the rotor blade. All thermocouples utilized in measurements were T-type Omega TJC100-CPSS-M075G-150 probes with the sheath diameter of 0.75mm, length of 150mm and the accuracy of $\pm$0.5°C according to the manufacturer.

4.3.2.2. Pitot-static tube and pressure transducers

The turbine was instrumented with a Pitot-static tube at the turbine inlet pipe to measure the total and static pressures simultaneously. Each of the Pitot tube ports were connected directly to two 10bar GE UNIK 5000 pressure transducers. A 6bar Druck PTX 1400 pressure transducer were fitted at the turbine exit duct for measuring the exit static pressure. All pressure transducers were 4-20 mA current output with accuracy of $\pm$0.04% full scale according to the manufacturer. 100 ohms resistances were connected to the data logger external terminal board to convert the current signal to voltage signal (up to 2 volt). The pressure transducers were excited with 0.005A and a voltage of 24V from ISO-TECH IPS4303 laboratory DC power supply. The electrical wiring of the pressure transducers with the data logger and power supply is illustrated in Figure 4-7 below.

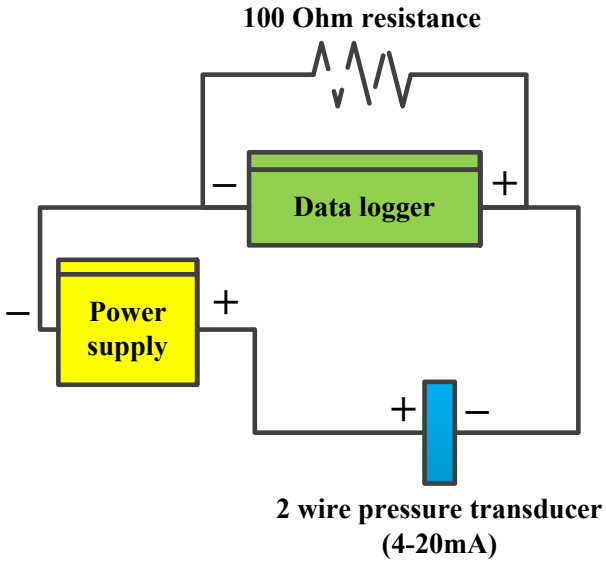

Figure 4-7 Electrical wiring diagram of the pressure transducer

4.3.2.3. Flow meter

The air flow meter is a variable area (Rotameter) series FR5000I-5A55 acrylic flow meter manufactured by KEY instruments Ltd ranging from 400 to 4000litre/min and the accuracy of ±2% full scale according to the manufacturer.

4.3.2.4. Torque transducer

A contactless rotary torque transducer series RS425-S1-HS was built by Datum electronics Ltd according to the specifications of torque range (0-10Nm), rotational speed (max 20,000rpm) and samples per second (100) to measure the turbine's torque, power and speed. Such configuration was advantageous as it is not limited by speeds found in the traditional inline torque transducers and has no wear and tear on the transducer. The torque transducer was factory-calibrated and certified with the accuracy of ±0.1% full scale according to the certification. The torque transducer was paired up with the Datum universal interface (DUI) to give a complete range of outputs (connected with PC) and a digital display of torque, speed and power. The rotational speed was also measured with

the torque meter that has a built-in Hall-Effect sensor with the accuracy of one pulse per revolution.

4.3.2.5. Data acquisition

All the thermocouples were connected directly to a Pico TC-08 data logger which was connected to a PC. The pressure transducers were connected to a Pico 1012 general purpose voltage input data logger which was connected to an external terminal board (for connecting 100Ohm resistances) to convert current signal into readable voltage single and was also connected to the PC. The signals from the torque transducer were transferred to the DUI which was directly connected to the PC for recording the torque, speed, and power.

4.3.3. Instruments calibration

Different instruments were employed in the experiments for measuring temperature and pressure. The readings were used for evaluating the performance of the turbine and hence all the instruments were calibrated and their uncertainties were evaluated.

4.3.3.1. Calibration of thermocouples

The thermocouples used in the experiments were calibrated against standard PT 100 Platinum Resistance Temperature Detector (RTD). All the thermocouples and the RTD were immersed in a water bath at the same level and the heat supplied to the water was controlled by a thermostat. The calibration process was started by adjusting the thermostat to a specific temperature. Readings of the thermocouples and the RTD were sent to the Pico TC-08 data logger and retrieved in a PC after reaching a steady state (about 5 minutes). The thermostat was then set to a new temperature and the procedure was repeated. The calibration apparatus is shown in Figure 4-8 while the calibration curve for one of thermocouples is presented in Figure 4-9. The calibration formulas for the rest of thermocouples are summarized in section 4.3.5.

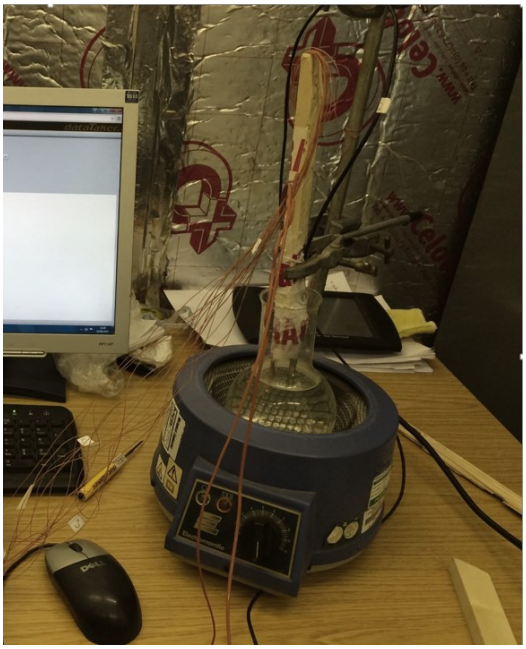

Figure 4-8 Apparatus for calibration of the thermocouples

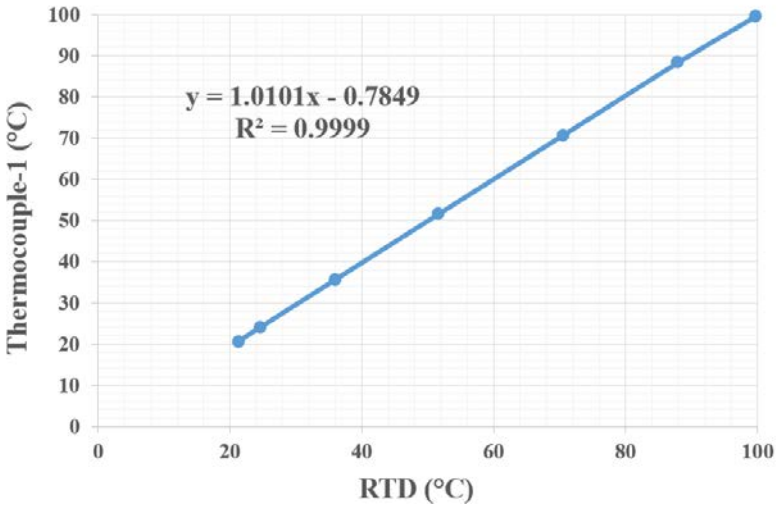

Figure 4-9 Calibration curve for thermocouple-1

4.3.3.2. Calibration of pressure transducers

The gauge pressure transducers were calibrated against a certified accurate pressure gauge (with accuracy of $\pm$0.0397bars) in pressurized water cylinder (Water Dead-Weight Testers). The pressure was increased to the desired value using a rotating screwed shaft. The voltage reading from the transducer was recorded against the corresponding pressure on the gauge. The calibration apparatus and the calibration curve for one of the

transducers are depicted in Figure 4-10 and 4-11 respectively. The calibration formulas for the rest of transducers are summarized in section 4.3.5.

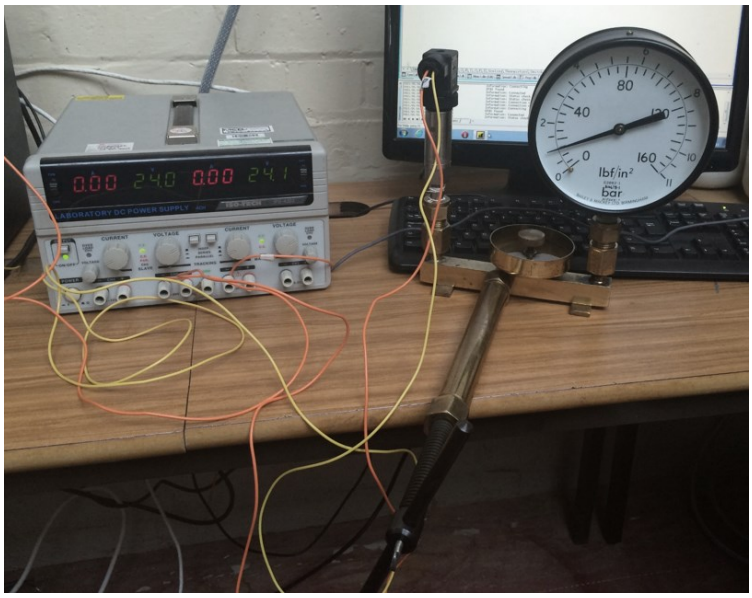

Figure 4-10 Apparatus for calibration of the pressure transducers

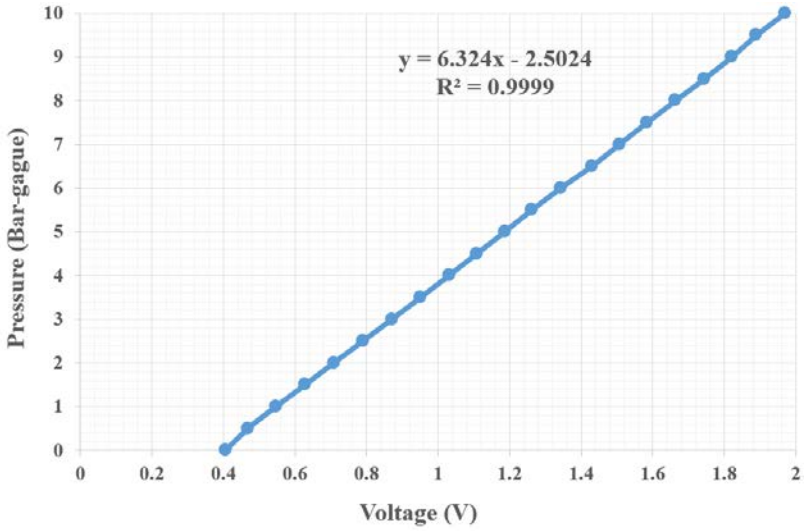

Figure 4-11 Calibration curve for one of GE UNIK 5000 transducer

4.3.4. Measurement accuracy

All thermocouples and pressure transducers were calibrated to guarantee accurate measurements. The overall accuracy of any measuring device consists of systematic (bias) error and random (precision) error as following:

$$\zeta_{overall} = \pm\sqrt{\zeta_{random}^2 + \zeta_{systematic}^2} \qquad \text{Equation 4-1}$$

Proper calibration can correct systematic error while random error can be removed by uncertainty analysis. The latter is statistical in nature and was determined from the mean standard deviation with 95% confidence interval as:

$$\zeta_{random} = t_{N-1.95\%} S_{\bar{x}} \qquad \text{Equation 4-2}$$

Where $S_{\bar{x}}$ is the standard deviation from sample population and is defined by $S_{\bar{x}} = \frac{1}{\sqrt{N}}\sqrt{\frac{\sum_{i=1}^{N}(X_i-\bar{X})^2}{N-1}}$ and $t_{n\text{-}1.95\%}$ is the student distribution factor for a degree of freedom N-1(N is the number of data points in the sample). The systematic errors include the calibration errors, data acquisition error and hysteresis errors and were estimated as following:

$$\zeta_{systematic} = \sqrt{\sum_{i=1}^{M} \delta_{i,systematic}^2} \qquad \text{Equation 4-3}$$

Where M is the number of systematic error sources. $\zeta_{systematic}$ can be based on the manufacturer data or laboratory calibration.

4.3.5. Uncertainty propagation

The measured variables (i.e. temperature and pressure) were characterized by some uncertainty, the results of calculations that involve these variables will consequently have uncertainty. Therefore, EES software was used to conduct the uncertainty propagation in the experimental results (i.e. power and efficiency) using Root Sum Square (RSS) method. RSS assumes that the measurements are normally distributed quantities that are

uncorrelated and also that there are no systematic errors. If the calculated quantity (Y) is a function of k measurements (x_1 to x_k) each with its own uncertainty (ζ_{x_1} to ζ_{x_k}), then the uncertainty in $Y(\zeta_y)$ can be divided into its elemental uncertainties due to each of measured variables as following:

$$Y = f(x_1, x_2, x_3, \dots., x_k) \qquad \text{Equation 4-4}$$

$$\zeta_{Y,x_i} = \frac{\partial Y}{\partial x_i}\zeta_{x_i} \qquad \text{Equation 4-5}$$

The elemental uncertainties are combined to provide the total uncertainty in Y as below:

$$\zeta_y = \sqrt{\left(\frac{\delta Y}{\delta x_1}\zeta_{x_1}\right)^2 + \left(\frac{\delta Y}{\delta x_2}\zeta_{x_2}\right)^2 + \cdots + \left(\frac{\delta Y}{\delta x_k}\zeta_{x_k}\right)^2} \qquad \text{Equation 4-6}$$

4.3.5.1. Uncertainty propagation in temperature measurements

As previously mentioned, T-type thermocouples were used in the current test rig and they were all calibrated against PT100 RTD thermocouple with the accuracy of $\pm$0.04˚C (refer to Appendix A). Table 4-1 summarizes the calibration curve formulas for all thermocouples and their associated uncertainty. Details of the uncertainty calculation for thermocouples based on the discussion in section 4.3.5 are presented in Appendix A. According to Table 4-1 average uncertainty of the thermocouples was found to be $\pm$0.699˚C.

Table 4-1 Summary of the calibration formula and uncertainty of thermocouples

Thermocouple number	Curve fit formula	R^2	Uncertainty (˚C)
Thermocouple-1	1.0101×T-0.7849	0.9999	±0.764
Thermocouple-2	1.0127×T-0.9378	1	±0.712
Thermocouple-3	1.0124×T-0.8724	1	±0.697
Thermocouple-4	1.0121×T-0.2993	1	±0.653
Thermocouple-5	1.01×T-0.3848	0.9999	±0.607
Thermocouple-6	1.0105×T+0.2354	0.9999	±0.735
Thermocouple-7	1.0148×T-0.3227	1	±0.726

4.3.5.2. Uncertainty propagation in pressure measurements

Two 10 bar pressure transducers (GE UNIK 5000) were connected to the inlet Pitot-static tube while a 6bar (Druck PTX 1400) was fitted at the turbine exit. Since the transducers were 4-20mA transducers, 100 ohm resistances were soldered to the external board of data logger for conversion of current to voltage. Table 4-2 summarizes the curve fit formula and uncertainty of each transducer. Details of uncertainty calculations are described in Appendix A.

Table 4-2 Summary of the calibration formula and uncertainty of pressure transducers

Transducer	Curve fit formula	R^2	Uncertainty (Bar)
GE UNIK 5000-1	6.324× volt-2.5024	0.9999	±0.0421
GE UNIK 5000-2	6.3001× volt-2.4748	0.9999	±0.0416
Druck PTX 1400	3.7506× volt -1.4925	0.9999	±0.0414

4.3.6. Experimental results and validation of the CFD model

The experiments were conducted at a range of turbine inlet temperature, pressure, flow rate and rotational speed. Initially based on the required turbine inlet temperature the value is adjusted using the control box to control the heat flux from the heater tape and as soon as the temperature reaches the required level at turbine inlet the heat is cut off automatically by the control box. For each set of experiments the turbine inlet temperature was fixed while varying other above-mentioned parameters. Then the turbine

inlet pressure was varied using the pressure regulator to create a series of off-design points at various speeds and mass flow rates. Apparently, as the turbine inlet pressure was increased the turbine rotational speed was also increased. Therefore to fix the turbine rotational speed, the load on the DC generator was adjusted using the variable resistance while increasing the turbine inlet pressure. Obviously, the higher the turbine inlet pressure the larger the required load on the turbine shaft. Such technique allows for creation of turbine maps at various constant speeds while varying the turbine inlet pressure and allows better comparison of performance. The recorded temperatures at the turbine inlet and exit were averaged to obtain a single value for each operating point. Then for each experimental point, the recorded measurements were used for calculation of efficiency using Equation 3-35 while the power was calculated using Equation 4-7.

$$Power = \tau\omega \qquad \text{Equation 4-7}$$

Where τ is the torque (Nm) produced by the turbine and recorded by the torque meter and ω is the rotational speed (rad/s). The reason for not directly using the power output from the torque meter was due to the intention of including the uncertainty into the calculation of power and efficiency as described below.

Although the employed torque meter was amongst the highest speed transducers in the market, it was unable to be spun more than 20000rpm (based on the manufacturer). Therefore, it was not possible to run the turbine up to its design speed of 55000rpm and the test facility was used to obtain the turbine performance under off-design operating conditions. The experiments were conducted at five different levels of turbine rotational speed as 4000rpm, 8000rpm, 12000rpm, 16000rpm and 20000rpm while the turbine inlet temperature was varied from 20°C to 40°C at steps of 5°C. The turbine inlet pressure was increased for all of the above inlet temperatures and rotational speeds and the results are presented in Figure 4-12 to 4-16. As it is evident in these figures, for each

experimental data point the error bars are also included. Such errors were obtained by including the uncertainty of the measuring devices (thermocouples, pressure transducers and torque meter) described in section 4.3.5 into the EES software while it automatically calculated the propagated uncertainty into power and efficiency (Equation 3-35 and 4-7) using Equation 4-6. The uncertainty in the calculated efficiency from experimental measurements is considerably higher than the uncertainty in the calculated power. Such characteristic underlines the sensitivity of the turbine efficiency to the measuring devices such as thermocouples and pressure transducers.

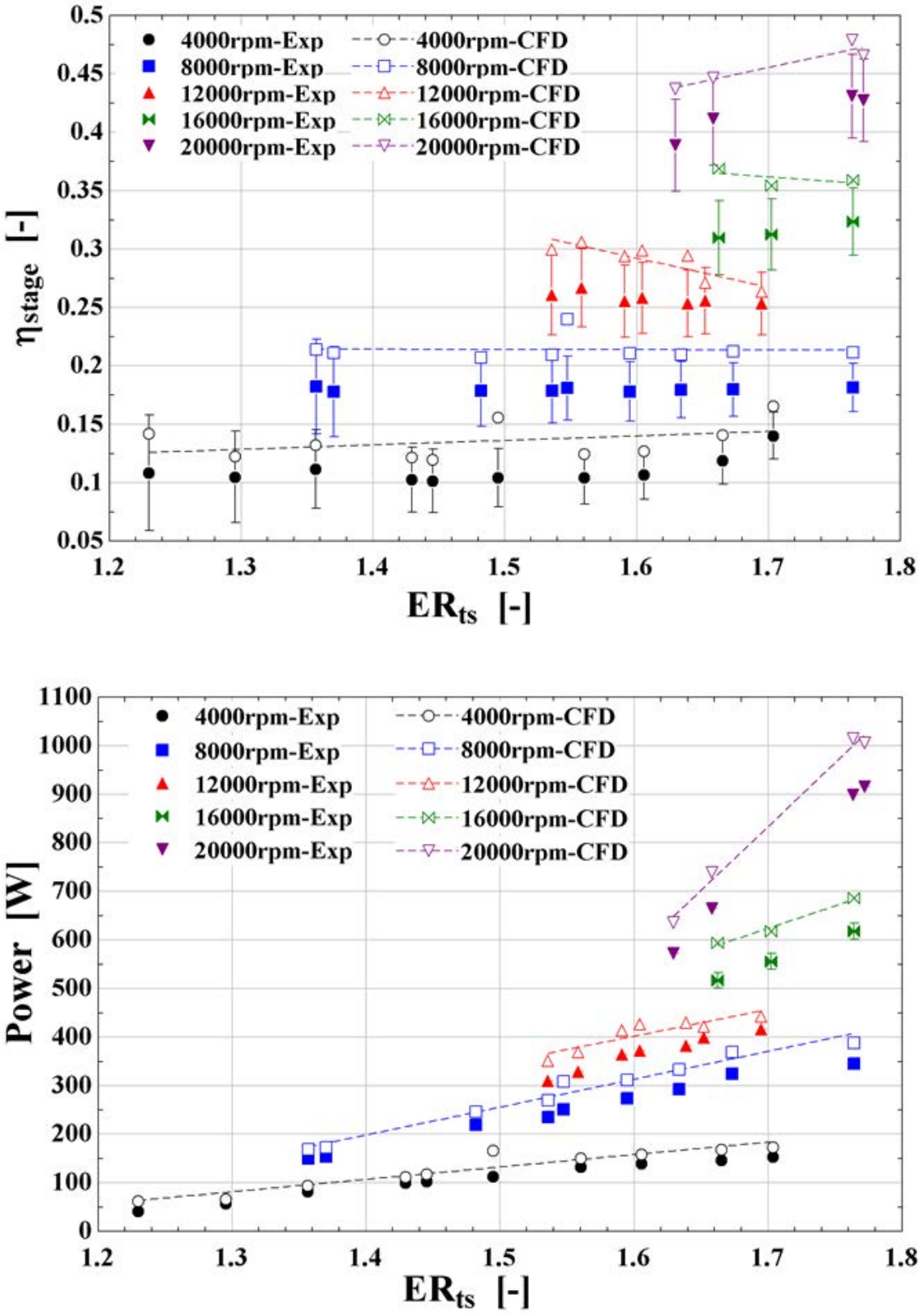

Figure 4-12 Validation of CFD model with experimental results (power and efficiency) for the turbine inlet temperature of 20°C

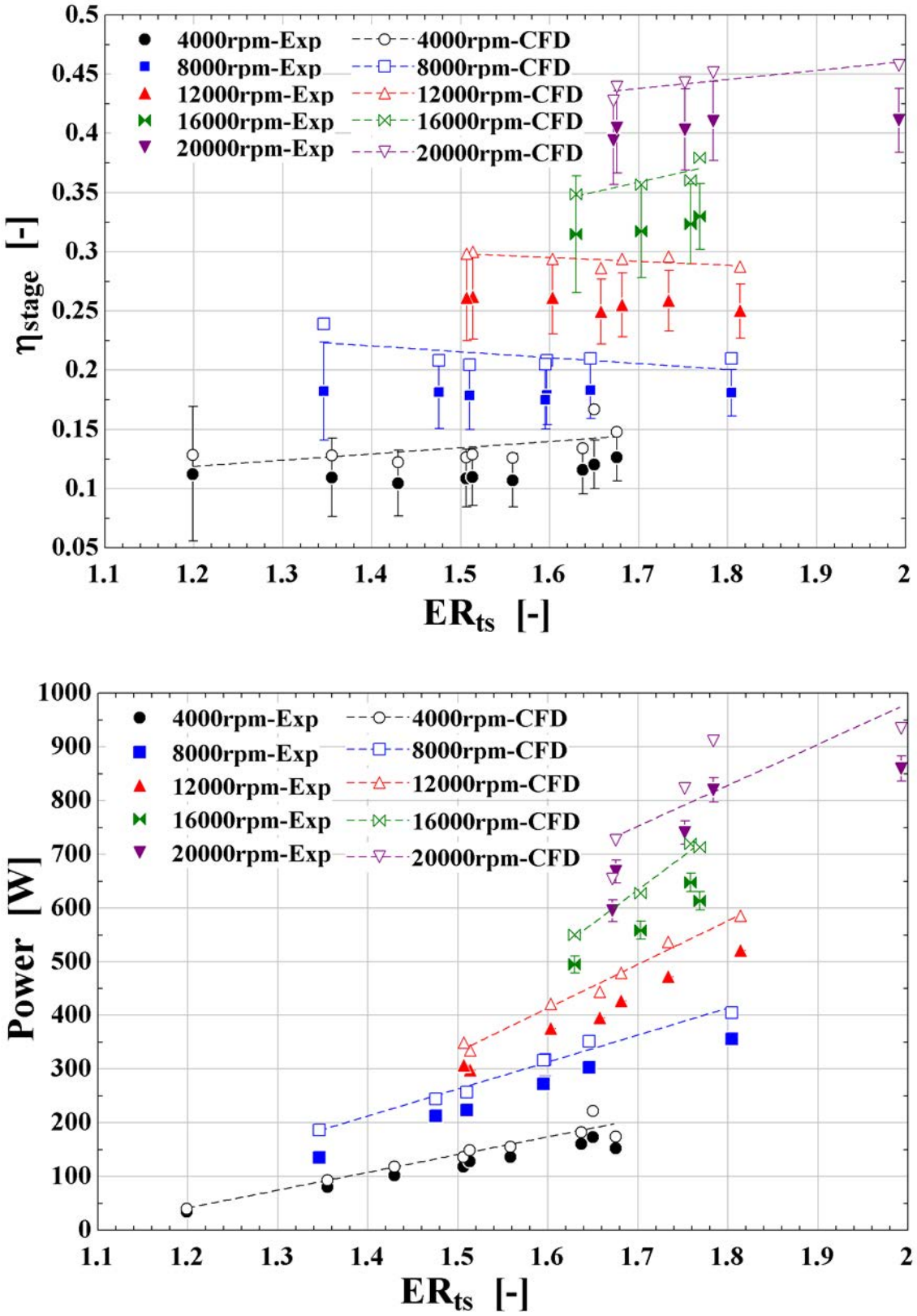

Figure 4-13 Validation of CFD model with experimental results (power and efficiency) for the turbine inlet temperature of 25°C

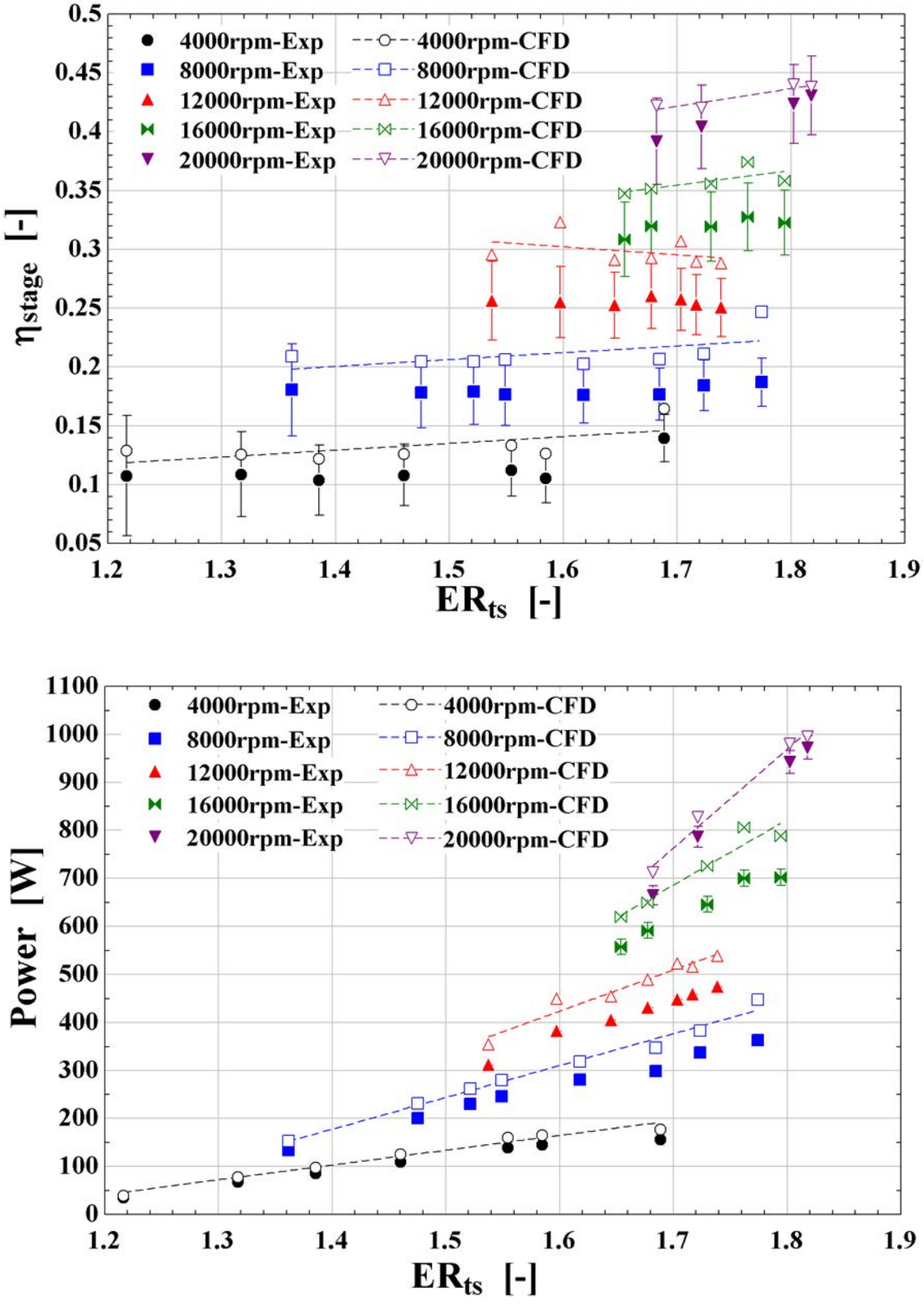

Figure 4-14 Validation of CFD model with experimental results (power and efficiency) for the turbine inlet temperature of 30°C

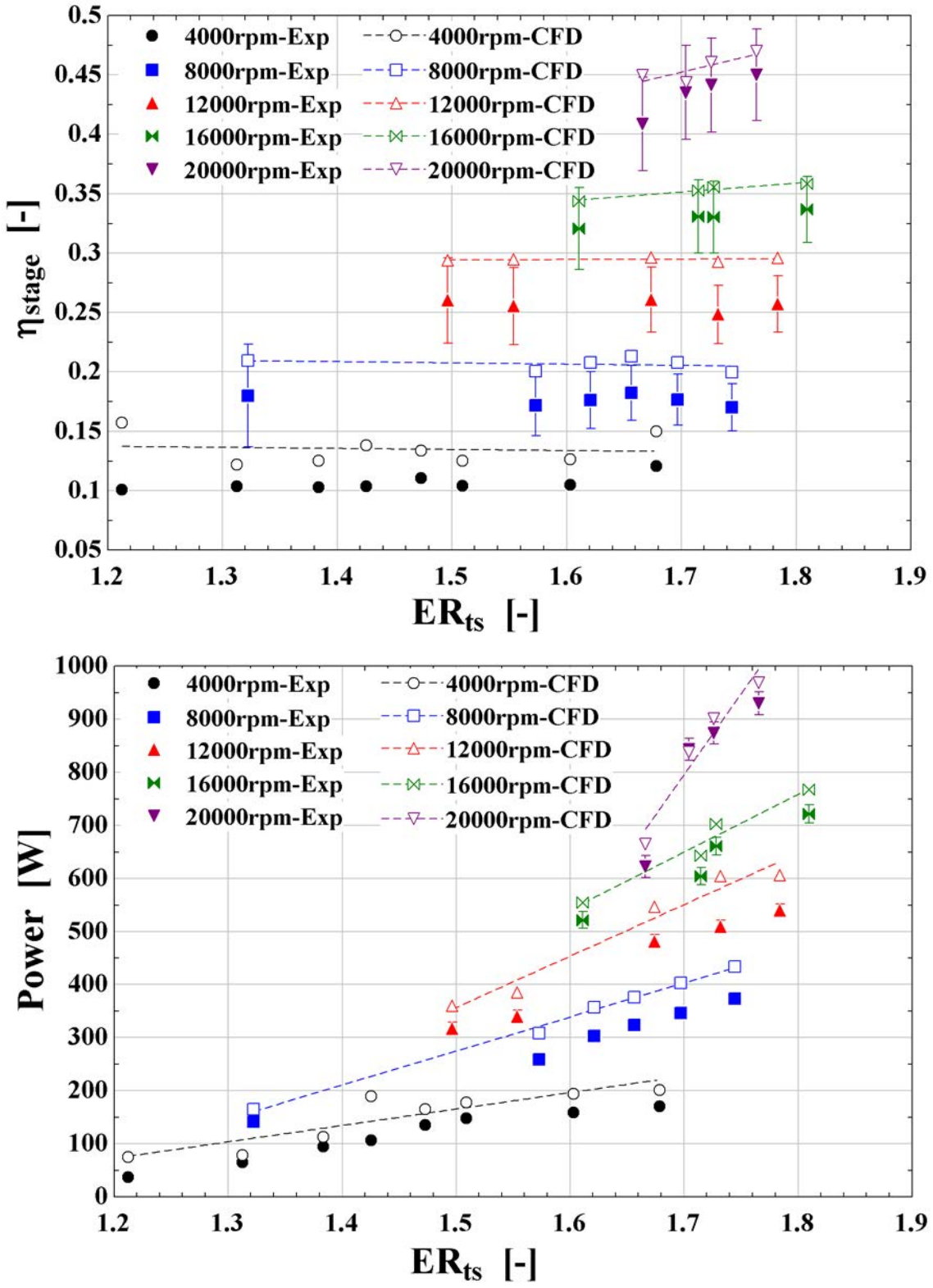

Figure 4-15 Validation of CFD model with experimental results (power and efficiency) for the turbine inlet temperature of 35°C

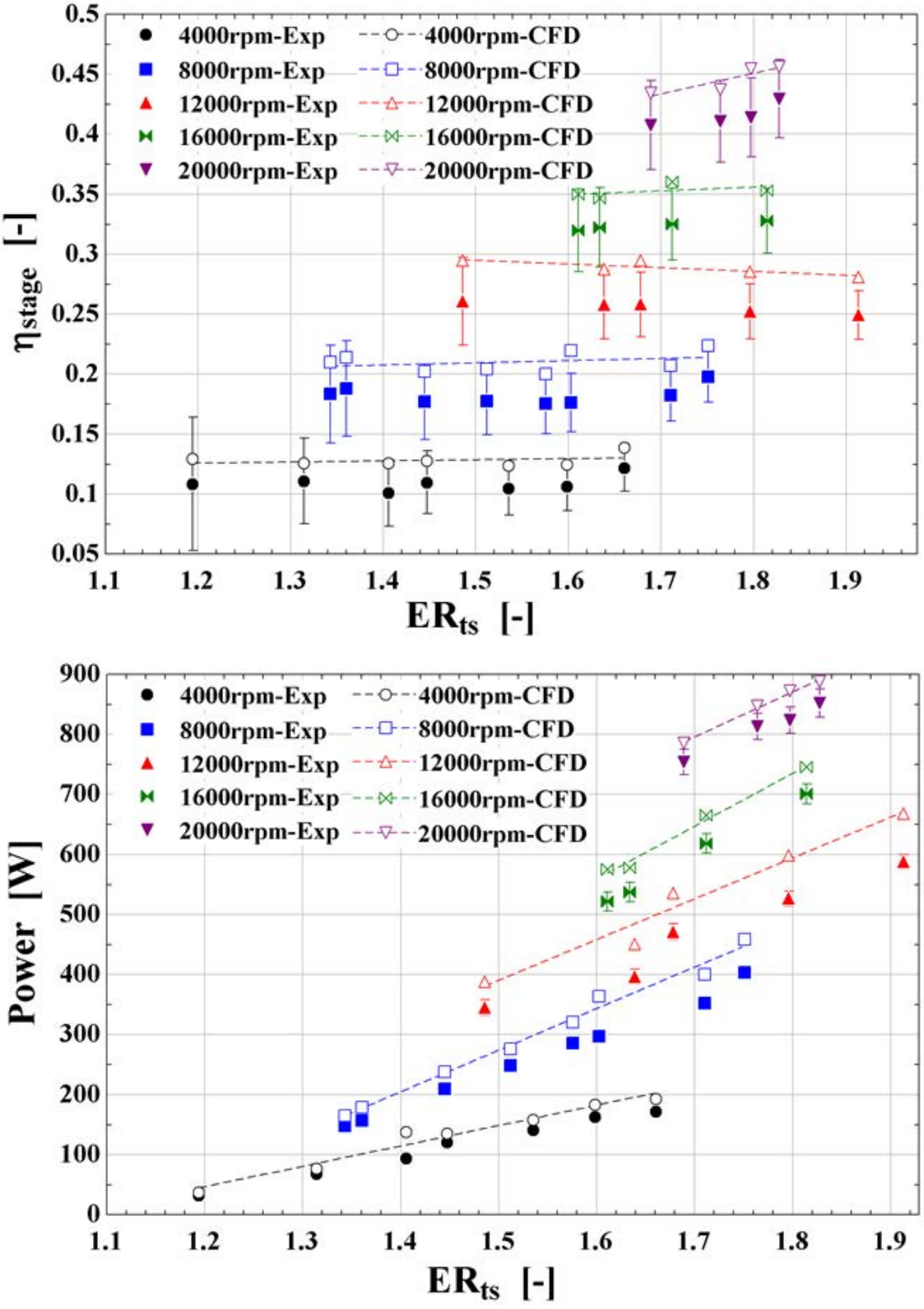

Figure 4-16 Validation of CFD model with experimental results (power and efficiency) for the turbine inlet temperature of 40°C

At the same time, the CFD model of the complete turbine assembly (casing, full nozzle ring and full rotor wheel) developed in section 3.6.3.6 was employed to validate the accuracy of the CFD simulations. The same turbulence model, convergence criteria and boundary conditions were applied to the model. The measured turbine inlet total pressure and temperature were specified at the casing inlet duct while the measured static pressure was specified at the rotor exit and the measured rotational speed was specified to the rotor wheel. The CFD simulations were conducted for all experimental data points and the results are overlaid on Figure 4-12 to 4-16 for comparison.

As it is evident from the results, the turbine efficiency is more affected by the rotational speed while the turbine power output is considerably affected by both the turbine expansion ratio as well as the rotational speed. Moreover, in all of the investigated data points, the CFD simulations were over-predicting the power and efficiency. Such feature can be attributed to a series of factors as:

I. Surface roughness of the manufactured turbine blade compared to almost smooth blade assumption in CFD simulations.

II. Exclusion of the rotor back plate flow leakage (windage loss) in CFD compared to the actual experimental conditions.

III. Steady state simulation with CFD while the actual experiment had slightly transient behaviour.

IV. Mechanical losses in bearings (two sided rubber seal bearings were used to minimize flow leakage) which reduced the power output of the experimental results compared to CFD.

Overall, to effectively compare the accuracy of the developed CFD model, all the experimental data and CFD simulations were plotted in one graph for both power and efficiency as shown in Figure 4-17 and 4-18. The boundary error lines were obtained from Equation 4-8.

$$Error\ (\%) = \frac{|Experimental - CFD|}{CFD} \times 100 \qquad \text{Equation 4-8}$$

Since the aim of these comparisons was to validate the CFD model, it is at the denominator of Equation 4-8.

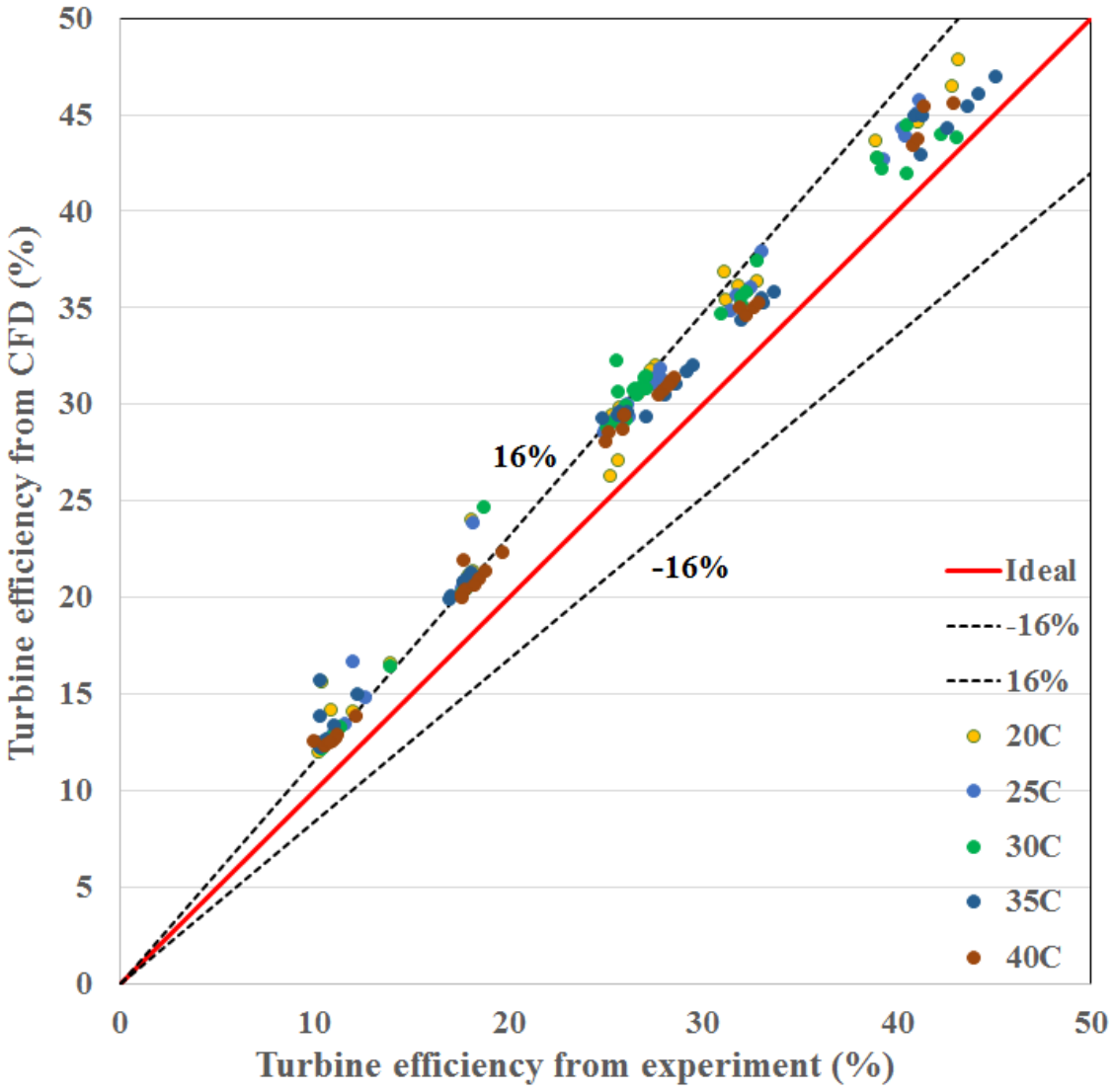

Figure 4-17 Comparison of efficiency from CFD simulations with experiments for all data points

The CFD predictions of the turbine efficiency for majority of experimental data were in the range of ±16% of the ideal line as depicted in Figure 4-17 while the CFD predictions of the turbine power for majority of experimental data were in the range of ±13% as presented in Figure 4-18. As was shown in these figures, the relative error in CFD predictions is comparatively higher at lower rotational speeds (i.e. 4000rpm and 8000rpm) when comparing the results for CFD simulations at higher rotational speeds with experiments.

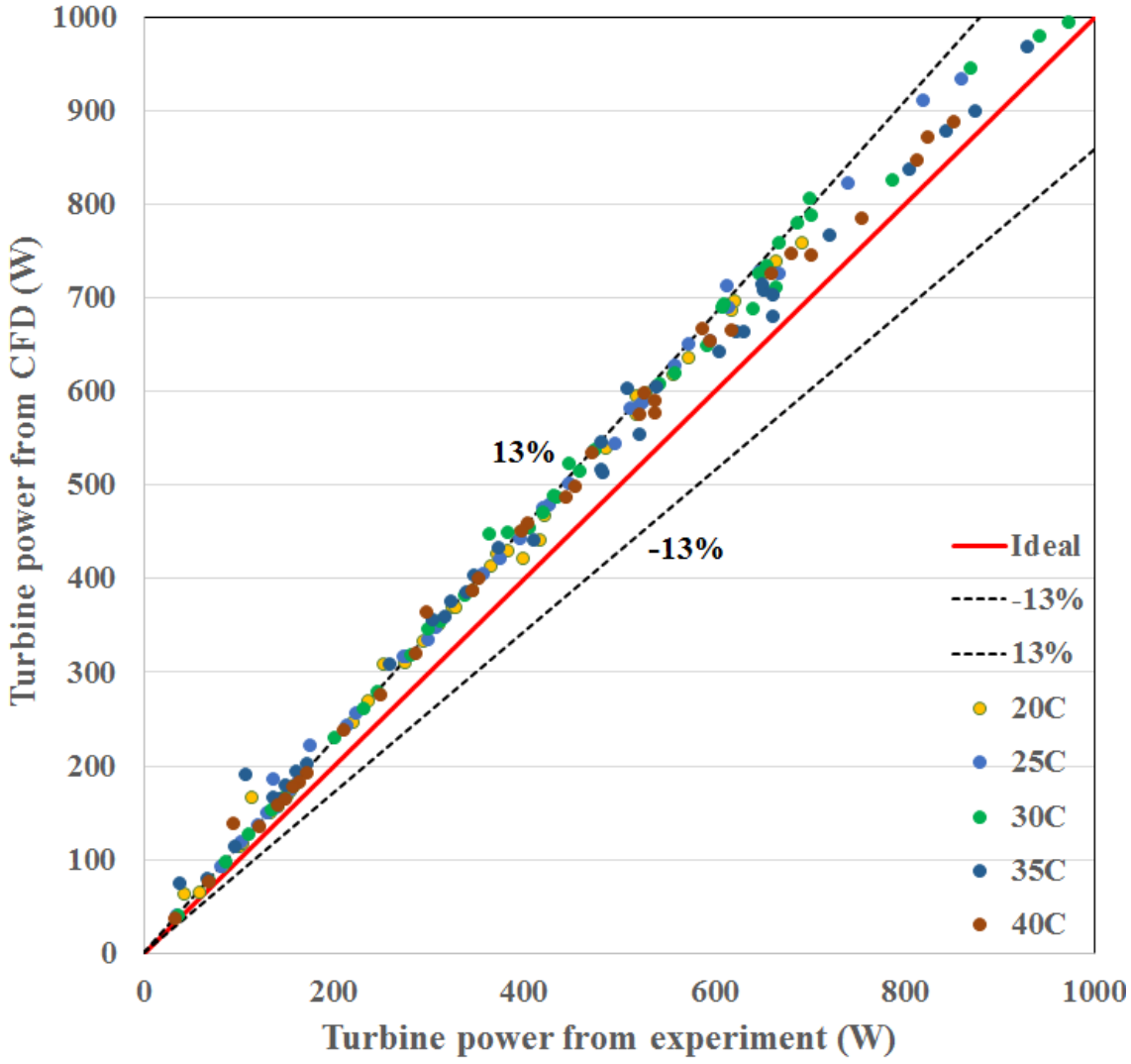

Figure 4-18 Comparison of power from CFD simulations with experiments for all data points

In other words, as the turbine rotational speed increases, the CFD simulations can capture the turbine behaviour more accurately compared to lower speeds. Referring to these figures not only confirms that, as the rotational speed increased both the turbine power and efficiency were also increased but also the performance prediction errors in such CFD simulations were reduced considerably. In addition, if the torque meter was capable of operating at higher rotational speeds then it was expected that the error in CFD predictions would be reduced further. Such results show that the developed CFD model can fairly accurately predict the performance of the radial turbine and the proposed modelling strategy can be used as a benchmarking model for developing small-scale RITs.

4.4. Summary and conclusions

Following the proposed methodology in chapter three, it was required to manufacture the developed RIT stage and conduct the experiments to validate such methodology. The RIT was fabricated using additive layer manufacturing technique. The experimental facility was built and the turbine was instrumented in order to measure the turbine performance under a range of off-design operating conditions. The details of instruments calibration as well as uncertainty analyses were explained. Such results were used to calculate the propagated error into the measured power and efficiency. The experimental results showed that the turbine efficiency was more sensitive to the turbine rotational speed while the turbine power was sensitive to both expansion ratio and rotational speed. The CFD model of the complete turbine assembly was validated with experiments for all the data points. Results showed that the CFD model can predict the turbine efficiency with the accuracy of $\pm 16\%$ while the turbine power was predicted with the accuracy of $\pm 13\%$. The CFD model can predict the turbine performance with better accuracy at higher rotational speeds compared to lower speeds. It was expected that if the

fabricated experimental facility was capable of running at higher rotational speeds (i.e. the torque meter), the above-mentioned error could even reduce further. Overall, such results underline the effectiveness of the proposed methodology and the CFD model can fairly accurately predict the turbine performance over a wide range of operating conditions. Such model can be used as benchmarking model for analyses of small-scale RITs with reasonable accuracy.

CHAPTER 5

MEAN-LINE MODELLING AND OPTIMIZATION OF ORGANIC RIT AND INTEGRATION WITH CYCLE ANALYSIS PROGRAMME

5.1. Introduction

The unusual properties of high-density organic working fluids and the near-critical operating conditions of the ORC require special treating of the RIT modelling procedure. In addition, the operating conditions of the ORC are usually such that the organic fluid behaviour is far from the ideal-gas (compressibility factor, $Z_{compressability}$, considerably lower than unity) and such formulation is not satisfactory. Therefore, it is vital to describe the turbine expansion by employing the real-gas equation of state (EoS) to specify the fluid properties (both thermodynamic and transport) and capture the non-ideal behaviour of working fluids.

Furthermore, in all of the ORC modelling and optimization studies described in chapter two, an arbitrary constant turbine efficiency was used for a wide range of operating conditions and for various working fluids without assuring that the specified turbine efficiency can be achieved by the imposed thermodynamic conditions in practice. This assumption does not necessarily yield accurate results (as will be shown in this chapter) where each fluid may exhibit different performance under different operating conditions. To alleviate such major deficiency, it is required to carry out the integrated mean-line modelling of organic RIT with ORC analysis code. Such approach replaces the constant turbine efficiency with a dynamic efficiency that is unique for each set of cycle operating conditions and working fluid properties. This allows overcoming any arbitrary assumption of the turbine efficiency, unlike the previous literature, that can result in improved performance prediction of the ORC systems.

Moreover, the mean-line modelling normally requires adjustment of the design parameters iteratively in order to achieve desirable results and if unacceptable the process will be repeated (Figure 3-5). However, this procedure does not necessarily ensure that the optimum combination of the turbine input parameter is achieved for the optimum performance. Also, it does not consider a broad range for the input parameters which increases the possibility of overlooking the best solution. In addition, the results should be manually checked to certify that the ORC and turbine constraints are fulfilled. Hence, coupling the integrated ORC-RIT code with an optimization scheme (i.e. genetic algorithm) allows performing the true analytical optimization of a wide range of performance indexes (i.e. cycle thermal efficiency and turbine isentropic efficiency) and ensuring that the optimum combination of input parameters is achieved. The optimizing algorithm can be constrained based on the ORC and organic RIT requirements to limit the design space size generated by the optimizer.

In additions, the available research that used RIT (Table 2-3) is limited to single-stage configuration with expansion ratios limited to about 5. The reason being that increasing the expansion ratio beyond this limit increases the Mach number at the rotor inlet leading to supersonic flow regime with strong shock waves that deteriorates the turbine efficiency. However, from the thermodynamics point of view it is desirable to increase the pressure difference in the ORC (between evaporator and condenser as shown in Figure 2-2) in order to increase the cycle thermal efficiency. Therefore, in this chapter a novel transonic dual-stage organic RIT was developed to both preserve the turbine efficiency while maintaining high expansion ratios and consequently high cycle thermal efficiency.

Finally, three new correlations were developed based on linear regression analysis to predict with good accuracy the maximum obtainable turbine isentropic efficiency and the corresponding turbine overall size and rotor size for a wide range of operating conditions and various working fluids. Such correlations use only few key design parameters without the need of knowledge of working fluid properties or the need for performing the complete turbine design procedure.

This chapter utilizes the validated methodology in chapters three and four as a proof-of-concept approach and extend it to fulfil all the aforementioned goals. The outcomes of this chapter are the core contributions of the present thesis to the field.

5.2. Organic working fluid selection

According to the discussion in section 2.4 regarding the selection criteria of the working fluids and also the summary of the best fluids listed in Figure 2.14 the working fluids presented in Table 5-1 were selected for further screening. Figure 5.1 shows the

temperature-entropy diagram of all selected fluids overlaid in one plot for comparison. As can be seen in this graph all of the selected fluids have negative slope that allows eliminating the need for superheating equipment. Moreover, majority of the selected fluids have very good thermodynamic properties with acceptable environmental and safety characteristics and therefore selected for preliminary screening.

Table 5-1 Selected organic working fluids and their properties

Fluid	Molecular weight (g/mol)	T_{cr} (K)	P_{cr} (kPa)	T_{nbp} (K)	GWP (100yr)	ODP	Atmospheric life time (yr)	Safety data (ASHREA 34)	Reference
Isobutane	58.12	408	3640	261.3	~20	0	0.019	A_3	(Pan *et al.* 2013)
n-pentane	72.15	469	3360	309.1	~20	0	0.01	A_3	(Tchanche *et al.* 2009)
R236ea	152.04	412	3410	279.34	1200	0	8	-	(Pan *et al.* 2013)
R134a	102.03	374	4060	246.9	1430	0	13	A_1	(Pan *et al.* 2013)
R152a	66.05	385	4450	249	124	0	1.4	A_2	(Pan *et al.* 2013)
R123	152.93	456	3660	300.8	77	0.02	1.3	B_1	(Pan *et al.* 2013)
R236fa	152.04	397.9	3200	271.6	9810	0	240	A_1	(Pan *et al.* 2013)
R245fa	134.05	426	3610	288.14	950	0	7.2	B_1	(Pan *et al.* 2013)
R365mfc	148.07	459.9	3266	313.18	794-997	0	8.7	-	(Tchanche *et al.* 2009)
R1234yf	114	367.9	3382	243.7	4	0	0.035	A_{2L}	(Klein 2013)
R1233zd	130.5	438.8	3573	291.5	1	0	0.11	A_1	(Klein 2013)
R1234ze	114	382.5	3632	253.9	1	0	0.044	A_{2L}	(Klein 2013)

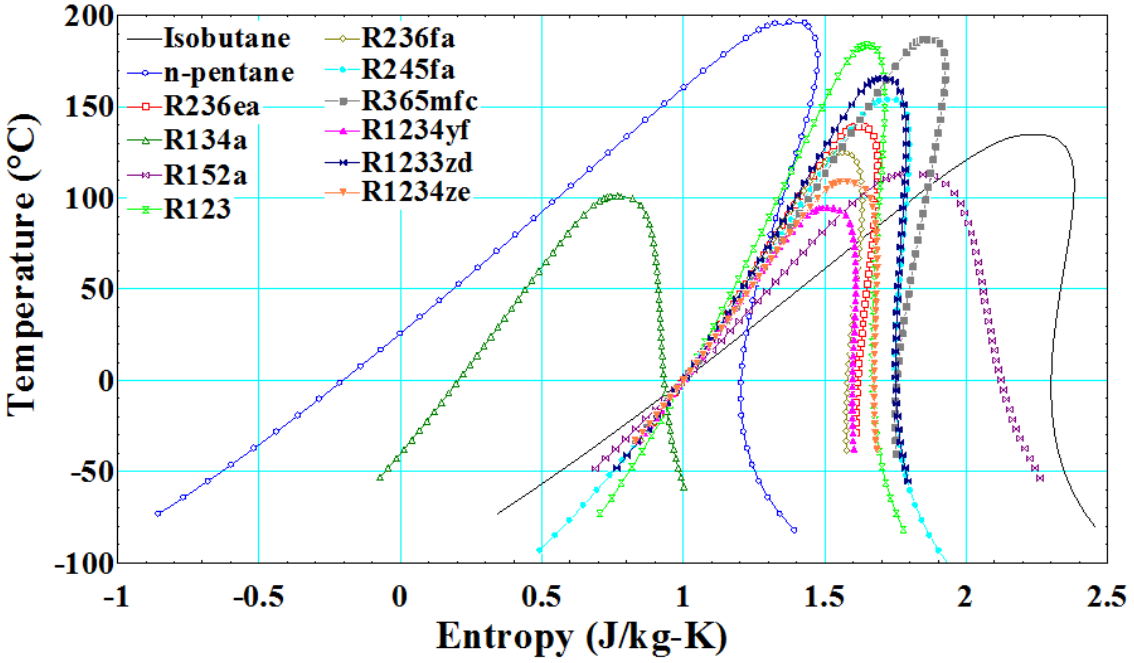

Figure 5-1 Temperature-entropy diagram of the selected fluids

5.3. Organic Rankine cycle modelling

This section describes the fundamental governing equations and assumptions used for developing a standalone ORC analysis code with constant turbine efficiency capable of setting the operating conditions for each of the points defining the process for a simple ORC cycle (refer to Figure 5-2).

5.3.1. ORC standalone model - calculation of state points

The calculation methodology for a steady-state ORC analysis code is developed based on the simple ORC cycle shown in Figure 5-2 (states 1 and 5 are the corresponding state points at entry and exit of the organic RIT described in the next section). The code assumes that pressure and heat losses occurring in all components (evaporator, condenser, pump and turbine) and connecting pipes are negligible. Following the majority of the studies reported in chapter two, saturated vapour or superheated vapour but with small degree of superheating (maximum of 5 degrees) was assumed at the turbine inlet while the condenser outlet was considered to be at saturated liquid state.

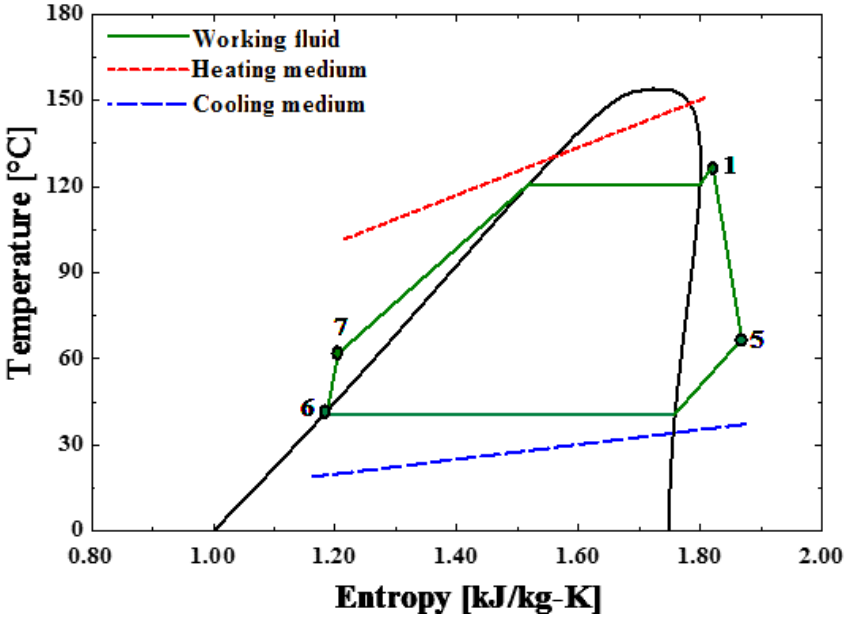

Figure 5-2 Schematic of simple ORC layout

Furthermore, only subcritical cycles are considered in this chapter to avoid using excessively high pressures in the evaporator, thus alleviating the safety concerns and complexities of the system. In addition, constant isentropic efficiencies were prescribed to the turbine and pump. Table 5-2 lists the ORC standalone code input variables.

Table 5-2 ORC standalone model input variables

Parameter	Unit	Value/Range
Turbine inlet temperature (T_1)	K	310 – 423
Turbine inlet pressure (P_1)	kPa	[a]
Degree of superheating ($\Delta T_{superheat}$)	K	1 – 5
Expansion ratio [b] (ER_{ts})	-	1.5 – 10
Mass flow rate of working fluid ($\dot{m}_{wf}$)	(kg/s)	0.03 – 0.5
Turbine efficiency ($\eta_{stage,ts}$)	-	0.8
Pump efficiency (η_{pump})	-	0.70
Generator efficiency ($\eta_{generator}$)	-	0.96
Mechanical efficiency ($\eta_{mechanical}$)	-	0.96

[a] Corresponding saturated vapour pressure at the selected T_1.

[b] Expansion ratio corresponds to specifying the condensation pressure.

The known turbine inlet temperature (T_1) and pressure (P_1) were used to determine all the other thermodynamic properties at turbine inlet using EoS. The turbine is modelled to have a constant isentropic efficiency defined by:

$$\eta_{stage,ts} = \frac{h_1 - h_5}{h_1 - h_{5,s}} \qquad \text{Equation 5-1}$$

Where $h_{5,s}$ is the turbine exit enthalpy after an isentropic expansion. For the turbine outlet, the isentropic expansion state point ($S_{5,s}$=S_1 & $P_{5,s}$= P_6) were used to determine all other properties with the known turbine isentropic efficiency. P_6 itself was obtained from the given expansion ratio in Table 5-2 and the with the known P_6 and quality (x_6=0) at the condenser exit assuming that pressure losses are negligible and the condenser exit is at saturated liquid state T_6 is obtined (T_6 =EoS(P_6, x_6)). The power generated by the turbine was obtained by:

$$W_{turbine} = \dot{m}_{wf}(h_1 - h_5) \qquad \text{Equation 5-2}$$

All the heat rejection occurs in a single counter-flow condenser (with adiabatic assumption) and the condenser is constrained with a minimum pinch-point temperature difference of 5K. Heat balance on the condenser is defined by:

$$Q_{out} = \dot{m}_{wf}(h_5 - h_6) = \dot{m}_{coolant}\left(h_{coolant,out} - h_{coolant,in}\right) \qquad \text{Equation 5-3}$$

The condenser inlet coincides with turbine outlet and its outlet properties were determined with the known T_6 and x_6. The performance of the pump is governed by a constant isentropic efficiency defined as:

$$\eta_{pump} = \frac{h_{7,s} - h_6}{h_7 - h_6} \qquad \text{Equation 5-4}$$

Where $h_{7,s}$ is the enthalpy at state 7 under an isentropic compression. The pump power consumption was determined by:

$$W_{pump} = \dot{m}_{wf}(h_7 - h_6) = \frac{\dot{m}_{wf}(P_7 - P_6)}{\rho_6 \eta_{pump}} \quad \text{Equation 5-5}$$

The pump inlet coincides with condenser outlet while all other properties at pump outlet are calculated as a function of EoS(P_7=P_1, h_7). Similar to the condenser, the evaporator is modelled so that all the cycle heat addition (i.e. preheating, vaporizing and superheating) occurs in a single counter-flow heat exchanger (with adiabatic assumption) and has the same pinch-point value. Heat balance for the evaporator gives:

$$Q_{in} = \dot{m}_{wf}(h_1 - h_7) = \dot{m}_{HTF}(h_{HTF,in} - h_{HTF,out}) \quad \text{Equation 5-6}$$

The net electric power output from the ORC is denoted by:

$$W_{net,cycle} = \left(W_{turbine}\eta_{mechanical}\eta_{generator}\right) - W_{pump} \quad \text{Equation 5-7}$$

Where $\eta_{mechanical}$ accounts for the mechanical losses due to the friction in bearings and couplings and $\eta_{generator}$ accounts for the generator losses. The ORC thermal efficiency was then determined by:

$$\eta_{thermal,cycle} = \frac{W_{net,cycle}}{Q_{in}} \quad \text{Equation 5-8}$$

5.4. Mean-line modelling of organic RIT with real-gas formulation

5.4.1. Overview of modelling procedure

The main program described in chapter three was employed and advanced with the key difference that instead of using the ideal-gas assumption, the real-gas formulation is implemented where the fluid properties are defined by the built-in EoS in EES using two known thermodynamic properties at each key station (Figure 3-2). Furthermore, instead of determining the fluid properties at the rotor inlet station (in the beginning of the calculation procedure) and then using ideal-gas formulas to calculate the rotor outlet flow conditions, the code performs this recursively for both inlet and exit stations of the RIT. Besides, at the start of the calculation the model evaluates the compressibility factor

($Z_{compressibility}$) based on the operating conditions at turbine inlet ($P_{t,1}$, $T_{t,1}$) to ensure that the fluid has real-gas behaviour. If $Z_{compressibility}$ lays in the region of 0.98 to 1.02 where fluids behave as an ideal gas (Green *et al.* 2008) it terminates by returning an error message; if Z falls outside this region the code continues the calculation using the real-gas formulation. Irrespective of the turbine expansion formulation (either ideal or real), the same enthalpy-entropy diagram (Figure 3-2) and solving algorithm (Figure 3-5) with the above-mentioned differences were used for modelling of the organic RIT.

5.4.2. Rotor modelling

Following the discussion in section 3.5.2 the choice of non-dimensional parameters is arbitrary depending on the available information and performance correlation charts. In contrast to the isentropic velocity ratio (v) used in chapter three, in this chapter the combination of the loading (ψ) and flow (φ) coefficients were used for modelling of the rotor. Such non-dimensional parameters are advantageous as they require fewer turbine input data (four) compared to v which requires six turbine input parameters. Moreover, the set of (ψ-φ) can better describe the geometry of the organic RIT compared to v as the organic turbine rotor geometry can be considerably different from that of conventional radial turbines operating with air. Recalling Equation 3-6 and 3.7 from chapter three they can be further expanded as following (Baines 2003):

$$\varphi = \frac{C_{m5}}{U_4} = \frac{C_{m4}}{\xi U_4} \qquad \text{Equation 5-9}$$

$$\psi = \frac{\Delta h_{actual}}{U_4^2} = \frac{\Delta h_{actual}}{(r_4\omega)^2} = \frac{C_{\theta,4}}{U_4} - \left(\frac{r_5}{r_4}\frac{C_{\theta,5}}{U_4}\right) \qquad \text{Equation 5-10}$$

$$\xi = \frac{C_{m4}}{C_{m5}} \qquad \text{Equation 5-11}$$

Where ξ is the absolute meridional velocity ratio at the inlet and outlet of rotor.

The performance of conventional RIT is correlated against φ and ψ using a large number of experimental data reported in (Baines 2003). Most of these turbines are operating at very high turbine inlet temperatures of between 600°C to 1000°C for turbochargers and gas turbines. In these applications the simultaneous existence of high centrifugal and thermal stresses limited the design and geometry of the rotor to be radial at inlet with zero inlet blade angle ($\beta_{4,blade}$=0) and with ψ values less than unity (Rohlik *et al.* 1968, Whitfield *et al.* 1990, Baines 2003) as illustrated in Figure 5-3(a). Due to the large pressure gradient in the rotor (from pressure to suction surface) the optimum incidence occurs at the relative flow angle (β_4) of between -20° to -40° (Baines 2003, Dixon *et al.* 2010), and the inlet velocity triangle is aligned to fulfil such condition as shown in Figure 5-3(a). In contrast, the ORC turbines are operating at much lower inlet temperatures of about 350°C or less. This enables to adopt a general shape for the rotor with non-zero inlet blade angle ($\beta_{4,blade}$>0) as presented in Figure 5-3(b) and ψ values in excess of unity. By virtue of the lower ORC temperature, the additional and centrifugal stresses due to the non-zero inlet blade angle could be tolerated. To preserve the optimum incidence at rotor inlet, the inlet velocity triangle is aligned with positive relative flow angle (β_4) as depicted in Figure 5-3(b). Considering the same wheel speed (U_4), the rotor with non-zero inlet blade angle results in larger inlet tangential velocity ($C_{\theta,4}$) as demonstrated in Figure 5-3 and consequently leads to higher specific work output as expressed by Equation 3-19 assuming that both configurations have equal exit velocities (U_5 and C_5). Such configuration results in highly loaded and compact organic RIT suitable for small-scale ORC units.

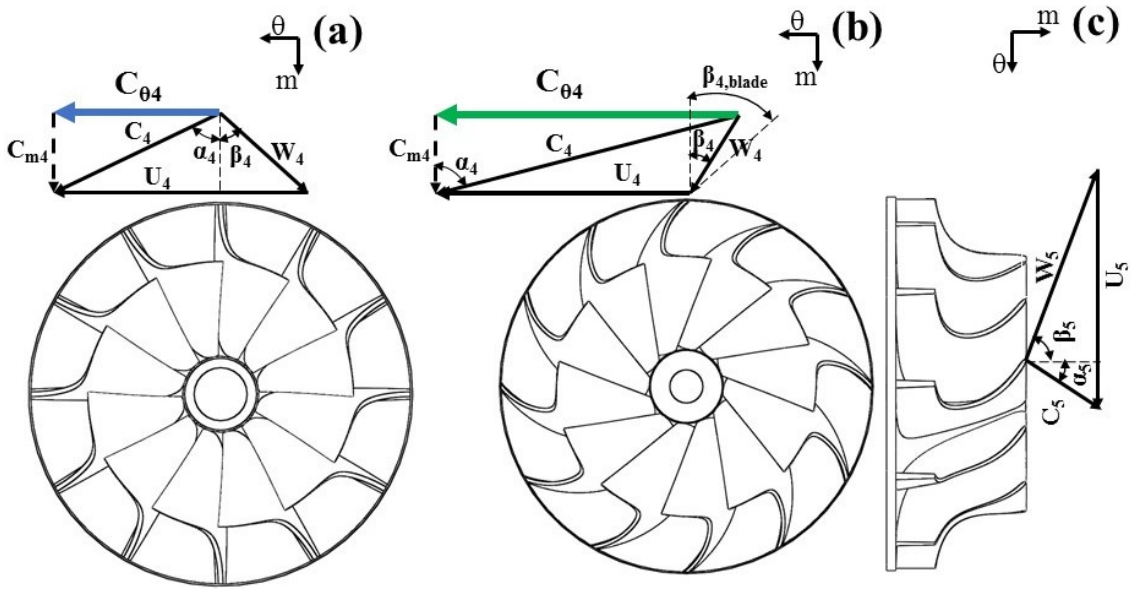

Figure 5-3 Schematic of the rotor blade profiles and velocity triangles, rotor with zero inlet blade angle (a), rotor with non-zero inlet blade angle (b and c)

Similar to the approach presented in chapter three, the mean-line code requires a set of input parameters to carry out the modelling. Table 5-3 lists the input parameters used for mean-line modelling of organic RIT throughout this chapter.

Table 5-3 Input parameters of the turbine mean-line model

Parameter	Unit	Range
Turbine design parameters		
Loading coefficient (ψ)	-	0.8 – 1.5
Flow coefficient (φ)	-	0.15 – 0.5
Rotational speed (ω)	rpm	30000 – 80000
Rotor exit absolute flow angle (α_5)	degree	-15 – 15
Rotor exit hub to inlet radii ratio ($r_{5,hub}/r_4$)	-	0.3 – 0.4
Rotor meridional velocity ratio (ξ)	-	0.6 – 1.2
Nozzle inlet to exit radii ratio (r_2/r_3)	-	1.2 – 1.3

Turbine ideal enthalpy drop (Δh_{ideal}) is calculated using the turbine expansion ratio (ER_{ts}) given in Table 5-2 and the isentropic expansion state point (5,s) shown in Figure 3-2 together with the following equations.

$$P_5 = P_{5,s} = \frac{P_{t,1}}{ER_{ts}} \quad \text{Equation 5-12}$$

$$S_{5,s} = S_{t,1} \quad \text{Equation 5-13}$$

$$h_{5,s} = EoS(S_{5,s}, P_{5,s}) \quad \text{Equation 5-14}$$

$$\Delta h_{ideal} = h_{t,1} - h_{5,s} \quad \text{Equation 5-15}$$

The main mean-line modelling principles described in section 3.5.1 were also implemented in this chapter with the main difference of using real-gas formulation. Therefore from the previous total to static efficiency ($\eta_{stage,ts}$) solution (i.e. the current iteration guess for the total to static efficiency), the actual enthalpy drop (Δh_{actual}), turbine power output (W_{urbine}) and rotor inlet wheel velocity (U_4) were obtained as following:

$$\Delta h_{actual} = \Delta h_{ideal} \eta_{stage,ts} \quad \text{Equation 5-16}$$

$$W_{turbine} = \dot{m}_{wf} \Delta h_{actual} \quad \text{Equation 5-17}$$

$$U_4 = \sqrt{\frac{\Delta h_{actual}}{\psi}} \quad \text{Equation 5-18}$$

With the assumption of zero exit swirl (α_5=0), Equation 3-19 can be readily solved for $C_{\theta,4}$ and hence the velocity triangles in Figure 5-3 (b) and (c) were obtained accordingly with the known ξ value given in Table 5-3 and trigonometric rules. If any other value is selected for α_5 the same algorithm shown in Figure 3-7 was also applied to the current model (but with real-gas formulation) to cover these cases as well. The turbine inlet total thermodynamic properties ($S_{t,1}$, $h_{t,1}$, $\rho_{t,1}$) were obtained using the real gas EoS as a function of $T_{t,1}$ and $P_{t,1}$. The total thermodynamic properties at the rotor inlet ($T_{t,4}$, $S_{t,4}$,$h_{t,4}$, $\rho_{t,4}$) were calculated using the real gas EoS as a function of $P_{t,4}$ and $h_{t,4}$ (adiabatic assumption, $h_{t,4}$=$h_{t,1}$), where the former was obtained by Equation 3-17. Then the static thermodynamic properties (T_4, h_4, ρ_4) at the rotor inlet were obtained with the calculated flow velocities (C_4, W_4). Similarly, the total, relative total and static thermodynamic

parameters at the rotor outlet ($S_{t,5}$, $T_{t,5}$, $\rho_{t,5}$, $P_{t,5}$, $P_{t,5,rel}$, $h_{t,5,rel}$, T_5, h_5, ρ_5) were determined using the isentropic expansion state point (h_{5s}, S_{5s}=S_1), Δh_{actual} and (C_5, W_5). The rotor exit flow area (A_5) and the rotor exit tip radius ($r_{5,tip}$) were obtained as below using the known r_{5hub}/r_4 ratio given in Table 5-3.

$$A_5 = \frac{\dot{m}_{wf}}{\varphi U_4 \rho_5 (1 - BK)} \quad \text{Equation 5-19}$$

$$r_{5,tip} = \sqrt{\frac{A_5}{\pi} + r_{5,hub}^2} \quad \text{Equation 5-20}$$

Same value for BK was used similar to chapter three and the same correlation was employed for specifying Z_{rotor} shown in Equation 3-26. In order to determine the rotor blade inlet angle ($\beta_{4,blade}$) the below equations were used (Aungier 2006).

$$\kappa = 1 - \frac{Z_{rotor} t_4}{2\pi r_4 \cos \beta_{4,blade}} \quad \text{Equation 5-21}$$

$$C_{\theta,4} = \left(1 - \frac{\sqrt{\cos \beta_{4,blade}}}{Z_{rotor}^{0.7}}\right)\left(U_4 - C_{m,4} \frac{\tan \beta_{4,blade}}{\kappa}\right) \quad \text{Equation 5-22}$$

Where t_4 is the rotor blade inlet thickness equal to $0.04r_4$ according to (Aungier 2006). EES can iteratively solve the two above explicit equations for $\beta_{4,blade}$.

5.4.3. Nozzle modelling

Modelling of nozzle is similar to section 3.5.3 with the only difference that the ratio of nozzle inlet to exit (r_2/r_3) was taken as a free parameter shown in Table 5-3. In addition, instead of using the cambered vanes shown in Figure 3-8, un-cambered nozzle vane geometry was created as the nozzle ring was located after the volute.

5.4.4. Volute modelling

To transfer the fluid uniformly around the periphery of the nozzle ring, the ratio of the volute inlet area to inlet radius (A_1/r_1) should be a linear function of the polar angle. Assuming circular cross section for the volute shown in Figure 5-4, key geometry and

static thermodynamic properties were determined iteratively with the known turbine inlet total thermodynamic properties, nozzle inlet properties and below equations.

$$A_1 = \frac{\dot{m}_{wf}}{\rho_1 C_1} \quad \text{Equation 5-23}$$

$$r_1 = \frac{r_2 C_{\theta,2}}{C_1 SC} \quad \text{Equation 5-24}$$

$$r_{volute} = \sqrt{\frac{A_1}{(0.75\pi + 1)}} \quad \text{Equation 5-25}$$

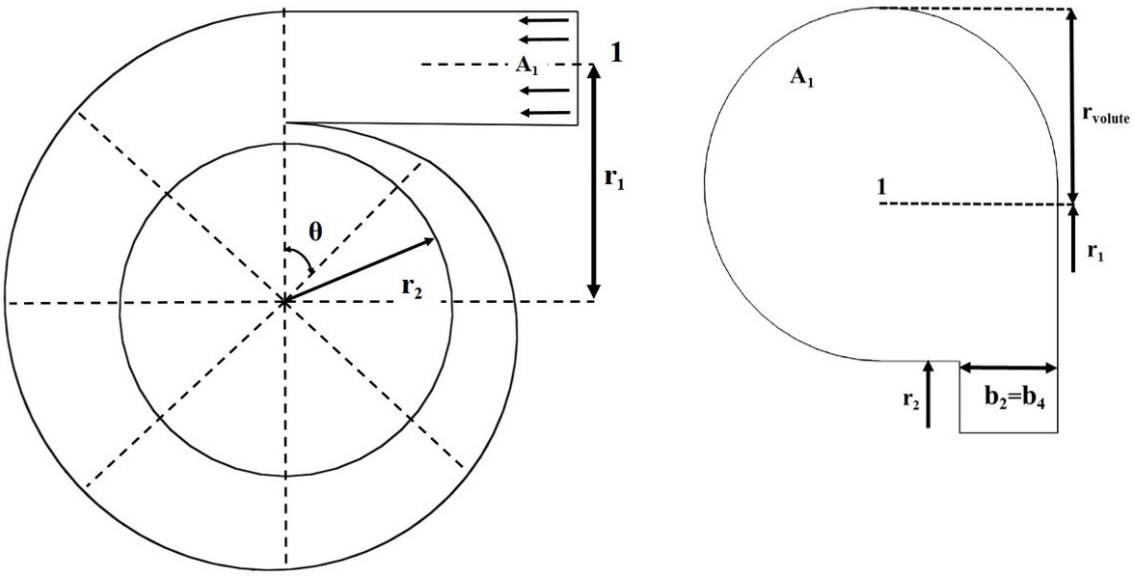

Figure 5-4 Schematic of the volute geometry

Where *SC* is the swirl coefficient that accounts for the effect of wall friction and boundary layer growth with the value of 0.9 suggested in (Baines 2003). The turbine overall packaging size and the volute loss were attained by:

$$d_{max} = 2(r_1 + r_{volute}) \quad \text{Equation 5-26}$$

$$\Delta h_{loss,volute} = \frac{k_{volute} C_2^2}{2} \quad \text{Equation 5-27}$$

Where k_{volute} is the volute total pressure loss coefficient with the value of 0.1 as suggested in (Baines 2003). The volute area and mean radius distribution was obtained using (Aungier 2006):

$$A(\theta) = SP(\theta r_{mean}(\theta) b_2 \cot \alpha_2) \quad \text{Equation 5-28}$$

$$SP = \frac{\rho_2}{\rho_1} \quad \text{Equation 5-29}$$

Where r_{mean} is the mean passage radius at various polar angles (θ) and it is equal to r_1 at the volute inlet (θ =0) corresponding to A_1. For other stations the same iterative technique was used to specify $A(\theta)$ and $r_{mean}(\theta)$ at various θ. Sizing parameter (SP) expresses the ratio of the actual volute area to the value satisfying the ideal conservation of angular momentum (Aungier 2006).

5.4.5. Performance estimation with losses

The same loss models described in section 3.5.4 were employed for performance prediction of the organic RIT using Equation 3-34 with the only difference that the term $\sum \Delta h_{losses}$ also includes the loss associated with the volute (Equation 5-27).

5.5. Integration of ORC model with organic RIT model

The approach presented in the literature relies on achieving a feasible turbine design that is able to deliver the specified efficiency as well as satisfying the application requirements for various working fluids and for wide range of operating conditions. However, such method does not consider feasibility of turbine design or any other factors that influence that nor the performance or suitability of the turbine for a given application. This is a rather simplistic approach as it may lead to non-optimal or inaccurate results such as leading to operating conditions that require unrealistic turbine design or even designs that do not fit the application constraints. Also, such approach could lead to the choice of optimum working fluid that is not optimum if turbine efficiency was calculated

based on constant turbine efficiency approach. Therefore to overcome this major deficiency, the integration between the ORC model and organic RIT model was conducted in an iterative manner where the main cycle state points and cycle feasibility are determined with the ORC model (section 5.3) while the turbine internal state points, efficiency, power and condensation temperature (T_6) are calculated with the organic RIT model (section 5.4). The turbine efficiency itself is obtained dynamically using the loss models (section 3.5.4) and imposed thermodynamic conditions and is unique for each working fluid. The aforementioned methodology is depicted in Figure 5-5. Further details regarding the developed code based on real-gas formulation is provided in Appendix (B).

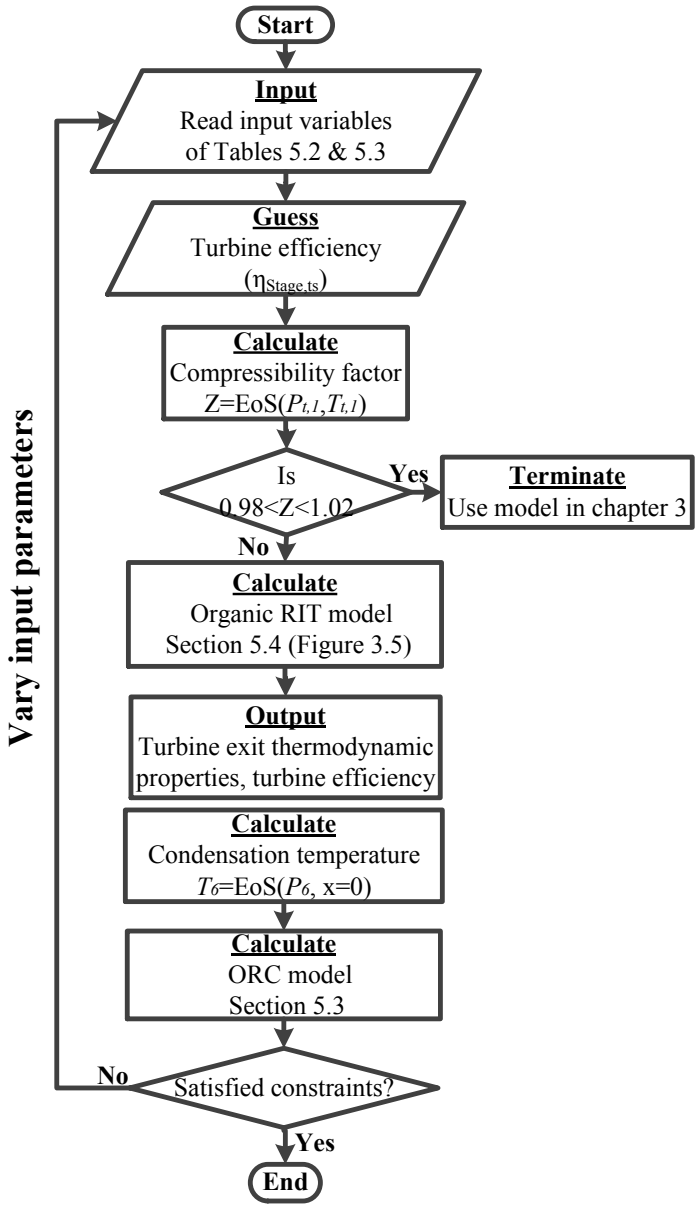

Figure 5-5 Algorithm for integration of organic RIT model and ORC model based on real-gas formulation

5.6. Methodology for one-dimensional optimization with genetic algorithm

Following the discussion in section 5.1, to assure that optimum combination of ORC-RIT input parameters are achieved (instead of manual-iterative procedure used in few available literature), genetic algorithm (GA) optimization technique was coupled with the ORC-RIT model (Figure 5-5) for optimizing the performance metrics (i.e. cycle thermal efficiency and/or turbine efficiency). GA is based on the biological evolution

and it is initiated with the creation of an initial population whose elements are randomly selected in the whole design space. Different procedures are then applied in order to successively generate new population containing better elements. The performance of an individual is measured by its fitness. Pairs of individuals are selected from this population based on their objective function values. Then each pair of individuals undergoes a reproduction mechanism to generate a new population in such a way that fitter individuals will spread their genes with higher probability. The children replace their parents and as this proceeds, inferior traits in the pool die out due to the lack of reproduction. At the same time, strong traits tend to combine with other strong traits to produce children who perform better. This procedure is repeated for the next generation until the maximum specified number of generations is reached.

GA can deal with complex optimization problems such as multi-dimensional, non-continuous, and non-linear problems. Moreover, GA locates the global optimal values reliably from a population of solutions even if many local optima exist and prevents the convergence to sub-optimal solutions. This distinguishes GA from the traditional optimization techniques that rely on the initial guesses, while GA is far less sensitive to the initial conditions enforced on it. GA will eventually reject any solution that does not show enough promise which helps to provide more flexibility and robustness during the optimization (Gen *et al.* 2000).

In the present thesis GA was employed to conduct optimization of various objective functions (*OF*):

$$OF_1 = \eta_{thermal,cycle} \quad \text{Equation 5-30}$$

$$OF_2 = \eta_{stage,ts} \quad \text{Equation 5-31}$$

Figure 5-6 shows the implementation of GA optimization loop into the ORC-RIT model (Figure 5-5). The initial estimates of input parameters of the ORC-RIT model and $\eta_{stage,ts}$ were used to commence the optimization, then GA optimizes these inputs leading to the optimum *OF*. The new optimized values of the input parameters were used again as initial guesses and the process was repeated until convergence was achieved to the specified tolerance.

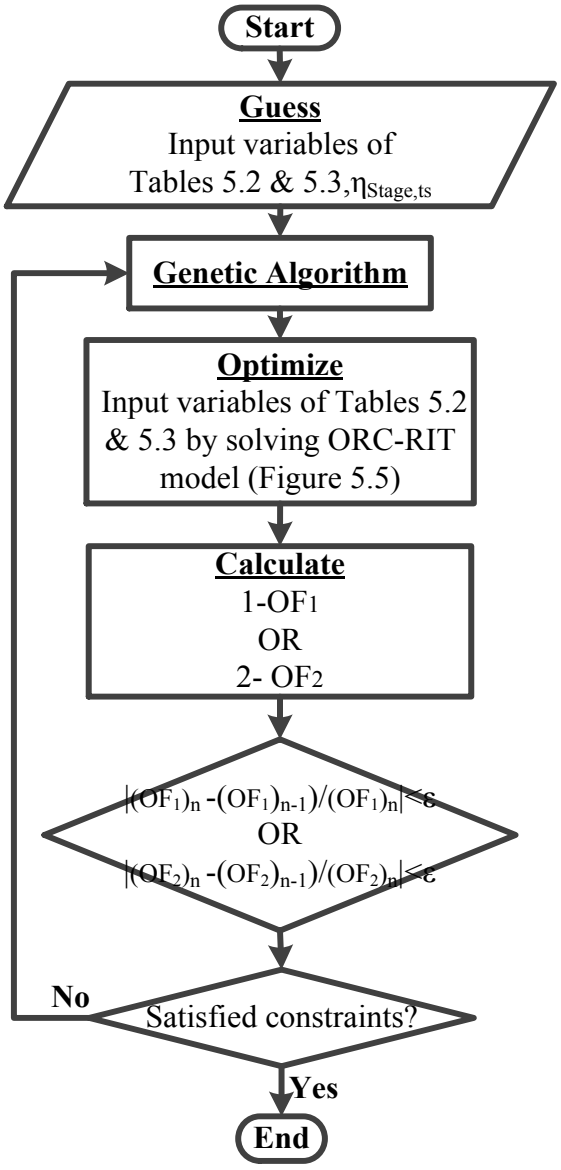

Figure 5-6 Integration of the genetic algorithm with the ORC-RIT model (Figure 5-5)

5.6.1. Optimization constraints

Some of the critical turbine geometry parameters, flow features and ORC properties were constrained during the optimization. These constraints were required to be satisfied simultaneously to ensure high aerodynamic performance, feasibility of the optimized turbine design and high cycle efficiency.

- α_4 < 82º. This value was set to achieve reasonable Z_{rotor}, Equation 3-26, and minimize the associated tip clearance and friction losses (EquationsEquation 3-37 and 3.45).

- $\beta_{5,tip}$ > -75º: This value was set to compromise between the rotor exit kinetic loss and the rotor passage loss (summation of secondary and friction losses) (Baines 2003) and manufacturing limitations.

- $\beta_{4,blade}$ <70º. This value was set as an upper limit for manufacturing.

- $Ma_{5tip,rel}$ < 1. This value was set to prevent supersonic loss (shock waves) at the rotor exit.

- $d_{5,hub}/d_{5,tip}$ > 0.4. This value was set to avoid the possibility of flow blockage due to closely spaced vanes, as suggested in (Rohlik *et al.* 1968).

- d_4>0.01 (m). This value was selected as the minimum threshold size for manufacturability.

- r_{5tip}/r_4 < 0.7. This limit was set to both accommodate the expanding fluid with significant decrease in density and to avoid excessive tip curvature and the associated secondary loss.

- Q_{in}<16kW. Limit of heat source for future laboratory testing.

- $P_{t,1} < 10^6$ (Pa). This value was set to avoid excessive pressure and alleviate safety concerns as the system was aimed for small-scale (i.e. domestic) applications.
- $P_5 > 10^5$ (Pa). This value was set to prevent air or water contamination in the condenser and alleviate additional complexities from the ORC (no vacuum equipment).
- 293K < T_6 < 313K. This range was set for the efficient performance of the condenser with the minimum thermal losses.
- W_{net}<10kW. Suitable for small-scale DPG systems.

5.7. Parametric studies

5.7.1. Parametric studies with ORC-RIT model

Prior to the optimization, it was vital to conduct comprehensive parametric studies using the integrated ORC-RIT model (Figure 5-5) to investigate the effect of input variables (Table 5-2 and 5.3) on the defined *OF*s and the turbine overall size. These studies were based on simultaneous variation of the two input parameters in the range shown in the same tables, while keeping the other variables as constants. Figures Figure 5-7 to 5.12 show the output of such parametric studies using R245fa as the working fluid.

Figure 5-7 presents the effect of flow (φ) and loading (ψ) coefficients on the cycle thermal efficiency ($\eta_{thermal,cycle}$), turbine stage total-to-static efficiency ($\eta_{stage,ts}$), and the turbine overall diameter (d_{max}), As it is evident, the effect of ψ is remarkable on all outputs. Increasing ψ from 0.8 to 1.5, increases $\eta_{thermal,cycle}$ and $\eta_{stage,ts}$ by 1.5% and 12% respectively while it reduces d_{max} by maximum value of 19.8%. This is directly related to Equation 5-10 where increasing ψ resulted in larger actual enthalpy drop with constant rotational speed and consequently larger $\eta_{thermal,cycle}$ and $\eta_{stage,ts}$ (with fixed Δh_{ideal}) and smaller d_{max} were achieved.

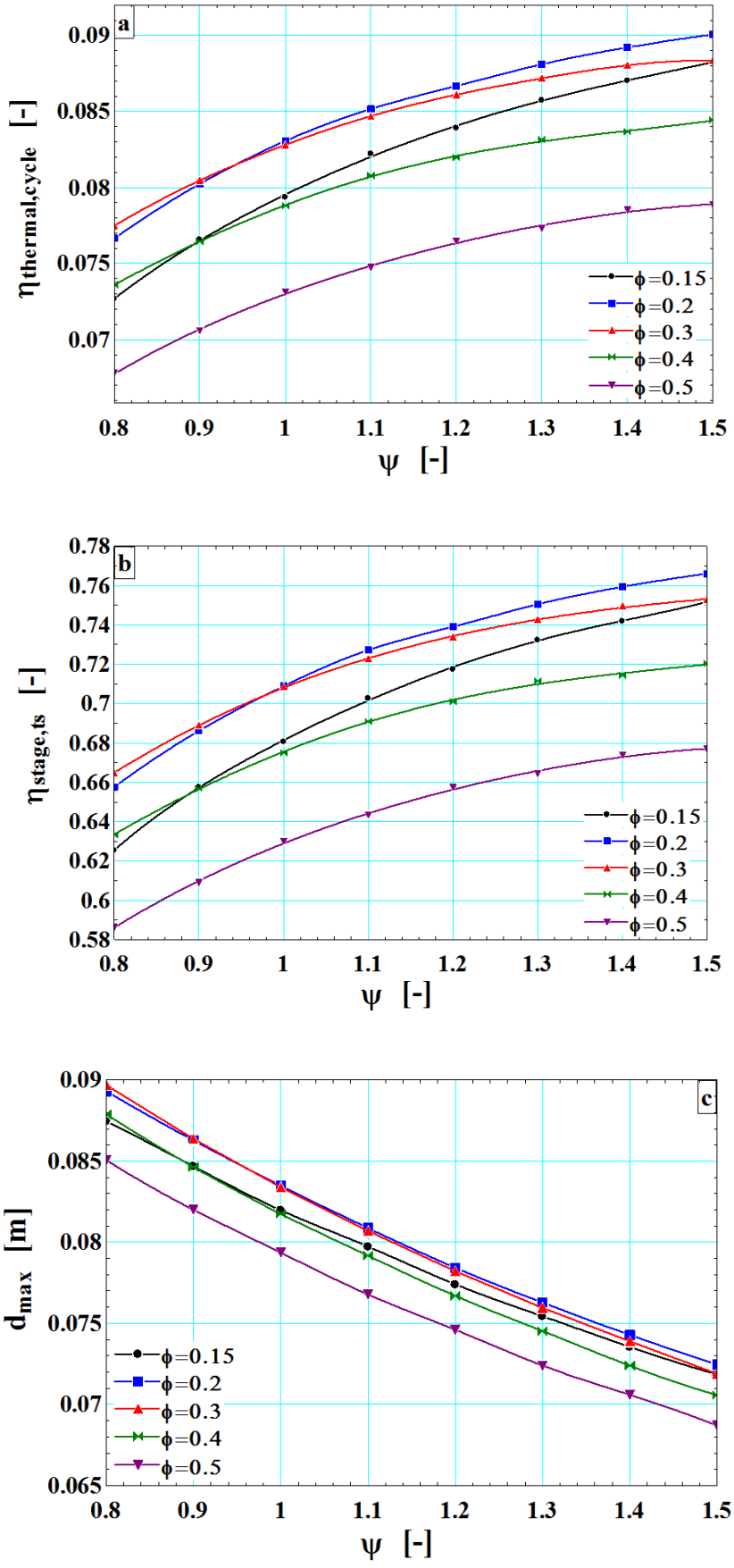

Figure 5-7 Variation of φ and ψ and their effects on $\eta_{thermal,cycle}$, $\eta_{stage,ts}$ and d_{max}

This also highlights the advantages of employing rotor with non-zero inlet blade angle which allows obtaining large ψ values and more compact turbine while preserving the optimum incidence. In contrast, increasing φ is detrimental to $\eta_{thermal,cycle}$ and $\eta_{stage,ts}$ as increasing φ from 0.15 to 0.5 led to reduction in $\eta_{thermal,cycle}$ and $\eta_{stage,ts}$ by up to 2.2% and 17.9% respectively. Increasing φ led to larger absolute meridional velocity at rotor exit (C_{m5}) according to Equation 5-9. The larger the C_{m5}, the larger the exit kinetic loss (Equation 3-49) and consequently lower turbine efficiency ($\eta_{stage,ts}$) was achieved. Since $\Delta h_{isentropic}$ was fixed by the constant $T_{t,1}$ and ER_{ts} , reduction in $\eta_{stage,ts}$ results in smaller actual enthalpy drop and consequently led to smaller W_{net} and $\eta_{thermal,cycle}$ according to EquationsEquation 5-7, 5-8, 5-16 and 5-17. It is clear from Figure 5-7(b) that there exists an optimum value for φ in the region of 0.2 to 0.3. Such results are in agreement with the generalized performance correlations charts reported in (Baines 2003, Dixon *et al.* 2010). On the other hand, increasing φ has the advantage of reducing d_{max} by a maximum value of 5.4% revealing the conflict between d_{max} and the other two performance parameters.

The effect of working fluid mass flow rate ($\dot{m}_{wf}$) and expansion ratio (ER_{ts}) on $\eta_{thermal,cycle}$, $\eta_{stage,ts}$ and d_{max} are substantial as depicted in Figure 5-8. With the rise of $\dot{m}_{wf}$, the actual enthalpy drop (Δh_{actual}) and $W_{turbine}$ increased leading to larger $\eta_{stage,ts}$ and then variation of $\eta_{thermal,cycle}$ can be immediately related to Equations Equation 5-8, 5-16 and 5-17. Even though the cycle heat input (Q_{in}) increased with larger $\dot{m}_{wf}$, Equation 5-6 , the rise in $W_{turbine}$ was dominant over the rise in Q_{in} and led to higher $\eta_{thermal,cycle}$ as illustrated in Figure 5-8(a). Similarly, with higher Δh_{actual} larger r_4 is achieved based on Equation 5-10. Conservation of mass at the rotor inlet achieved larger rotor inlet width (b_4) and larger nozzle exit radius (r_3) based on Equation 3-27. Therefore, larger d_{max} was achieved as shown in Figure 5-8(c).

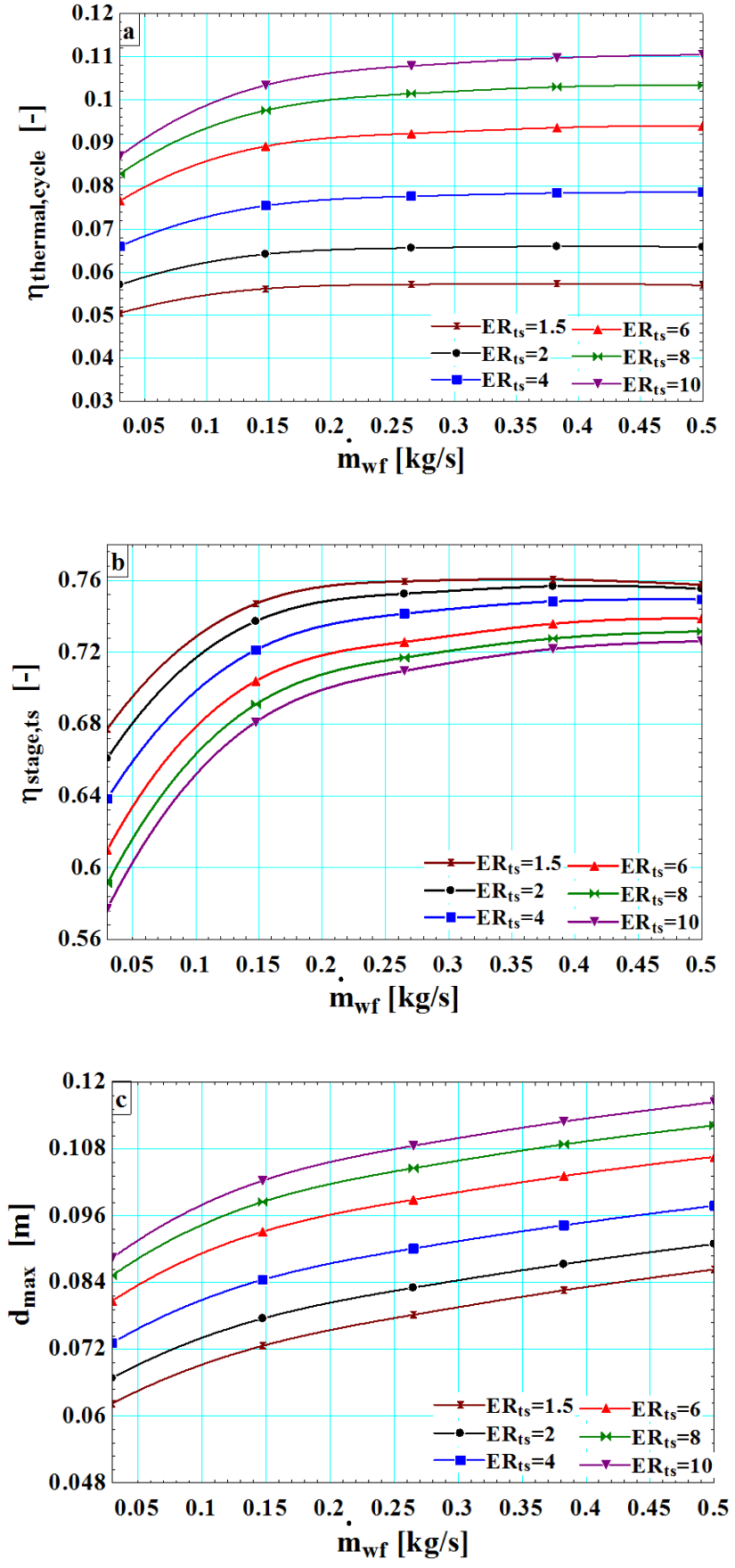

Figure 5-8 Variation of $\dot{m}_{wf}$ and ER_{ts} and their effects on $\eta_{thermal,cycle}$, $\eta_{stage,ts}$ and d_{max}

It was only for $\eta_{thermal,cycle}$ that larger value of ER_{ts} was advantageous while it had adverse effects on $\eta_{stage,ts}$ and d_{max}. Both Δh_{ideal} and Δh_{actual} were increasing with the rise of ER_{ts} which led to larger r_4 and $W_{turbine}$ based on Equations Equation 5-10 and 5-17. Consequently larger $\eta_{thermal,cycle}$ was achieved as shown in Figure 5-8(a). The larger the r_4 the larger is the wetted area of blade surfaces in contact with the fluid and consequently larger friction and secondary losses were achieved (EquationsEquation 3-37 and 3.44) leading to smaller $\eta_{stage,ts}$ as shown in Figure 5-8(b). The effect of increasing expansion ratio and consequently the actual enthalpy drop was stronger than the effect of reduction in $\eta_{stage,ts}$ hence increasing ER_{ts} increased the $\eta_{thermal,cycle}$. Thermodynamically, the larger the pressure difference (expansion ratio) across the cycle the higher the $\eta_{thermal,cycle}$. But the larger the expansion ratio across the turbine the larger the turbine size and hence the lower the $\eta_{stage,ts}$. Such results underline the challenges regarding the development of an efficient small-scale RIT for ORC applications. Therefore, if the turbine can be designed so that even at high expansion ratios it can exhibit high isentropic efficiency, then $\eta_{thermal,cycle}$ can be further improved.

Figure 5-9 illustrates the effect of turbine inlet total temperature ($T_{t,1}$) and degree of superheating ($\Delta T_{superheat}$) on $\eta_{thermal,cycle}$, $\eta_{stage,ts}$ and d_{max}. Clearly there exists an optimum inlet temperature of about 353K as increasing $T_{t,1}$ from 310K to 423K. As $T_{t,1}$ increased, the rotor inlet density (ρ_4) increased leading to smaller b_4 based on the conservation of mass and consequently smaller r_3 was achieved (Equation 3-27). In addition, with constant $\dot{m}_{wf}$, larger values of $T_{t,1}$ resulted in larger turbine inlet density (ρ_1) and smaller A_1 and r_1 according to Equations Equation 5-23 and 5-24. The accumulative effects of these two parameters (reduction in r_3 and r_1) reduced d_{max} as shown in Figure 5-9(c). In contrast, increasing $T_{t,1}$ had negative effects on $\eta_{thermal,cycle}$ and $\eta_{stage,ts}$ with the maximum reduction of 1.5% and 6.8% respectively.

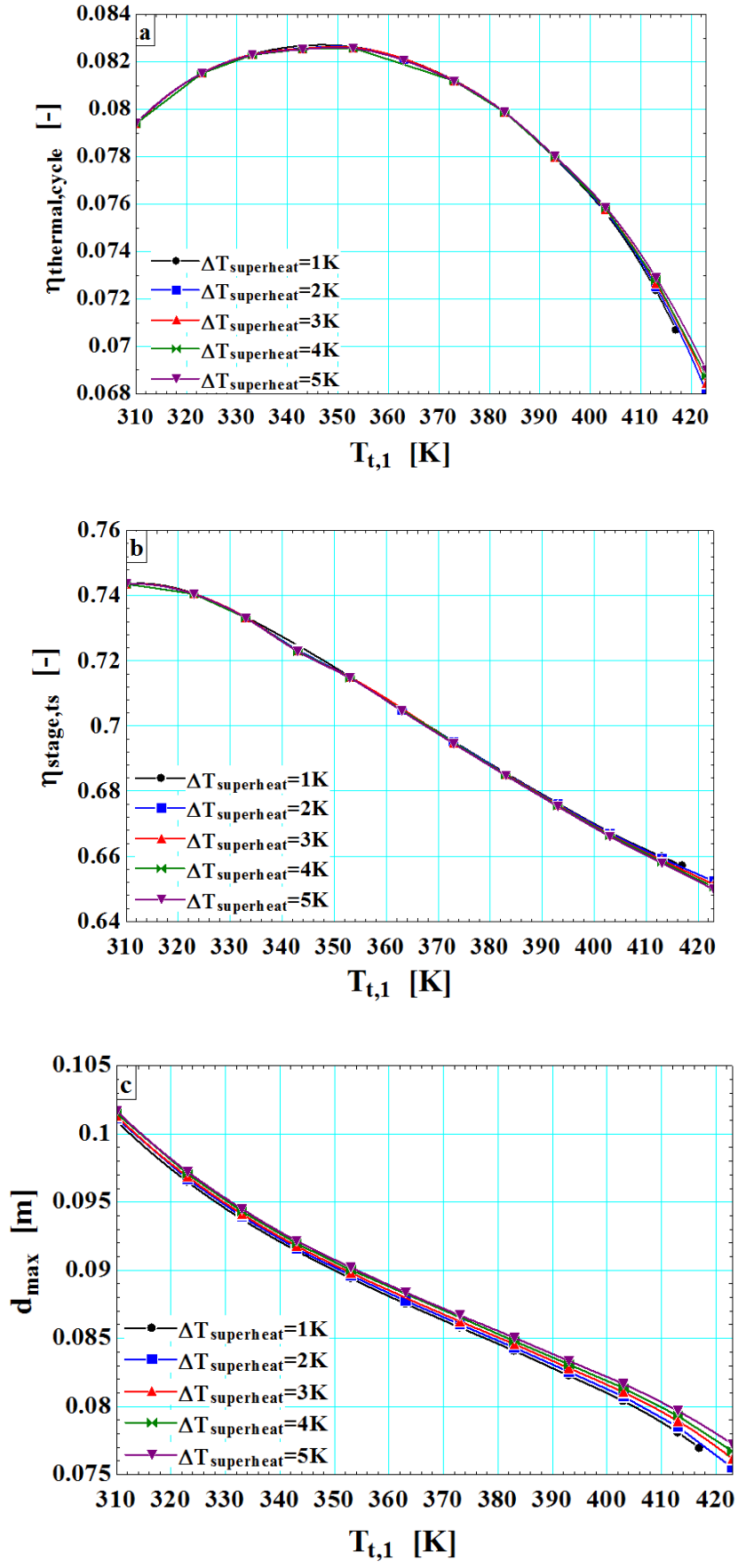

Figure 5-9 Variation of $T_{t,1}$ and $\Delta T_{superheat}$ and their effects on $\eta_{thermal,cycle}$, $\eta_{stage,ts}$ and d_{max}

Following the above discussion, b_4 was reduced with larger $T_{t,1}$ and the rotor tip clearance became a large fraction of inlet height and consequently resulted in large tip clearance loss (Equation 3-45) and reduced $\eta_{stage,ts}$ as shown in Figure 5-9 (b). At the same time, as $T_{t,1}$ increased the pump outlet pressure ($P_{t,1}=P_7$) was also increased (since ER_{ts} was kept constant) while the pump inlet density (ρ_6) was reduced because of the higher condenser saturation temperature (T_6). The combined effects of P_7 and ρ_6 increased W_{pump} based on Equation 5-5. Consequently, with smaller $\eta_{stage,ts}$ and larger W_{pump} the cycle thermal efficiency was reduced at temperatures above 353K as shown in Figure 5-9(a). Moreover, the effect of $\Delta T_{superheat}$ was very limited on all investigated outputs as it is evident in Figure 5-9.

Figure 5-10 depicts the effects of rotational speed (ω) and absolute meridional velocity ratio (ξ) on $\eta_{thermal,cycle}$, $\eta_{stage,ts}$ and d_{max}. As shown in Figure 5-10 (c), the effect of ω is substantial on d_{max}. Increasing RPM from 30000 to 80000 reduced d_{max} by about 55%. Recalling Equation 5-10 and with constant ψ, the rotor inlet radius (r_4) is inversely proportional to ω and increasing RPM reduced r_4 and consequently d_{max}. With smaller r_4, the associated turbine friction and secondary losses were reduced (Equations Equation 3-37 and 3.44) leading to larger $\eta_{stage,ts}$. With fixed Δh_{ideal}, higher $\eta_{stage,ts}$ resulted in larger W_{net} and consequently higher $\eta_{thermal,cycle}$ as shown in Figure 5-10 (a). In contrast, the effect of ξ was limited on all investigated parameters with maximum variation of about 2% for $\eta_{stage,ts}$.

Figure 5-11 shows the effects of the rotor exit absolute flow angle (α_5) and the ratio of rotor hub radius at the exit to the rotor radius at the inlet ($r_{5,hub}/r_4$) on $\eta_{stage,ts}$ and d_{max}. As shown in Figure 5-11(a), slightly better performance was achieved at smaller (negative) α_5.

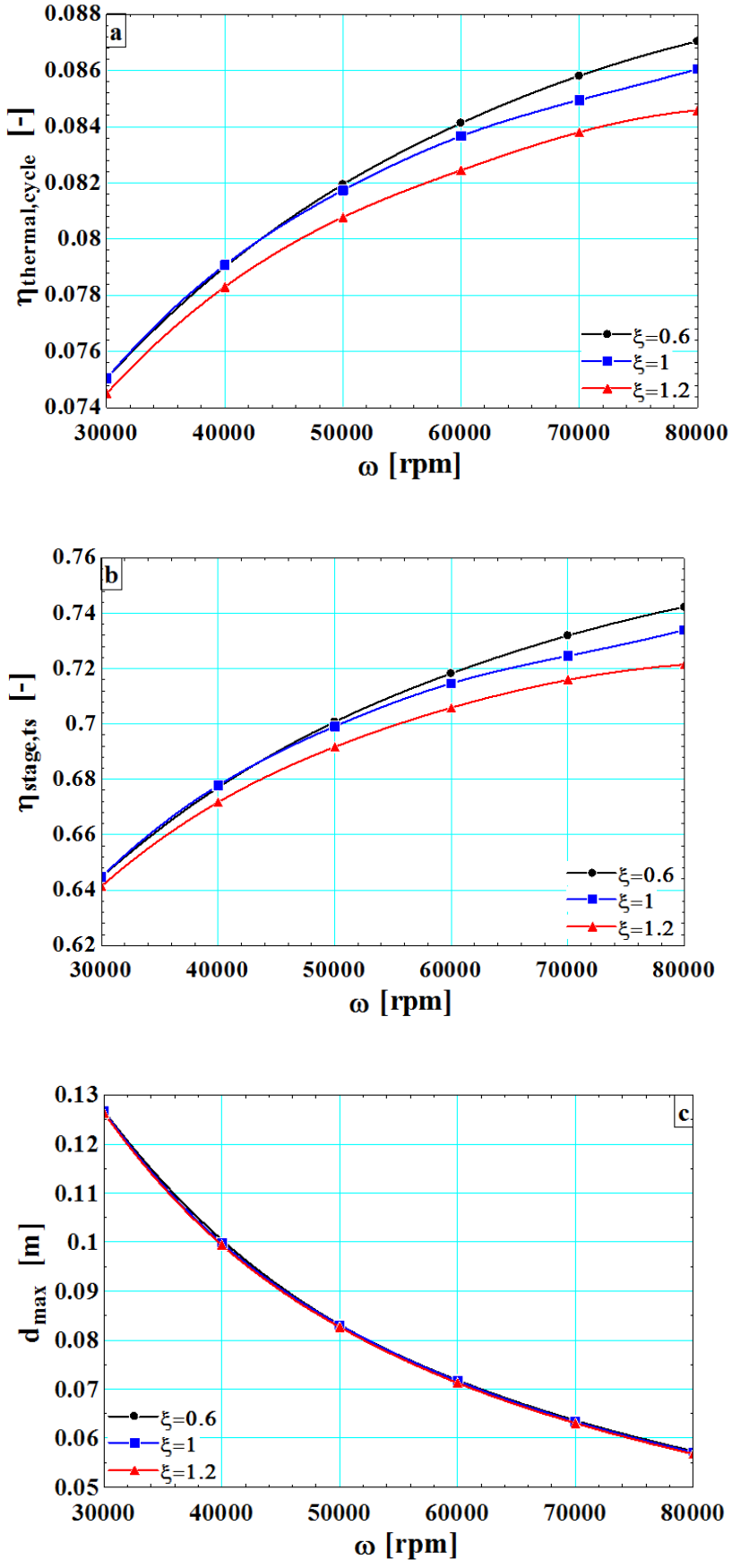

Figure 5-10 Variation of ω and ξ and their effects on $\eta_{thermal,cycle}$, $\eta_{stage,ts}$ and d_{max}

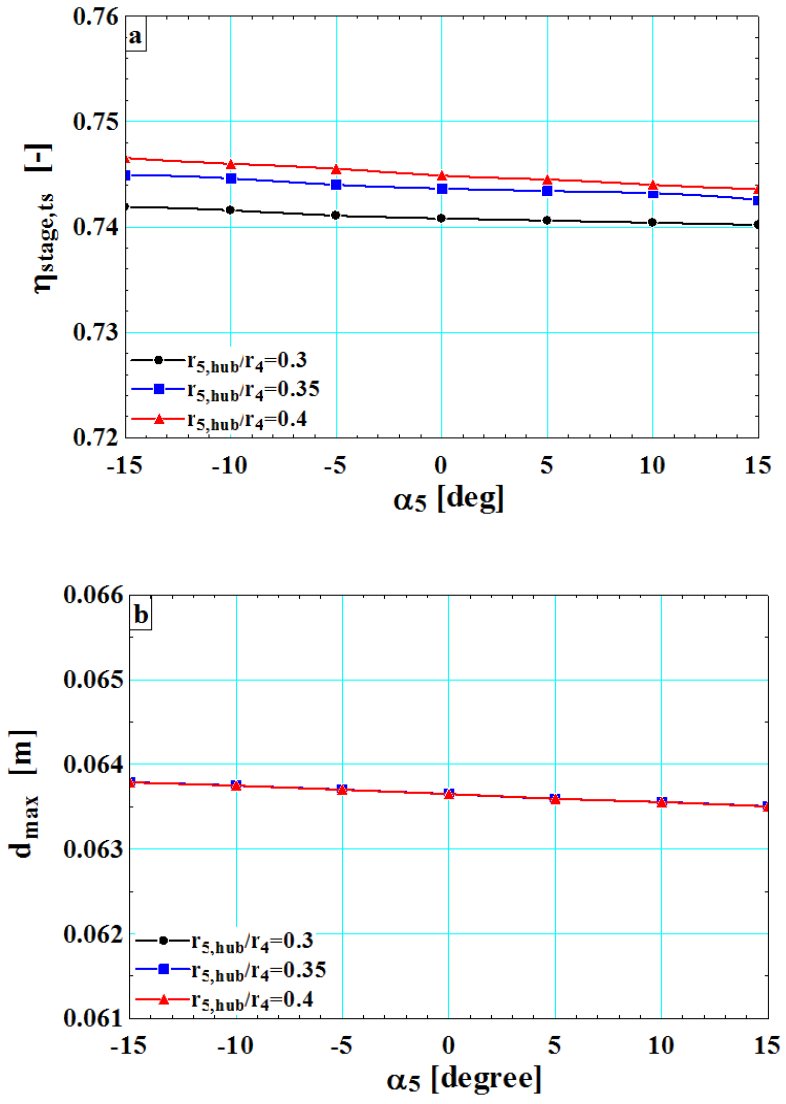

Figure 5-11 Variation of α_5 and $r_{5,tip}/r_4$ and their effects on $\eta_{stage,ts}$ and d_{max}

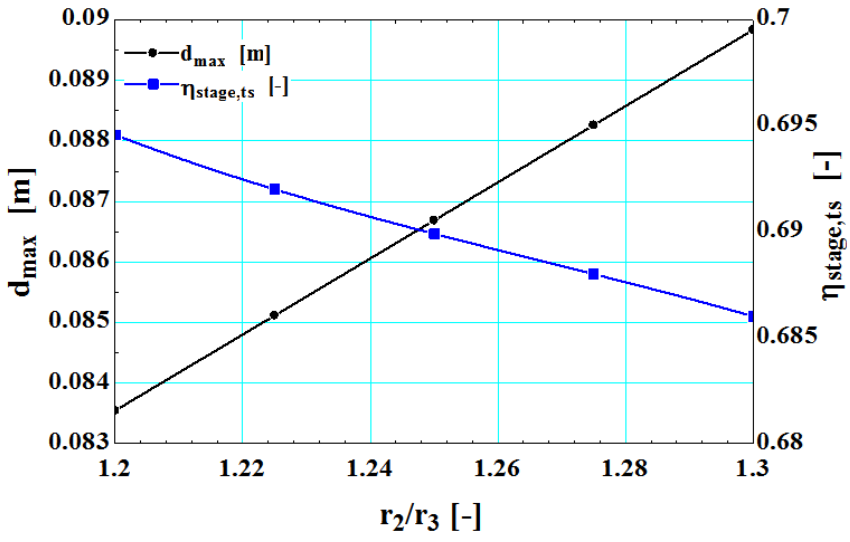

Figure 5-12 Variation of r_2/r_3 and its effect on $\eta_{stage,ts}$ and d_{max}

This is due to the fact that at smaller (negative) α_5 and with fixed $\dot{m}_{wf}$ and ER_{ts}, the rotor exit area (A_5) was increased leading to smaller absolute meridional velocity at rotor exit (C_{m5}) and consequently smaller exit loss according to Equation 3-49.

Figure 5-12 presents the effect of nozzle inlet to nozzle exit radii ratio (r_2/r_3) on $\eta_{stage,ts}$ and d_{max}. It is clear that, d_{max} was linearly proportional to r_2/r_3 shown in stage configuration (Figure 3-2). Increasing r_2/r_3 resulted in larger nozzle hydraulic length (Equation 3-54) and therefore larger nozzle friction loss, though, $\eta_{stage,ts}$ was a weak function of r_2/r_3 as shown in Figure 5-12.

5.7.2. Effect of ORC standalone model with constant turbine efficiency on the parametric study results

The ORC standalone model developed in section 5.3 was compared with the integrated ORC-RIT model developed in section 5.4 to highlight deficiency of assuming constant turbine efficiency while preforming similar parametric studies as in section 5.7.1. The same values of ER_{ts} (5) and $\dot{m}_{wf}$ (0.1kg/s) were assigned to both models while varying $T_{t,1}$ and $\Delta T_{superheat}$ and the results are presented in Figure 5-13. As it is evident there exist considerable deviation in $\eta_{thermal,cycle}$ of the two models with the maximum difference of about 2% at the turbine inlet temperature of 423K and maximum difference of 15.02% (80% - 64.98%) in the turbine efficiency (refer to Figure 5-9(a)). Moreover, the point of optimum cycle efficiency has been shifted from the inlet temperature of about 353K in ORC-RIT model to about 383K in the ORC standalone model. The same procedure was repeated for the rest of fluids in Table 5-1 and the results are only presented for the maximum difference between the two models as summarized in Figure 5-14 (the upper boundary of temperature ($T_{t,1}$) was specified to be close to the critical point for each individual fluid).

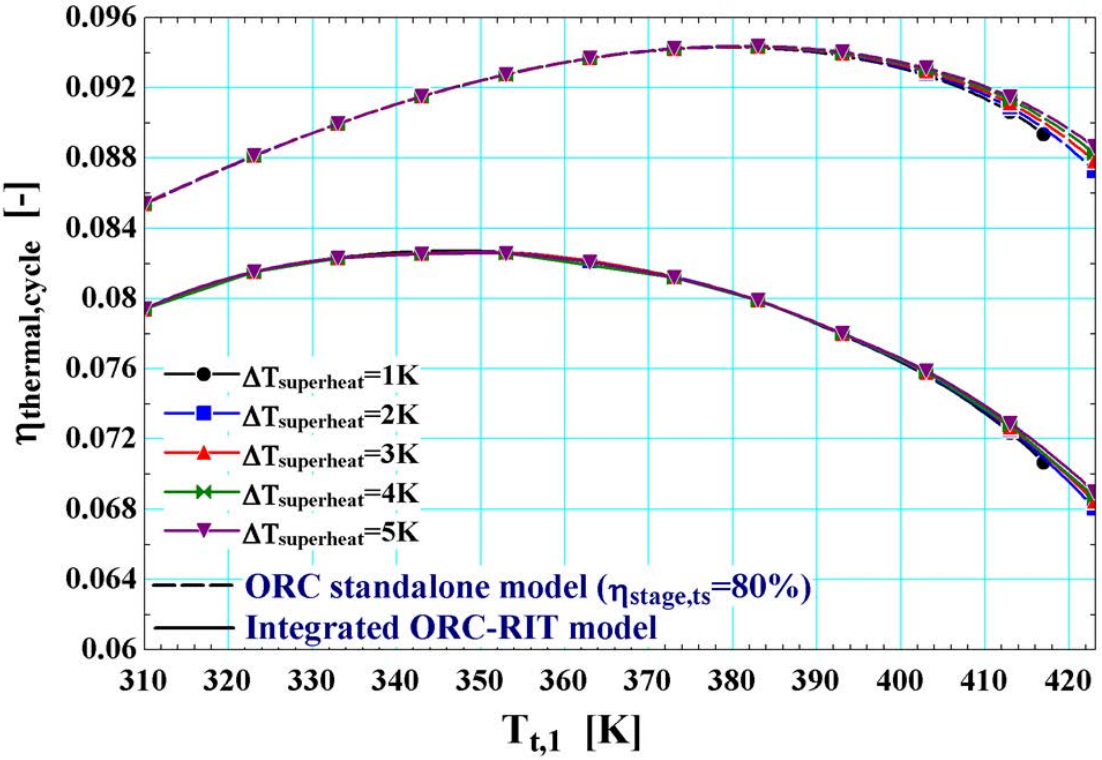

Figure 5-13 Variation of $T_{t,1}$ and $\Delta T_{superheat}$ and their effects on $\eta_{thermal,cycle}$ for both ORC standalone model and integrated ORC-RIT model with R245fa, $\dot{m}_{wf}$=0.1kg/s and ER_{ts}=5 assigned to both models

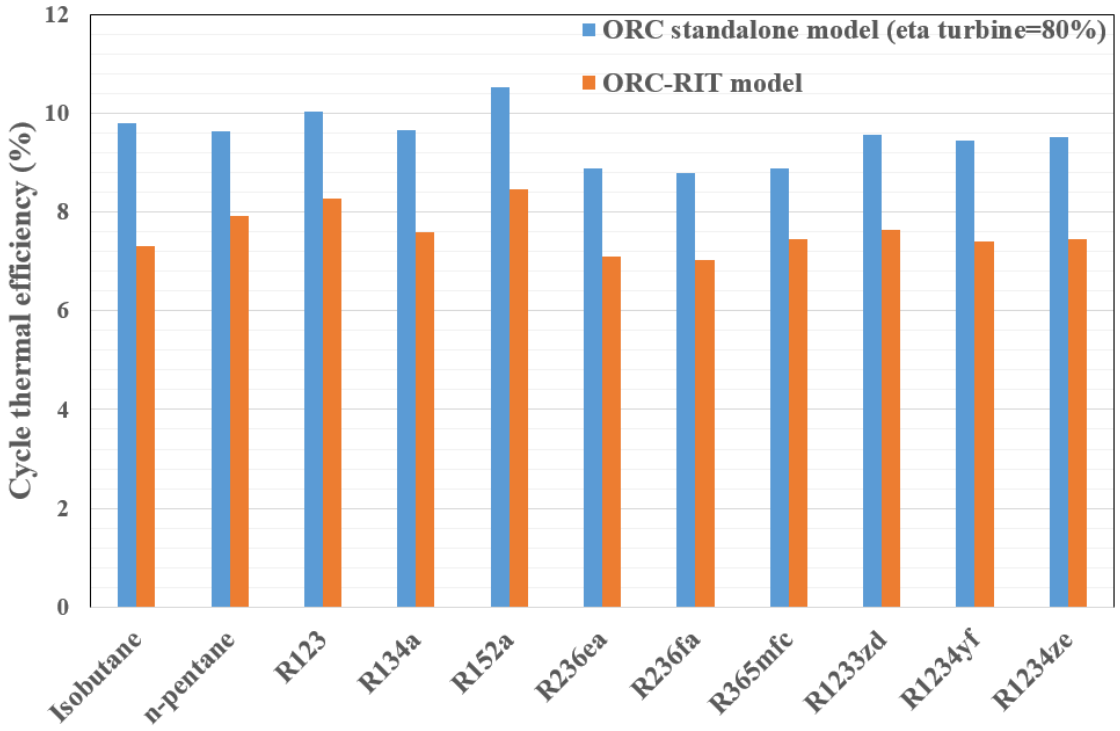

Figure 5-14 Maximum predicted difference in $\eta_{thermal,cycle}$ of the ORC standalone and ORC-RIT integrated models by variation of $T_{t,1}$ and $\Delta T_{superheat}$ for all investigated fluids

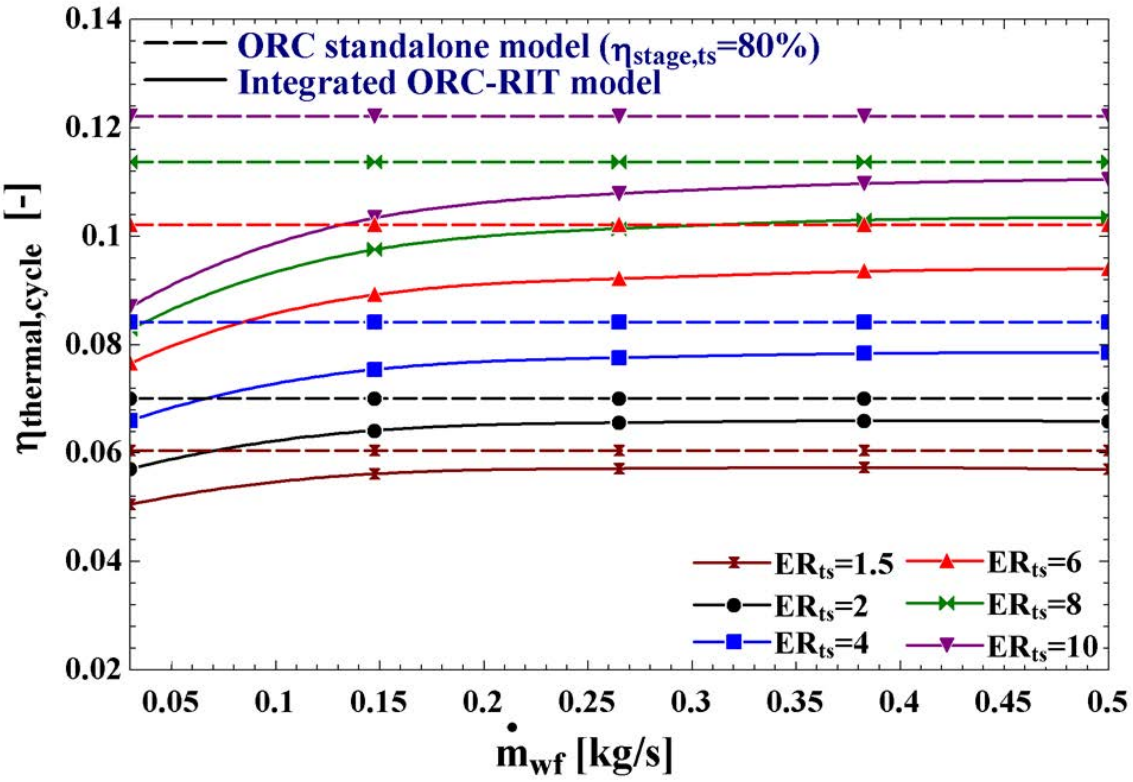

Figure 5-15 Variation of $\dot{m}_{wf}$ and ER_{ts} and their effects on $\eta_{thermal,cycle}$ for both ORC standalone model and integrated ORC-RIT model with R245fa, $T_{t,1}$=373K and $\Delta T_{superheat}$=3 assigned to both models

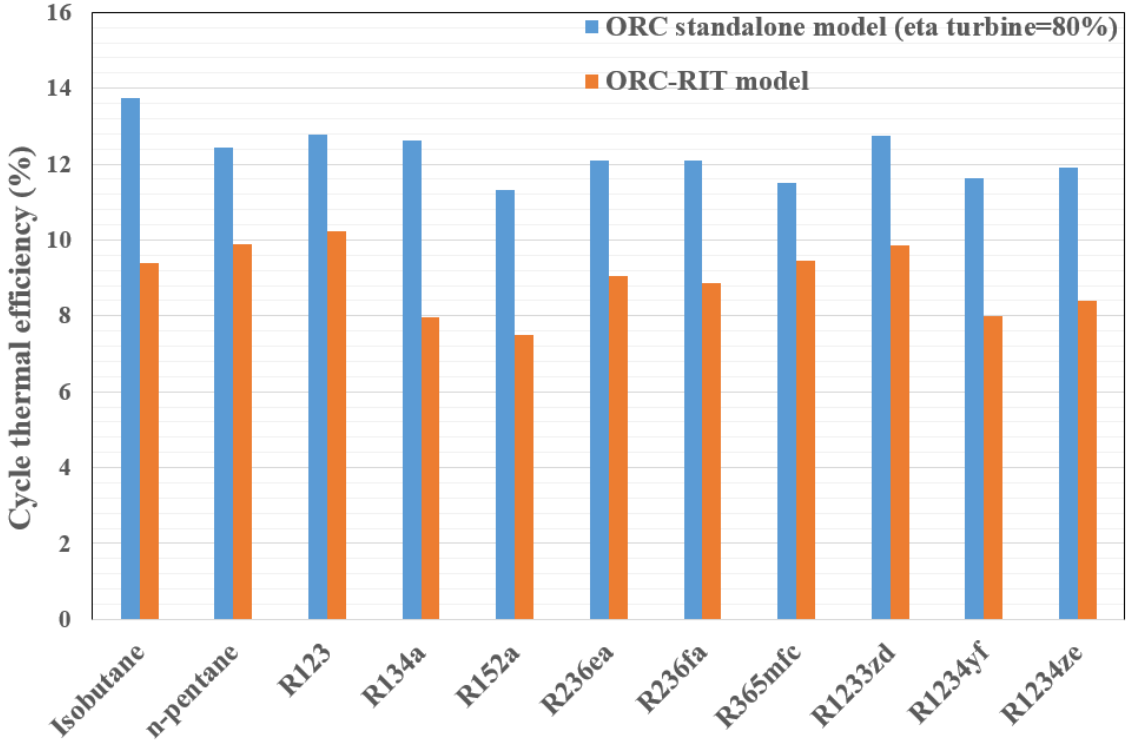

Figure 5-16 Maximum predicted difference in $\eta_{thermal,cycle}$ of the ORC standalone and ORC-RIT integrated models by variation of $\dot{m}_{wf}$ and ER_{ts} for all investigated fluids

There is substantial variation between $\eta_{thermal,cycle}$ of the two models with the maximum difference of about 2.5% at the turbine inlet temperature of 403K for isobutane. Similar parametric studies were conducted for ER_{ts} and $\dot{m}_{wf}$ while keeping $T_{t,1}$ and $\Delta T_{superheat}$ as constants and the results are shown in Figure 5-15. There exist a maximum difference of 3.42% in $\eta_{thermal,cycle}$ of the two models at ER_{ts}=10 and $\dot{m}_{wf}$=0.03kg/s. Clearly, the predicted difference in $\eta_{thermal,cycle}$ by the two models is substantial specially at high ER_{ts} and low $\dot{m}_{wf}$ which are in fact the typical operating conditions of the small-scale ORC systems. This is due to the fact that at the low $\dot{m}_{wf}$ and high ER_{ts} the turbine efficiency drops drastically (Figure 5-8(b)) leading to reduction in $\eta_{thermal,cycle}$.

The same procedure was repeated for the rest of working fluids in Table 5-1 and the results are only presented for the maximum difference between the two models as presented in Figure 5-16 with a maximum difference of about 4.65% for R134a. Such results underline the deficiencies of assuming constant turbine efficiency and the inaccuracies in the cycle analysis results.

5.8. GA optimization results and candidate configuration

As shown in section 5.7.1 all of the investigated ORC-RIT model input parameters as φ, ψ, $\dot{m}_{wf}$, ER_{ts}, $T_{t,1}$, $\Delta T_{superheat}$, ω, ξ, α_5, $r_{5,tip}/r_4$ and r_2/r_3 have considerable effects on at least one of the defined *OF*s and were included in the constrained optimization with the GA.

5.8.1. GA control parameters

Three control operators, as the number of populations, number of generations and mutation rate are used in the GA in which the first two are considered as the most important ones. A sensitivity analysis was conducted to decide on the number of populations and number of generations while the mutation rate was set to 0.2 in all studies

as suggested in (Gen *et al.* 2000). The results are presented for R245fa and only $\eta_{stage,ts}$ (OF_2) was considered as the objective function, however, the results for the other $OF(\eta_{thermal,cycle})$ led to the same conclusions. As it is evident from the results in Table 5-4, GA will eventually converge to almost similar value for $\eta_{stage,ts}$ irrespective of the number of populations if the number of generations is large enough. GA optimization led to the maximum $\eta_{stage,ts}$ of 87.28% with 500 generations and 200 population, though, in a very time consuming process. Therefore as a compromise between the accuracy of the results and computational time, 500 generations and 20 populations were selected for all the following optimization studies in this chapter.

Table 5-4 Sensitivity analysis results of the GA control parameters

Number of population	Number of generations					
	50		100		500	
	$\eta_{stage,ts}$ (-)	CPU time(s)	$\eta_{stage,ts}$ (-)	CPU time (s)	$\eta_{stage,ts}$ (-)	CPU time (s)
20	0.8196	1146	0.8402	2589	0.8716	10981
100	0.8331	6470	0.844	10873	0.8721	62505
200	0.8461	12353	0.8488	23965	0.8728	83293

5.8.2. Comparison of GA with traditional optimization techniques

Superiority of the GA optimization technique is highlighted by comparing it with three traditional optimization methods as the conjugate directions, variable metric and Nelder-Mead simplex described in (Press *et al.* 1989). The maximum function calls of 10^3 and relative convergence tolerance of 10^{-5} were specified for all these three methods while the GA control operators were assigned similar to section 5.8.1. Figure 5-17 shows that with the same initial guesses of all input variables in all four methods, GA resulted in at least 3.26% higher $\eta_{stage,ts}$ and can reliably find the global optimum without converging to the sub-optimal solutions.

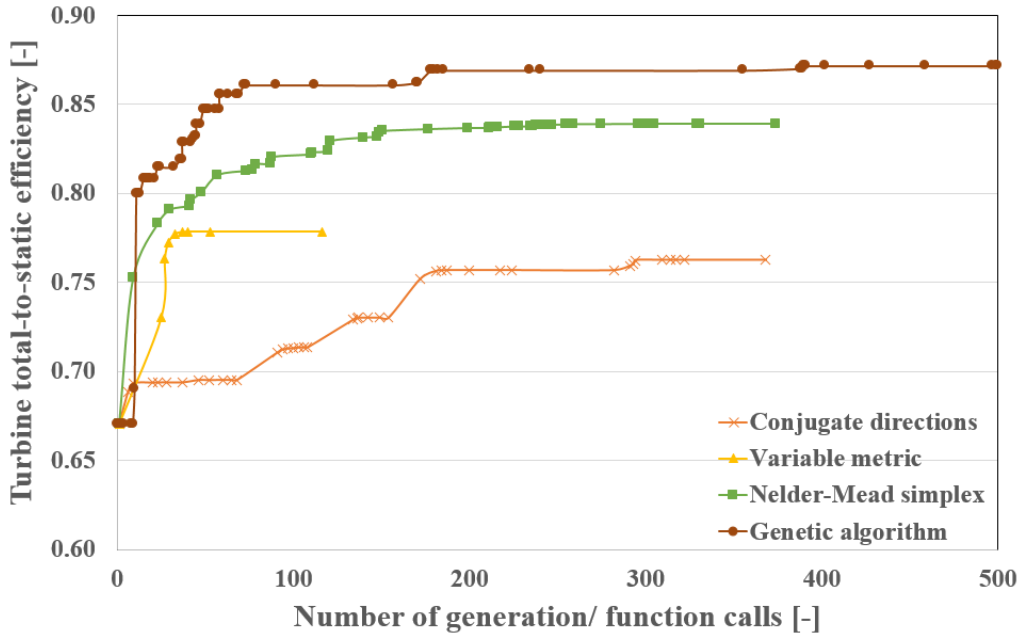

Figure 5-17 Comparison of GA with traditional optimization techniques - convergence history

5.8.3. Optimization results for ORC standalone model and ORC-RIT model

GA optimization technique outlined in section 5.6 and all the constraints of section 5.6.1 with similar control operators as in section 5.8.1 were used to maximize $\eta_{thermal,cycle}$ (OF_1) for all the fluids shown in Table 5-1 using both ORC standalone model and ORC-RIT model. For the former $T_{t,1}$, $\Delta T_{superheat}$, $\dot{m}_{wf}$ and ER_{ts} were considered as the optimization parameters with ranges shown in Table 5-2 while for the latter φ, ψ, $\dot{m}_{wf}$, ER_{ts}, $T_{t,1}$, $\Delta T_{superheat}$, ω, ξ, α_5, $r_{5,hub}/r_4$ and r_2/r_3 were all considered as the optimization parameters with ranges shown in both Tables Table 5-2 and 5-3. The optimized input variables of each individual fluid that led to maximum $\eta_{thermal,cycle}$ for both ORC standalone model and ORC-RIT model are shown in Tables Table 5-5 and 5-6 respectively. The optimization results including $\eta_{thermal,cycle}$, turbine geometry, velocity triangles and cycle parameters for both models are listed in Tables Table 5-7 and 5-8 and satisfying all the constraints in section 5.6.1.

Table 5-5 Optimized input parameters of the ORC standalone model ($\eta_{stage,ts}$=80%) for all working fluids

Parameter	$T_{t,1}$ (K)	$P_{t,1}$ (kPa)	$\Delta T_{superheat}$ (K)	ER_{ts} (-)	$\dot{m}_{wf}$ (kg/s)
Isobutane	339.4	999.999	2.286	3.327	0.03451
n-pentane	398.2	999.538	1	9.995	0.03
R123	384.2	1000	5	10	0.04631
R134a	312.5	1000	5	1.756	0.06018
R152a	316.7	1000	5	1.956	0.04118
R236ea	353	1000	1.458	5.829	0.0379
R236fa	343.9	1000	1.044	4.383	0.08007
R245fa	362.8	1000	5	8.218	0.04921
R365mfc	396.7	1000	1	10	0.05977
R1233zd	371.3	1000	5	9.319	0.04753
R1234yf	312.4	1000	5	1.698	0.06541
R1234ze	323.3	999.99	4.897	2.342	0.0825

Table 5-6 Optimized input parameters of the ORC-RIT model for all working fluids

Parameter	$T_{t,1}$ (K)	$P_{t,1}$ (kPa)	$\Delta T_{superheat}$ (K)	ER_{ts} (-)	$\dot{m}_{wf}$ (kg/s)	φ (-)	ψ (-)	ω (rpm)	ξ (-)	α_5 (-)	$r_{5,hub}/r_4$ (-)	r_2/r_3 (-)
Isobutane	339.4	1000	2.479	3.327	0.04013	0.2106	1.078	68611.7	0.734	1.74	0.3445	1.236
n-pentane	398.2	999.99	1.08	10	0.03198	0.2344	1.183	66090.7	0.774	-2.01	0.3541	1.261
R123	384.2	998.97	2.518	9.989	0.0723	0.2079	0.915	79984.9	0.618	1.08	0.3587	1.258
R134a	312.5	1000	3.211	1.756	0.08205	0.2313	0.919	69385	0.629	0.698	0.3047	1.238
R152a	316.7	1000	5	1.956	0.05232	0.1608	0.909	43945.8	0.782	2.001	0.3229	1.273
R236ea	353	999.99	4.964	5.817	0.07836	0.2386	1.09	74198.04	0.648	0.025	0.3559	1.203
R236fa	343.8	998.68	3.823	4.375	0.087	0.206	0.918	77072.4	0.69	1.032	0.3221	1.287
R245fa	362.8	1000	3.879	8.225	0.06499	0.1887	1.06	79727.1	0.6	0.89	0.3321	1.204
R365mfc	396.7	999.99	1.153	10	0.06051	0.2028	1.048	78036.9	0.725	1.164	0.3704	1.218
R1233zd	371.3	1000	1.827	9.319	0.06487	0.1569	0.939	71266.4	0.857	0.02	0.3791	1.295
R1234yf	312.4	1000	1.547	1.698	0.06205	0.197	0.916	51327.5	0.648	-1.81	0.3506	1.216
R1234ze	323.3	1000	3.848	2.342	0.08212	0.1885	0.912	71123.2	0.728	3.021	0.3461	1.25

Table 5-7 ORC standalone model ($\eta_{stage,ts}$ =80%) optimization results for all working fluids

Parameter	Isobutane	n-pentane	R123	R134a	R152a	R236ea	R236fa	R245fa	R365mfc	R1233zd	R1234yf	R1234ze
$\eta_{thermal,cycle}$ (%)	8.44	12.57	12.9	4.181	5.042	9.967	8.807	11.41	11.62	12.46	4.04	5.968
$W_{turbine}$ (W)	1326	2115	1494	570.6	720.7	855	1450	1558	2059	1658	515.1	1098
W_{net} (W)	1160	1886	1336	495.7	632.7	756.8	1272	1390	1835	1481	440.1	954.6
Q_{in} (W)	13744	15003	10356	11854	12547	7593	14445	12182	15792	11883	10900	16000
Q_{out} (W)	12480	12952	8903	11314	11858	6769	13059	10669	13796	10273	10419	14959
T_5 (K)	308	348.7	330.1	298.7	295.4	315.7	310.1	318.1	352.4	318.9	301.7	303.9
P_5 (kPa)	300.57	100.5	100	569.416	511.213	171.910	228.163	121.787	100	107.311	588.427	427.521
T_6 (K)	293	308.6	300.6	293	293	293	293	293	313	293	293	293
T_7 (K)	293.6	309.2	301.1	293.3	293.4	293.5	293.5	293.5	313.4	293.6	293.5	293.4
$Z_{compressibility}$ *(-)*	0.7992	0.7828	0.8037	0.8129	0.8164	0.7858	0.7719	0.8028	0.7762	0.7995	0.7919	0.8048

Table 5-8 ORC-RIT model optimization results for all working fluids

Parameter	Isobutane	n-pentane	R123	R134a	R152a	R236ea
α_4 (deg)	81.83	81.3	82	80.98	82	82
β_4 (deg)	26.55	45.84	-33.03	-29.75	-36.47	34.32
$\beta_{4,blade}$ (deg)	49.74	48.4	0	0	0	54.32
$\beta_{5,hub}$ (deg)	-58.56	-56.5	-59.9	-52.8	-63.53	-56.36
$\beta_{5,tip}$ (deg)	-64.3	-62.09	-71.4	-67.63	-68.58	-68.14
U_4 (m/s)	183.4	230.3	177.9	101.2	132.5	143.1
$U_{5,tip}$ (m/s)	80.25	102	109.9	56.9	54.3	84.43
C_2 (m/s)	159.7	216.2	128	72.88	94.58	127.7
C_4 (m/s)	199.6	276.9	164.6	93.97	121.3	159.6
C_5 (m/s)	38.62	54.05	36.99	23.42	21.3	33.88
W_4 (m/s)	31.7	60.09	27.28	16.98	20.72	26.61
$W_{5,hub}$ (m/s)	74.05	97.91	73.76	38.73	47.78	61.16
$W_{5,tip}$ (m/s)	89.06	115.5	115.9	61.53	58.32	90.98
Ma_4 (-)	1.1077	1.678	1.4584	0.6841	0.7927	1.248
$Ma_{4,rel}$ (-)	0.1584	0.3031	0.2048	0.1174	0.115	0.2081
$Ma_{5tip,rel}$ (-)	0.4323	0.5692	0.8533	0.419	0.3104	0.6935
d_{max} (m)	0.07171	0.09151	0.06286	0.04758	0.08388	0.05403
d_1 (m)	0.06764	0.08795	0.085854	0.04172	0.07885	0.04958
d_2 (m)	0.06356	0.08439	0.05421	0.03586	0.07383	0.04514
d_3 (m)	0.05143	0.06692	0.04309	0.02896	0.05799	0.03752
d_4 (m)	0.05105	0.06663	0.04248	0.02787	0.05756	0.03683
$d_{5,tip}$ (m)	0.0201	0.0267	0.02145	0.0126	0.02124	0.01795
$d_{5,hub}/d_{5,tip}$ (-)	0.7873	0.8001	0.5808	0.5421	0.7877	0.6031
b_4 (m)	0.000667	0.000492	0.001126	0.00177	0.000788	0.00130
b_5 (m)	0.002376	0.002947	0.005499	0.00358	0.002505	0.00431
$r_{5,tip}/r_4$ (-)	0.4376	0.4426	0.6176	0.562	0.4099	0.5902
Z_{rotor} (-)	21	20	21	19	21	21
Z_{nozzle} (-)	29	28	29	30	29	29
R (-)	0.4712	0.4138	0.5558	0.5603	0.5531	0.4549
N_s (-)	0.1679	0.1559	0.3417	0.3641	0.1521	0.3155
υ (-)	0.5914	0.5491	0.63	0.6613	0.6332	0.5976
$Z_{compressibility}$ (-)	0.7997	0.7829	0.7977	0.8077	0.8164	0.7964
$\eta_{stage,ts}$ (%)	75.48	71.4	72.72	80.4	72.88	77.81
$\eta_{,stage,tt}$ (%)	76.57	72.49	73.87	82.3	73.66	79.41
$W_{turbine}$ (W)	1455	2011	2094	772.8	834.6	1748
T_6 (K)	293	308.6	300.6	293	293	293
$\eta_{thermal,cycle}$ (%)	7.93	11.16	11.67	4.194	4.573	9.67
W_{net} (W)	1269	1786	1866	671	729.1	1547
Q_{in} (W)	16000	16000	15993	16000	15943	15999
Q_{out} (W)	14588	14010	13913	15246	15137	14270

Table 5-8 (*Continued*)

Parameter	R236fa	R245fa	R365mfc	R1233zd	R1234yf	R1234ze
α_4 (deg)	81.1	79.09	82	79.81	82	81.52
β_4 (deg)	-32.89	16.08	19.09	-13.08	-31.98	-30.2
$\beta_{4,blade}$ (deg)	0	36.08	39.09	0	0	0
$\beta_{5,hub}$ (deg)	-57.4	-44.33	-61.3	-50.73	-60.67	-61.43
$\beta_{5,tip}$ (deg)	-70.76	-55.88	-71.74	-58.74	-68.49	-72.09
U_4 (m/s)	138.5	169.7	175.1	182.44	91.19	119.4
$U_{5,tip}$ (m/s)	81.72	85.16	107.6	93.15	45.58	69.68
C_2 (m/s)	97.15	148.4	149.2	132.7	67.89	85.1
C_4 (m/s)	127.3	183	185.8	177.9	84.81	111.1
C_5 (m/s)	28.52	57.71	35.51	56.55	17.96	22.51
W_4 (m/s)	23.45	36.04	27.23	49.77	13.68	19.96
$W_{5,hub}$ (m/s)	52.94	80.67	73.95	89.33	36.37	47.07
$W_{5,tip}$ (m/s)	86.55	102.9	113.3	109	48.99	73.22
Ma_4 (-)	1.034	1.32	1.354	1.259	0.6454	0.8049
$Ma_{4,rel}$ (-)	0.1905	0.26	0.1986	0.3522	0.1041	0.1374
$Ma_{5tip,rel}$ (-)	0.6753	0.7312	0.8022	0.7572	0.3627	0.5159
d_{max} (m)	0.0547	0.05808	0.06103	0.07244	0.05174	0.05175
d_1 (m)	0.04992	0.05388	0.05696	0.06821	0.0469	0.04646
d_2 (m)	0.04514	0.04968	0.05289	0.06397	0.04206	0.04116
d_3 (m)	0.03507	0.04126	0.04343	0.0494	0.03459	0.03293
d_4 (m)	0.03431	0.04066	0.04286	0.04888	0.03393	0.0320
$d_{5,tip}$ (m)	0.01631	0.0204	0.02175	0.02198	0.01465	0.01538
$d_{5,hub}/d_{5,tip}$ (-)	0.5457	0.6619	0.6027	0.7423	0.7014	0.5933
b_4 (m)	0.00126	0.000819	0.001049	0.0005	0.00121	0.001472
b_5 (m)	0.004599	0.003449	0.005233	0.00322	0.00253	0.003805
$r_{5,tip}/r_4$ (-)	0.5902	0.5017	0.6146	0.5107	0.4999	0.58374
Z_{rotor} (-)	19	17	21	18	21	20
Z_{nozzle} (-)	26	24	29	24	29	28
R (-)	0.563	0.5061	0.4824	0.5448	0.5492	0.5454
N_s (-)	0.3475	0.3075	0.3033	0.2786	0.2512	0.3234
υ (-)	0.6462	0.6048	0.5965	0.6219	0.6572	0.6567
$Z_{compressibility}$ (-)	0.7814	0.7995	0.7767	0.7914	0.7807	0.8017
$\eta_{,stage,ts}$ (%)	76.62	77.6	74.61	72.7	79.16	78.72
$\eta_{,stage,tt}$ (%)	78.01	80.88	75.66	75.32	80.48	79.94
$W_{turbine}$ (W)	1531	1985	1945	2027	472.8	1069
T_6 (K)	293	293	313	293	293	293
$\eta_{thermal,cycle}$ (%)	8.407	11.06	10.8	11.27	3.992	5.866
W_{net} (W)	1341	1769	1729	1803	402.9	928.4
Q_{in} (W)	15956	15999	16000	16000	10094	15828
Q_{out} (W)	14460	13967	14081	13934	9644	14795

From the results in TablesTable 5-5 and 5-6, the optimized $P_{t,1}$ and $T_{t,1}$ are almost the same for both models. Moreover, with $P_{t,1}< 10^6$ (Pa) constraint, the obtained $T_{t,1}$ for all fluids in both models is very close to the saturation temperature at 10bar in order to maximize $\eta_{thermal,cycle}$ within specified constraints. It is clear from Table 5-6 that majority of fluids have ψ values in excess of unity leading to highly loaded and small turbine, while for the rest of fluids such value is very close to the optimum of 0.918 as suggested by Baines 2003. The values of φ are in the range of 0.157 to 0.239 which is the high efficiency region as illustrated in Figure 5-7 (a). Majority of fluids have φ value very close to the optimum of 0.215 as suggested by Baines 2003 and Dixon *et al*. 2010. Furthermore, almost all the investigated fluids have α_5 values very close to zero to minimize the exit kinetic loss and hence higher isentropic efficiency.

From the optimization results in Tables Table 5-7 and 5-8 it is clear that all of the investigated fluids had very strong real-gas behaviour at the turbine inlet as their $Z_{compressibility}$ was far from unity and confirms the rational of solving algorithm based on the real-gas formulation. Moreover, the values of N_s and υ varied between 0.152 to 0.3641 and 0.549 to 0.661 respectively. For majority of fluids these values are in the optimal range of turbine efficiency as suggested by the generalized performance correlation charts for N_s and υ reported in (Baines 2003, Aungier 2006, Dixon *et al.* 2010). This confirms the validity of the optimization approach developed in this thesis to achieve highly efficient turbines. Furthermore, the values of N_s in Table 5-8 justify the exclusion of the diffuser from the analysis. Following the discussion in (Moustapha *et al.* 2003), for N_s values significantly lower than 0.7, which is the case of present thesis, the gain of using the diffuser is much less and implementation of the diffuser requires an economic analysis which is beyond the scope of this thesis. Among the investigated fluids, hydrocarbons led to larger turbine sizes due to their larger enthalpy drop across the turbine. Figure 5-18

presents the contribution of the rotor aerodynamic losses at the optimized conditions obtained by the ORC-RIT model. The proportion of the losses is almost similar for all fluids with the tip clearance and secondary losses having the highest contribution, varying from 42% to 59% and 19% to 39% respectively. The large tip clearance loss was due to the large density (small specific volume) of organic fluids at the turbine inlet and due to the low mass flow rate which resulted in small inlet blade height (b_4). At such conditions the running clearance became a large portion of the inlet blade height which explains the large tip clearance contribution. Moreover, the large passage turning obtained from high $\beta_{4,blade}$ and $\beta_{5,tip}$ (refer to Table 5-8) is responsible for the considerable contribution of secondary loss in reducing the turbine efficiency. The thermodynamic properties and ORC state points obtained by the ORC-RIT model at optimized conditions for all investigated fluids are presented on the temperature–entropy diagram in Figure 5-19.

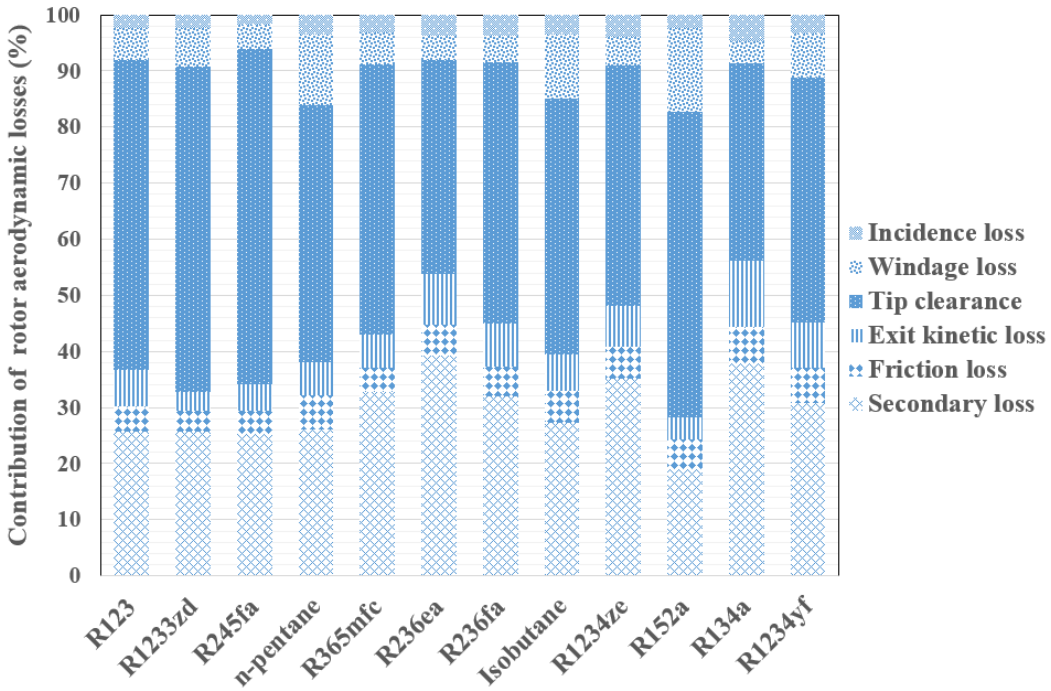

Figure 5-18 Contribution of the rotor aerodynamic losses for all fluids at the optimized conditions

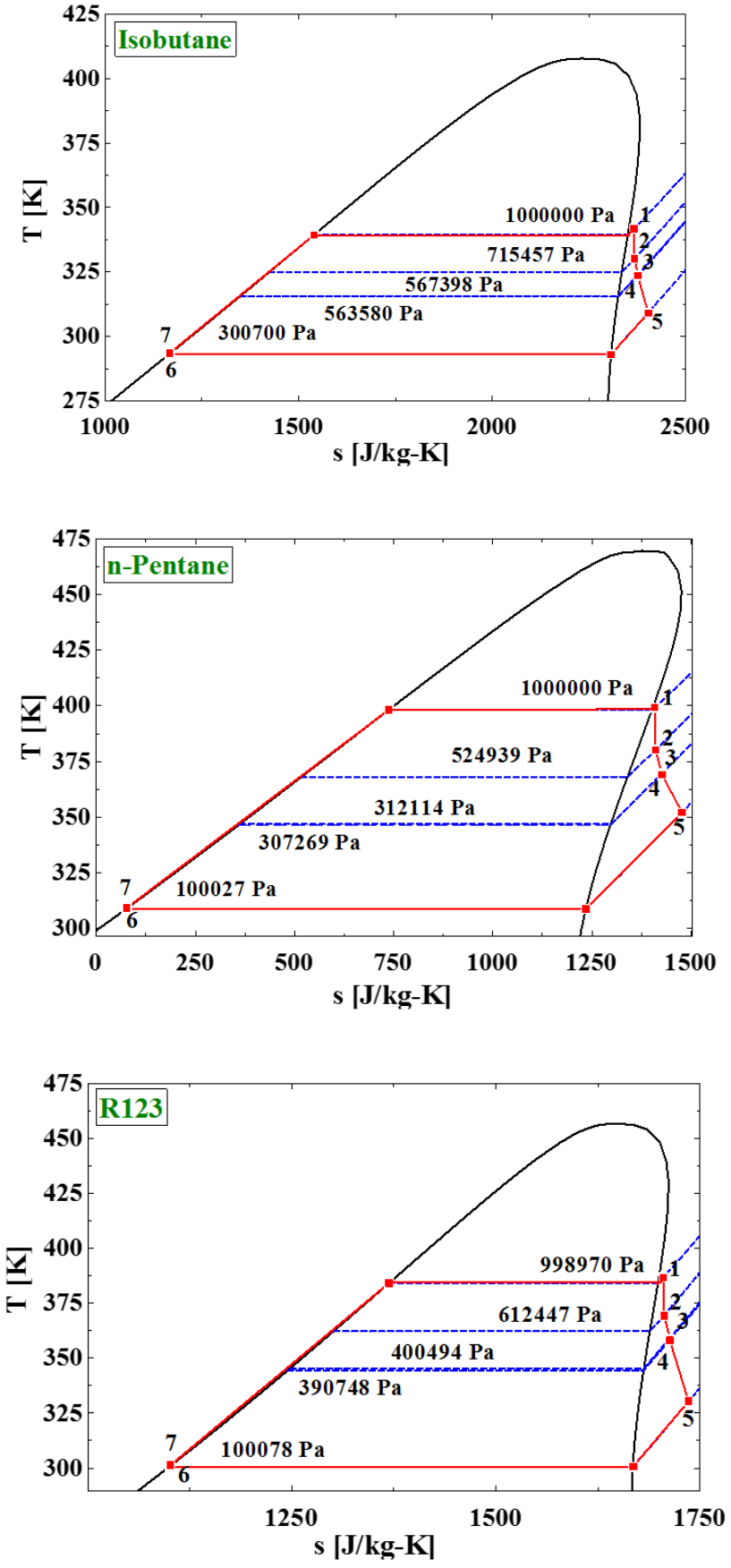

Figure 5-19 ORC state points obtained by the ORC-RIT model at optimized conditions for 12 fluids

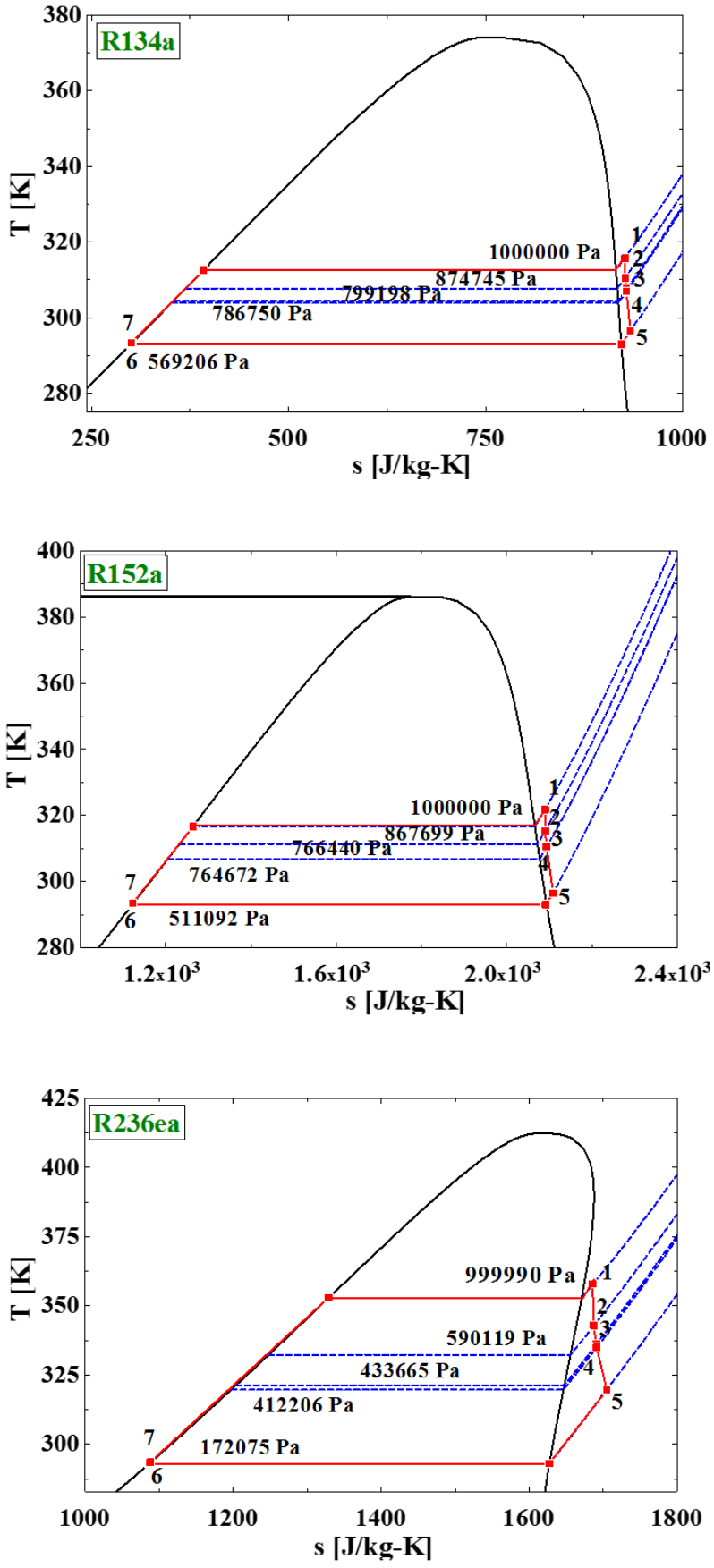

Figure 5-19 (*Continued*)

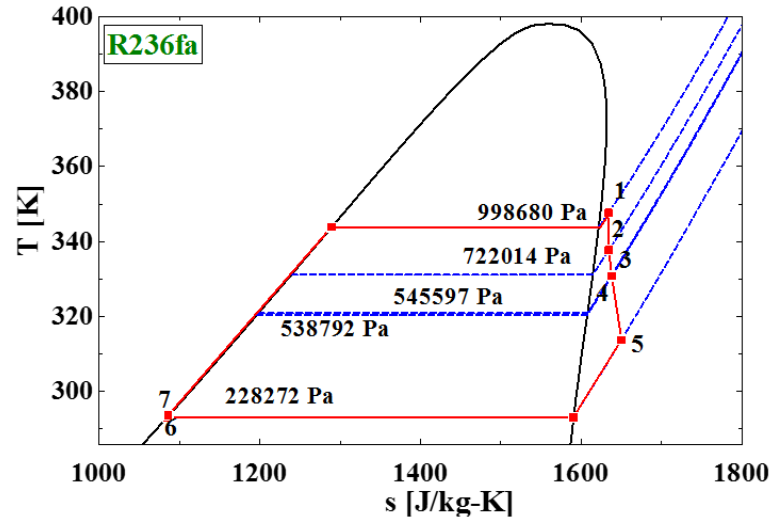

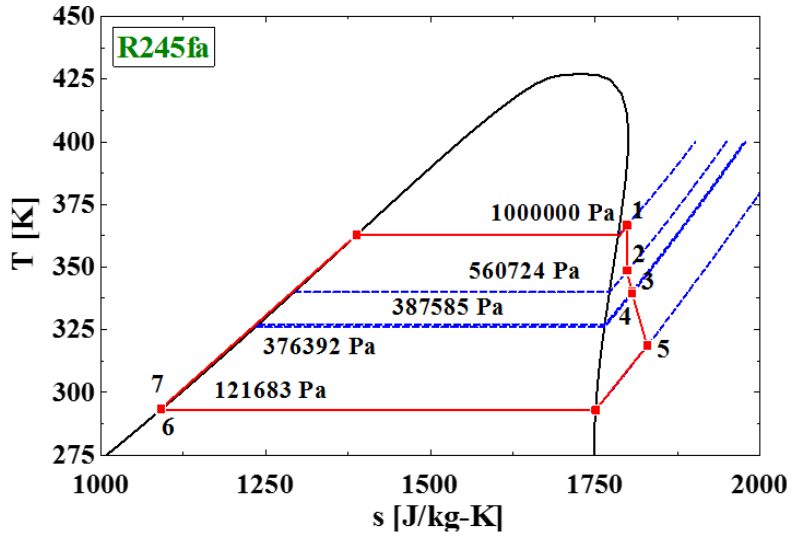

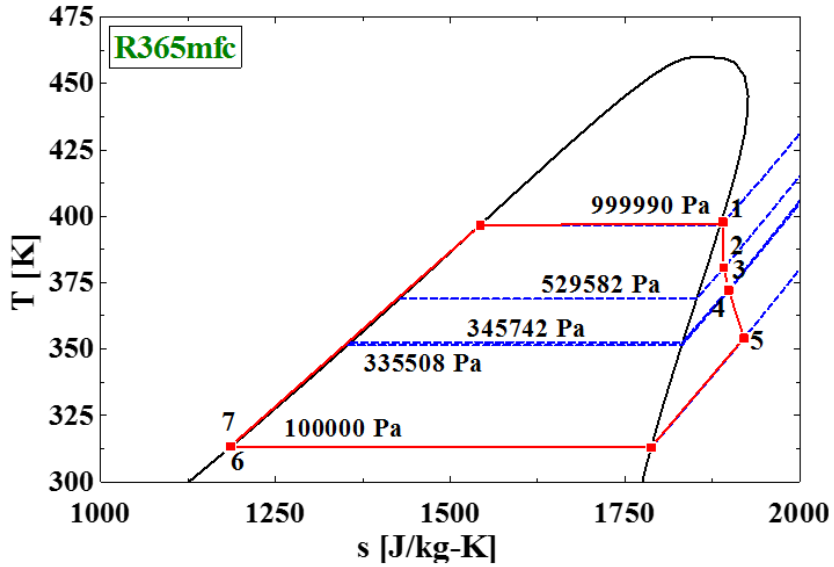

Figure 5-19 (*Continued*)

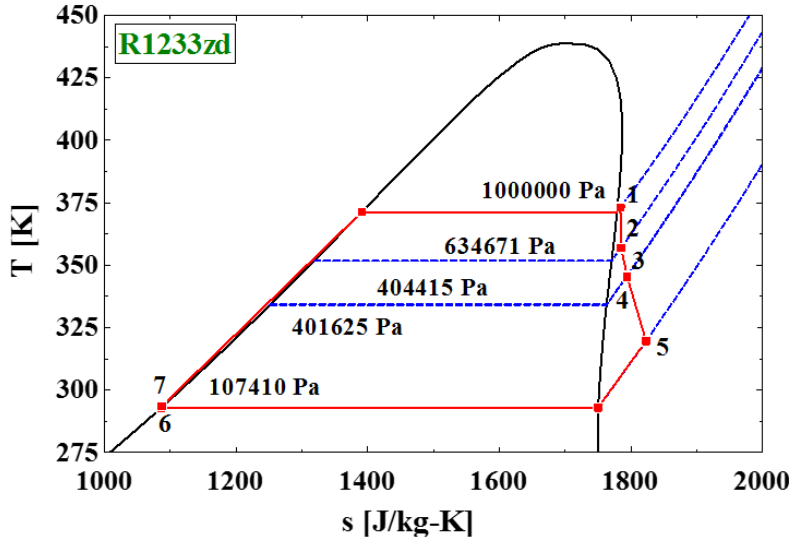

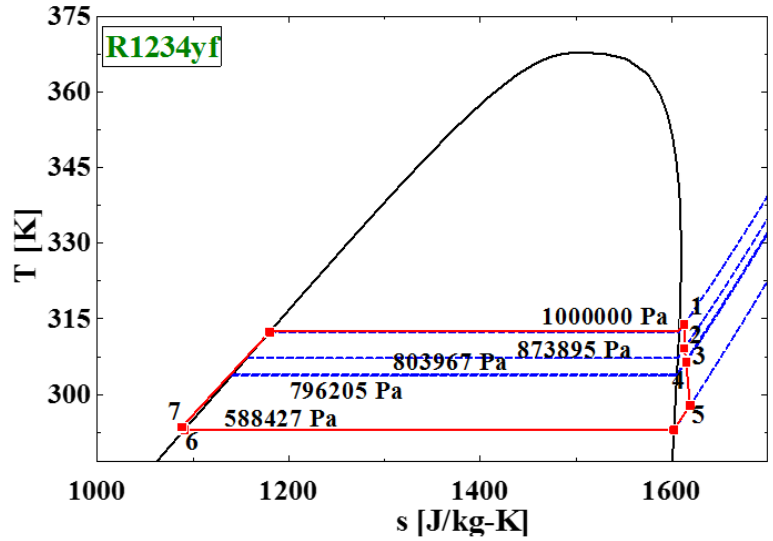

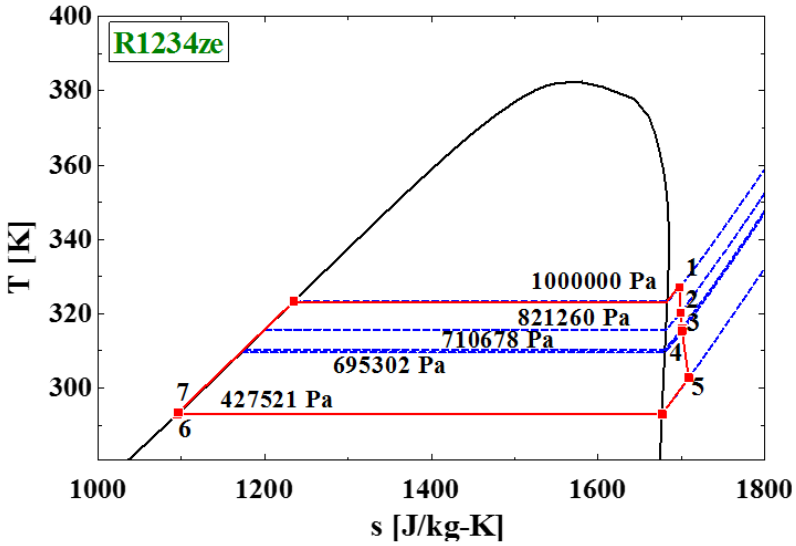

Figure 5-19 (*Continued*)

Figure 5-20 summarizes the optimized $\eta_{thermal,cycle}$ for both ORC standalone and ORC-RIT models (extracted from TablesTable 5-7 and 5-8) for all investigated fluids. For each fluid there is a difference between optimized $\eta_{thermal,cycle}$ with each model and the difference varies from one to another. Clearly, the ORC standalone model over-predicts $\eta_{thermal,cycle}$ for majority of fluids by a maximum value of 1.4% for n-pentane. This is due to the fact that turbine efficiency was selected arbitrarily without assuring that the RIT is capable of achieving such efficiency level under the imposed cycle operating conditions. Optimization by the ORC standalone model selects ER_{ts} as high as possible (subjected to the imposed constraints) while overlooking the resulting turbine losses. R123 exhibits the highest $\eta_{thermal,cycle}$ of 12.9% and 11.67% with standalone and integrated models respectively. Besides, the ranking order of the working fluids (from the highest $\eta_{thermal,cycle}$ to lowest) can vary depending on the operating conditions, constraints and type of working fluids being considered.

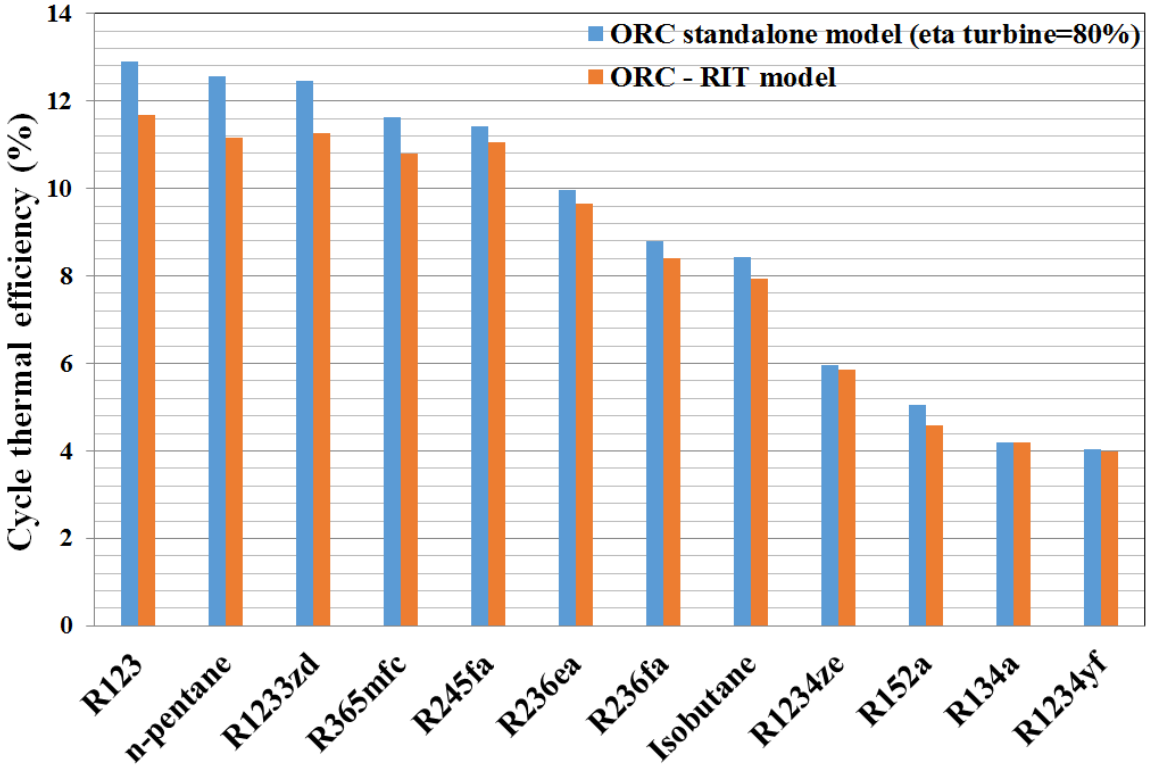

Figure 5-20 Optimized $\eta_{thermal,cycle}$ for both models and for all 12 working fluids

There exist variations in the ranking order of R1233zd, n-pentane, R365mfc and R245fa working fluids between the two models. Consequently, the ORC standalone model can bring unfairness to the analysis and reduce the accuracy and reliability of the results if arbitrary $\eta_{stage,ts}$ is selected and also result in critical errors while selecting the most efficient working fluids.

One of the future work recommended in chapter seven is the experimental testing of the ORC which required selection of the best fluid in terms of $\eta_{thermal,cycle}$ from the optimization results obtained with ORC-RIT model (Table 5-8). Among the top four working fluids, R123 could not be selected due to its complete phase out from early January 2015 in the UK. Communications with major manufacturers and sellers of the refrigerants in the UK including Dean & wood, HRP, A-Gas, Dupont, BOC and many more revealed that R1233zd was newly introduced refrigerants (at that time) and its availability and cost was the main reason for not selecting it. Due to the health and safety regulations, n-pentane could not be selected due to its high flammability characteristic (Table 5-1) and requirements of ATEX and costly equipment and thus could not be used. Therefore, R245fa with no flammability, reasonable price and competitive $\eta_{thermal,cycle}$ was selected to further analysed using CFD simulations.

5.9. Optimization of the dual-stage transonic RIT

The rotor inlet Mach numbers (Ma_4) of Table 5-8 reveal that all of the investigated fluids except for R134a, R152a, R1234yf and R1234ze have Mach numbers in excess of unity with supersonic expansion at nozzle outlet and rotor inlet. Such characteristics is due to the requirements of high expansion ratios to maximize $\eta_{thermal,cycle}$ and also the low speed of sound for highly dense and high molecular mass organic fluids (i.e. for R245fa sound speed is about 1/3 of air at 100˚C). Therefore, the organic fluid easily becomes supersonic with chocked flow at nozzle throat and at such conditions (Ma_4>1) the

formation of shock waves and the consequent losses become inevitable and can result in strong unsteady interaction between nozzle and rotor and substantial deterioration of turbine isentropic efficiency. On the other hand, depending on the value of Ma_4 the converging nozzle may be unable to accelerate the flow velocity to supersonic levels (requires further CFD analysis) and hence utilization of converging-diverging nozzle becomes unavoidable. The latter itself requires very tight tolerances and costly manufacturing process for achieving accurate throat area and also has very poor off-design performance (Baines 2003). In general, either converging or converging-diverging nozzle is used, as long the flow regime is supersonic at nozzle outlet (rotor inlet) the turbine efficiency will be deteriorated and complex transient fluid dynamics analysis will be needed to investigate the unsteady interaction of nozzle and rotor blades caused by the propagation of oblique shock waves. Therefore, in order to alleviate such drawbacks, a novel dual-stage transonic RIT configuration with a vane-less return channel in between the two stages was proposed. Such configuration was advantageous as by limiting the Ma_4 to transonic flow regime better turbine efficiency can be achieved with simplified fluid dynamics. Figure 5-21 illustrates the schematic of the dual-stage organic RIT meridional channel. The rotor exit total operating conditions ($T_{t,5}$, $P_{t,5}$) of the 1st stage was set as the nozzle inlet operating conditions of the 2nd stage (assuming negligible losses in the return channel). For the 2nd stage the mass flow rate and rotational speed are the same as the 1st stage since they have a common rotating shaft with negligible external leakage. Similar to section 5.8.3, the ORC-RIT model coupled with the GA optimization technique with similar control operators and all the constraints of section 5.6.1 in addition of $Ma_4<0.96$ were used to maximize $\eta_{thermal,cycle}$ using R245fa as the working fluid. Table 5-9 presents the optimized input parameters of both stages while the optimization results are summarized in Table 5-10 .

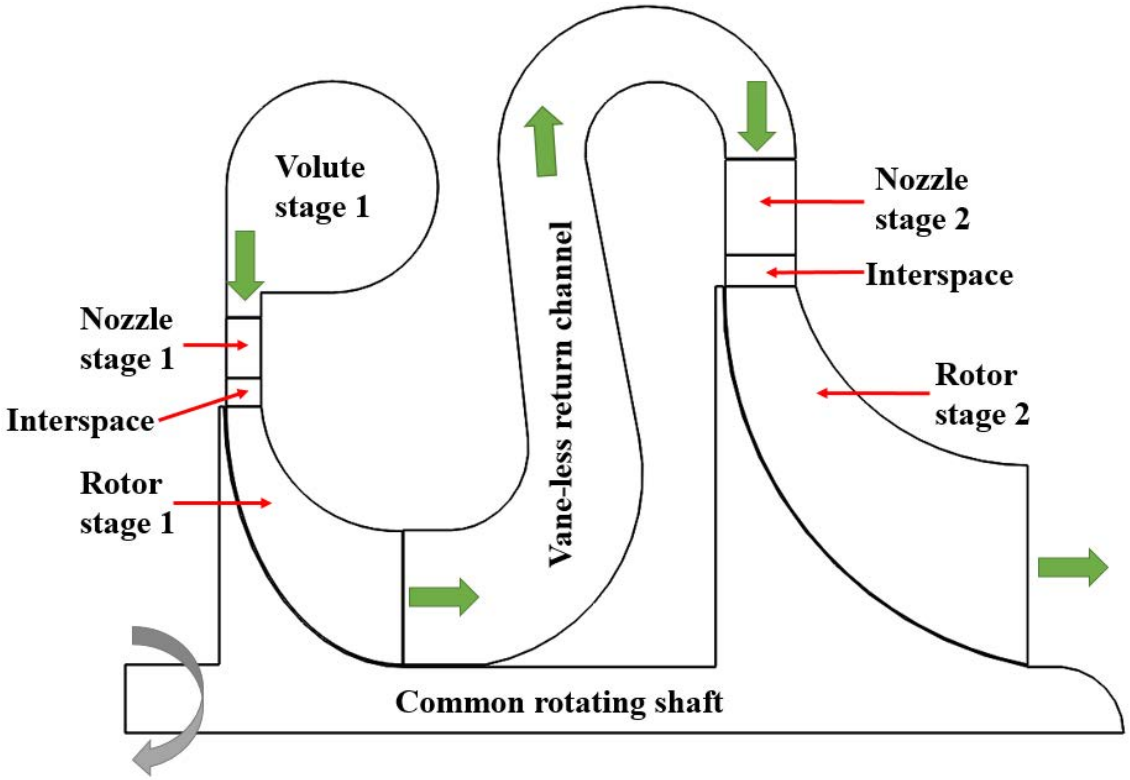

Figure 5-21 Schematic of the dual-stage organic RIT (meridional view)

Table 5-9 Optimized input parameters of the dual-stage RIT obtained by the ORC-RIT model for R245fa

Parameter	Stage one	Stage two
$T_{t,1}$ (K)	362.8	342.8
$P_{t,1}$ (kPa)	1000	414.479
$\Delta T_{superheat}$ (K)	3.88	0
ER_{ts} (-)	2.434	3.41
$\dot{m}_{wf}$ (kg/s)	0.06499	0.06499
φ (-)	0.169	0.1963
ψ (-)	1.229	0.8466
ω (rpm)	60078.24	60078.24
ξ (-)	1.03	0.6078
α_5 (-)	1.191	-0.978
$r_{5,hub}/r_4$ (-)	0.3884	0.3104
r_2/r_3 (-)	1.284	1.244

Table 5-10 Optimization results for the dual-stage RIT obtained by the ORC-RIT model for R245fa

Parameter	Stage one	Stage two	Overall
α_4 (deg)	81.95	81.98	-
β_4 (deg)	42.22	-39.45	-
$\beta_{4,blade}$ (deg)	46.03	0	-
$\beta_{5,hub}$ (deg)	-66.49	-57.69	-
$\beta_{5,tip}$ (deg)	-74.4	-69.85	-
U_4 (m/s)	103.3	152.9	-
$U_{5,tip}$ (m/s)	62.55	81.78	-
C_2 (m/s)	97.6	102.5	-
C_4 (m/s)	128.4	130.8	-
C_5 (m/s)	17.47	30.01	-
W_4 (m/s)	29.86	29.63	-
$W_{5,hub}$ (m/s)	43.78	56.14	-
$W_{5,tip}$ (m/s)	64.94	87.11	-
Ma_4 (-)	0.9512	0.9338	-
$Ma_{4,rel}$ (-)	0.2211	0.2116	-
$Ma_{5tip,rel}$ (-)	0.4689	0.6205	-
d_{max} (m)	0.05183	0.07546	-
d_1 (m)	0.04741	0.06859	-
d_2 (m)	0.04299	0.06171	-
d_3 (m)	0.03348	0.04961	-
d_4 (m)	0.03285	0.04859	-
$d_{5,tip}$ (m)	0.01988	0.026	-
$d_{5,hub}/d_{5,tip}$ (-)	0.6417	0.5802	-
b_4 (m)	0.001135	0.001853	-
b_5 (m)	0.003562	0.005456	-
$r_{5,tip}/r_4$ (-)	0.6052	0.535	-
Z_{rotor} (-)	21	21	-
Z_{nozzle} (-)	23	24	-
R (-)	0.3832	0.5904	-
N_s (-)	0.2428	0.3435	-
υ (-)	0.567	0.709	-
$T_{t,5}$ (K)	342.8	315.4	-
$P_{t,5}$ (kPa)	414.479	124.497	-
T_5 (K)	342.5	314.9	-
P_5 (kPa)	411.194	121548	-
$Z_{compressibility}$ (-)	0.7995	0.902	-
$\eta_{stage,ts}$ (%)	78.96	85.09	-
$\eta_{,stage,tt}$ (%)	79.73	86.76	-
$W_{turbine}$ (W)	853.1	1286	2139.1
T_6 (K)	-	-	293
$\eta_{thermal,cycle}$ (%)	-	-	11.94
W_{net} (W)	-	-	1911
Q_{in} (W)	-	-	16000
Q_{out} (W)	-	-	13951

Because the temperature and pressure of the working fluid in the 2nd stage were lower than that of 1st stage, the flow velocity grew more slowly than the sound speed and hence there was more room to expand in the 2nd stage before reaching the imposed constraint on Ma_4. Clearly there exists about 7.95% relative improvement in $\eta_{thermal,cycle}$ when comparing the results of $\eta_{thermal,cycle}$ in Tables Table 5-8 and 5-10 for R245fa. Considering that the maximum achievable $\eta_{thermal,cycle}$ between the heat source temperature of 93.7˚C and heat sink temperature of 20˚C is 20.09% (based on Carnot ideal cycle), such improvement in $\eta_{thermal,cycle}$ is equivalent to about 4.4% increase when compared to maximum achievable $\eta_{thermal,cycle}$. Therefore, such novel dual-stage transonic organic RIT configuration is advantageous to both alleviate the complex fluid dynamics and degradation of turbine efficiency due to shock losses and also increase $\eta_{thermal,cycle}$ for maximum utilization of waste heat.

5.10. Correlations for optimum isentropic efficiency and size of single-stage organic RIT using regression analysis

The proposed methodology for integrated modelling of ORC with organic RIT based on real-gas formulation and coupled with GA optimization proved to be effective for accurate performance estimation of the ORC. Such approach was employed to obtain new correlations based on linear regression analysis to estimate the maximum turbine isentropic efficiency ($\eta_{stage,ts}$) and the corresponding optimum turbine size (d_4 and d_{max}) without performing the complete turbine modelling process. Instead, using only few non-dimensional design parameters, $\eta_{stage,ts}$ can be estimated with good accuracy based on the imposed operating conditions and explicitly from the turbine losses.

To achieve such correlations, the ORC-RIT model with the same inputs and ranges as in sections 5.3 and 5.4 and GA control operators and constraints (except for Q_{in} to extend the generality of the correlations for small-scale applications) as in sections 5.6.1

and 5.8.1 were used to maximize $\eta_{stage,ts}$ (OF_2). Then to correlate the variation of the optimized $\eta_{stage,ts}$ with non-dimensional parameters following specifications for the main turbine and cycle design parameters were set to cover a wide range of designs.

$$T_{t,1} \in (323 : T_{upper} : 10) \quad \text{Equation 5-32}$$

$$\psi \in (0.8 : 1.5 : 0.1) \quad \text{Equation 5-33}$$

$$\varphi \in (0.15 : 0.5 : 0.05) \quad \text{Equation 5-34}$$

Where the first and second terms are the lower and upper boundaries and third term is the step of variation for each parameter. T_{upper} was selected to be close to the critical temperature of each working fluid. Every possible combination of the above three parameters were created for all the fluids in Table 5-1 and the ORC-RIT model were used to optimize the rest of inputs using GA for maximum $\eta_{stage,ts}$. The results were 1797 optimized cases that were used in the linear regression analysis to obtain the correlations.

Prior of obtaining the correlations, to include the effect of compressibility factor into the $\eta_{stage,ts}$ correlation, another non-dimensional parameter called volumetric expansion ratio (VR) introduced by (Macchi *et al.* 1981) was also included in the model (as an output) to address the effect Mach number. VR explicitly correlates the degradation of turbine efficiency due to the high Mach numbers (Macchi *et al.* 1981). In other words, VR accounts for the compressibility effect in a more generalized way than Mach number and is defined as following:

$$VR = \frac{Q_5}{Q_1} \quad \text{Equation 5-35}$$

Its value can be estimated from the cycle operating conditions (based on the desired requirements) and without the need for completing the turbine design procedure.

Moreover, shape factor (*SF*) was also included in the model (as an output) to account for the size effects of small-scale turbines (i.e. larger relative thickness and clearance compared to large turbines) when obtaining the correlations for the turbine size.

$$SF = \frac{Q_5^{0.5}}{\Delta h_{ideal}^{0.25}} \quad \text{Equation 5-36}$$

Consequently, EES software was employed to conduct the linear regression analysis based on all the 1797 optimized cases and the results are presented in Equations 5-37 to 5-39, Table 5-11 and Figure 5-22.

$$\eta_{stage,ts} = 0.9211 - 0.4391\varphi - 0.02966VR + 0.3471Q_5 + 0.01582ER_{ts} \quad \text{Equation 5-37}$$

$$d_4 = 0.08864 + 1.722SF - 68.56SF^2 + 0.7159Q_5 - 0.9986Q_5^2 - 0.00001824\omega + 1.245 \times 10^{-9}\omega^2 \quad \text{Equation 5-38}$$

$$d_{max} = 0.1146 + 2.468SF + 4.411SF^2 + 0.7707Q_5 - 2.009Q_5^2 - 0.00002232\omega + 1.479 \times 10^{-9}\omega^2 \quad \text{Equation 5-39}$$

Table 5-11 Regression analysis statistics

Parameter	R^2 (%)	RMS error	Bias error	Number of points
$\eta_{stage,ts}$	92.52	1.3656e-2	-1.8309e-19	1797
d_4	96.38	4.3245e-3	4.7289e-20	1797
d_{max}	97.29	6.2172e-3	-7.4579e-20	1797

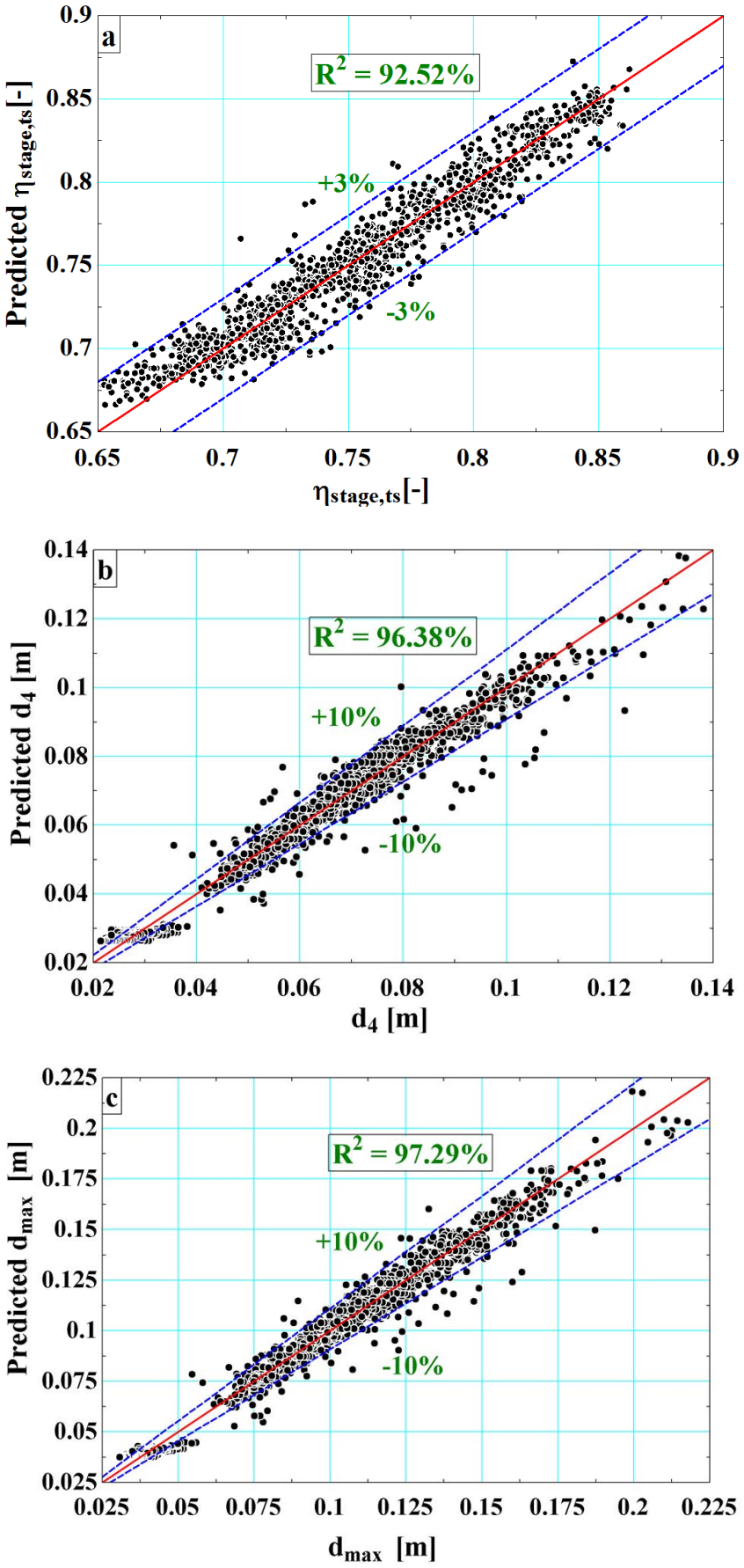

Figure 5-22 Linear regression analysis results (a) optimized $\eta_{stage,ts}$ (b) d_4 (c) d_{max}

According to Table 5-11, the R^2 values for d_4 and d_{max} are higher than $\eta_{stage,ts}$ (as expected since 2nd order polynomial were used for them while for $\eta_{stage,ts}$ 1st order polynomial was used for simplicity), though, majority of the optimized points laid in the region of $\pm$3% of the ideal line (R^2=100%) as it is depicted in Figure 5-22(a). Therefore, Equation 5-37 can estimate $\eta_{stage,ts}$ with good accuracy only by knowing Q_5, ER_{ts}, VR and φ where only the latter is a turbine design parameter while the rest can be readily obtained from cycle operating conditions. φ can be assigned to the pre-defined range of 0.16 to 0.215 corresponding to the high efficiency region of the RIT based on generalized performance correlation charts (Baines 2003, Dixon *et al.* 2010) and also based on the optimization results obtained in section 5.8.3. Similarly, in the correlations for d_4 and d_{max} it is only the turbine rotational speed (ω) that need to be set based on the requirements of applications (i.e. inverter-rectifier frequency, generator speed or use of gearbox) while the rest can be achieved from the cycle operating conditions.

To highlight the effectiveness of the proposed correlations (especially correlation for $\eta_{stage,ts}$) same optimizations as in section 5.8.3 with the ORC standalone model were re-conducted but instead of setting the constant turbine efficiency of 80%, Equation 5-37 was used for estimation of $\eta_{stage,ts}$ and the optimization results are presented in Figure 5-23. As it is evident, the difference in $\eta_{thermal,cycle}$ between the ORC standalone model with correlation and the ORC-RIT model is reduced for almost all investigated fluids. The maximum difference in $\eta_{thermal,cycle}$ has reduced to 0.89% for R365mfc compared to the 1.4% for n-pentane when assuming $\eta_{stage,ts}$ =80%. More importantly, the ranking order of the fluids is exactly the same in the ORC standalone model with Equation 5-37 compared to the ORC-RIT model. Such results highlight the potential of the proposed correlations (especially for $\eta_{stage,ts}$) not only to eliminate any arbitrary assumption of $\eta_{stage,ts}$ but also to provide rationale basis for selection of suitable working fluid that could

have been wrongly selected if arbitrary $\eta_{stage,ts}$ had been used. Such correlations can be used in general optimization procedures of the ORC systems and combined cycle analysis to further improve the performance estimation and working fluid selection.

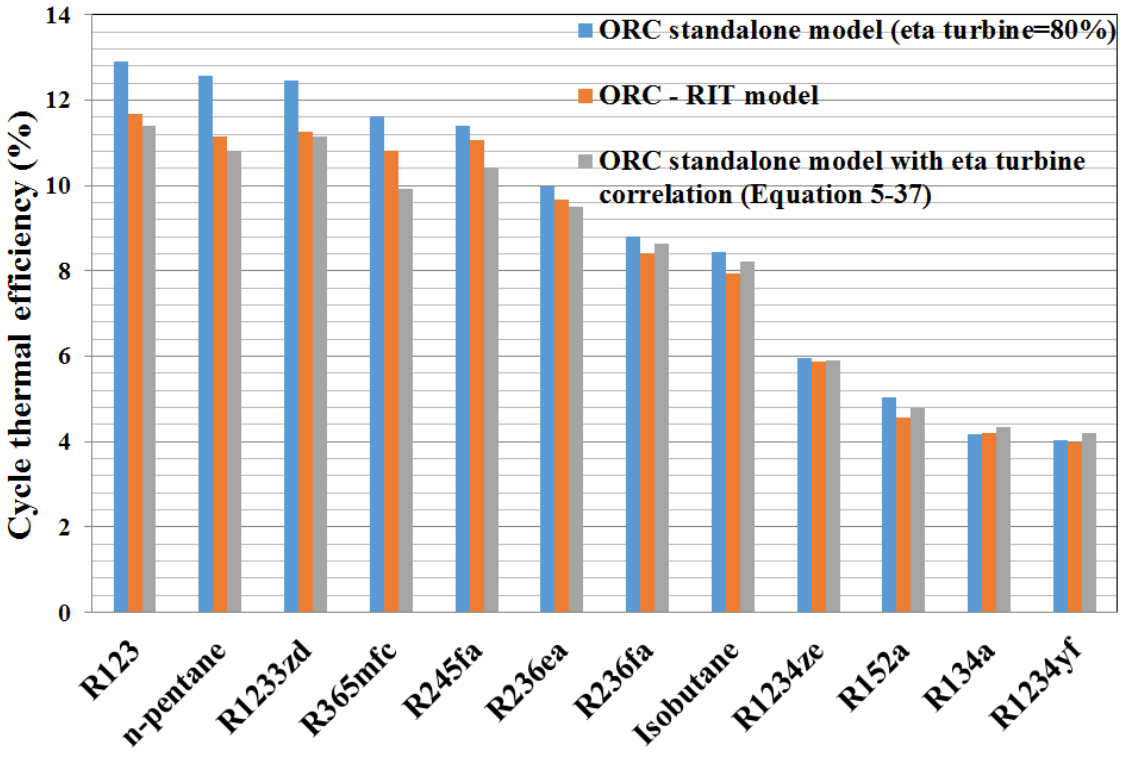

Figure 5-23 Comparison of the optimized $\eta_{thermal,cycle}$ obtained by the ORC standalone model, ORC-RIT model and ORC standalone model with the turbine correlation (Equation 5-37) for all fluids

5.11. Comparison of the optimized approach with literature

To highlight the potential of the proposed integrated optimized modelling approach (ORC-RIT model) described in previous sections, comparisons were conducted with the results of few available published studies that performed modelling of the organic RIT for ORC. To make fair comparisons the ranges of turbine and ORC input parameters (Table 5-2 and 5-3) were adjusted to cover the reported ranges in the published studies and details can be found in the published works of the author (Rahbar *et al.* 2015 [a], Rahbar *et al.* 2015 [b]). In the former study the turbine stage isentropic efficiency was defined as the *OF* while in the latter the ratio of the cycle net power out to the turbine

overall size was specified as the *OF*. Such *OF* is an amalgamated performance indicator that allows evaluating the relation between the ORC power capacity and the turbine overall size (Rahbar *et al.* 2015 [b]). Clearly, greater net power output from a smaller turbine is more desirable than less power from a larger turbine when considering the economic factors in the analysis (Rahbar *et al.* 2015 [b]). Both studies were conducted for the common fluids reported in the literature and only the final outcomes are presented for brevity. Figure 5-24 depicts the optimized turbine stage total-to-static efficiencies ($\eta_{stage,ts}$) obtained with proposed methodology of the present thesis and the results from the literature. It can be seen that the proposed constrained optimization methodology produced significantly higher $\eta_{stage,ts}$ compared to the other studies for a wide range of working fluids. It is possible to achieve a maximum of 14.7% higher turbine efficiency when comparing n-pentane efficiency in (Fiaschi *et al.* 2012) considering that both have similar turbine inlet total temperature of 420K. Figure 5-25 presents the results of optimizing the ratio of cycle net power output to the turbine overall size obtained by the proposed approach in the present thesis compared to the literature values. As it is evident, all of the optimization results obtained by the present thesis approach were superior for both isobutane and R245fa compared to (Clemente *et al.* 2013) with the maximum of 62.6% larger W_{net}/d_4 for isobutane. Similarly, assessing the performance of the working fluids with (Fiaschi *et al.* 2012) showed that employing the optimization methodology is advantageous for all fluids as presented in Figure 5-25.

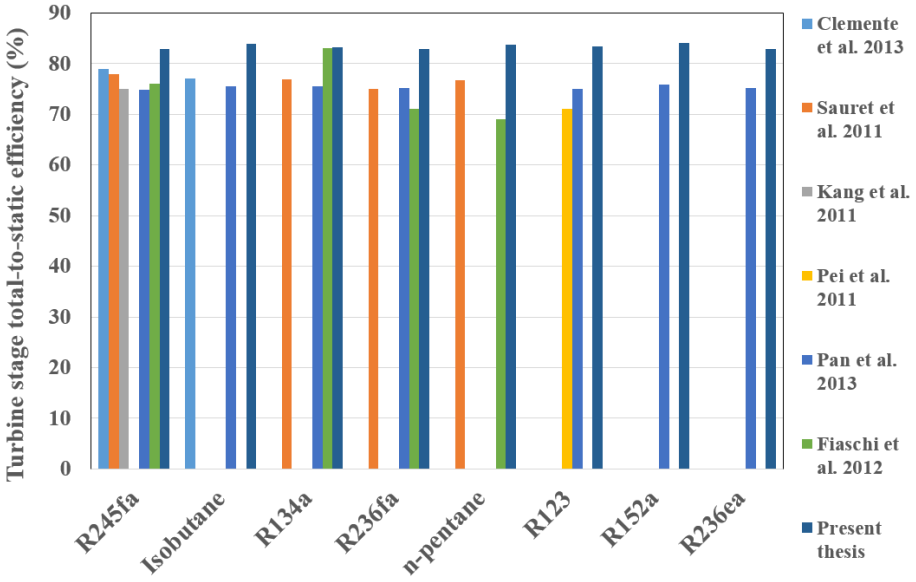

Figure 5-24 Comparison of the proposed approach in the thesis with literature (Rahbar *et al.* 2015 [a])

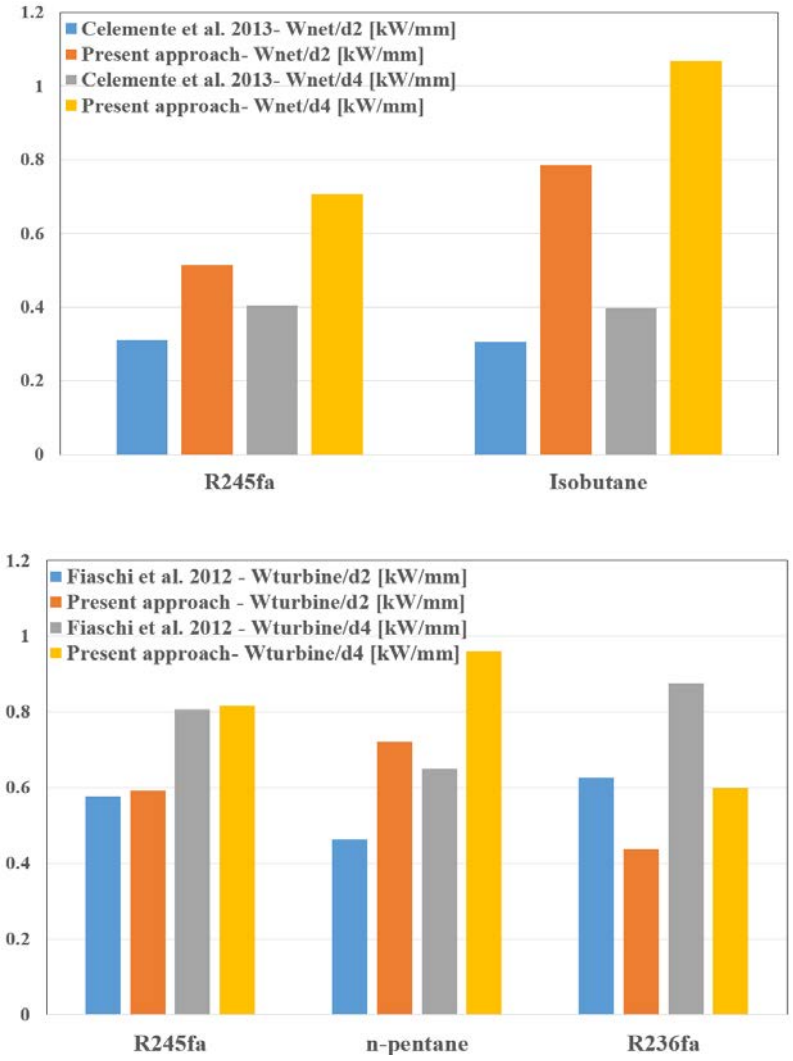

Figure 5-25 Comparison of the proposed approach in the thesis with literature (Rahbar *et al.* 2015 [b])

It is only for R236fa that about 29.9% and 31.7% larger $W_{turbine}/d_2$ and $W_{turbine}/d_4$ are achieved in (Fiaschi *et al.* 2012) respectively compared to the present thesis approach. Such results exhibit that, employing the RIT-ORC model integrated with the constrained GA optimization technique is very effective in obtaining high performance, compact and practically feasible ORC systems when compared to the other studies and highlights its advantages.

5.12. Summary and conclusions

In this chapter a novel one-dimensional approach was proposed for modelling of organic RIT. Such approach was based on mean-line modelling with real-gas formulation and GA optimization technique to not only capture the non-ideal behaviour of the organic fluids (for reliable performance estimation) but also effectively maximize the ORC thermal efficiency based on a wide range of input variables. A screening of 12 organic fluids (both hydrocarbons and refrigerants) was performed with the above approach to identify the working fluid that provides the maximum cycle thermal efficiency considering the imposed constraints. Among the investigated fluids R245fa was selected due to its competitive performance, safety, availability and cost. Moreover, to prevent the deterioration of the turbine efficiency at high expansion ratios (typical operating conditions of ORCs), a novel transonic dual-stage organic RIT with vane-less return channel and $Ma_4<1$ in both stages was proposed. Optimization was performed for both stages and the results will be used in the next chapter for further CFD analyses. Furthermore, to alleviate arbitrary assumption of the turbine efficiency while performing ORC analysis, three correlations (one for $\eta_{stage,ts}$ and two for turbine size) were proposed using linear regression analysis. The correlation for turbine efficiency can reliably estimate $\eta_{stage,ts}$ while assuring that similar ranking order of fluids will be achieved if the

ORC-RIT model is employed. Finally, the superiority of the proposed modelling technique based on GA optimization was highlighted by comparing the results with the literature studies.

CHAPTER 6

THREE-DIMENSIONAL CFD OPTIMIZATION OF THE DUAL-STAGE ORGANIC RIT

6.1. Introduction

The CFD analysis in chapter three required several trials in order to improve the turbine performance by variation of geometry parameters such as blade angle and thickness distributions, shape of leading edge and the number of rotor blades. Such manual modifications could be very time consuming and the outcome strongly depends on the expertise and intuition of the designer. Recalling the multi-level optimization in Figure 3-4, there is a need for an automated and computerized CFD (3-D) optimization analogous to the mean-line (1-D) optimization outlined in section 5.6 to efficiently and accurately search for the optimum turbine geometry. This chapter presents details of the 3-D CFD optimization procedure of the dual-stage organic RIT developed in chapter five using the Design Exploration^{TM}, the optimization module of ANSYS^{R15} software, to further optimize the performance. Moreover, CFD analyses were conducted for the volute and return channel to ensure good aerodynamic performance. Finally, the CFD simulation

of the complete dual-stage organic RIT was performed to create the full performance maps. Such maps are beneficial to determine the performance of the ORC under a range of off-design operating conditions.

6.2. Methodology for three-dimensional CFD optimization

Quantifying the influence of design variables on the performance of the turbine is an exhaustive procedure. ANSYS provides a so-called Design Exploration™ module that consists of Design of Experiments (DOE), Meta-models (surrogate models) and optimization algorithms in order to replace the lengthy, and time-consuming process of trial-and-error in the search for the optimum design. Generally speaking, optimization methods attempt to determine the design variables (X_i) that maximize or minimize an objective function (OF_l) as below:

$$OF_l = OF_l(U(X_i), X_i), \;\; i = 1 \; to \; N, \;\; l = 1 \; to \; M \qquad \text{Equation 6-1}$$

Where N is the number of design parameters and M is the number of objective functions. Moreover, $U(X_i)$ is the solution of the flow equations $R(U(X_i),X_i)=0$ and subject to n_A performance and n_G geometrical constrains as following (Van den Braembussche 2008):

$$A_j(U(X_i), X_i) \leq 0, \;\; j = 1, n_A \qquad \text{Equation 6-2}$$

$$G_k(X_i) \leq 0, \;\; k = 1, n_G \qquad \text{Equation 6-3}$$

The design variables are the parameters used to define the blade geometry while the objective function is the turbine performance. The goal of 3-D CFD optimization is to modify the blade geometry to maximize the turbine performance by minimizing the passage losses (i.e. entropy generation) and reducing the flow non-uniformity (i.e. the secondary flows). Such numerical optimization comprises of three main stages as following:

I. Choice of the independent design variables and their ranges (i.e. turbine geometry parameters) analogous to the mean-line input optimization parameters (Tables Table 5-2 and 5-3).

II. Definition of the objective function (*OF*) that quantifies the RIT performance together with the constraints (if any).

III. Search algorithm for finding the optimum combination of the design variables corresponding to the optimum *OF*.

Similar to the optimization strategy in chapter five, to avoid convergence to sub-optimal solutions (local optima), genetic algorithm (GA) was employed as the search mechanism to ensure convergence to global optimum. However, GA requires numerous function evaluations before reaching the global optimum. Simultaneously, the RANS solver itself (i.e. ANSYS CFX) requires substantial computational time depending on the mesh resolution (Table 3-3). Therefore, integration of the RANS solver with the GA optimization could be prohibitive in terms of computer effort and became ineffective for finding the global optimum. To improve such drawback, it is possible to utilize fast but approximate prediction methods such as Meta-models (approximation functions) which are then further verified and refined by the accurate RANS solver. Meta-model is a mathematical function which performs with a very low computational cost, the same task as the high fidelity tool such as CFD RANS solvers (Pasquale *et al.* 2013). Hence, it is possible to build a Meta-model of the original RANS solver that can be integrated in the optimization loop (i.e. GA) instead of the RANS solver. Consequently, the performance evaluation by the Meta-model is no more time-consuming and the number of function evaluations performed by the GA is no longer critical. The Meta-model not only needed to be fast but must also be accurate to drive the GA to the real optimum. The accuracy of

the Meta-model strongly depends on the sample points which the model is created from. Such samples are obtained by the actual CFD RANS solves and therefore are required to efficiently distribute over the design space and provide the maximum insight with minimum number of the sample points. For such goal design of experiment (DOE) was integrated with the 3-D CFD optimization algorithm to explore design space efficiently and build accurate Meta-model. Figure 6-1 details the overall 3-D CFD optimization procedure.

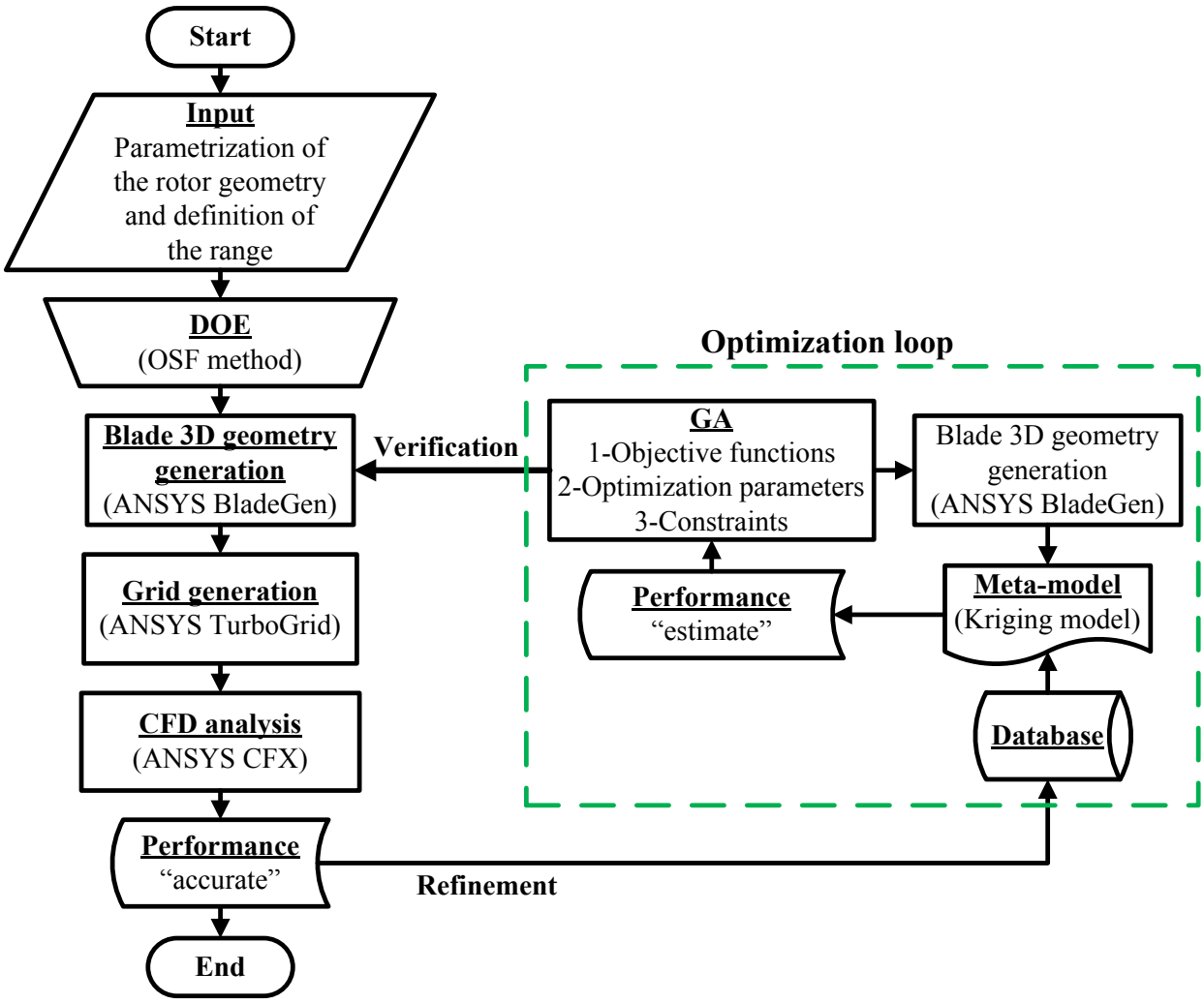

Figure 6-1 Flowchart of the 3-D CFD optimization

6.2.1. Design of experiments (DOE)

DOE is a technique used to scientifically determine the location of sampling points. DOE locates the sampling points such that the space of random input parameters is explored in the most efficient way, or obtains the required information with a minimum number of sampling points (Montgomery 2006). Sample points in efficient locations will not only reduce the required number of sampling points, but also increase the accuracy of the Meta-model that is obtained from the results of the sampling points. In other words, DOE provides a database of information to the Meta-model about the dependency of the performance on the geometric changes (i.e. variation of the rotor blade shape). The most time consuming step in the optimization procedure is the creation of database samples. Therefore, it is vital to create the smallest possible database that contains the maximum amount of information about the whole design space with minimal redundancy while including the impact of every design parameter (X_i), but only once. Figure 6-2 presents the sampling points for three DOE methods namely Monte Carlo sampling, Latin hypercube sampling and optimal space filling sampling (OSF). Clearly, Monte Carlo method is not as efficient as the other two methods as there are sample points with shared rows and columns so that the effect of each parameter is included more than one time in the database (redundancy of data). In contrast, Latin hypercube sampling which is an advanced form of the Monte Carlo avoids clustering of the samples and assures no two points share the same value (i.e. no shared rows or columns) as depicted in Figure 6-2. OSF is the Latin hypercube sampling that is extended with post-processing to distribute the design parameters equally throughout the design space with the objective of gaining the maximum insight with the fewest number of points (no shared rows or columns) as illustrated in Figure 6-2. Therefore, OSF was selected as the DOE method for the creation of the database during the CFD optimization.

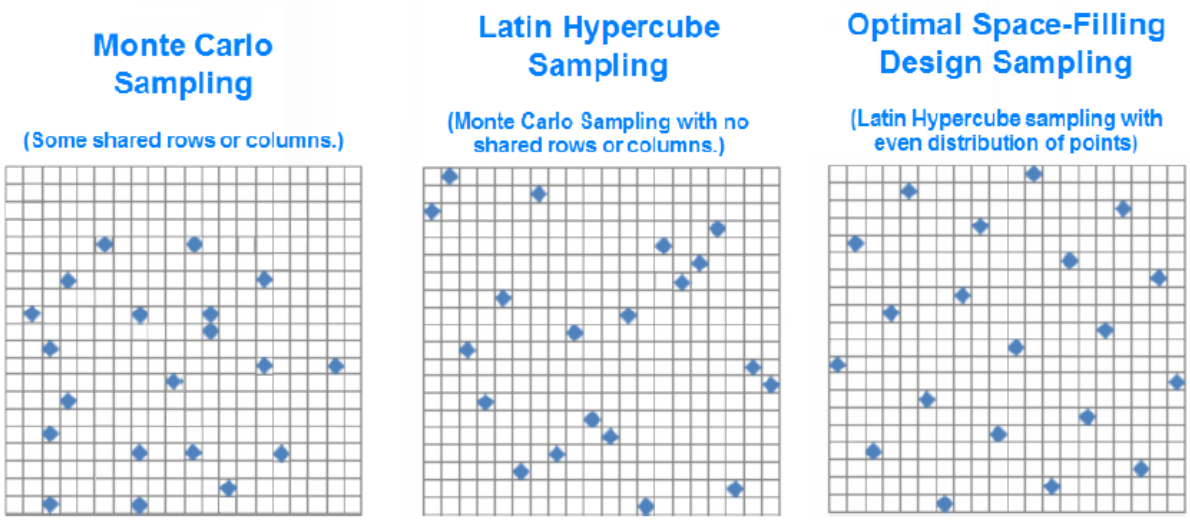

Figure 6-2 Comparison of various DOE techniques: (left) Monte Carlo, (middle) Latin hypercube, (right) optimal space filling (Montgomery 2006)

6.2.2. Meta-model (surrogate model)

As discussed in section 6.2, integrating the CFD RANS solver directly with the GA optimization algorithm is not a feasible solution in terms of computational time. To alleviate such drawback it is possible to utilize Meta-models to assist the GA optimization for reducing the computational time. Meta-models can be built for each output parameter (i.e. turbine efficiency and power) based on the independent design variables (i.e. turbine geometry). Figure 6-3 presents the schematic of the database sampling points and the Meta-model created based on them. The accuracy of Meta-model depends on the complexity of the variations of the design variables, number of sample points in the database and type of Meta-model. In this chapter Kriging method was employed as the Meta-model due to its advantages (described below) compared to the other methods such as 2nd order polynomial. Kriging is a Meta-model that fits high order variations of the output parameters. It is an accurate multi-dimensional interpolation combining a polynomial model, which provides a global model of the design space, plus local deviations to interpolate the database sampling points (Simpson *et al.* 2001).

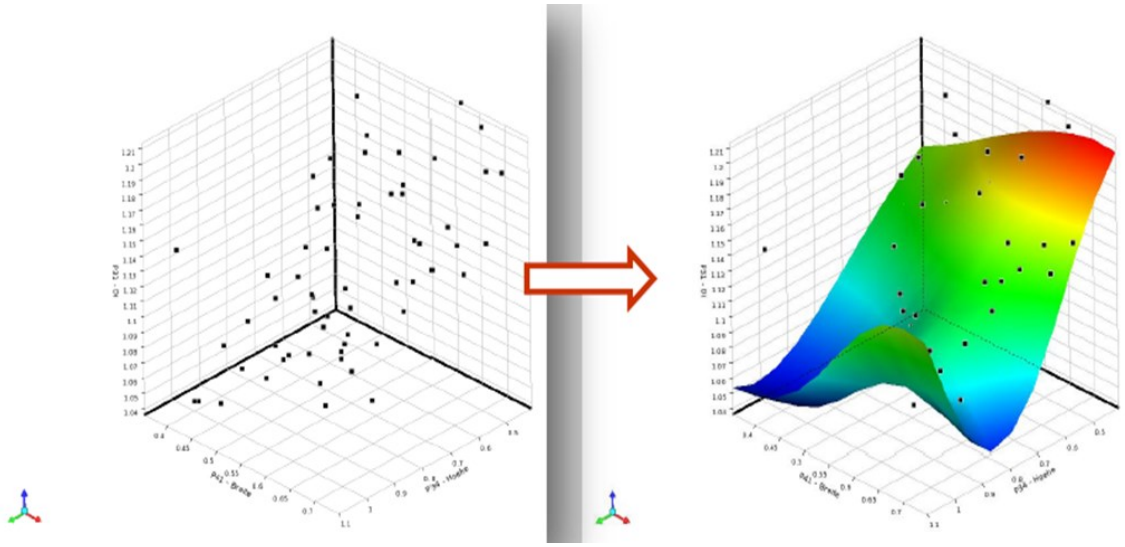

Figure 6-3 Example of the DOE sample points (left), Meta-model fitted the samples (right) (Montgomery 2006)

The effectiveness of the Kriging algorithm is based on the ability of its internal error estimator to improve Meta-model quality by generating refinement points and adding them to the areas in need of improvement (Martin *et al.* 2005). The goodness of fit for the created Kriging Meta-model can be measured based on a number of metrics such as coefficient of determination (should be close to unity) or maximum relative residual (should be close to zero).

6.2.3. Genetic algorithm optimization method

As discussed in section 5.6, GA is based on the biological evolution in which a population of individuals (different geometries) is chosen randomly from the range of independent parameters and they are assessed based on their fitness value (aerodynamic performance). A new generation of populations is generated in a stochastic manner by breeding the selected members of the current population according to their fitness value. It goes through several iterations retaining the elite percentage of the individuals through each iteration allowing the individuals to genetically evolve until the global optimum is found.

6.3. Parameterization of rotor geometry and definition of objectives and constraints

The geometry parametrization is an essential aspect of effective optimization procedure as it needs to generate a wide variety of realistic geometries within smallest set of design parameters together with a careful choice of the design variables and their ranges. The parametrization and 3-D CFD optimization were only conducted for rotors in both stages while the geometries of the nozzles were kept fixed.

The meridional channel was described by means of 3rd-order Bezier curves both at hub and shroud while the blade angle and thickness distributions were specified by means of B-splines as illustrated in Figure 6-4 . The coordinates of the control points for both Bezier and B-spline curves were used by the optimization algorithm and their possible variation in the axial and radial directions are shown by arrows in the same figure. In order to prevent the transformation of the entire geometry in the meridional channel, the hub and shroud control points at rotor LE as well as TE at hub and shroud were fixed during all optimizations. The blade camber angle distribution both at hub and shroud was divided equally by five control points (only shroud curve is shown in Figure 6-4 for brevity while the hub curve is the same in terms of parametrization) with flexibility of variation only for the blade angle. The range of variation for each control point was defined so that the entire blade angle range from LE to TE was covered both at hub and shroud and for both stages. For the thickness distribution three control points was defined at hub curve and it was assumed that the thickness is uniform from the hub to shroud. Moreover, as the number of blades was a discrete parameter two additional values as 19 and 23 were specified apart from 21 (refer to Table 5-10) for both stages to allow the optimizer finding the optimum number of blades.

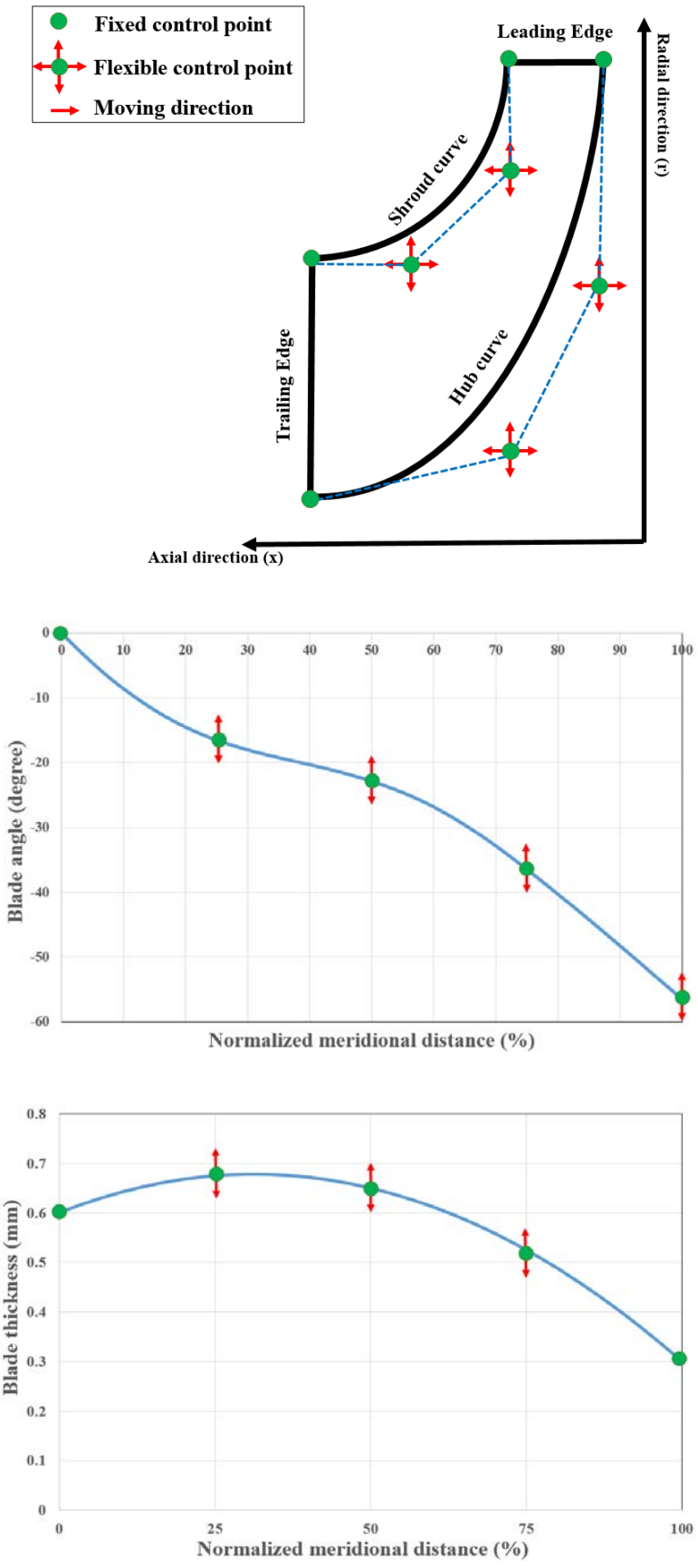

Figure 6-4 Parametrization of the meridional channel (top), blade camber angle distribution (middle), blade thickness (bottom)

A total of twenty design parameters were specified for the rotor in each stage in order to control the blade angle and thickness distributions and the shape of the meridional channel both at the hub and shroud.

For each stage the optimization was conducted at the design operating conditions shown in Table 5-9. The turbine isentropic efficiency defined by Equation 3-34 was specified as the objective function for the GA to be maximized in both stages. Two constraints as the mass flow rate and power output were defined during the optimization. The former to avoid excessive over-prediction compared to the design value while the latter to ensure that RIT delivers the minimum required power at the design point.

$$Constriant_1 = \left|\dot{m}_{computed} - \dot{m}_{design}\right| - \Delta\dot{m} < 0 \qquad \text{Equation 6-4}$$

$$Constriant_2 = \left|Power_{computed} - Power_{design}\right| - \Delta Power < 0 \qquad \text{Equation 6-5}$$

6.4. Baseline geometry generation of the dual-stage organic RIT

Prior to the optimization, it was required to create the initial 3-D geometry of the nozzle and rotor for each stage (called baseline design onward) based on the mean-line modelling optimization results summarized in Table 5-10. The nozzle geometry was kept fixed and only the rotor geometry was optimized for both stages. Figures Figure 6-5 and 6-6 present the baseline geometry of nozzle and rotor for stage one and two respectively. Due to the use of volute, the nozzle in the first stage was un-cambered to obtain the correct incidence angle while for the second stage it was created as cambered vane as it is followed by the return channel.

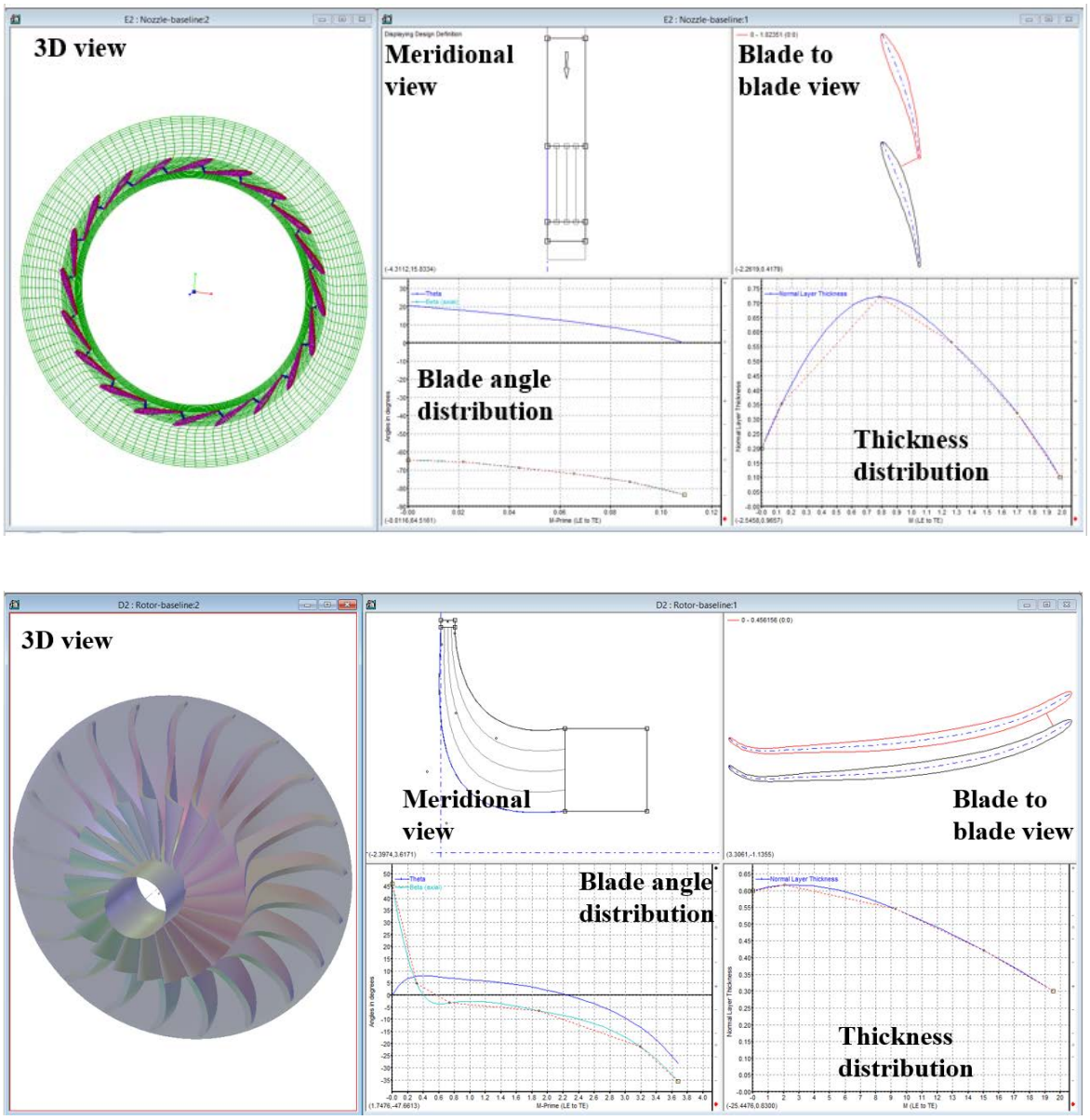

Figure 6-5 Baseline geometry of the nozzle and rotor for stage one

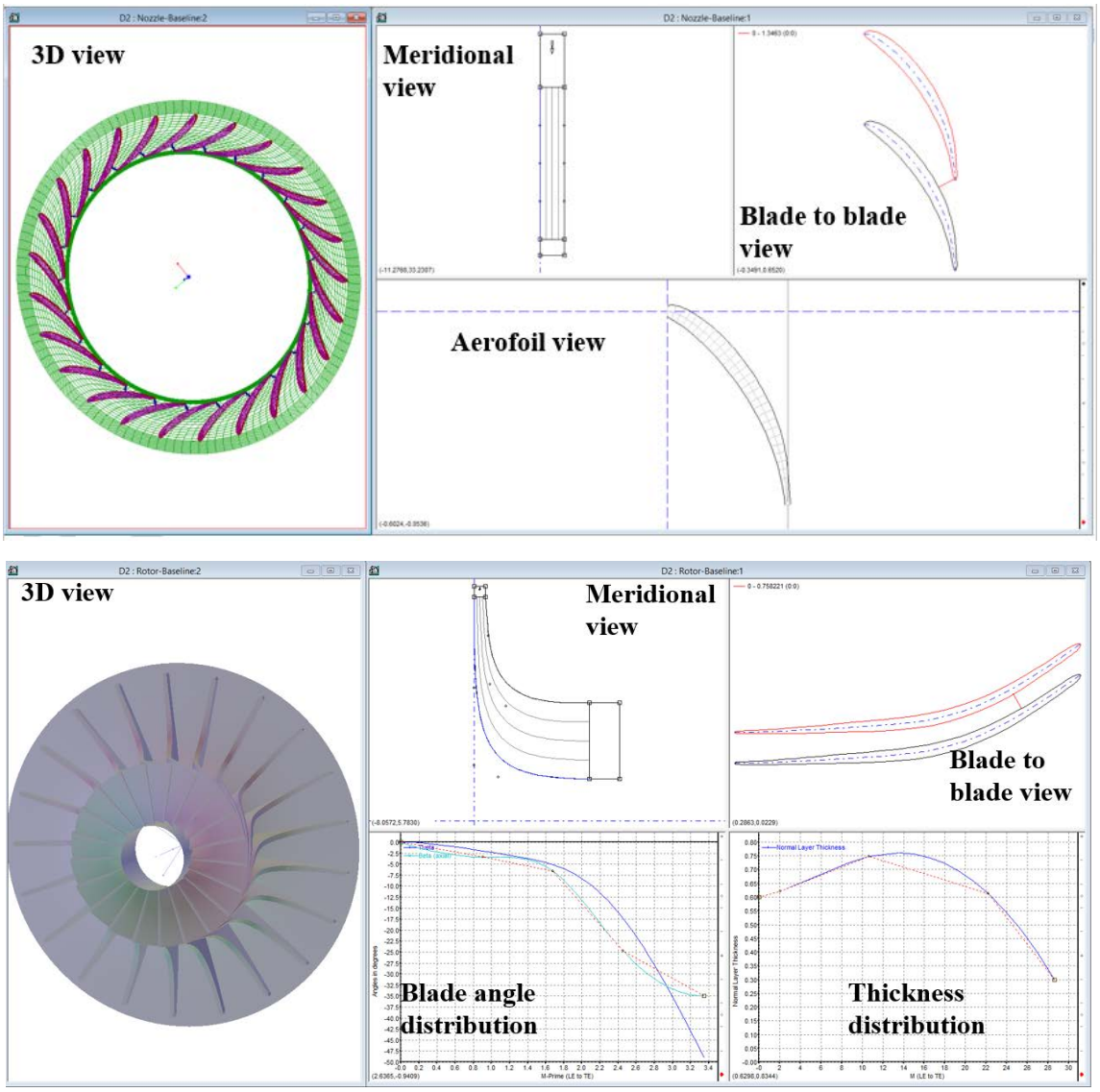

Figure 6-6 Baseline geometry of the nozzle and rotor for stage two

6.5. Grid generation and CFD setup

Initially the CFD optimizations were conducted for the rotor of each stage (nozzle plus rotor) separately and then the CFD analysis of the complete dual-stage organic RIT including the volute and return channel were performed. The CFD setup in terms of turbulence model, boundary conditions, interfaces and convergence criteria are similar to section 3.6.3.1. Based on the mean-line modelling results the tip clearances of 0.143mm and 0.22mm were specified for the rotors in stage one and two respectively. The thermo-physical properties of R245fa were defined in the CFX solver to employ the "Aungier

modified Redlich-Kwong" real-gas EoS with fourth order polynomial for the specific heat capacity to determine the flow properties during simulations. Table 6-1 summarizes R245fa properties defined in the CFX for CFD simulations.

Table 6-1 Thermo-physical properties of R245fa used in ANSYS CFX for real-gas EoS

Molar Mass (kg/kmol)		134
Critical temperature (K)		427.2
Critical pressure (bar)		36.397
Critical volume (cm^3/mol)		259.7
Acentric factor (-)		0.3796
Boiling temperature (K)		288.3
Specific heat capacity coefficients	a_0 (J/mol-K)×R	60
	a_1 (J/mol-K^2) ×R	0.2
	a_2 (J/mol-K^3) ×R	9.601e-15
	a_3 (J/mol-K^4) ×R	-1.657e-17
	a_4 (J/mol-K^5) ×R	1.0604e-20

Mesh independence study was conducted for both stages similar to the procedure described in section 3.6.3.2. The results indicate that for rotor stage one and two, 1000823 and 956162 elements were required respectively to achieve mesh independence with Y^+ values around unity. Similarly, 396543 and 412846 elements were required for mesh independence for the nozzle in stage one and two respectively. The CFD setup with baseline rotor geometries and corresponding boundary conditions are illustrated in Figure 6-7.

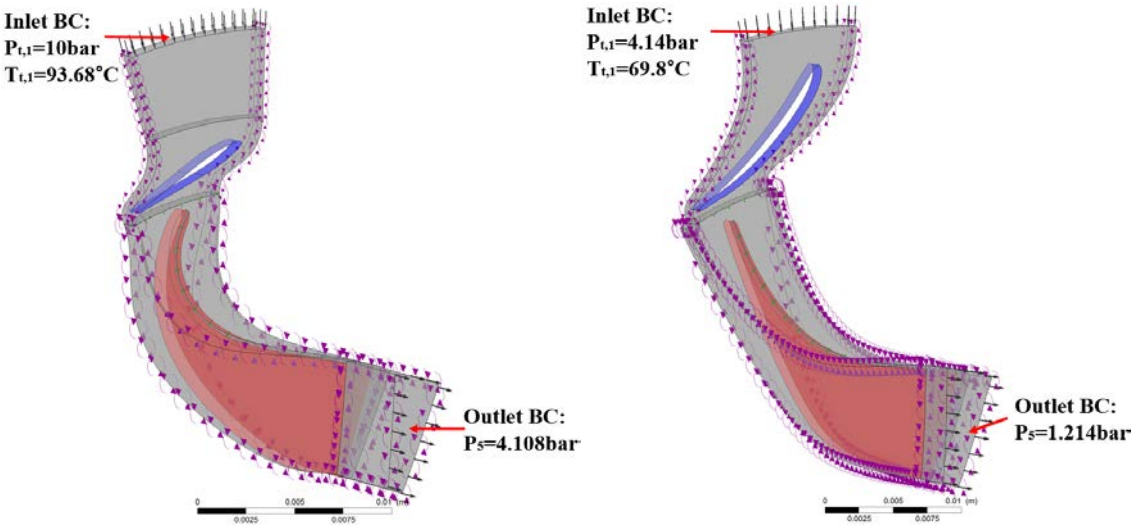

Figure 6-7 CFD setup for the baseline rotor geometries, (left) stage one, (right) stage two

6.6. CFD optimization results of the dual-stage organic RIT

Optimizations were solved on an Intel® CPU core i7 - 4790@ 3.60GHz with 32GB RAM in parallel run with 4 CPU cores. Figure 6-8 depicts the screen shot of the ANSYS GUI for the completed stage one optimization.

The accuracy and quality of the Kriging Meta-model was assessed based on the goodness of fit for both stage one and stage two rotors as presented in Figure 6-9. Clearly, the selected Meta-model exhibited excellent accuracy with the coefficient of determination close to unity and maximum relative residual close to zero for both stages. Therefore, such model is able to drive the GA optimizer to reliably find the global optimum geometry.

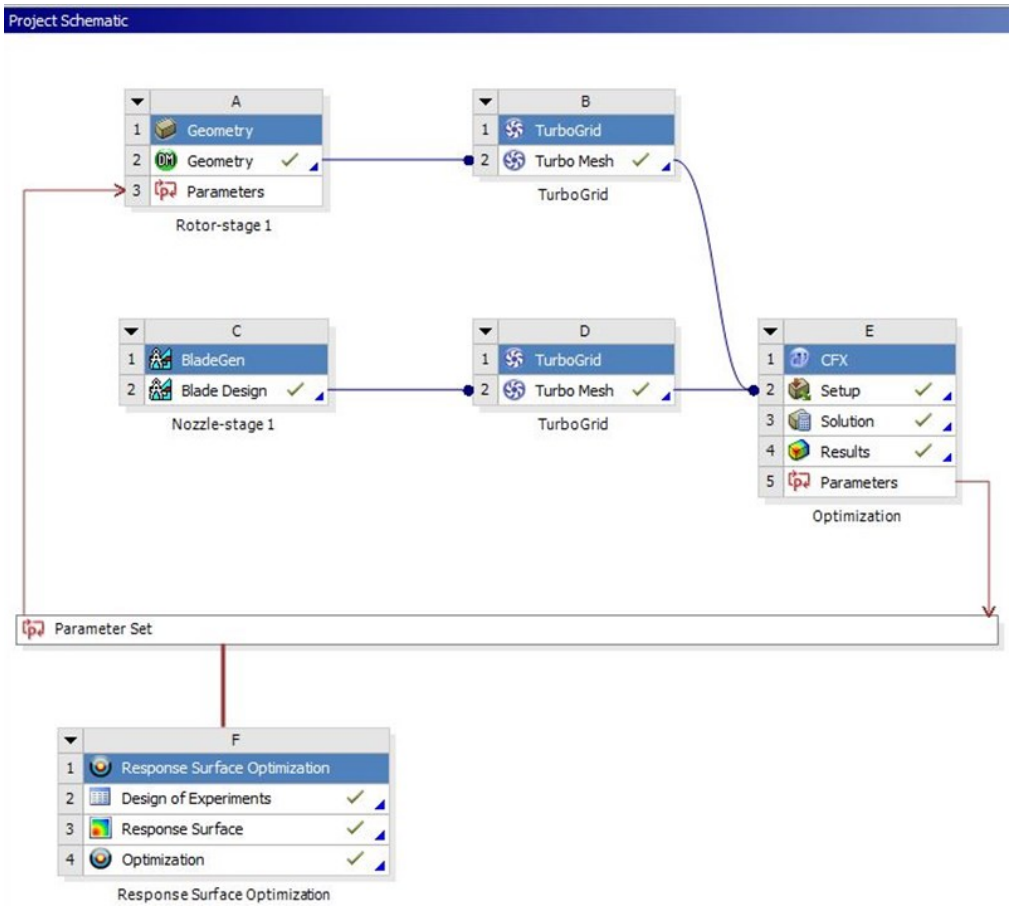

Figure 6-8 Screen shot of the ANSYS GUI for the completed stage one optimization

There exists one unique response for the predicted efficiency by the Kriging Meta-model based on each of the design variables parametrized in section 6.3. For brevity Figure 6-10 shows the turbine isentropic efficiency versus one of the rotor shroud meridional points and one of the blade angle distribution points for both stages. However, similar graphs with different efficiency prediction can be obtained for other design variables. As it is evident for example there is an optimum value of about 9mm for the shroud meridional point of stage two that yields maximum efficiency.

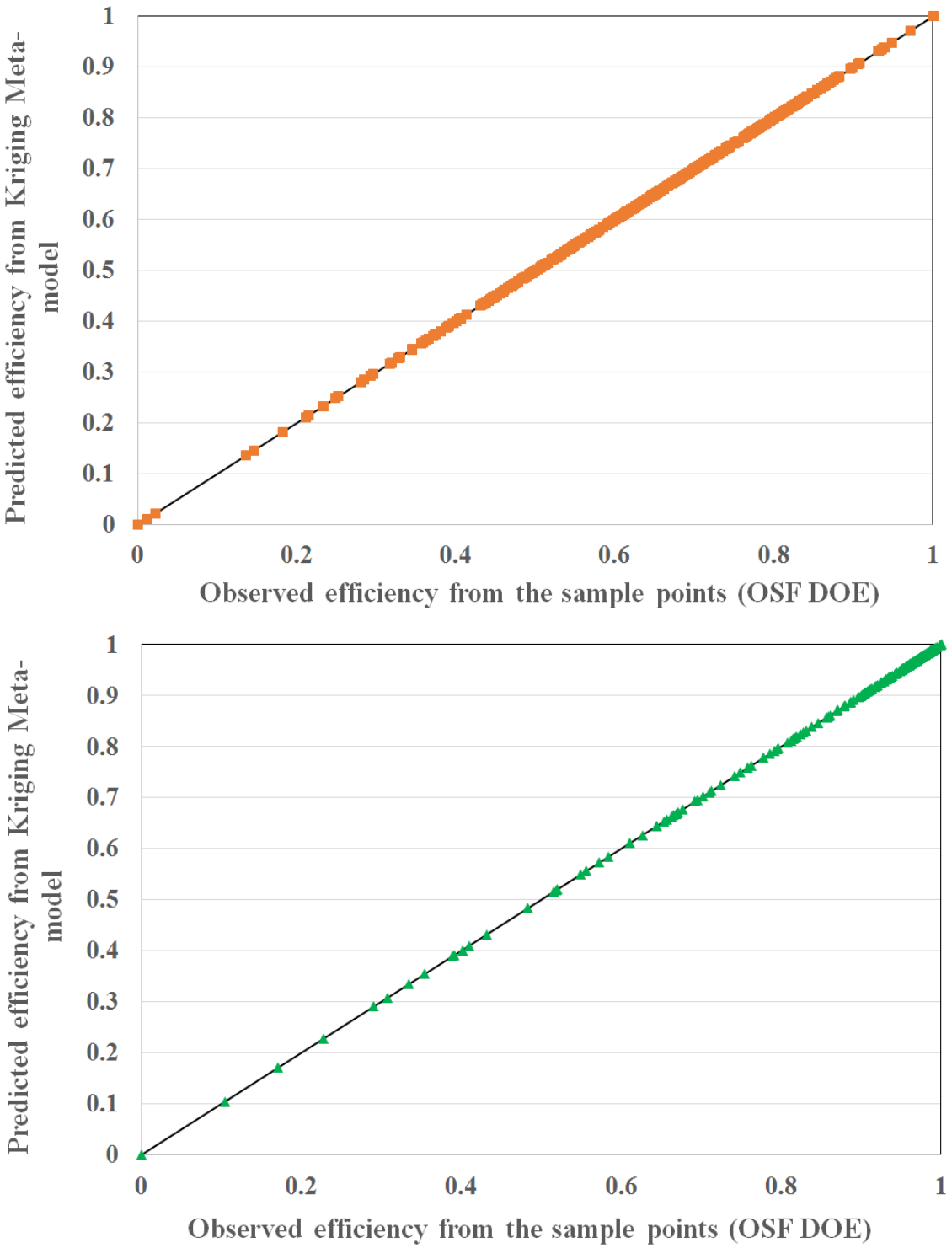

Figure 6-9 Normalized observed efficiency from the sample points Vs the predicted efficiency by the Kriging Meta-model for stage one (top) and stage two (bottom)

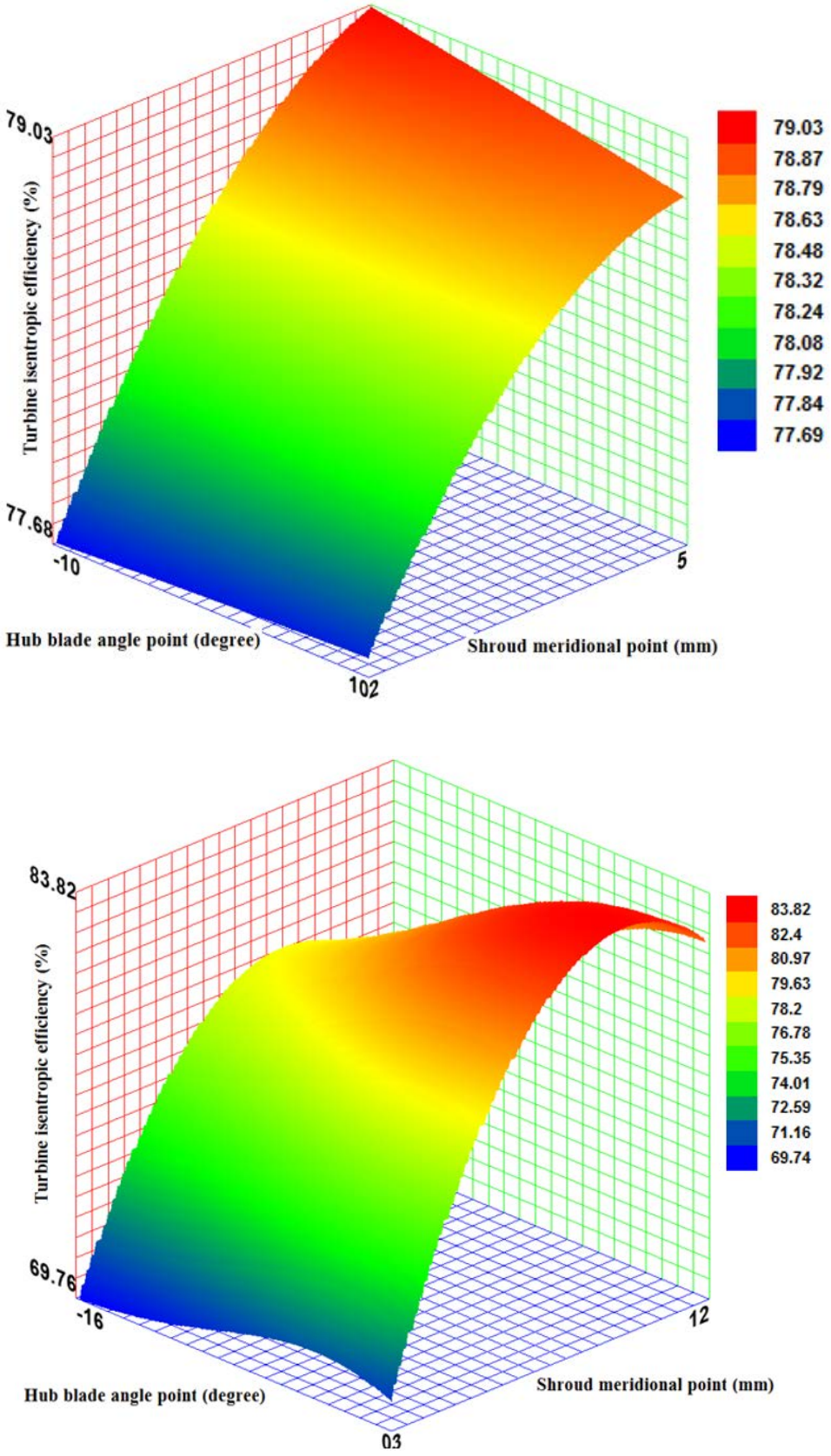

Figure 6-10 Predicted turbine efficiency with Kriging Meta-model based on two design variables, (top) stage one, (bottom) stage two

The GA will use these results in order to search for the optimum geometry. Figure 6-11 presents the convergence history of the GA for both stages improving the geometry of the baseline rotor until reaching the optimum geometry with maximum efficiency.

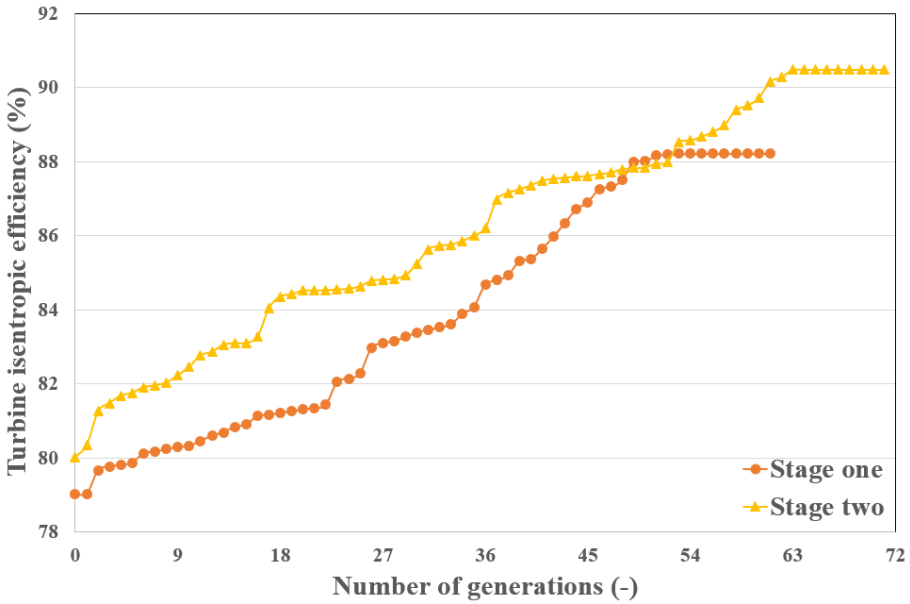

Figure 6-11 GA optimization convergence history for stage one and two

Clearly the optimization method was very effective as it improved stage one and stage two efficiencies by 9.2% and 10.5% respectively. Table 6-2 summarizes the global performance parameters obtained from CFD simulations for both baseline and optimized designs. The power was increased by 11.4% and 13.4% for stage one and two respectively while the optimum number of rotor blades remained constant for stage one and it reduced from 21 to 19 for stage two.

Table 6-2 Summary of global performance parameters for baseline and optimized designs for the dual-stage organic RIT

	$\eta_{stage,ts}$ (%)	Power (kW)	Mass flow (kg/s)	Z_{rotor} (-)
Stage one-Baseline	79.03	1.123	0.06571	21
Stage one-Optimized	88.22	1.251	0.06568	21
Stage two-Baseline	80.02	1.32	0.06501	21
Stage two-Optimized	90.49	1.497	0.0657	19

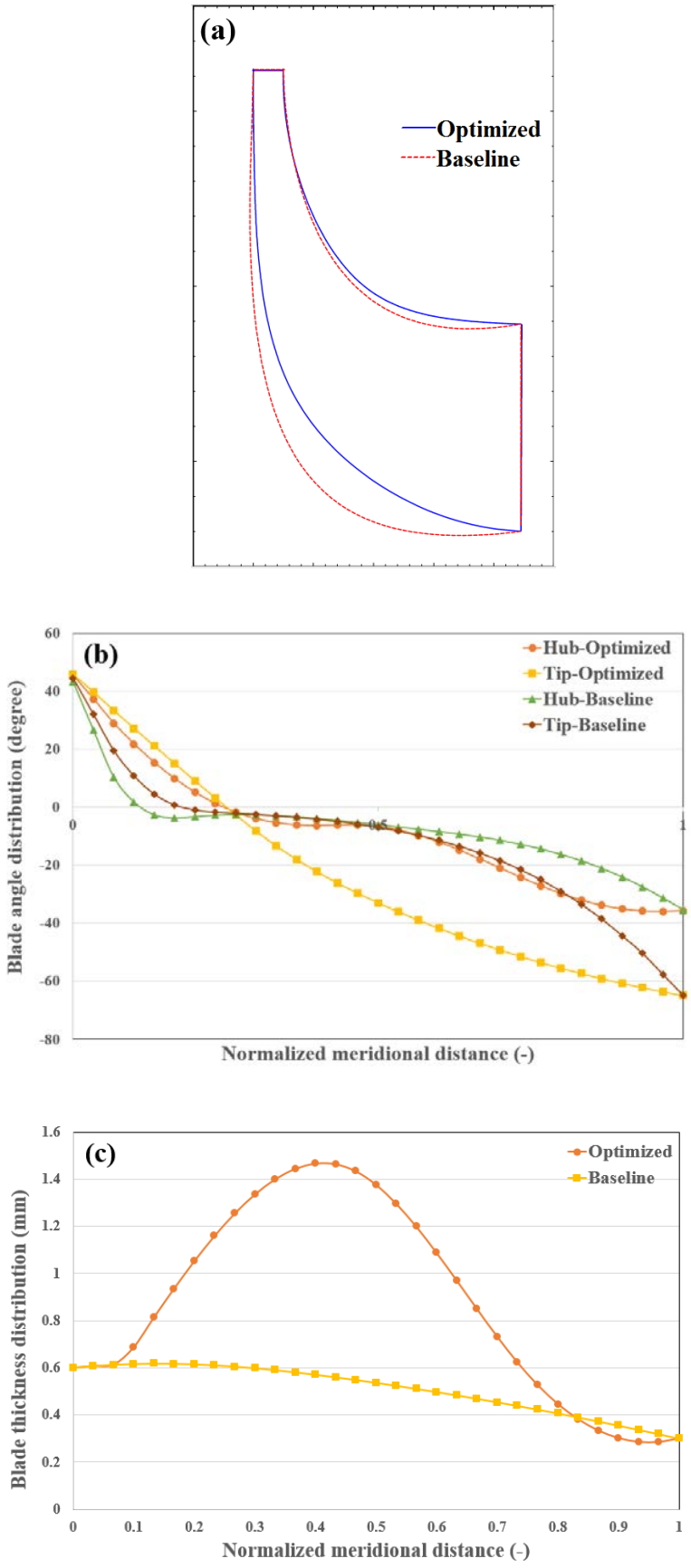

Figure 6-12 Comparison of stage one optimized and baseline geometries (a) meridional channel (b) blade angle distribution (c) blade thickness distribution

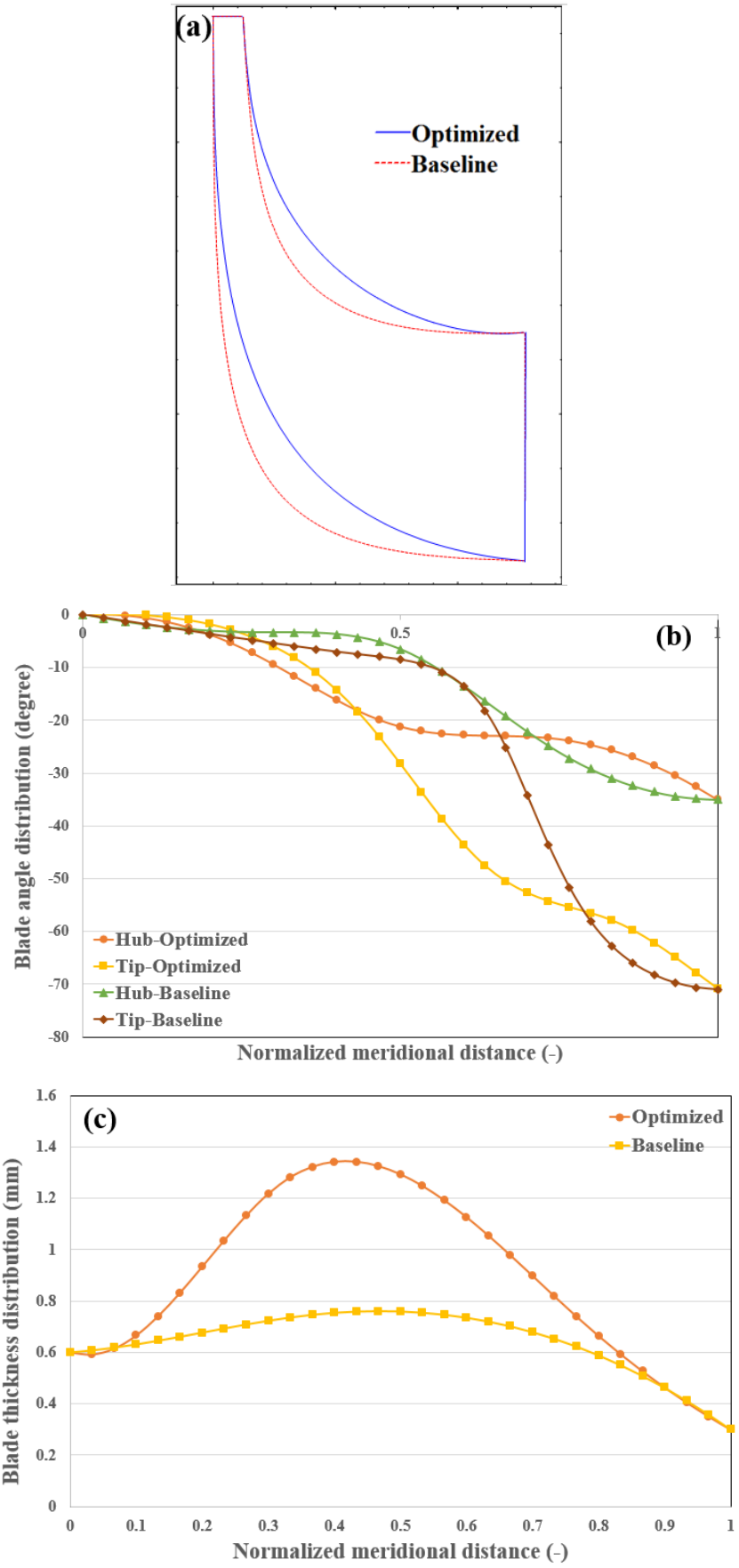

Figure 6-13 Comparison of stage two optimized and baseline geometries (a) meridional channel (b) blade angle distribution (c) blade thickness distribution

Figures Figure 6-12 and 6.13 illustrate the variations in the blade geometry in terms of meridional channel, blade angle and thickness distributions from the baseline configurations to optimized shapes for stage one and two respectively. Such results showed that the blade geometry parametrization and the ranges of the design variables were effective as they provide enough flexibility for the optimizer to search for the optimum geometry.

The flow field of the optimized and baseline configurations in both stages was compared in terms of velocity vectors and entropy distribution and presented in Figures Figure 6-14 to 6.19. For both stages the optimized configurations have preferential and smooth flow shown by velocity vectors with no flow reversal anywhere in the passage as depicted in Figures Figure 6-14 and 6.15. In contrast, the baseline designs suffer from strong secondary flows in early part of passage that led to flow separation. Although flow reattached to the blade surface later in the passage, the initial flow separation and the formation of secondary flows resulted in substantial entropy generation that propagated downstream the rotor passage as it is evident in FiguresFigure 6-16 and 6.17 for baseline geometries. Such entropy generation occupied majority of the baseline passage and led to significant losses and hence reduced efficiency. Although not completely eliminated, comparing the entropy distribution of the optimized designs in the same figures with the baseline designs shows that the entropy generation has considerably reduced during optimization. Such improvements in the aerodynamics of the flow in the rotor blade-to-blade passage partially explain the increase in the turbine efficiency of the optimized configurations as summarized in Table 6-2. The variation of blade meridional shape has also considerable contribution in increasing the turbine efficiency of both stages as presented in Figures Figure 6-18 and 6.19.

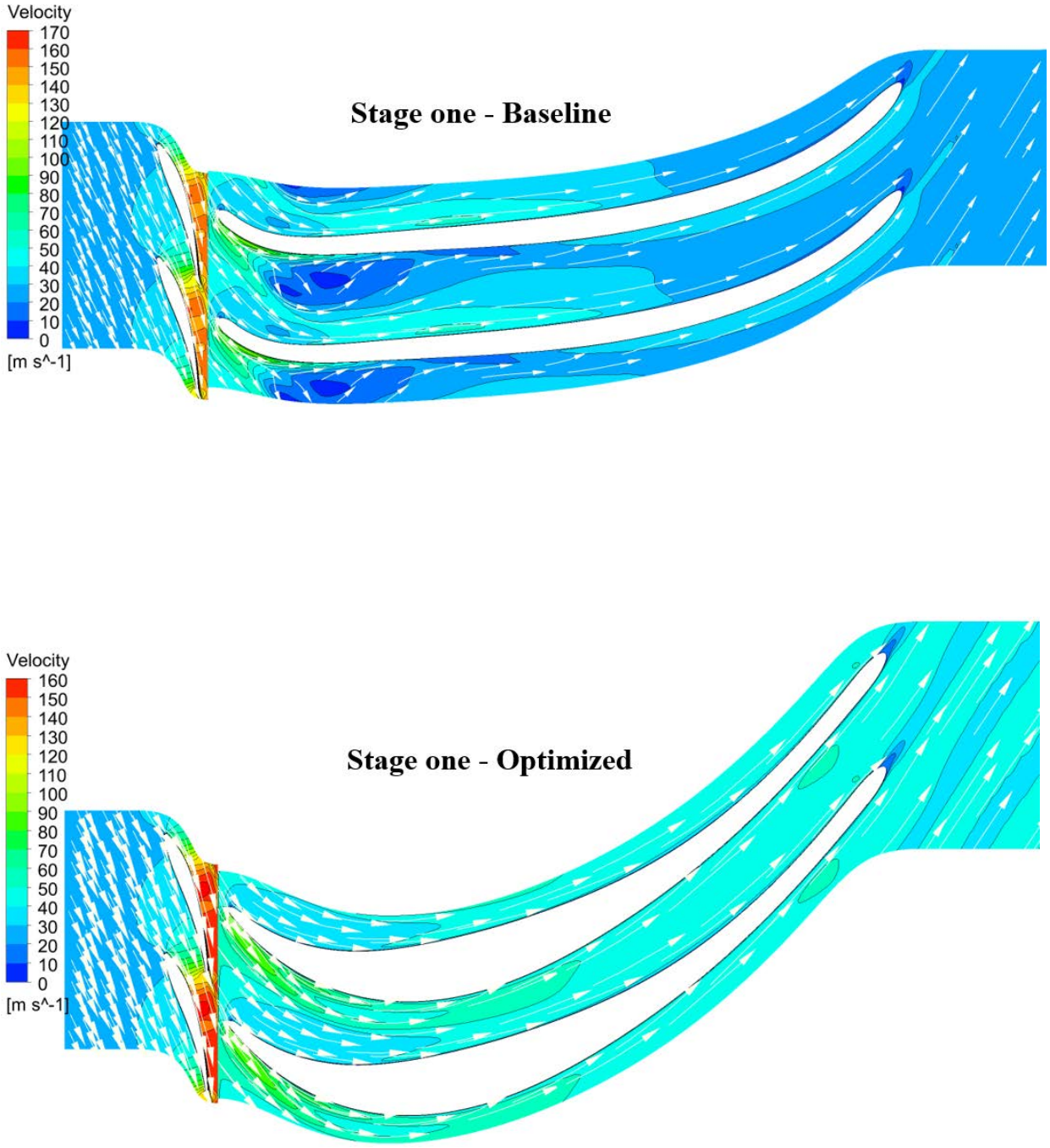

Figure 6-14 Velocity vectors at half span for stage one baseline (top) and optimized (bottom)

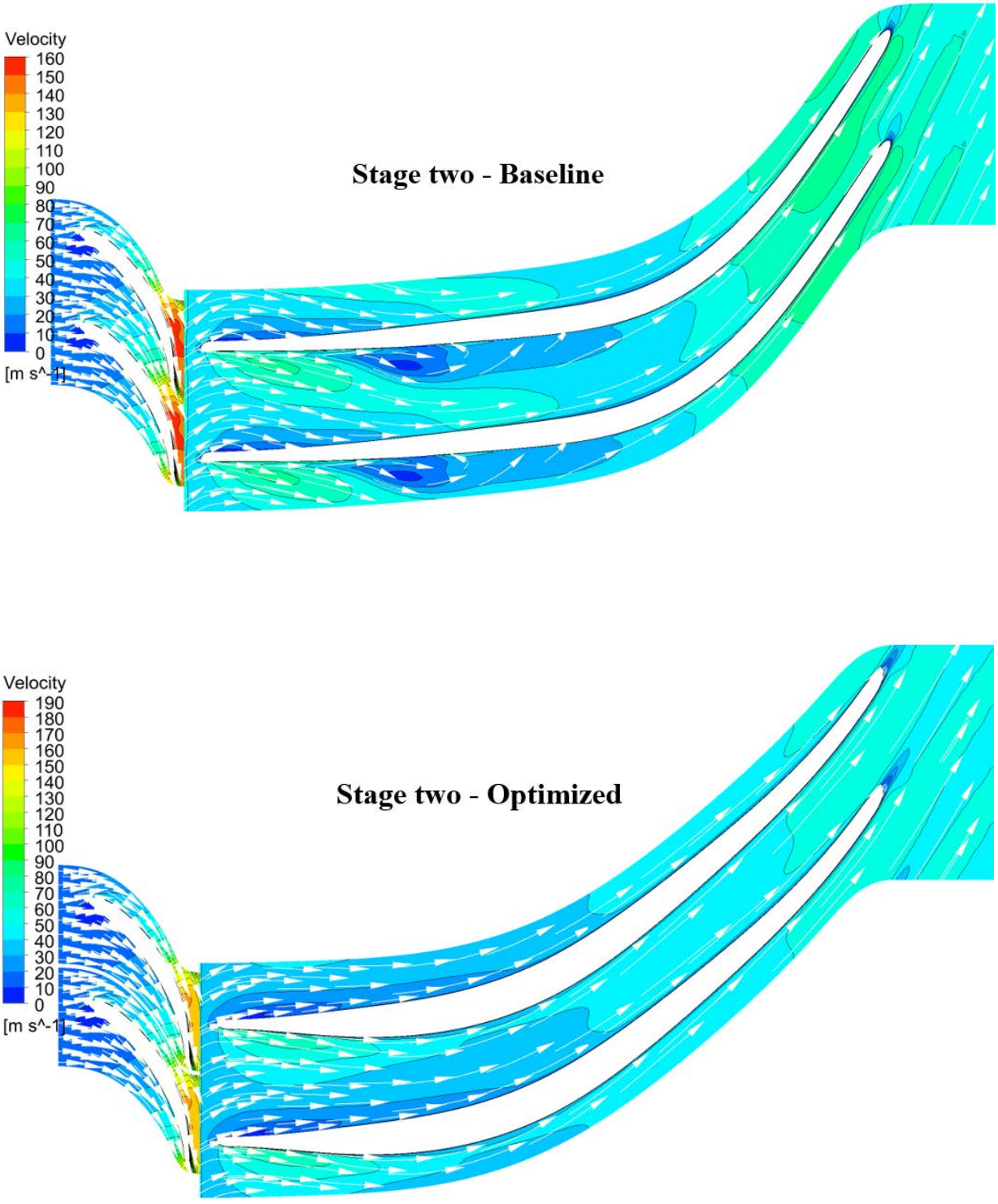

Figure 6-15 Velocity vectors at half span for stage two baseline (top) and optimized (bottom)

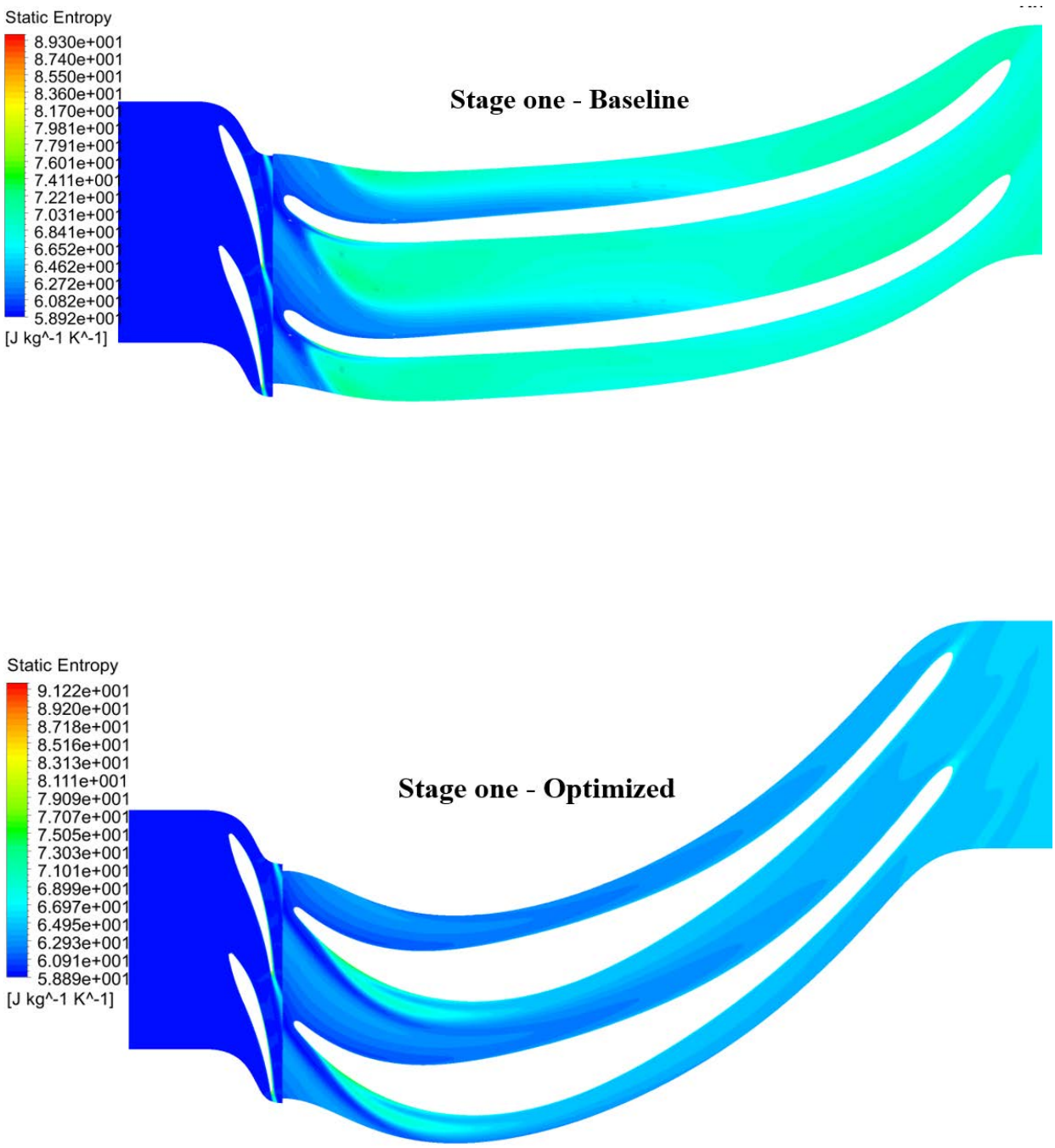

Figure 6-16 Entropy distribution at half span for stage one baseline (top) and optimized (bottom)

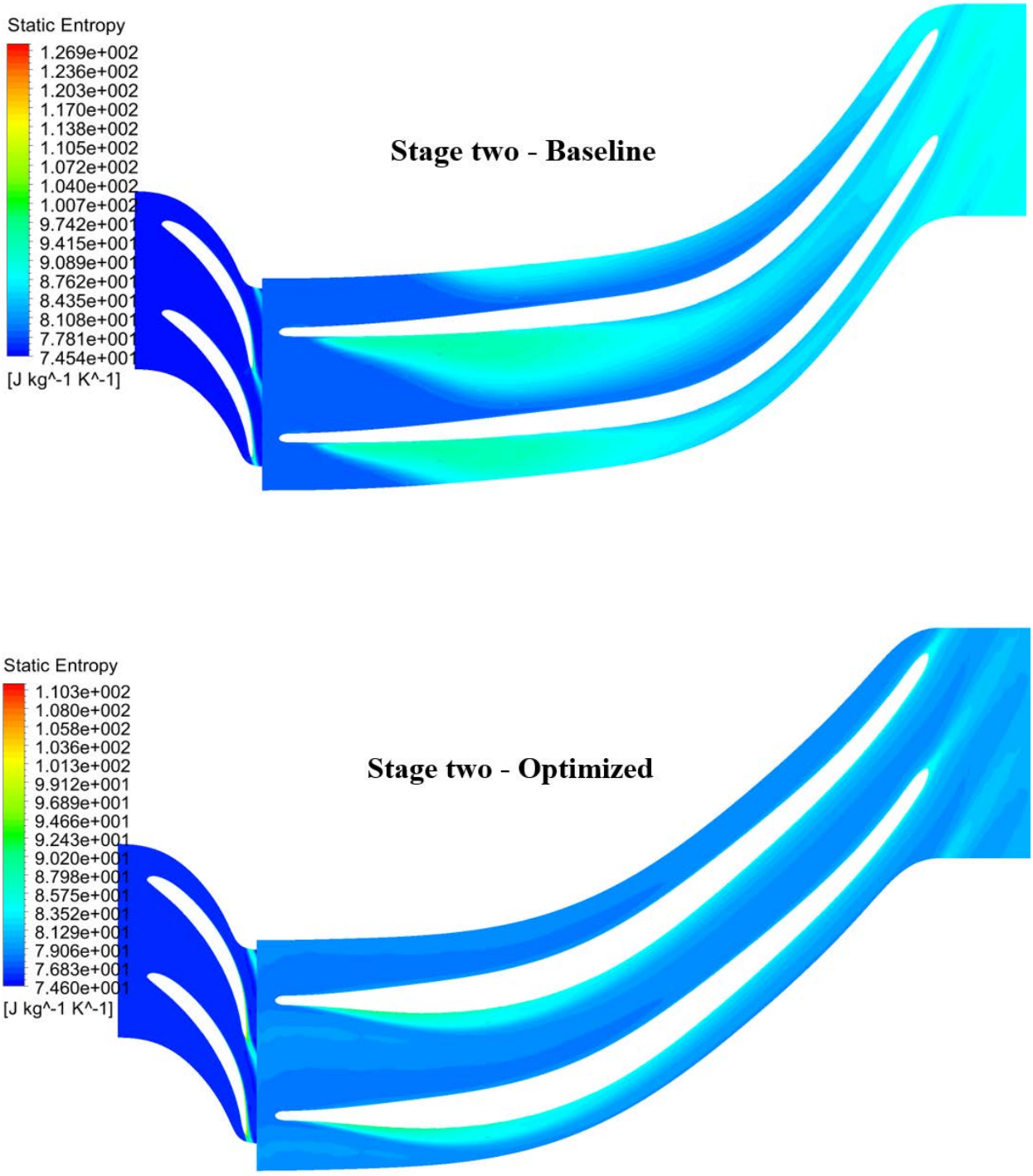

Figure 6-17 Entropy distribution at half span for stage two baseline (top) and optimized (bottom)

Evidently, the formation of the secondary flows in the blade-to-blade plane has been propagated to the meridional plane of the baseline designs at various spans as illustrated in Figures Figure 6-18 and 6.19. The entropy generation has occupied majority of the meridional channel of the baseline designs with greater intensity in stage one compared to stage two. Such phenomena has been amplified further by the rotor tip leakage flow travelling away from the SS and mixed out with the secondary flows and hence increased the entropy generation even more. In contrast, for the optimized geometries the intensity of the entropy generation and losses has been relaxed and only accumulated near the rotor tip region. Apparently, the optimizer was unable to further improve the meridional passage to completely remove the entropy generation as it was not possible due to the requirement of the running clearance between the blade and casing and inevitable tip leakage flows and consequent losses.

Mach number contours in the meridional channel for the baseline and optimized designs for both stage one and two are presented in FiguresFigure 6-20 and 6.21 respectively. As it is evident, the highest Mach number is obtained at the interspace between nozzle and rotor in all cases. Although from mean-line modelling it was assured to avoid Mach numbers in excess of unity, due to the inclusion of the interspace and its detailed design through CFD (slight variation in its length) the Mach number is slightly higher than unity. But such feature has no significant effect on the performance of the turbine as was shown previously from the optimization results.

The final three-dimensional geometry of the optimized rotors and their corresponding nozzle rings are shown in Figure 6-22 for both stages.

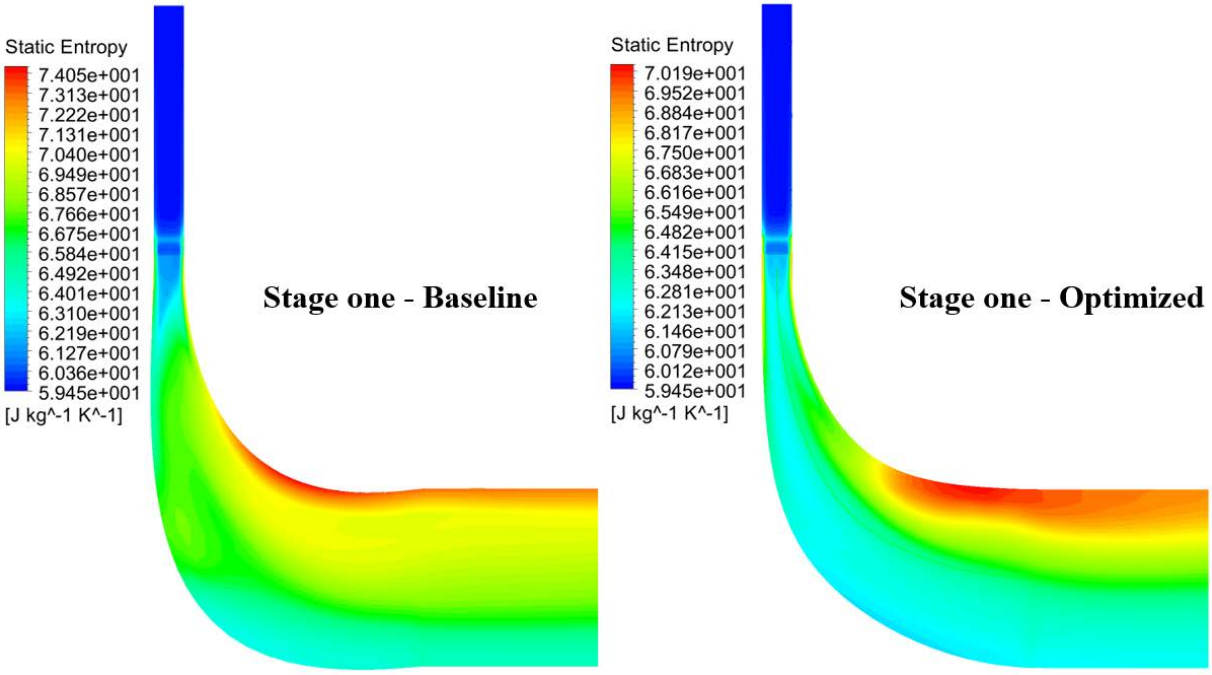

Figure 6-18 Entropy distribution at meridional channel for stage one baseline (left) and optimized (right)

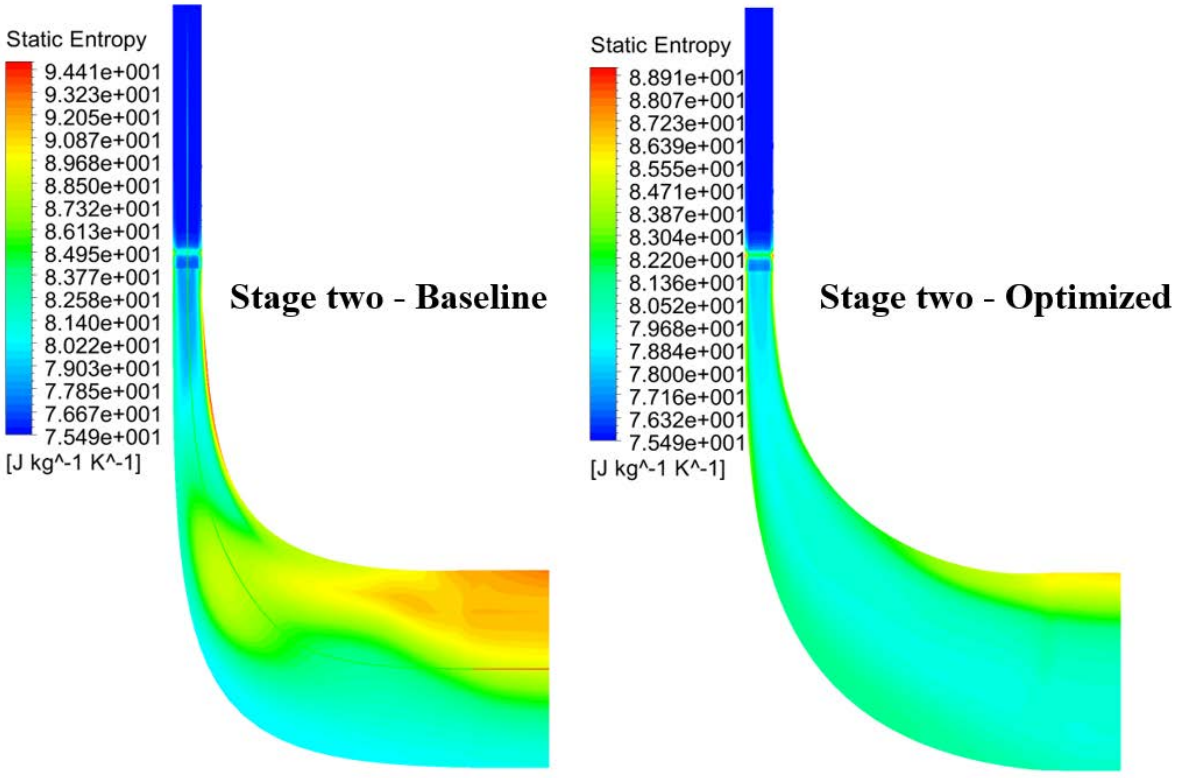

Figure 6-19 Entropy distribution at meridional channel for stage two baseline (left) and optimized (right)

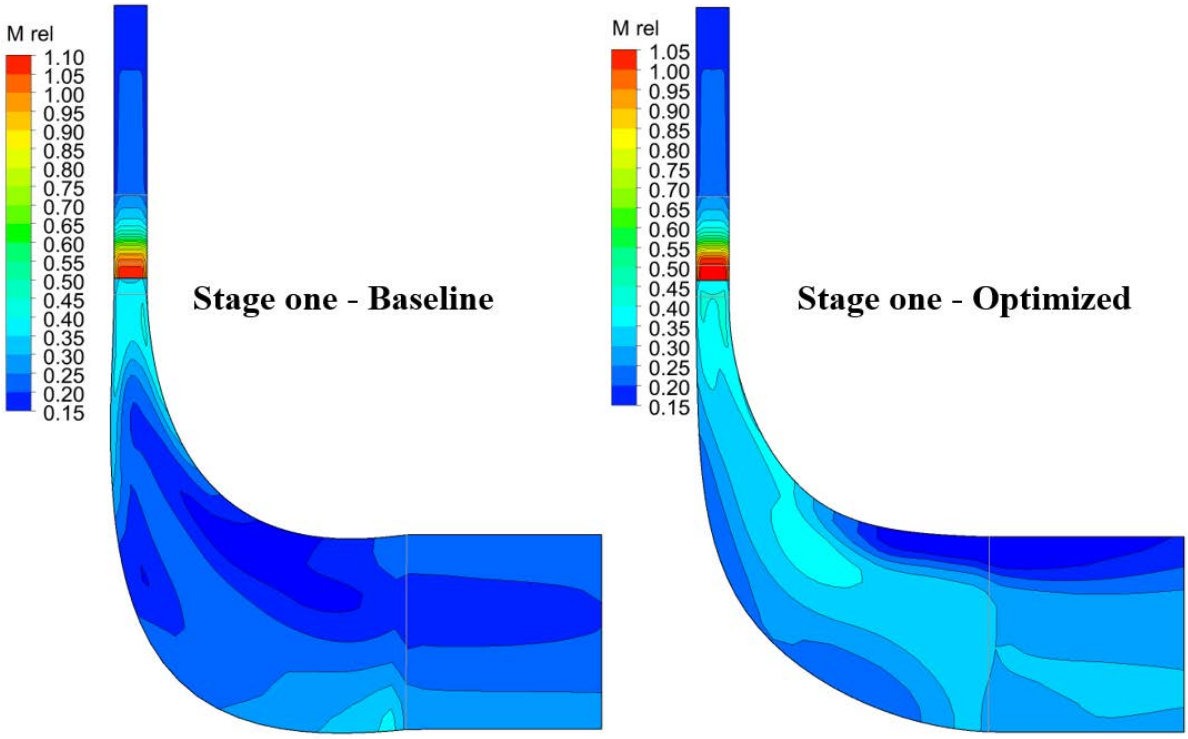

Figure 6-20 Mach number distribution at meridional channel for stage one baseline (left) and optimized (right)

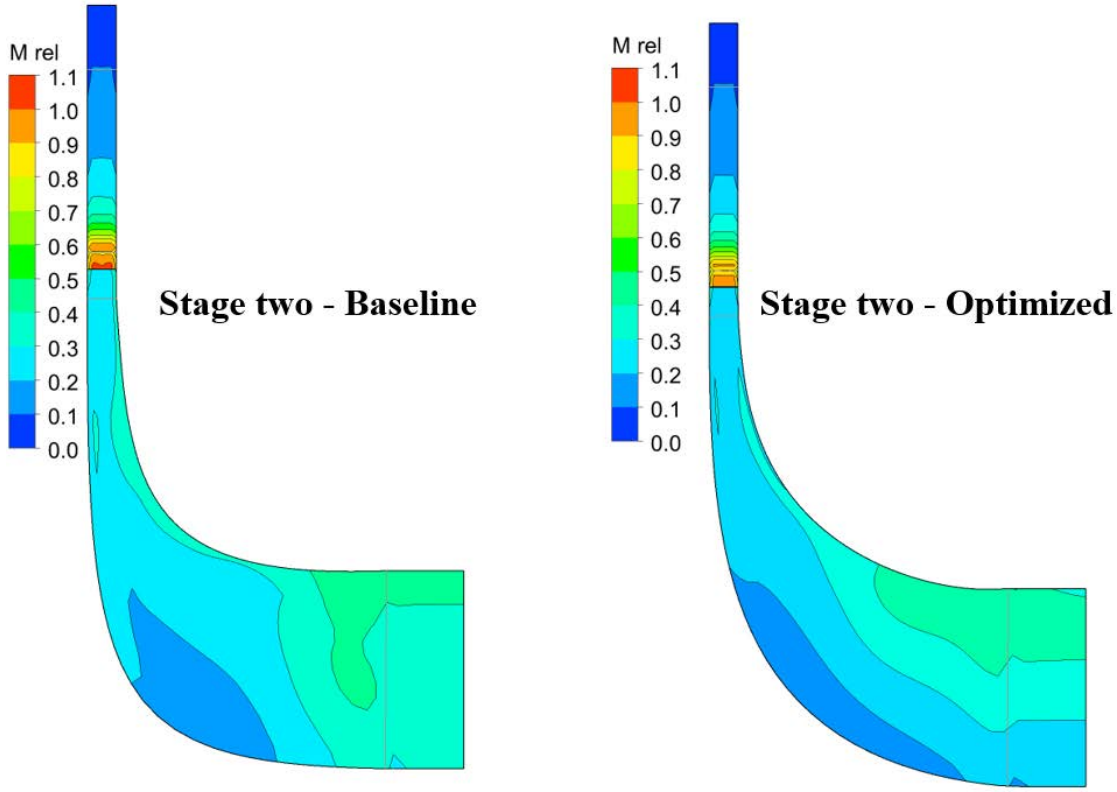

Figure 6-21 Mach number distribution at meridional channel for stage two baseline (left) and optimized (right)

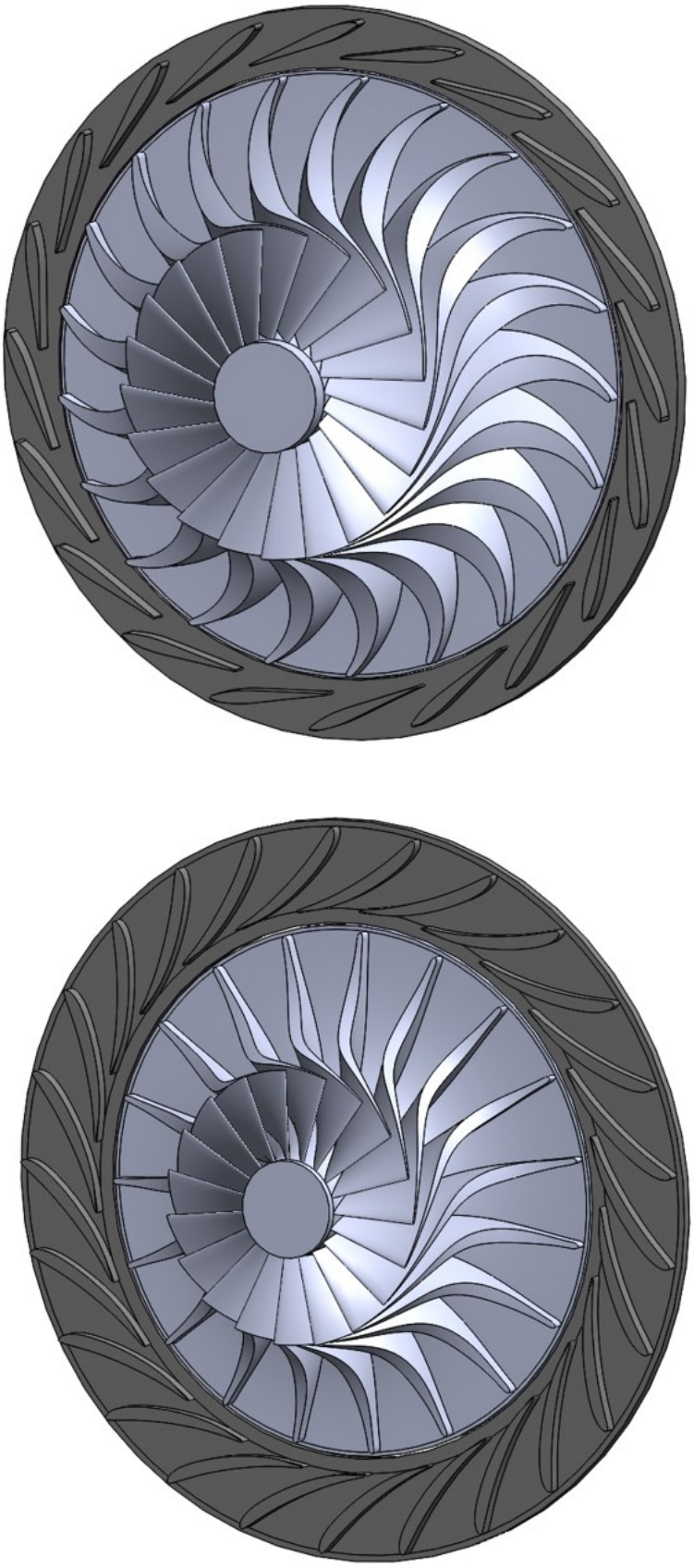

Figure 6-22 3-D geometry of the final optimized rotor and nozzle for stage one (top) and stage two (bottom)

For the ORC systems where the heat source is supplied by renewables (i.e. solar energy or geothermal heat), it is typical for the system to operate under off-design conditions most of the times for example due to the seasonal variations or environmental changes. Therefore, to assess the performance of the ORC RIT at off-design conditions, CFD simulations were conducted for each stage individually using the optimized rotor geometries.

The turbine rotational speed was varied from 40% to 100% of the design speed (60078.24rpm) while the expansion ratio was changed from 1.2 to 3.5 for each stage. The off-design CFD simulations results are presented in Figures Figure 6-23 and 6.24 for stage one and two respectively. For each stage the design point is equivalent to the highest efficiency as it is evident in FiguresFigure 6-23(a) and 6.24(a) and highlights the effectiveness and reliability of the mean-line and CFD optimizations. At the design rotational speed, stage one exhibited fairly uniform efficiency over a wide range of expansion ratios. But as the rotational speed decreases the maximum efficiency moves toward lower expansion ratios for both stages. Moreover, from the results in Figures Figure 6-23(b) and 6.24(b) the design point of each stage was very close to the choking conditions due to the low sound speed of R245fa, but to obtain the required power output and hence maximizing $\eta_{thermal,cycle}$ such conditions were unavoidable. In addition, as the turbine rotational speed reduces the mass flow rate increases at the same expansion ratio which usually observed in the RIT off-design conditions reported by (Baines 2003, Aungier 2006, Dixon *et al.* 2010).

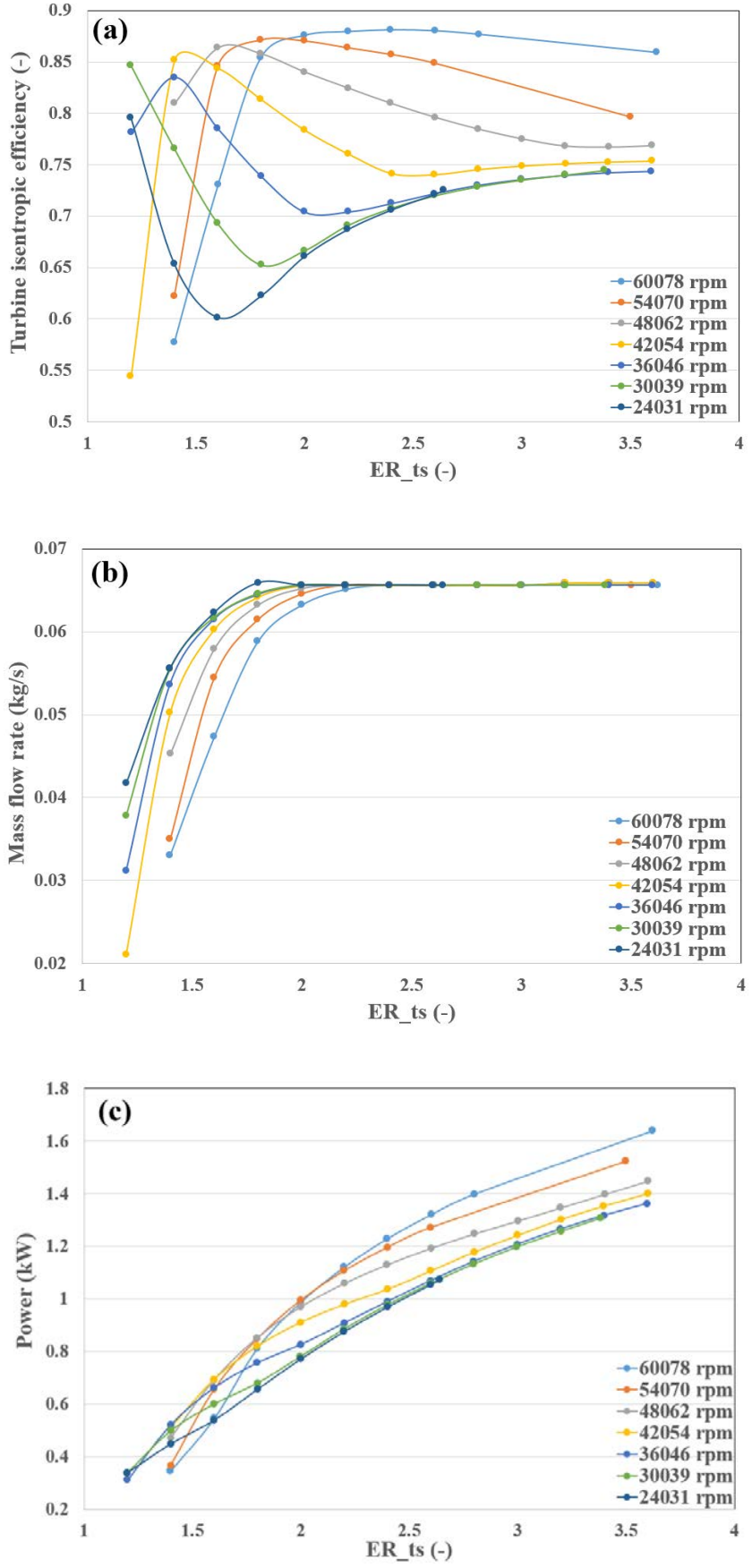

Figure 6-23 Off-design performance prediction of the optimized stage one using CFD

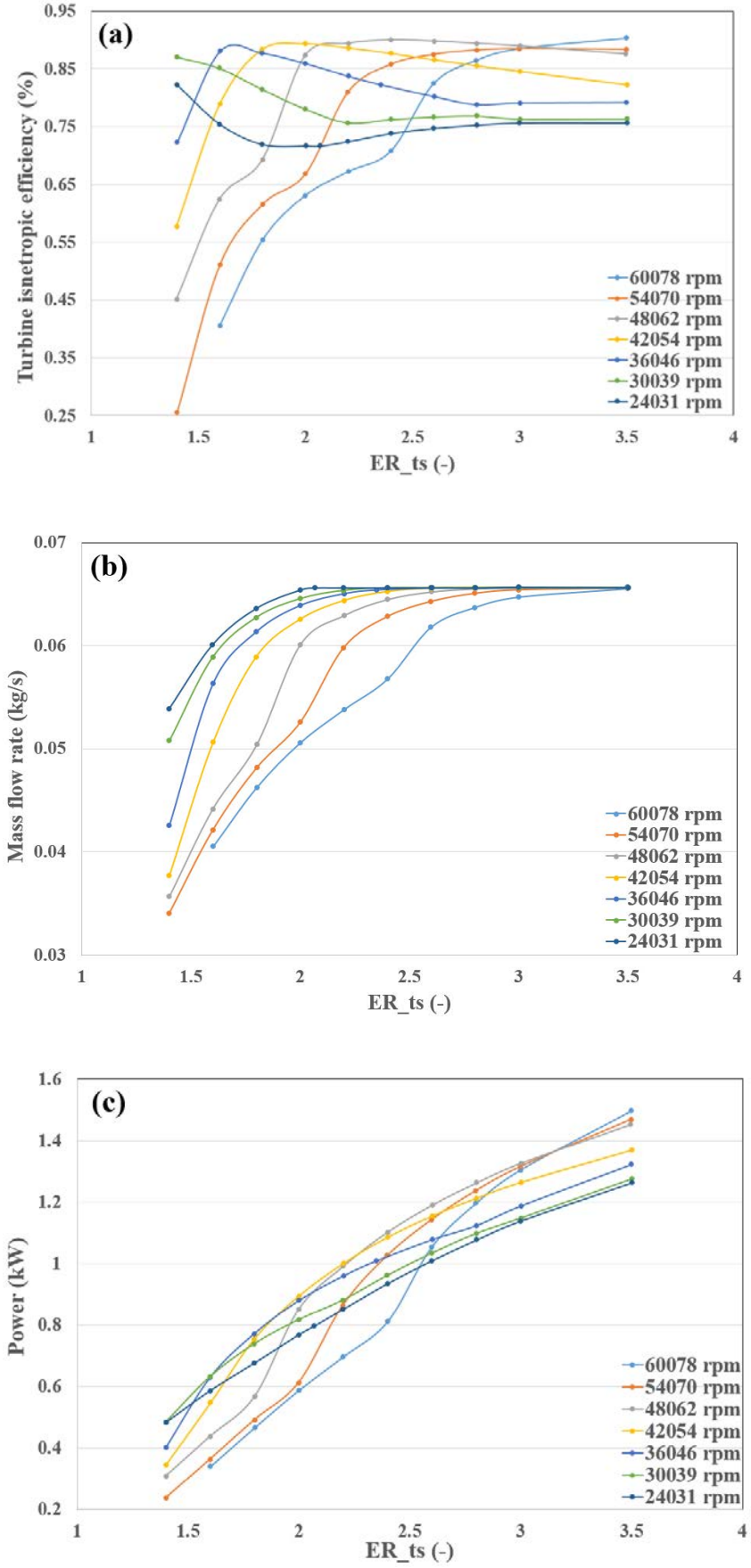

Figure 6-24 Off-design performance prediction of the optimized stage two using CFD

6.7. Modelling and CFD analysis of the Volute

Following the discussion in section 5.4.4, the volute is aimed for distributing the flow around the periphery of nozzle ring with almost uniform flow rate and static pressure. At the same time the total pressure drop should be minimized to avoid performance deterioration. Following the equations in section 5.4.4 and the mean-line results for stage one (Tables Table 5-9 and 5-10), the progression of the volute area (for a circular cross section) and mean and maximum radii were achieved. Based on such results the spiral coordinates at the outer diameter of the volute (d_{max}), Equation 5-26, against the polar angle were calculated and presented in Figure 6-25.

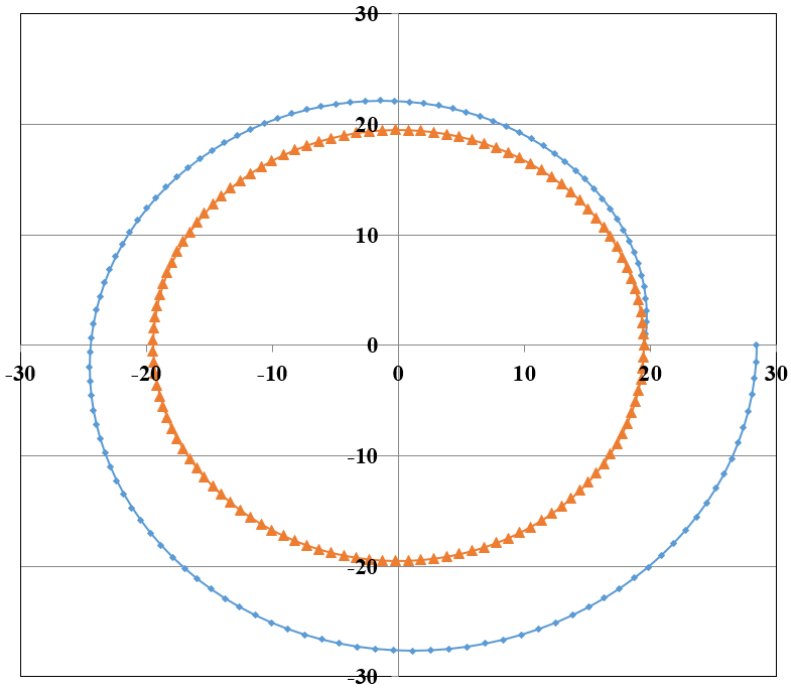

Figure 6-25 Volute spiral coordinates at the outer diameter

With the known area and radius progression, the volute cross sections (circular) were created at 15 equi-spaced planes (based on the polar angle). Then the cross sections were lofted together to create the volute solid geometry as presented in Figure 6-26. Theoretically, volute area should be zero at θ=360° (refer to Figure 6-25) but due to the

manufacturing limitation such value is not feasible, therefore the volute tongue was created at θ=345° and the area was kept fixed to θ=360°.

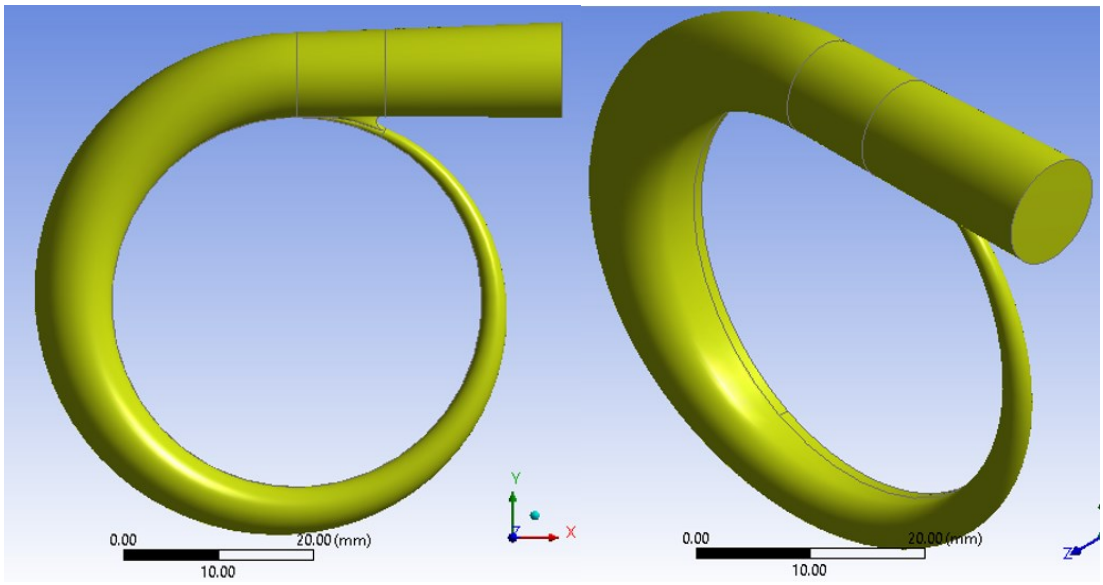

Figure 6-26 Volute 3-D geometry

Due to the complexity of the volute geometry, especially at the tongue, tetrahedron elements were employed to create the volute mesh using ANSYS^{R15} meshing. The mesh independence study for achieving minimum total pressure drop variation and also uniform flow angle at the volute exit resulted in 1130415 elements as depicted in Figure 6-27. The CFD setup for the volute was similar to section 6.5 except for the boundary conditions. The inlet total temperature and pressure of stage one organic RIT (refer to Table 5-9) was specified at the volute inlet while the mass flow rate was set at the volute outlet as the outlet static pressure was unknown. Figure 6-28 presents the CFD setup for the volute. The results of CFD analysis are depicted in Figure 6-29. As it is clear, the volute provides a very uniform and smooth flow around its periphery without any flow reversal. The flow velocity was low as expected in majority of the volute volume except for the region near the tongue where it was accelerated due to considerably small cross sectional area.

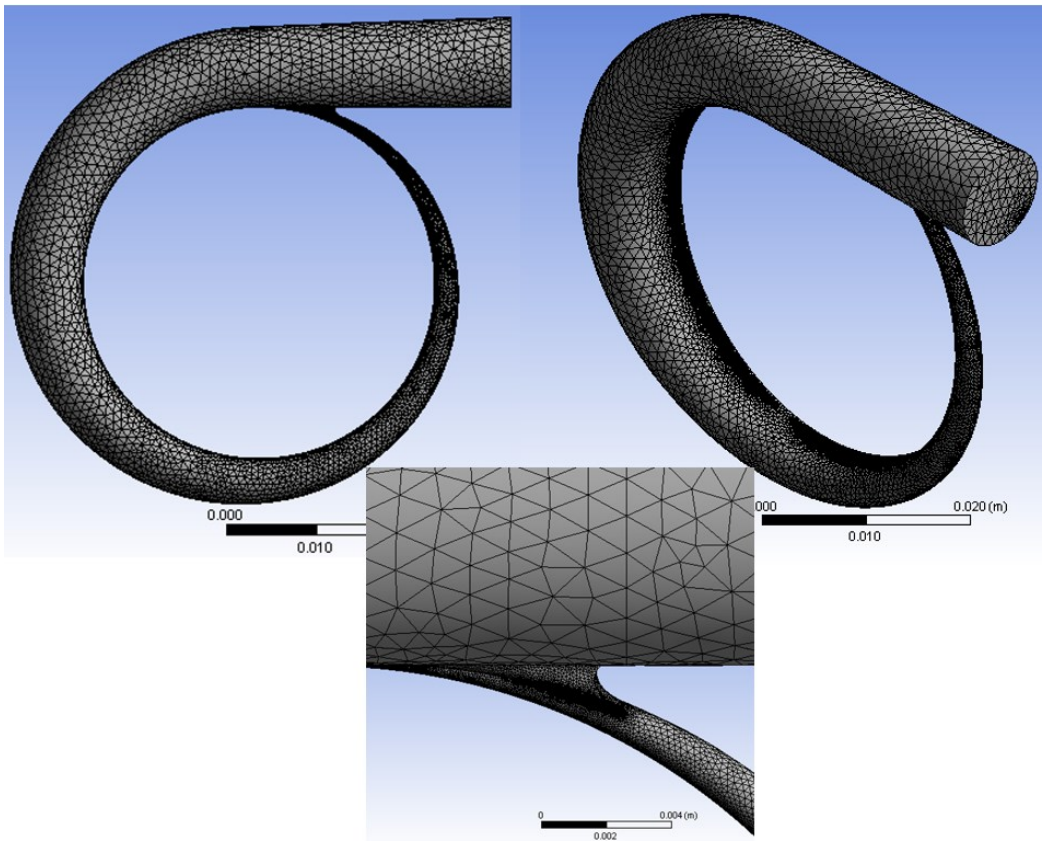

Figure 6-27 Volute tetrahedron mesh (top) overall geometry (bottom) zoom-in the volute tongue

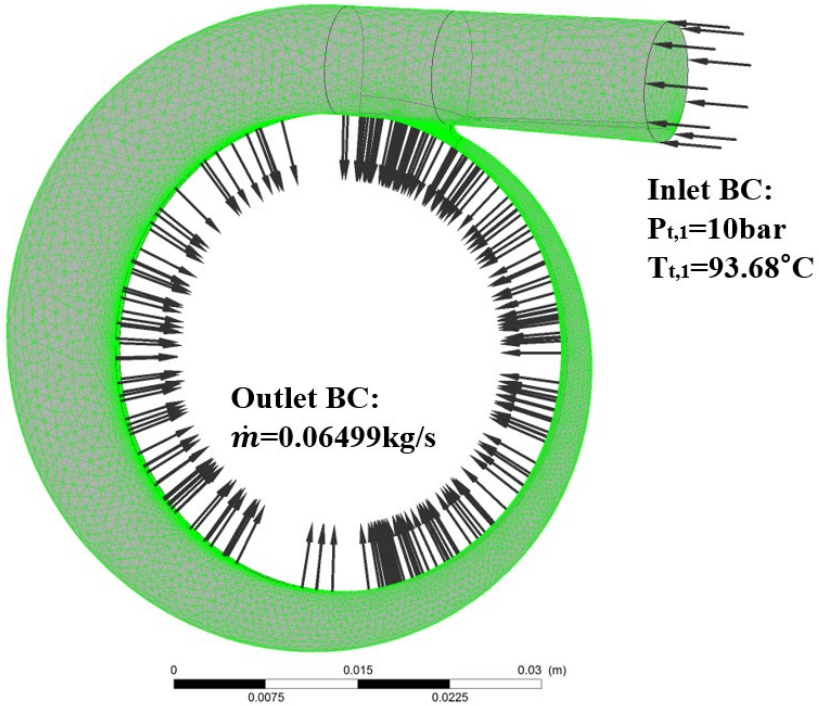

Figure 6-28 Volute CFD setup

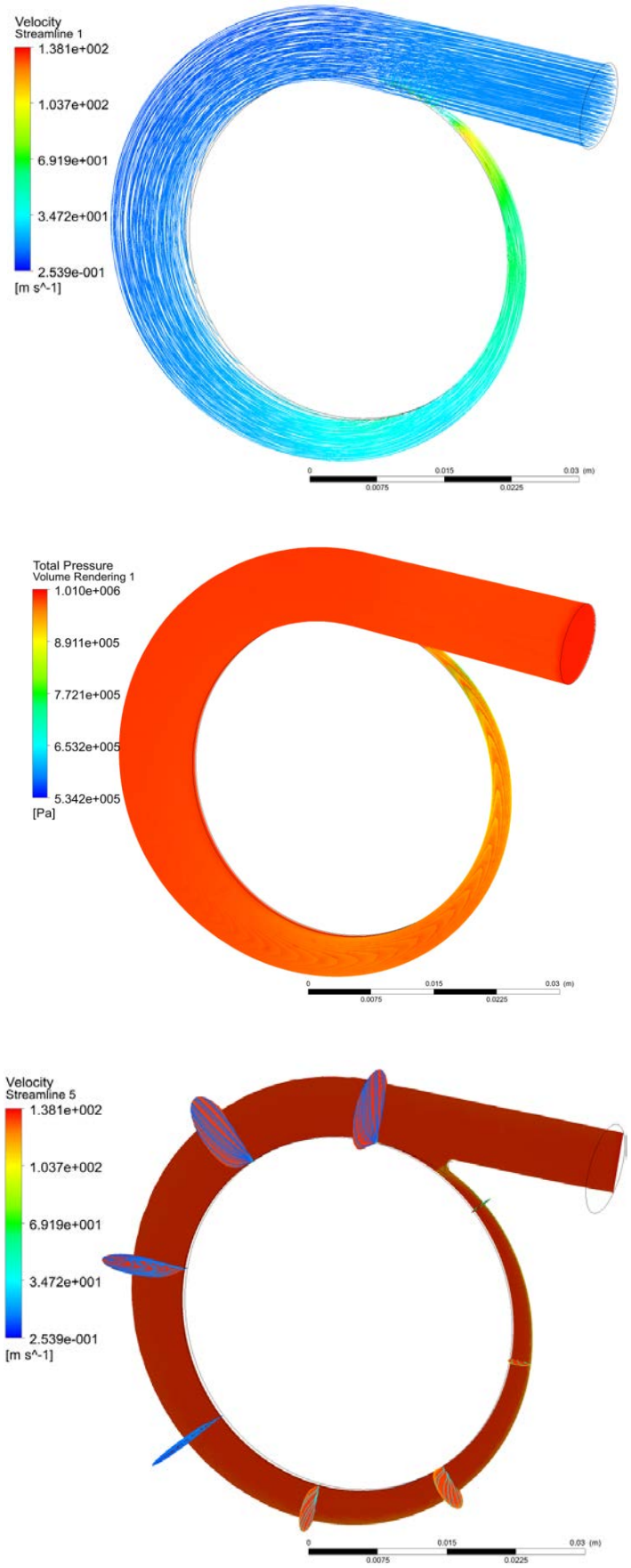

Figure 6-29 Volute CFD results

The contours of total pressure in the same figure depicts that the total pressure was almost constant around the volute with the value of about 10bars as needed. Such results indicate that the volute has very good aerodynamic performance with minimal losses. Also the section planes with velocity streamlines in the same figure confirm the uniformity of the total pressure with preferential flow in the volute.

6.8. Modelling and CFD analysis of the return channel

Figure 6-30 presents a schematic of the return channel employed between the two stages. It consists of an inlet 90° turn, a vane-less channel and a 180° crossover bend which redirects the flow back to the inlet of the second stage. The choice of the contours (i.e. circular or elliptical) for the inlet turn and crossover are followed by the recommendations of (Aungier 2000).

The systematic construction of the return channel provides a straightforward design with high aerodynamic performance. Designing such component requires the specification of $r_{5,hub}$ and $r_{5,tip}$ from stage one and b_1 (equal to b_3 in Figure 6-30) and r_2 (equal to r_3 in Figure 6-30) from stage two. For the inlet bend it's required to specify A_{turn} and r_{turn} together with Z_{rc}. Then the centre point for both the hub elliptical arc and the shroud circular arc is located at $z=Z_{rc}$ and $r= r_{turn}+ r_{1,tip}$ while the hub elliptical contour were determined as below:

$$B_{turn} = r_{1,tip} - r_{1,hub} + r_{turn} \qquad \text{Equation 6-6}$$

$$r = r_{1,tip} + r_{turn} - B_{turn}\sqrt{1 - \frac{(z - Z_{rc})^2}{{A_{turn}}^2}} \qquad \text{Equation 6-7}$$

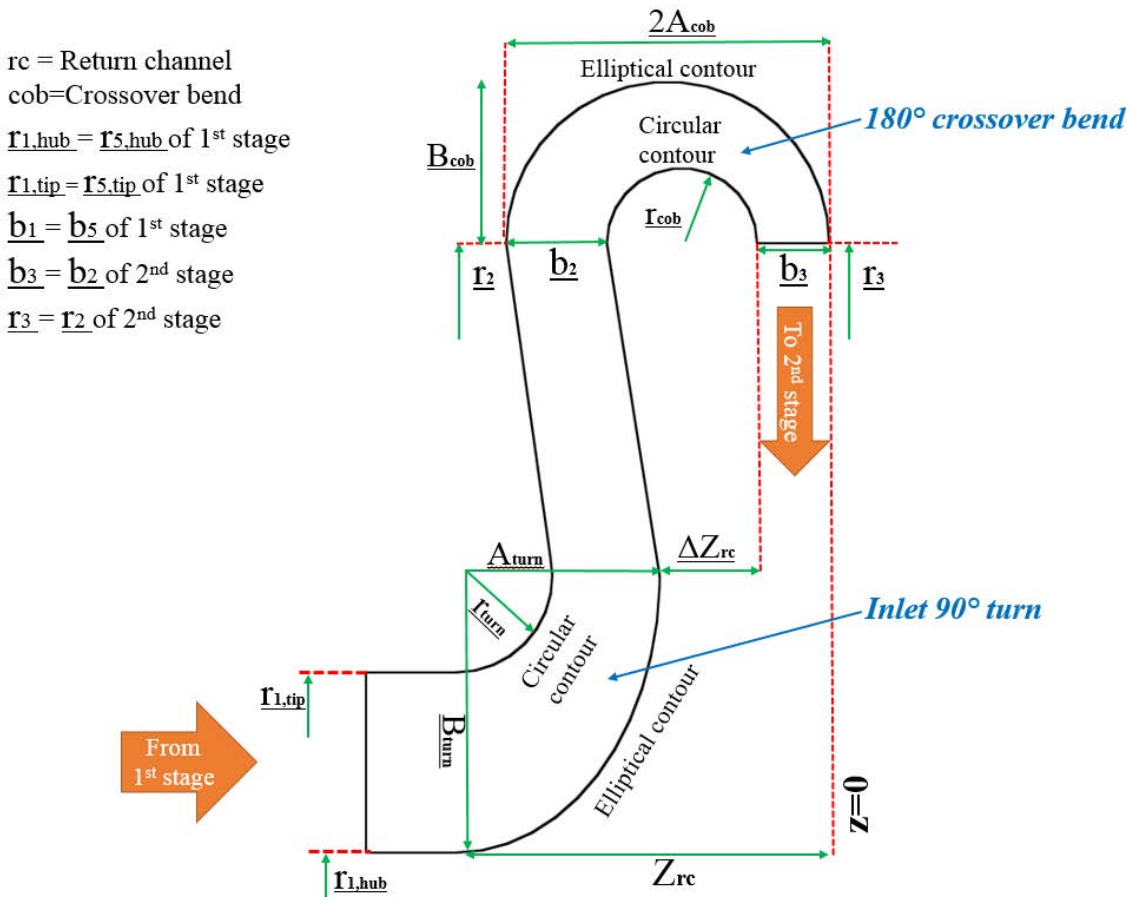

Figure 6-30 Schematic of the return channel geometry

The crossover r_{cob} and b_2 in Figure 6-30 should be specified as inputs in the following ranges suggested by (Aungier 2000).

$$b_3 \leq b_2 \leq 2b_3 \qquad \text{Equation 6-8}$$

$$r_{cob} = \frac{(b_2 + b_3)}{2} \; while \; r_{cob} \geq 0.8\left(\left(r_{5,tip} - r_{5,hub}\right) - b_2\right) \qquad \text{Equation 6-9}$$

Then the centre point of the crossover circular arc is located at $z = b_3 + r_{cob}$ and $r = r_3$ while the shroud contour was calculated as following:

$$A_{cob} = r_{cob} + \frac{(b_2 + b_3)}{2} \qquad \text{Equation 6-10}$$

$$r = r_3 + B_{cob}\sqrt{1 - \frac{(z - A_{cob})^2}{{A_{cob}}^2}} \qquad \text{Equation 6-11}$$

Where B_{cob} was specified as input based on the maximum packaging size.

Based on the above formulation, the 3-D geometry of the return channel was created and the grid was generated using ANSYS^{R15} meshing as depicted in Figures Figure 6-31 and 6.32 respectively. The mesh independence study for achieving minimum total pressure drop and also uniform flow at the inlet of second stage nozzle resulted in 322001 elements. The CFD setup for the return channel was similar to the volute in terms of the boundary conditions. The exit total temperature and pressure of the stage one rotor were specified at the inlet of return channel while the mass flow rate was set at the outlet. Figure 6-33 presents the CFD setup and the results are depicted in Figure 6-34. Obviously, there is no significant temperature or pressure drop in the return channel as shown by the contours. Moreover, the return channel distributed the flow evenly and uniformly from inlet to exit with no stagnation area in the channel as shown by the velocity streamlines.

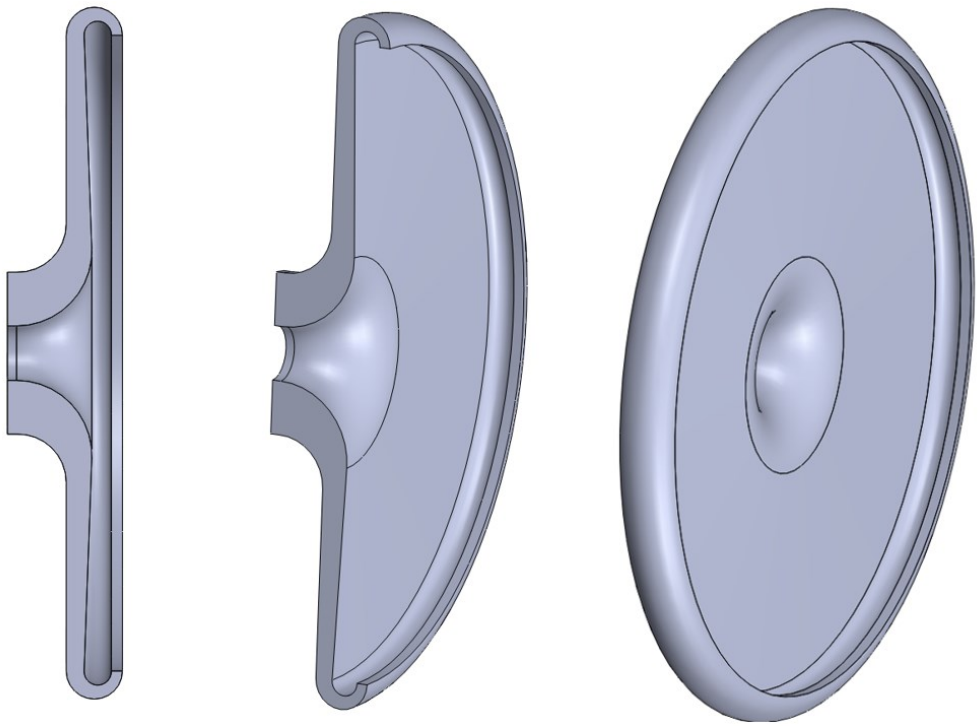

Figure 6-31 3-D geometry of the return channel

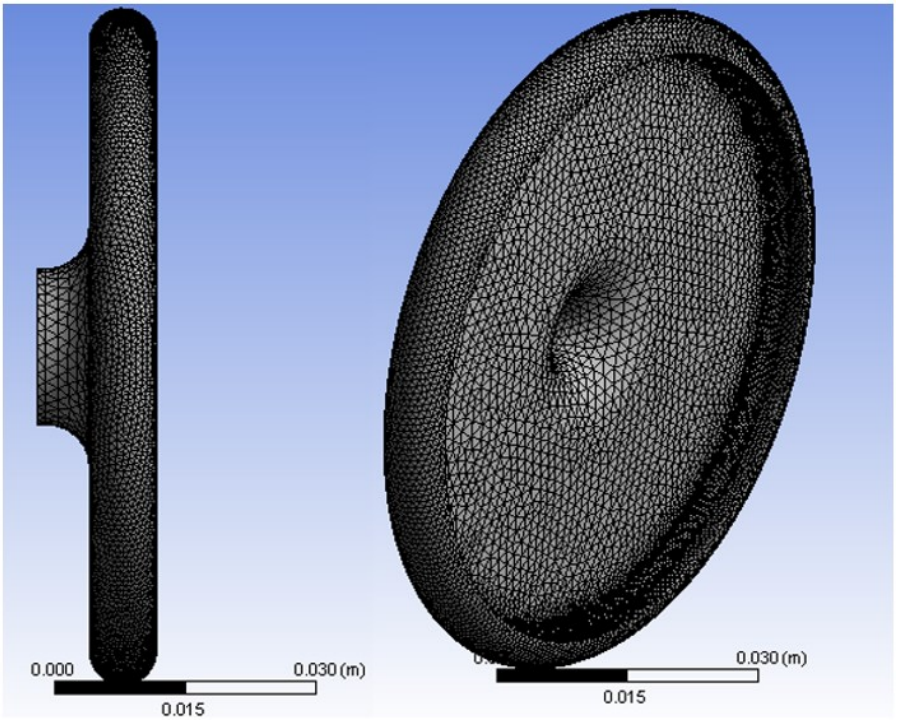

Figure 6-32 Generated tetrahedron mesh for the return channel

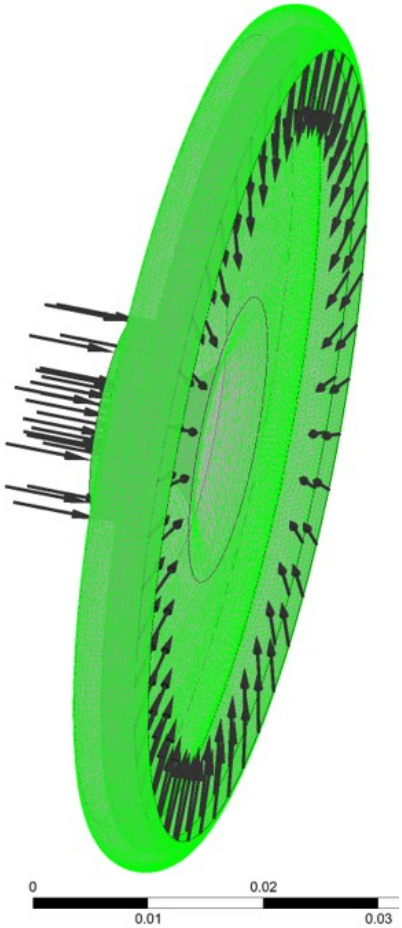

Figure 6-33 Return channel CFD setup

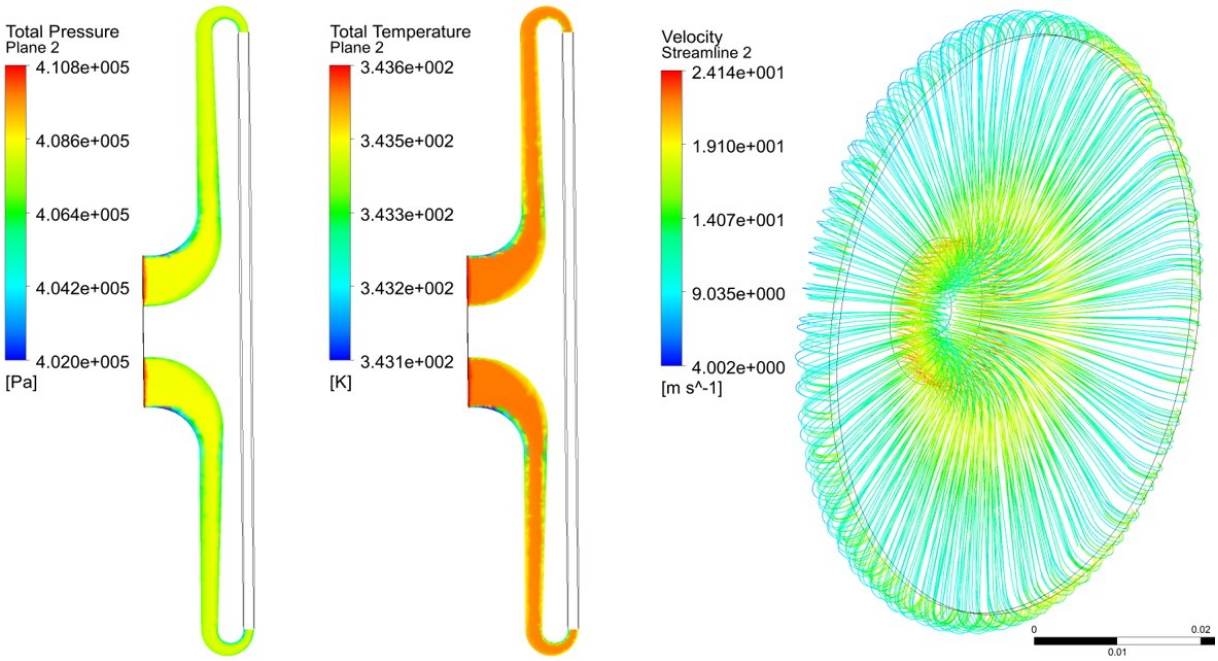

Figure 6-34 Return channel CFD results

6.9. CFD analysis of the optimized dual-stage organic RIT

Although results in Figures Figure 6-23 and 6.24 showed that both stages were effectively optimized, such results were obtained for each stage separately and without the inclusion of the volute and return channel. Therefore, the CFD model was set up for the complete dual-stage organic RIT including the volute, stage one nozzle and rotor, return channel and stage two nozzle and rotor to carry out the similar off-design CFD simulations as in section 6.6. The CFD setup of the dual-stage organic RIT with details of boundary conditions is presented in Figure 6-35. The mixing plane interface was specified between any adjacent rotating and stationary components while GGI connection was specified between any adjacent stationary parts. Initially the CFD analysis was performed at the design point operating condition (Table 5-9) with inlet total temperature and pressure specified at the inlet while static pressure was specified at the outlet. The results of such simulation are depicted in Figures Figure 6-36 to 6.38.

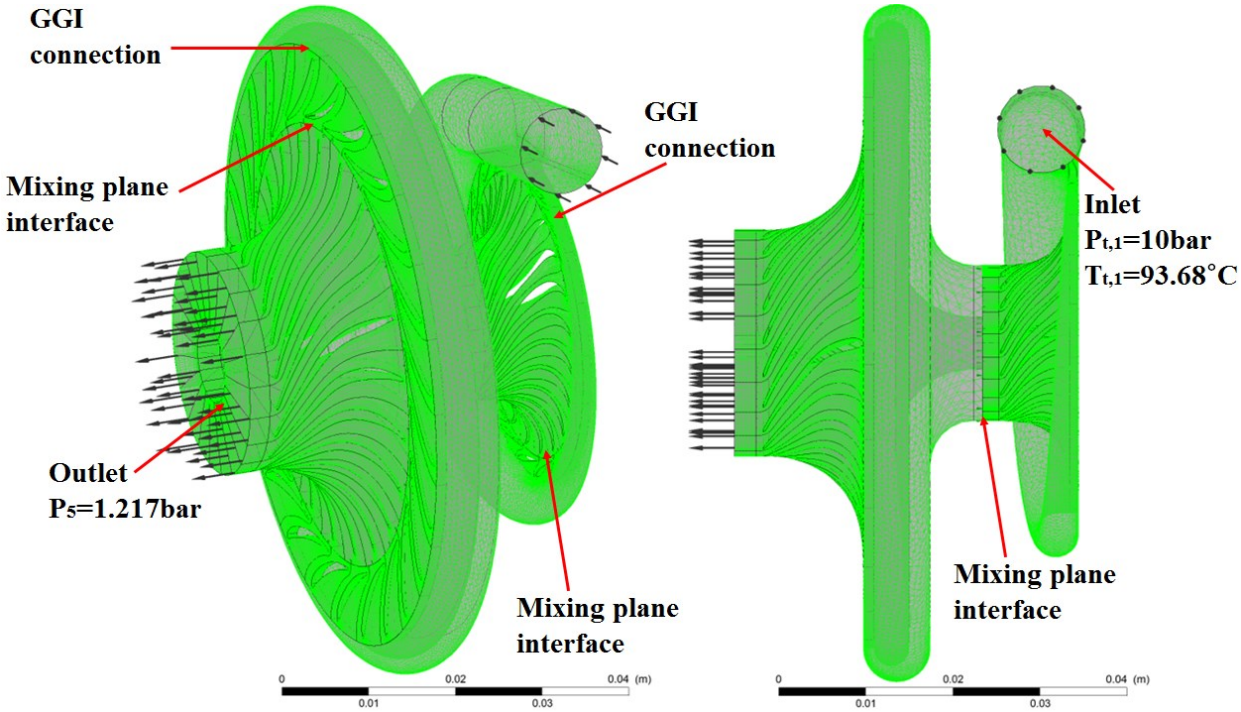

Figure 6-35 CFD setup for the dual-stage organic RIT including volute and return channel

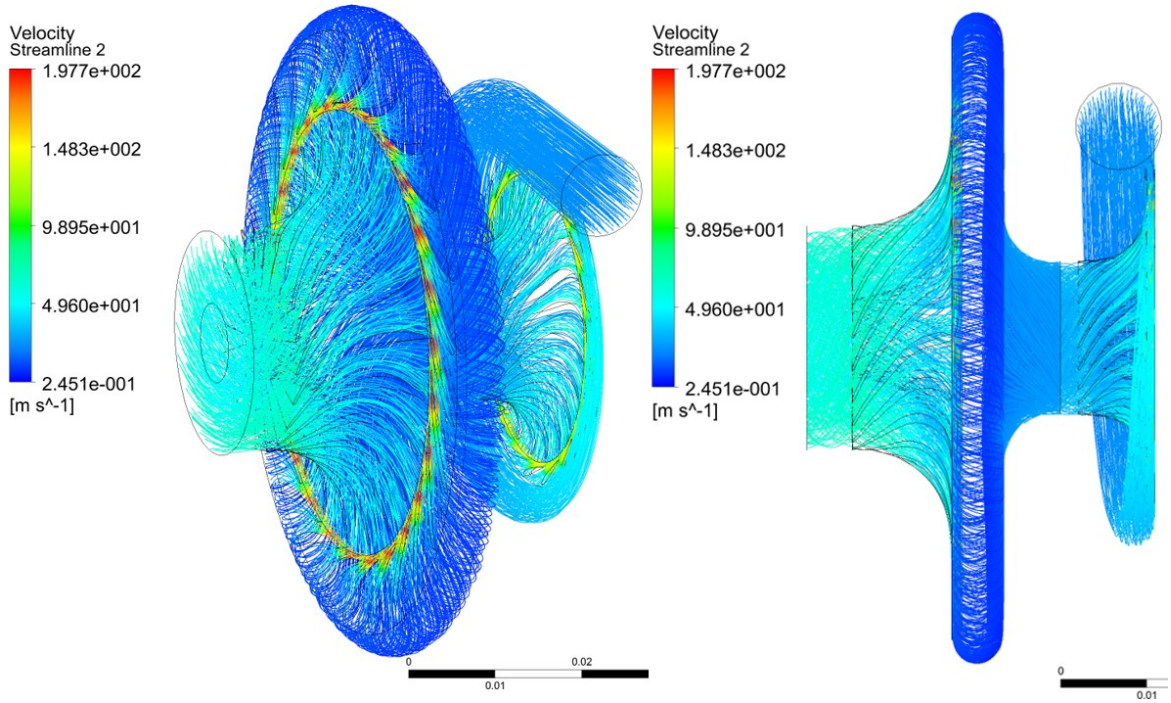

Figure 6-36 Dual-stage organic RIT CFD results at the design point - velocity streamlines

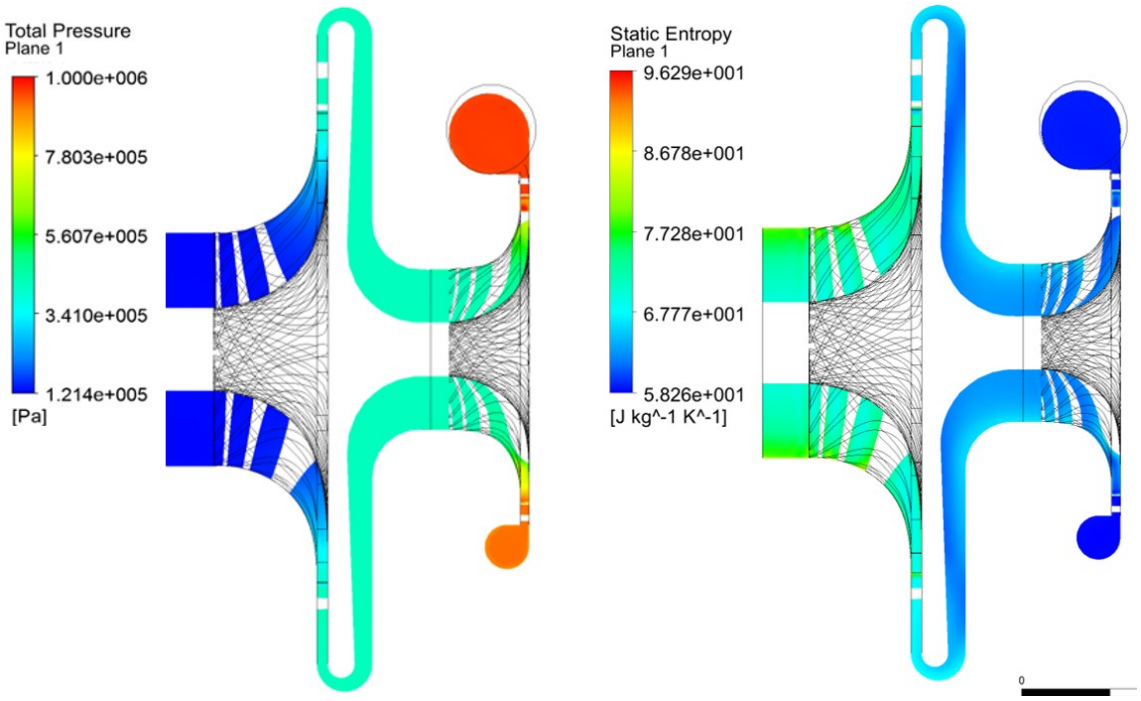

Figure 6-37 Dual-stage organic RIT CFD results at the design point- total pressure distribution (left) entropy distribution (right)

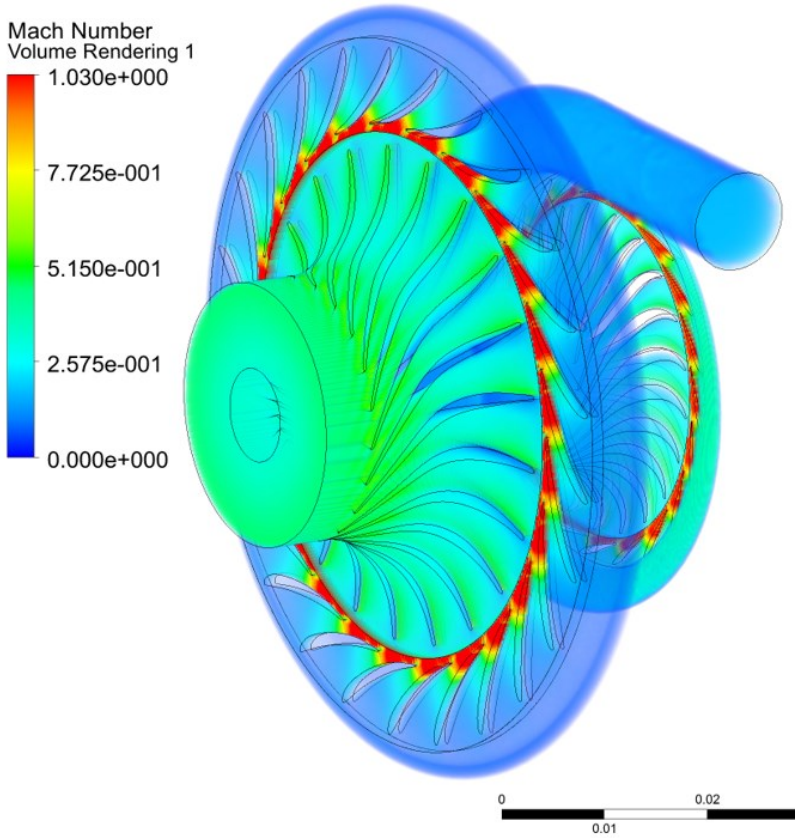

Figure 6-38 Dual-stage organic RIT CFD results at the design point- volume rendering of Mach number

As it is evident in Figure 6-36, both the volute and return channel were designed with high aerodynamic performance as they provided the flow at correct incidence angle and uniform flow around the periphery of the nozzles in both stages. There is no evidence of severe flow separation anywhere in the stage and the flow is preferential and smooth. The contours of the total pressure in Figure 6-37 illustrates that the pressure drop is distributed between the two stages while the entropy distribution shows fairly low losses in majority of the dual-stage turbine. Moreover, the volume rendering of the Mach number across the stage (Figure 6-38) ensures that there is no evidence of choking in the volute and return channel and thus no performance deterioration. Furthermore, the Mach number level at the interspace channel in both stages is slightly above unity due to the detailed CFD design of the interspaces as discussed previously but with entirely negligible effect on the performance.

The off-design performance prediction of the optimized dual-stage organic RIT was performed using the CFD model shown in Figure 6-35 by varying the rotational speed from 40% to 100% of the design speed (60078.24rpm) while the expansion ratio was varied from 3 to 8.22. The results of such simulations are presented in Figure 6-39. The maximum turbine efficiency of 87.12% was achieved at the design point with the rotational speed of 60078rpm and expansion ratio of 8.22 as presented in Figure 6-39(a). Such value is slightly lower than the efficiency of each stage individually due to small pressure losses in the volute and return channel. Moreover, the turbine exhibited fairly uniform performance over a wide range of expansion ratios and at each rotational speed. Such characteristic underlines the high aerodynamic performance of the developed turbine even under off-design operating conditions. Furthermore, as the rotational speed decreased the turbine efficiency reduced as well. The turbine at the design point was running very close to the choking conditions due to the low speed of sound for R245fa as

shown in Figure 6-39(b) while for the lower rotational speeds it was chocked at high expansion ratios. The mass flow rate was increased at the same expansion ratio while the rotational speed was reduced as depicted in the same figure. Moreover, at all off-design conditions the turbine power output was increased with the rise of the expansion ratio and at the design point the turbine produced a maximum power of 2.436kW as shown in Figure 6-39(c). Using the turbine performance parameters (i.e. power, efficiency and mass flow rate) at the design point (Figure 6-39) and setting those as inputs to the ORC standalone code (developed in chapter five) resulted in the cycle thermal efficiency of 13.19% compared to 11.94% obtained from the mean-line optimization (refer to Table 5-10) with relative improvement of 10.46%. Such results highlights the potential and effectiveness of the 3-D CFD optimization approach performed in this chapter to further improve the ORC performance. Utilizing the turbine performance parameters as the turbine isentropic efficiency, expansion ratio, power output and mass flow rate from Figure 6-39 and inserting them into the ORC-standalone code (chapter 5), the ORC off-design performance can be obtained as shown in Figure 6-40. As it is evident in Figure 6-40 (a), the ORC thermal efficiency is fairly uniform over a wide range of expansion ratios especially for ER_{ts} greater than 5. Such results exhibit good ORC off-design performance even if the heat source is supplied by the renewables such as solar or geothermal heats which significantly affected by the environmental changes. Such trend can be attributed to the fairly uniform off-design performance of the dual-stage organic RIT that was shown in Figure 6-39 (a). Apparently, the larger the ER_{ts} and rotational speed the larger the ORC net power output as presented in Figure 6-40 (b). Such results are substantially beneficial for assessing the system performance, component selection and cost analysis as well as integrating the ORC system with a topping cycle (cascading). The maximum obtained ORC thermal efficiency of 13.19% (at the cycle design point) is

significantly higher than the other studies in the literature (with almost the same temperature difference between the evaporator and condenser) and highlights the benefits of the high performance expander that can lead to high cycle efficiency. Such goal was achieved in this thesis by developing and implementing novel techniques and approaches such as mean-line optimization, dual-stage transonic RIT configuration and three-dimensional CFD optimization that were originated from a methodology that was validated with experimental results (chapter 4). Details of CAD drawings of the developed dual-stage transonic organic RIT including the nozzles, rotors, shaft, volute, return channel and all the complementary parts are provided in Appendix D and can be used for future manufacturing and experimental testing. In addition, the schematic of the ORC suitable for experimental testing of the the developed dual-stage RIT is provided in Appendix E.

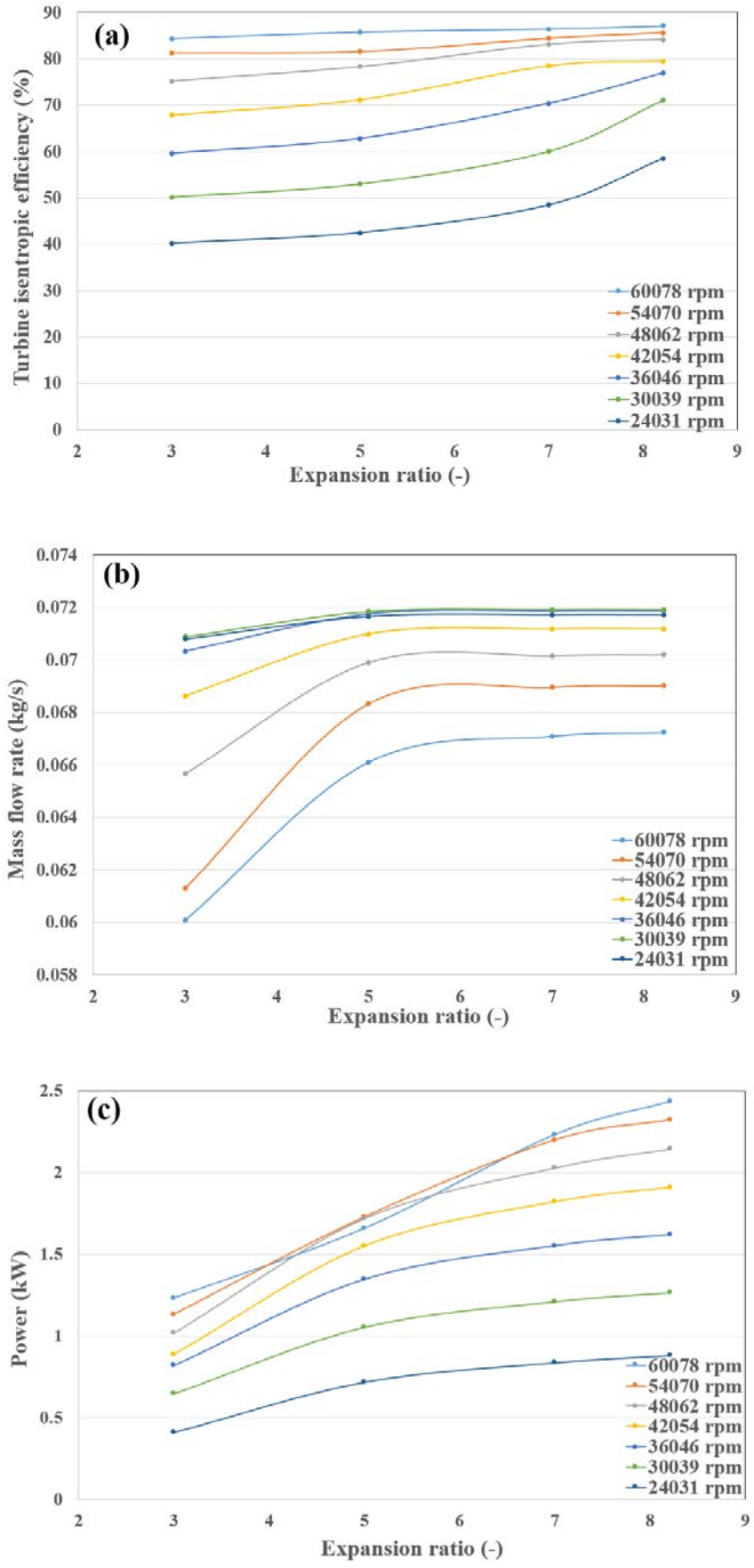

Figure 6-39 Off-design performance prediction of the optimized dual-stage organic RIT using CFD

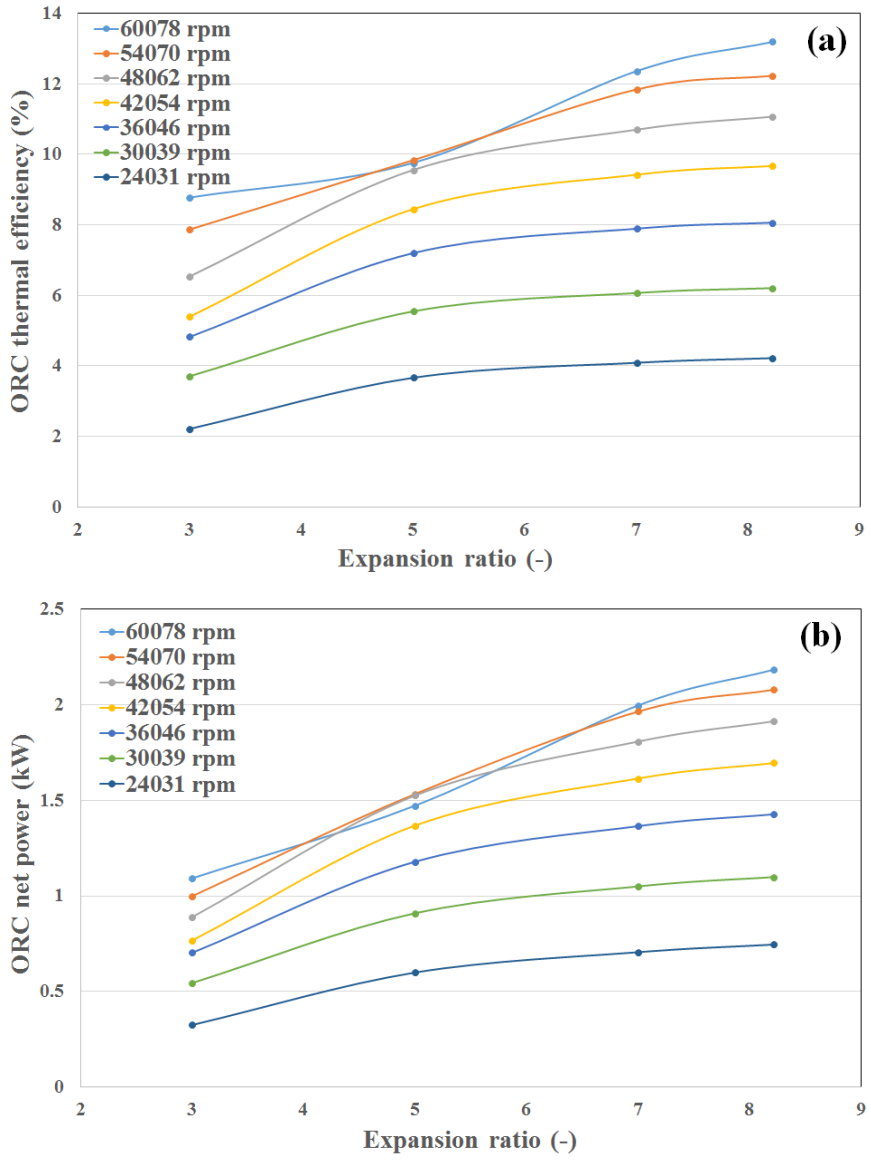

Figure 6-40 Off-design performance prediction of the ORC based on the dual-stage optimized RIT

6.10. Summary and conclusions

In this chapter a novel 3-D CFD optimization technique was employed to further maximize the performance of the dual-stage organic RIT developed in chapter five. The optimization method consists of optimal space filling (OSF) design of experiment (DOE), Kriging Meta-model and GA optimization technique. The OSF created a database of sample points to provide maximum insight about the design space. Then the Kriging Meta-model fits an approximation function through all the sample points to provide fast and accurate estimation of the turbine performance without the need of RANS solver.

Such Meta-model was employed by the GA to optimize the efficiency of each stage separately by variation of the blade geometry. The optimization results showed that the efficiencies of stage one and stage two were increased by 9.2% and 10.5% respectively compared to the baseline designs. Such improvements were explained by comparing the rotor flow field for both stages in terms of velocity vectors and entropy distribution both in blade-to-blade and meridional planes. In addition, off-design CFD simulations of each stage were conducted individually to investigate their performance at various rotational speeds and expansion ratios which can be used for performance estimation of the ORC systems that are mostly operating at off-design conditions (especially those that the heat source is supplied by renewables). The volute and return channel were designed and simulated using CFD to assure high aerodynamic performance with minimal losses. Eventually, the CFD analysis of the complete dual-stage organic RIT including the volute, nozzles and rotors in both stages and return channel were carried out both at the design point and many off-design points with the maximum relative improvement of 10.46% in the cycle thermal efficiency at the design point. Such results provide a reliable estimation of the developed organic RIT performance under various operating conditions and can be integrated with the ORC analysis code to determine the cycle thermal efficiency at various off-design conditions.

CHAPTER 7

CONCLUSIONS AND RECOMMENDATIONS FOR FUTURE WORK

7.1. Introduction

Adoption of environmentally benign and renewable energy conversion technologies is essential if our society is to retain its advanced lifestyle in the face of the global development. The use of diversified renewable/waste heat sources has been considered as part of an array of potential solutions for more efficient power generation systems throughout the world. Organic Rankine cycle (ORC) is becoming one of the most reliable technologies that can be used for efficient conversion of such low to medium grade heat applications. In this regard, expander is a key component in a relatively efficient ORC system and its performance has significant effect on the overall cycle efficiency. Due to the low temperature difference between the heat source and heat sink, the ORC thermal efficiency is normally low (but still higher than SRC as long as the heat source

temperature is below 350°C), therefore developing highly efficient expander is crucial for achieving high cycle performance.

7.2. Conclusions

The present study is a comprehensive investigation of different strategies for efficient design and optimization of radial inflow turbines (RIT) as the expander of small-scale ORC systems with the power capacities of less than 5kWE. Such strategies were developed to accommodate the complex characteristics of the ORC systems such as real-gas fluid behaviour and high expansion ratios.

The key findings and the core contributions of the present research can be summarized as following:

- A methodology for design, optimization and experimental study of the small-scale RITs was developed that encompasses the one-dimensional mean-line modelling and optimization, three-dimensional CFD analysis and optimization and experimental testing and validation. Such methodology proved to be effective as it allows systematic investigation of the key input parameters on the turbine performance and multi-level optimization to reliably find the optimum turbine geometry that led to maximum performance.

- Initially the methodology was employed for developing a small-scale compressed air RIT for validation purposes. Mean-line modelling enabled fast and fairly accurate estimation of the turbine performance as well as obtaining the key geometrical parameters of the RIT stage. Such unique feature allowed investigating the effect of a large group of input parameters on the turbine performance and size. The parametric studies with the developed mean-line model showed that the turbine efficiency was affected by almost all of the investigated input parameters whereas the turbine power

output was mostly affected by $T_{t,1}$, $\dot{m}$, ER_{ts}, v and α_4 and the turbine rotor inlet diameter was only affected by $T_{t,1}$, ER_{ts}, v and ω. The results of such parametric studies were substantially useful for selecting the best values for the turbine input parameters that led to high performance.

- Although effective, mean-line modelling couldn't capture the complete behaviour of the flow within the RIT blade passages due to the three-dimensional and complex nature of such flow. Therefore, CFD analysis was used to investigate in greater details the candidate RIT configuration suggested by the mean-line model. CFD analyses showed that a more realistic and efficient turbine design can be achieved by subtle variation of the blade geometry in terms of the blade angle and thickness distributions, shape of leading edge and the number of rotor blades while assessing both quantitative (efficiency and power) and qualitative (velocity vectors, secondary flows, entropy contours and blade loading) CFD results. Such CFD analyses proved to be effective as the compressed air RIT isentropic efficiency was increased from 81.3% obtained from the mean-line modelling to 84.5% obtained by the CFD.

- Experimental testing of the compressed air RIT showed that the turbine efficiency was more sensitive to the turbine rotational speed while the turbine power was sensitive to both expansion ratio and rotational speed. The CFD model of the turbine stage was validated with the experiments. Results showed that the CFD model can predict the turbine efficiency with accuracy of $\pm$16% while the turbine power was predicted with accuracy of $\pm$13%. The CFD model could predict the turbine performance with better accuracy at higher rotational speeds compared to lower speeds. It was expected that if the fabricated experimental facility was capable of running at higher rotational speeds the error could even decrease further. The results

underlined the effectiveness of the proposed methodology and showed that the CFD model can be used as benchmarking model for analyses of small-scale RITs with good accuracy.

- Screening of twelve organic fluids (both hydrocarbons and refrigerants) by extending the developed mean-line model for organic RITs showed that, the ideal-gas formulation was not satisfactory as the fluids exhibited strong real-gas behaviour at the turbine inlet with compressibility factors considerably lower than unity (about 0.8) and necessitated the use of real-gas equations both in mean-line modelling and CFD simulation.

- The proposed integrated mean-line modelling of organic RIT with the ORC analysis code based on real-gas formulation and coupled with genetic algorithm (GA) optimization technique proved to be very effective as it not only captured the real-gas behaviour of the organic fluids but also replaced the constant turbine efficiency with a dynamic efficiency that was unique for each set of cycle operating conditions and working fluid properties and ensured the optimum combination of input parameters that led to maximum cycle thermal efficiency (global optimum).

- Parametric studies with the ORC-RIT model showed that the $\eta_{thermal,cycle}$, $\eta_{stage,ts}$ and d_{max} were all affected by the variations of $T_{t,1}$, $\dot{m}$, ER_{ts}, ω, φ and ψ. Comparing the parametric study results of the ORC standalone model (with constant turbine efficiency assumption) with ORC-RIT model exhibited that there were significant differences in the $\eta_{thermal,cycle}$ of all investigated organic fluids especially at high ER_{ts} and low $\dot{m}_{wf}$ with the maximum difference of 4.65% for R134a. Such operating conditions were in fact typical for small-scale ORC systems and at such conditions $\eta_{stage,ts}$ dropped drastically leading to reduction in $\eta_{thermal,cycle}$. This critical feature was

overlooked by the ORC standalone model and underlined the deficiencies of assuming constant $\eta_{stage,ts}$ and the inaccuracies it caused in cycle analysis results.

- GA optimization of $\eta_{thermal,cycle}$ with both ORC standalone and ORC-RIT models demonstrated that not only the former model over-predicted $\eta_{thermal,cycle}$ of all investigated fluids (with maximum value of 1.4% for n-pentane) compared to the latter model (due to neglecting the effect of $\eta_{stage,ts}$) but also there were discrepancies in the ranking order of the most efficient organic fluids between the two models. R123 exhibited the highest $\eta_{thermal,cycle}$ of 12.9% and 11.67% with the ORC standalone and ORC-RIT models respectively but there were variations in the ranking order of R1233zd, n-pentane, R365mfc and R245fa working fluids between the two models. Such results showed that constant $\eta_{stage,ts}$ assumption with the ORC standalone model can bring unfairness to the analysis and reduce the accuracy of the results and can be miss-leading while selecting the most efficient working fluids. In contrast, the ORC-RIT model provided the reliable estimation of the turbine efficiency (based on turbine aerodynamic losses) and resulted in improved performance prediction and realistic analysis of the ORC based on small-scale organic RITs.

- The proposed GA optimization technique was very effective as it allowed the true analytical optimization of a broad range of ORC-RIT model input parameters that included the effects of both cycle and turbine design variables and led to maximum $\eta_{thermal,cycle}$. The GA optimizations were efficient and successful as the optimized non-dimensional parameters (ψ, φ, N_s) were in the range of optimum RIT performance suggested by the generalized performance correlation charts in the literature while simultaneously satisfying all the imposed constraints to ensure feasibility of the optimized organic RIT geometry.

- It was shown that, thermodynamically the larger the pressure difference (expansion ratio) across the cycle the higher the $\eta_{thermal,cycle}$. But the larger the expansion ratio across the turbine the larger the Mach number and turbine size and hence the larger the supersonic and friction losses respectively that deteriorated the $\eta_{stage,ts}$. Such results underlined the challenges regarding the development of an efficient small-scale RIT for ORC applications and revealed the reasoning for the maximum expansion ratio of 7 in majority of the published studies. Therefore, in this thesis a novel transonic dual-stage organic RIT was proposed using R245fa as the working fluid (due to its competetive performance, cost and availability) that not only preserved high $\eta_{stage,ts}$ but also maintained the high expansion ratio of 10 and consequently led to high $\eta_{thermal,cycle}$. Such configuration resulted in 7.95% relative improvement in $\eta_{thermal,cycle}$ when comparing the single-stage supersonic RIT with dual-stage transonic RIT both operating with R245fa. Therefore, such configuration proved to be advantageous as it both alleviated the complex fluid dynamics and degradation of $\eta_{stage,ts}$ due to shock losses while it increased $\eta_{thermal,cycle}$ for maximum utilization of waste heat.

- The developed correlations based on linear regression analysis proved to be effective as they could predict with good accuracy the maximum obtainable $\eta_{stage,ts}$ and the corresponding turbine size for a wide range of operating conditions and working fluids. Such correlations used only few key design parameters without the need of knowledge of working fluid properties or the need for performing the complete turbine design procedure. Replacing the constant $\eta_{stage,ts}$ assumption with the developed correlation for $\eta_{stage,ts}$ in the ORC standalone model showed that the differences in $\eta_{thermal,cycle}$ of the ORC standalone model and ORC-RIT model were reduced considerably for majority of investigated fluids. The maximum difference in

$\eta_{thermal,cycle}$ was reduced to 0.89% for R365mfc compared to the 1.4% for n-pentane when assuming constant $\eta_{stage,ts}$. More importantly, the ranking order of the fluids was exactly the same in the ORC standalone model using the developed correlation for $\eta_{stage,ts}$ compared to the ORC-RIT model. Such results highlighted that the developed correlations can be used in general optimization procedures of the ORC systems to further improve the performance estimation and working fluid selection.

- Conducting the 3D CFD optimization of the dual-stage transonic RIT operating with R245fa based on OSF DOE, Kriging Meta-model and GA optimization algorithm was very effective as it improved the stage one and stage two $\eta_{stage,ts}$ by 9.2% and 10.5% respectively while increasing the power by 11.4% and 13.4%. Such results showed that the parametrization of the rotor blade geometry was crucial in achieving such improvements and the approach employed in the thesis provided enough flexibility for the optimizer to effectively search for the best geometry. Moreover, it was shown that both the blade camber angle profile as well as the meridional channel shape were responsible for the improvements in $\eta_{stage,ts}$ by assessing the flow field in terms of velocity vectors and entropy distribution.

- Conducting the off-design CFD simulations for a wide range of expansion ratios and rotational speeds for each stage individually as well as the complete dual-stage RIT revealed that in all cases the design point was equivalent to the highest efficiency point and highlighted the effectiveness and reliability of both mean-line and CFD optimizations. Furthermore, the CFD simulations of the dual-stage RIT exhibited fairly uniform $\eta_{stage,ts}$ over a wide range of expansion ratios (good off-design performance) with the maximum $\eta_{stage,ts}$ of 87.12% and maximum power of 2.436kW achieved at the design operating point. Such results led to cycle thermal efficiency of

13.19% compared to 11.94% obtained from the mean-line optimization with relative improvement of 10.46% and underlined the effectiveness of the 3-D CFD optimization approach performed in this thesis to further improve the ORC performance.

- Such results were considerably higher than the reported values for other types of expanders in the literature and highlighted the potential and effectiveness of the combined mean-line and CFD optimizations approaches proposed and developed in the thesis. With the validated CFD model such tool can be used for further analysing and optimizing small-scale RITs to enhance the ORC performance.

7.3. Recommendations for future work

The present study is a step toward developing efficient RITs for small-scale ORC systems. However, more research is required in the following aspects:

- The developed mean-line model was capable of only *designing and optimizing* the RITs at their design point (new geometries are created based on each set of input parameters). However, it is suggested to extend the model so that it can also be used for the *analysis* of RITs where the geometry is obtained and fixed from the *design code* and then imported to the *analysis code* to assess its performance under off-design operating conditions. Such feature is particularly important as it allows the multi-point mean-line optimization of RITs for the ORC systems that are subjected to the heat source fluctuations (i.e. solar or geothermal heat) and is helpful for optimizing the cycle performance over a range of operating conditions and not only at a single design point.

- It is suggested to conduct the same optimizations as in chapter five but instead of the simple ORC layout, both the recuperated ORC and supercritical ORC systems be

investigated. Such analyses are beneficial for the cases that the turbine exit temperature is substantially high or the high pressure in the evaporator can be controlled at the higher initial investment cost (suitable for larger scale ORC systems).

- It's suggested to replace the toque meter with high-speed alternators (upon their availability and subject to cost) to extend the range of the experimental data to higher rotational speeds and assess the accuracy of the CFD models.
- Performance comparison of the developed dual-stage organic RIT is suggested with multi-stage axial flow or radial outflow turbines with the same power capacity. Such comparison can further validate the superiority and advantages of the RIT and possibly revealing the areas that need improvement.
- Experimental testing of the developed dual-stage organic RIT can be conducted by fabricating the ORC and the turbine (refere to Appendices D and E) and the effect different working fluids such as R245fa as well as R1233zd can be investigated.

List of References

Ackermann, T., G. Andersson and L. Söder (2001). "Distributed generation: a definition." *Electric Power Systems Research* **57**(3): 195-204.

Al-Sulaiman, F. A., F. Hamdullahpur and I. Dincer (2011). "Greenhouse gas emission and exergy assessments of an integrated organic Rankine cycle with a biomass combustor for combined cooling, heating and power production." *Applied Thermal Engineering* **31**(4): 439-446.

Aungier, R. H. (2000). *Centrifugal Compressors: A Strategy for Aerodynamic Design and Analysis*. New York, ASME press.

Aungier, R. H. (2006). *Turbine aerodynamics : axial-flow and radial-inflow turbine design and analysis*. New York, ASME Press.

Baines, N. (2003). Part 3: Radial Turbine Design. *Axial and Radial Turbines*. VT, Concepts NREC**:** pp. 197-326.

Balje, O. E. (1981). *Turbomachines : a guide to design selection and theory*. New York, Wiley.

Bao, J. and L. Zhao (2013). "A review of working fluid and expander selections for organic Rankine cycle." *Renewable and Sustainable Energy Reviews* **24**(0): 325-342.

Benson, R. (1970). "A Review of Methods for Assessing Loss Coefficients in Radial Gas Turbines." *International Journal of Mechanical Sciences* **12**(10): 905-932.

Bloch, H. and A. Godse (2006). *Compressors and Modern Process Applications*, Wiley.

Bracco, R., S. Clemente, D. Micheli and M. Reini (2013). "Experimental tests and modelization of a domestic-scale ORC (Organic Rankine Cycle)." *Energy* **58**(0): 107-116.

Brasz JJ, Smith IK and S. N (2000). Development of a twin screw expressor as a throttle valve replacement for water-cooled chillers. *International compressor engineering conferance*. School of Mechanical Engineering, Purdue University, IN, USA.

Bronicki, L. (1972). *The Ormat Rankine power unit*. Proceedings of IECEC, SanDiego, USA.

Capata, R. and C. Toro (2014). "Feasibility analysis of a small-scale ORC energy recovery system for vehicular application." *Energy Conversion and Management* **86**(0): 1078-1090.

Churchill, S. (1977). "Friction-factor equation spans all fluid-flow regimes." *Chemical Engineering* **84**: 91–92.

Cipollone, R., G. Bianchi, D. Di Battista, G. Contaldi and S. Murgia (2014). "Mechanical Energy Recovery from Low Grade Thermal Energy Sources." *Energy Procedia* **45**(0): 121-130.

Clemente, S., D. Micheli, M. Reini and R. Taccani (2013). "Bottoming organic Rankine cycle for a small scale gas turbine: A comparison of different solutions." *Applied Energy* **106**(0): 355-364.

Curran, H. M. (1981). "Organic Working Fluids in Rankine Engines." *Journal of Energy* **5**(4): 218-223.

de Souza, R. and G. Filho (2011). "Automotive Turbocharger Radial Turbine CFD and Comparison to Gas Stand Data." *SAE Technical Paper 2005-01-1171*.

Delgado-Torres, A. M. and L. García-Rodríguez (2010). "Analysis and optimization of the low-temperature solar organic Rankine cycle (ORC)." *Energy Conversion and Management* **51**(12): 2846-2856.

DiPippo, R. (2005). Geothermal Power Plants: Principles, Applications and Case Studies. *Geothermal Power Plants*. R. DiPippo. Oxford, Elsevier Science.

Dixon, S. L. and C. A. Hall (2010). *Fluid mechanics and thermodynamics of turbomachinery*. Burlington, MA, Butterworth-Heinemann/Elsevier.

Dolz, V., R. Novella, A. García and J. Sánchez (2012). "HD Diesel engine equipped with a bottoming Rankine cycle as a waste heat recovery system. Part 1: Study and analysis of the waste heat energy." *Applied Thermal Engineering* **36**(0): 269-278.

El Chammas, R. and D. Clodic (2005). "Combined Cycle for Hybrid Vehicles." *SAE Technical Paper 2005-01-1171*.

Fiaschi, D., G. Manfrida and F. Maraschiello (2012). "Thermo-fluid dynamics preliminary design of turbo-expanders for ORC cycles." *Applied Energy* **97**(0): 601-608.

Galloway, E. and L. Hebert (1836). *History and progress of the steam engine; with a practical investigation of its structure and application*. London, Printed for T. Kelly.

Gen, M. and R. Cheng (2000). *Genetic Algorithms and Engineering Optimizations*. Canada, John Wiley and sons.

Glassman, A. J. and C. Lewis Research (1976). *Computer program for design analysis of radial-inflow turbines*. Washington, D.C. : [Springfield, Va., National Aeronautics and Space Administration ; For sale by the National Technical Information Service].

Glavatskaya, Y., P. Podevin, V. Lemort, O. Shonda and G. Descombes (2012). "Reciprocating Expander for an Exhaust Heat Recovery Rankine Cycle for a Passenger Car Application." *Energies* **5**(6): 1751-1765.

Green, D. and R. Perry (2008). Property calculations for gases and vapors *Perry's Chemical Engineers' Handbook, Eighth Edition*, McGraw Hill Professional, Access Engineering.

Guo, T., H. X. Wang and S. J. Zhang (2011). "Fluids and parameters optimization for a novel cogeneration system driven by low-temperature geothermal sources." *Energy* **36**(5): 2639-2649.

Hoffren, J., T. Talonpoika, J. Larjola and T. Siikonen (2002). "Numerical Simulation of Real-Gas Flow in a Supersonic Turbine Nozzle Ring." *Journal of Engineering for Gas Turbines and Power* **124**(2): 395-403.

IEA, I. E. A. (2008). Key world energy statistics.

Ingley, H., R. Reed and D. Goswami (2005). *Optimization of a Scroll expander applied to an ammonia/water combined cycle system for hydrogen production*. In: Proceedings of the ISES solar world congress.

Inoue, N., A. Kaneko, H. Watanabe, U. Tomoyuki and K. Irie (2007). *Development of Electric Power Generation Unit Driven by Waste Heat: Study on Working Fluids and Expansion Turbines*. ASME Turbo Expo 2007: Power for Land, Sea, and Air, Montreal, Canada.

International Energy Agency, I. (2014). "Energy Technology Perspectives−ETP2014, Harnessing electricity's potential ".

Invernizzi, C., P. Iora and P. Silva (2007). "Bottoming micro-Rankine cycles for micro-gas turbines." *Applied Thermal Engineering* **27**(1): 100-110.

Japikse, D. and N. Baines (1994). *Introduction to Turbomachinery*, Concepts ETI, Inc. and Oxford University Press.

Kane, M., D. Larrain, D. Favrat and Y. Allani (2003). "Small hybrid solar power system." *Energy* **28**(14): 1427-1443.

Kang, S. H. (2012). "Design and experimental study of ORC (organic Rankine cycle) and radial turbine using R245fa working fluid." *Energy* **41**(1): 514-524.

Katsanos, C. O., D. T. Hountalas and E. G. Pariotis (2012). "Thermodynamic analysis of a Rankine cycle applied on a diesel truck engine using steam and organic medium." *Energy Conversion and Management* **60**(0): 68-76.

Klein, S. (2013). "Engineering equation solver: F-chart Software ".

Kokaew, V., M. Moshrefi-Torbati and S. M. Sharkh (2013). "Maximum Efficiency or Power Tracking of Stand-alone Small Scale Compressed Air Energy Storage System." *Energy Procedia* **42**: 387-396.

Lemofouet, S. and A. Rufer (2006). "A Hybrid Energy Storage System Based on Compressed Air and Supercapacitors With Maximum Efficiency Point Tracking (MEPT)." *Industrial Electronics, IEEE Transactions on* **53**(4): 1105-1115.

Lemort, V., S. Declaye and S. Quoilin (2012). "Experimental characterization of a hermetic scroll expander for use in a micro-scale Rankine cycle." *Proceedings of the Institution of Mechanical Engineers, Part A: Journal of Power and Energy* **226**(1): 126-136.

Lemort, V., S. Quoilin, C. Cuevas and J. Lebrun (2009). "Testing and modeling a scroll expander integrated into an Organic Rankine Cycle." *Applied Thermal Engineering* **29**(14–15): 3094-3102.

Lewis, N. S. and D. G. Nocera (2006). "Powering the planet: Chemical challenges in solar energy utilization." *Proceedings of the National Academy of Sciences* **103**(43): 15729-15735.

Li, J., G. Pei, Y. Li and J. Ji (2011). "Evaluation of external heat loss from a small-scale expander used in organic Rankine cycle." *Applied Thermal Engineering* **31**(14–15): 2694-2701.

Li, J., G. Pei, Y. Li, D. Wang and J. Ji (2012). "Energetic and exergetic investigation of an organic Rankine cycle at different heat source temperatures." *Energy* **38**(1): 85-95.

Liu, B., P. Rivière, C. Coquelet, R. Gicquel and F. David (2012). "Investigation of a two stage Rankine cycle for electric power plants." *Applied Energy* **100**(0): 285-294.

Liu, H., Y. Shao and J. Li (2011). "A biomass-fired micro-scale CHP system with organic Rankine cycle (ORC) – Thermodynamic modelling studies." *Biomass and Bioenergy* **35**(9): 3985-3994.

Macchi, E. and A. Perdichizzi (1981). "Efficiency Prediction for Axial-Flow Turbines Operating with Nonconventional Fluids." *Journal of Engineering for Power* **103**(4): 718-724.

Madhawa Hettiarachchi, H. D., M. Golubovic, W. M. Worek and Y. Ikegami (2007). "Optimum design criteria for an Organic Rankine cycle using low-temperature geothermal heat sources." *Energy* **32**(9): 1698-1706.

Mago, P. J. and R. Luck (2013). "Energetic and exergetic analysis of waste heat recovery from a microturbine using organic Rankine cycles." *International Journal of Energy Research* **37**(8): 888-898.

Manolakos, D., G. Papadakis, S. Kyritsis and K. Bouzianas (2007). "Experimental evaluation of an autonomous low-temperature solar Rankine cycle system for reverse osmosis desalination." *Desalination* **203**(1–3): 366-374.

Marcuccilli, F. and D. Thiolet (2010). *Optimizing binary cycles thanks to radial inflow turbines*. Proceedings world geothermal congress Bali, Indonesia.

Marcuccilli, F. and S. Zouaghi (2007). *Radial inflow turbines for kalina and organic rankine cycles*. Proceedings European geothermal congress, Unterhaching, Germany.

Martin, J. D. and T. W. Simpson (2005). "Use of Kriging Models to Approximate Deterministic Computer Models." *AIAA Journal* **43**(4): 853-863.

McMahan, A. (2006). *Design and optimization of organic Rankine cycle solar thermal power plants*. MSc Thesis, University of Wisconsin-Madison.

Meitner, P. L., A. J. Glassman and S. United (1983). *Computer code for off-design performance analysis of radial-inflow turbines with rotor blade sweep*. Washington, D.C.

: [Springfield, Va., National Aeronautics and Space Administration, Scientific and Technical Information Branch ; For sale by the National Technical Information Service].

Montgomery, D. C. (2006). *Design and Analysis of Experiments*, John Wiley & Sons.

Moustapha, H., M. Zelesky, N. Baines and D. Japikse (2003). *Axial and radial turbines*. White River Junction, VT, Concepts NREC.

Muñoz de Escalona, J. M., D. Sánchez, R. Chacartegui and T. Sánchez (2012). "Part-load analysis of gas turbine & ORC combined cycles." *Applied Thermal Engineering* **36**(0): 63-72.

Musgrave, D. (1980). *The Prediction of Design and Off-Design Efficiency for Centrifugal*

Compressor Impellers. Twenty-Fifth Annual International Gas Turbine Conference and Exhibit and Twenty-Second Annual Fluids Engineering Conference, New Orleans, Louisiana, USA, ASME.

Nguyen, V. M., P. S. Doherty and S. B. Riffat (2001). "Development of a prototype low-temperature Rankine cycle electricity generation system." *Applied Thermal Engineering* **21**(2): 169-181.

Pan, L. and H. Wang (2013). "Improved analysis of Organic Rankine Cycle based on radial flow turbine." *Applied Thermal Engineering* **61**(2): 606-615.

Pasquale, D., A. Ghidoni and S. Rebay (2013). "Shape Optimization of an Organic Rankine Cycle Radial Turbine Nozzle." *Journal of Engineering for Gas Turbines and Power* **135**(4): 042308-042308.

Pei, G., J. Li, Y. Li, D. Wang and J. Ji (2011). "Construction and dynamic test of a small-scale organic rankine cycle." *Energy* **36**(5): 3215-3223.

Pepermans, G., J. Driesen, D. Haeseldonckx, R. Belmans and W. D'haeseleer (2005). "Distributed generation: definition, benefits and issues." *Energy Policy* **33**(6): 787-798.

Peterson, R. B., H. Wang and T. Herron (2008). "Performance of a small-scale regenerative Rankine power cycle employing a scroll expander." *Proceedings of the Institution of Mechanical Engineers, Part A: Journal of Power and Energy* **222**(3): 271-282.

Press, W., B. Flannery, S. Teukolsky and W. Vetterling (1989). *Numerical recipes in Pascal*. Cambridge, Cambridge university press.

Pytilinski, J. T. (1978). "Solar energy installations for pumping irrigation water." *Solar Energy* **21**(4): 255-262.

Qiu, G., H. Liu and S. Riffat (2011). "Expanders for micro-CHP systems with organic Rankine cycle." *Applied Thermal Engineering* **31**(16): 3301-3307.

Qiu, G., Y. Shao, J. Li, H. Liu and S. B. Riffat (2012). "Experimental investigation of a biomass-fired ORC-based micro-CHP for domestic applications." *Fuel* **96**(0): 374-382.

Quoilin, S. (2011). *Sustainable energy conversion through the use of Organic Rankine Cycles for waste heat recovery and solar applications*. Doctor of Applied Sciences, University of Liège, Liège, Belgium.

Quoilin, S., V. Lemort and J. Lebrun (2010). "Experimental study and modeling of an Organic Rankine Cycle using scroll expander." *Applied Energy* **87**(4): 1260-1268.

Rabl, A. (1985). *Active Solar Collectors and their Applications*. New York, Oxford University Press.

Rahbar, K., S. Mahmoud, R. K. Al-Dadah and N. Moazami (2015 [a]). "Parametric analysis and optimization of a small-scale radial turbine for Organic Rankine Cycle." *Energy* **83**(0): 696-711.

Rahbar, K., S. Mahmoud, R. K. Al-Dadah and N. Moazami (2015 [b]). "Modelling and optimization of organic Rankine cycle based on a small-scale radial inflow turbine." *Energy Conversion and Management* **91**(0): 186-198.

Rashidi, M. M., N. Galanis, F. Nazari, A. Basiri Parsa and L. Shamekhi (2011). "Parametric analysis and optimization of regenerative Clausius and organic Rankine cycles with two feedwater heaters using artificial bees colony and artificial neural network." *Energy* **36**(9): 5728-5740.

Rayegan, R. and Y. X. Tao (2011). "A procedure to select working fluids for Solar Organic Rankine Cycles (ORCs)." *Renewable Energy* **36**(2): 659-670.

Rodgers, C. and R. Geiser (1987). "Performance of a High-Efficiency Radial/Axial Turbine." *Journal of Turbomachinery* **109**(2): 151-154.

Rohlik, H. E. and C. Lewis Research (1968). *Analytical determination of radial inflow turbine design geometry for maximum efficiency*. Washington, D.C. : Springfield, Va., National Aeronautics and Space Administration ; For sale by the Clearinghouse for Federal Scientific and Technical Information.

Safaei, H., D. W. Keith and R. J. Hugo (2013). "Compressed air energy storage (CAES) with compressors distributed at heat loads to enable waste heat utilization." *Applied Energy* **103**: 165-179.

Saitoh, T., N. Yamada and S.-I. Wakashima (2007). "Solar Rankine cycle system using scroll expander."

Saleh, B., G. Koglbauer, M. Wendland and J. Fischer (2007). "Working fluids for low-temperature organic Rankine cycles." *Energy* **32**(7): 1210-1221.

Sauret, E. and A. S. Rowlands (2011). "Candidate radial-inflow turbines and high-density working fluids for geothermal power systems." *Energy* **36**(7): 4460-4467.

Schuster, A. (2011). *Nutzung von Niedertemperaturewärme mit Organic-Rankine-Cycle-Anlagen kleiner Leistung*. Phd Thesis, TU München, Munich.

Schuster, A., S. Karellas, E. Kakaras and H. Spliethoff (2009). "Energetic and economic investigation of Organic Rankine Cycle applications." *Applied Thermal Engineering* **29**(8–9): 1809-1817.

Shengjun, Z., W. Huaixin and G. Tao (2011). "Performance comparison and parametric optimization of subcritical Organic Rankine Cycle (ORC) and transcritical power cycle system for low-temperature geothermal power generation." *Applied Energy* **88**(8): 2740-2754.

Shuman, F. (1907). " The direct acting solar engine - the prime mover of the immediate future."

Siemens power generation division (2014). "Waste heat recovery with organic Rankine cycle technology - http://www.energy.siemens.com/mx/pool/hq/power-generation/steam-turbines/downloads/brochure-orc-organic-rankine-cycle-technology_EN.pdf."

Simpson, T. W., J. D. Poplinski, P. N. Koch and J. K. Allen (2001). "Metamodels for Computer-based Engineering Design: Survey and recommendations." *Engineering with Computers* **17**(2): 129-150.

Song, P., M. Wei, L. Shi, S. N. Danish and C. Ma (2015). "A review of scroll expanders for organic Rankine cycle systems." *Applied Thermal Engineering* **75**(0): 54-64.

Sprouse Iii, C. and C. Depcik (2013). "Review of organic Rankine cycles for internal combustion engine exhaust waste heat recovery." *Applied Thermal Engineering* **51**(1–2): 711-722.

Stoppato, A. (2012). "Energetic and economic investigation of the operation management of an Organic Rankine Cycle cogeneration plant." *Energy* **41**(1): 3-9.

Suhrmann, J., D. Peitsch, M. Gugau, T. Heuer and U. Tomm (2010). *Validation and development of loss models for small size radial turbines.* Proceedings of ASME Turbo Expo : Power for land, sea and Air GT2010, Glasgow, UK.

Sun, F., Y. Ikegami, B. Jia and H. Arima (2012). "Optimization design and exergy analysis of organic rankine cycle in ocean thermal energy conversion." *Applied Ocean Research* **35**(0): 38-46.

Tabor, h. and L. Bronicki (1963). "Small turbine for solar energy power package : Tabor, H. and L. Bronicki, National Physical Laboratory of Israel, United Nations Conference on New Sources of Energy, Rome, 1961, 24 p., Illus." *Solar Energy* **7**(2): 82.

Tchanche, B. F., G. Lambrinos, A. Frangoudakis and G. Papadakis (2011). "Low-grade heat conversion into power using organic Rankine cycles – A review of various applications." *Renewable and Sustainable Energy Reviews* **15**(8): 3963-3979.

Tchanche, B. F., G. Papadakis, G. Lambrinos and A. Frangoudakis (2009). "Fluid selection for a low-temperature solar organic Rankine cycle." *Applied Thermal Engineering* **29**(11–12): 2468-2476.

Tempesti, D., G. Manfrida and D. Fiaschi (2012). "Thermodynamic analysis of two micro CHP systems operating with geothermal and solar energy." *Applied Energy* **97**(0): 609-617.

Twomey, B., P. A. Jacobs and H. Gurgenci (2013). "Dynamic performance estimation of small-scale solar cogeneration with an organic Rankine cycle using a scroll expander." *Applied Thermal Engineering* **51**(1–2): 1307-1316.

Van den Braembussche, R. (2008). Numerical Optimization for Advanced Turbomachinery Design. *Optimization and Computational Fluid Dynamics*. D. Thévenin and G. Janiga, Springer Berlin Heidelberg**:** 147-189.

Wang, E. H., H. G. Zhang, B. Y. Fan, M. G. Ouyang, Y. Zhao and Q. H. Mu (2011). "Study of working fluid selection of organic Rankine cycle (ORC) for engine waste heat recovery." *Energy* **36**(5): 3406-3418.

Wang, E. H., H. G. Zhang, Y. Zhao, B. Y. Fan, Y. T. Wu and Q. H. Mu (2012). "Performance analysis of a novel system combining a dual loop organic Rankine cycle (ORC) with a gasoline engine." *Energy* **43**(1): 385-395.

Wang, X. D. and L. Zhao (2009). "Analysis of zeotropic mixtures used in low-temperature solar Rankine cycles for power generation." *Solar Energy* **83**(5): 605-613.

Watanabe, I., I. Ariga and T. Mashimo (1971). "Effect of Dimensional Parameters of Impellers on Performance Characteristics of a Radial-Inflow Turbine." *Journal of Engineering for Gas Turbines and Power* **93**(1): 81-102.

Whitfield, A. and N. C. Baines (1990). *Design of radial turbomachines*. Harlow, Essex, England; New York, NY, Longman Scientific & Technical ; Wiley.

Wood, H. J. (1963). "Current Technology of Radial-Inflow Turbines for Compressible Fluids." *Journal of Engineering for Gas Turbines and Power* **85**(1): 72-83.

World Energy Council (2013). World Energy Perspective- Energy Efficiency Technologies.

Yagoub, W., P. Doherty and S. B. Riffat (2006). "Solar energy-gas driven micro-CHP system for an office building." *Applied Thermal Engineering* **26**(14–15): 1604-1610.

Yamamoto, T., T. Furuhata, N. Arai and K. Mori (2001). "Design and testing of the Organic Rankine Cycle." *Energy* **26**(3): 239-251.

Zanelli, R. and D. Favrat (1994). *Experimental investigation of a hermetic scroll expander-generator*. The 12th international compressor engineering conference, Purdue, USA.

Zhang, B., X. Peng, Z. He, Z. Xing and P. Shu (2007). "Development of a double acting free piston expander for power recovery in transcritical CO2 cycle." *Applied Thermal Engineering* **27**(8–9): 1629-1636.

Zhang, H. G., E. H. Wang and B. Y. Fan (2013). "A performance analysis of a novel system of a dual loop bottoming organic Rankine cycle (ORC) with a light-duty diesel engine." *Applied Energy* **102**(0): 1504-1513.

Zhang, Y.-Q., Y.-T. Wu, G.-D. Xia, C.-F. Ma, W.-N. Ji, S.-W. Liu, K. Yang and F.-B. Yang (2014). "Development and experimental study on organic Rankine cycle system with single-screw expander for waste heat recovery from exhaust of diesel engine." *Energy* **77**(0): 499-508.

Zhejiang Turbine Import & Export Trade Co., L. (2011). Retrieved 19/07/2014, from http://www.chinaztc.com/en/productdatils.aspx?id=80&tid=D06B21DFEFB2B526.

Appendix A: Instrument calibration uncertainties

A-1: Temperature

The uncertainty in thermocouples is defined as following:

$$\zeta_{TC} = \sqrt{\zeta^2_{standard} + \zeta^2_{curve-fit}} \qquad \text{Equation A.1}$$

Where ζ_{TC}, $\zeta_{standard}$ and $\zeta_{curve\text{-}fit}$ are the uncertainties of thermocouple, standard instrument employed in the calibration (i.e. RTD) and the curve fit error respectively. The RTD was calibrated with a bath of water filled with ice (to represent 0˚C) and traversed around the container and the results are shown in Figure A.1. As it is evident the maximum deviation of RTD is about ±0.04 ˚C which is negligible.

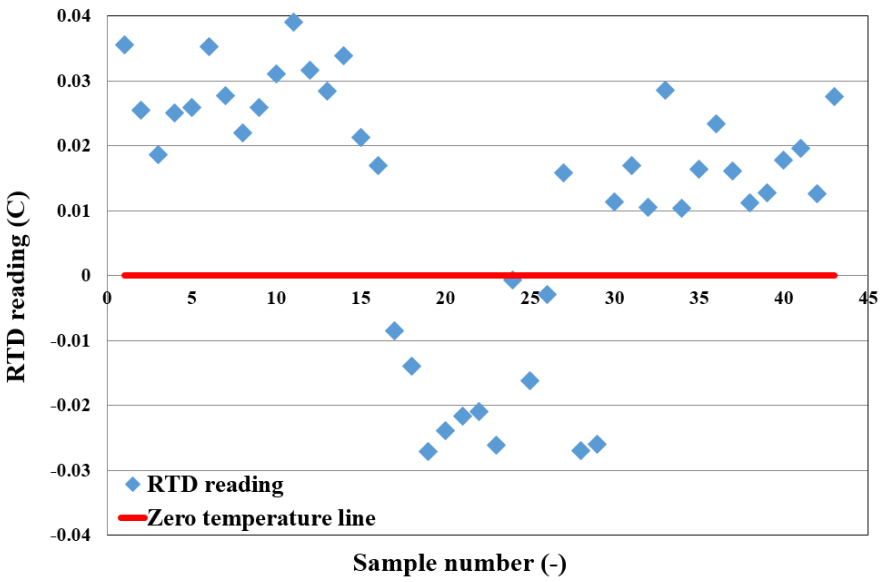

Figure A.1 Uncertainty in RTD thermocouple

So the uncertainty of the thermocouples will only correspond to the uncertainty associated with curve fitting process. The uncertainty of curve fitting was defined by standard deviation of mean as following:

$$\zeta_{curve-fit} = t_{N-1,95\%} S_{\bar{x}} \qquad \text{Equation A.2}$$

For brevity the uncertainty associated with thermocouple-1 is presented in Table A-1 while the same procedure was repeated for the rest of thermocouples.

Table A-1 Calculation of Thermocouple-1 associated curve fitting uncertainty

Data point (N)	RTD (˚C)	Average measured temperature ($TC_{measured}$)	Curve fit temperature(˚C) $TC_{corrected}$=1.0101× $TC_{measured}$-0.7849	Deviation^2
1	21.28	20.53	19.96	1.756
2	24.66	24.07	23.53	1.284
3	35.95	35.56	35.13	0.6741
4	51.66	51.54	51.275	0.15
5	70.53	70.66	70.59	0.004
6	87.94	88.31	88.42	0.228
7	99.68	99.49	99.70	0.0003
Degrees of freedom (N-1) = 6				
Standard deviation of the mean ($S_{\bar{x}}$) = 0.3123				
Student distribution factor ($t_{N-1,95\%}$)=2.447				
$\zeta_{curve-fit}$=0.764˚C				

A-2: Pressure transducers

Similar to section A-1 the uncertainty associated with the pressure transducers is the summation of the curve fitting and standard instrument (i.e. a certified accurate pressure gauge) used during calibration (Equation A.1). The certified gauge pressure has the uncertainty of $\pm$0.0397bars according to the manufacturer. Also, a similar procedure was performed for obtaining $\zeta_{curve-fit}$ as in section A-1. For brevity only the detailed results for one of the GE UNIK 5000 transducers is presented while the same procedure was repeated for the other two transducers. Table A-2 presents the summary of the results.

Table A-2 Calculation of Thermocouple-1 associated curve fitting uncertainty

Data point (N)	Gauge pressure (bar-gauge)	measured Voltage (Volt)	Curve fit pressure(bar-gauge) 6.324×volt-2.5024	Deviation^2
1	0	0.4069	0.07083	0.00501
2	0.5	0.469	0.46355	0.001328
3	1	0.5471	0.9574	0.00181
4	1.5	0.6287	1.4734	0.000702
5	2	0.7088	1.98	0.00039
6	2.5	0.7899	2.4929	5e-5
7	3	0.8715	3.008	8.04e-5
8	3.5	0.9513	3.5136	0.000186
9	4	1.0307	4.0157	0.000248
10	4.5	1.1082	4.5058	3.43e-5
11	5	1.1867	5.0022	5.25e-5
12	5.5	1.262	5.4784	0.000463
13	6	1.343	5.99	8.59e-5
14	6.5	1.4296	6.358	0.001474
15	7	1.507	7.027	0.00077
16	7.5	1.5836	7.5122	0.000151
17	8	1.664	8.0207	0.00043
18	8.5	1.744	8.5266	0.000711
19	9	1.821	9.0136	0.000185
20	9.5	1.89	9.4499	0.002504
21	10	1.97	9.955	0.001947
Degrees of freedom (N-1) = 20				
Standard deviation of the mean ($S_{\bar{x}}$) = 0.006652				
Student distribution factor ($t_{N-1,95\%}$)=2.086				
$\zeta_{curve-fit}$=0.0138bar				

Therefore the total uncertainty of the pressure transducers is $\pm$0.0421bars according to Equation A.1.

Appendix B: EES codes

B-1: ORC-RIT code with real-gas formulation

```
$UnitSystem SI MASS DEG PA K J
$Warnings ON
"1-Station numbering convention is the same as chapter three of the axial and radial book by N.C Baines
2-All angles are WRT radial direction"
"Functions, Procedures and Modules"
"External volute"
PROCEDURE VOLUTEEX(r[1],C_theta_1,SC,h[0,0],S[0,0],AR,R$,m_dot:C[0],h[0],S[0],rho[0],r[0],A[0],J,K)
i:=1
r[i]:=r[1]
Repeat
C[i]:=C_theta_1*r[1]/(SC*r[i])
h[i]:=h[0,0]-(0.5*C[i]^2)
S[i]:=S[0,0]
rho[i]:=DENSITY(R$,h=h[i],s=S[i])
A[i]:=m_dot/(rho[i]*C[i])
J[i]:=sqrt(A[i]/((0.75*pi+1)*AR))
K[i]:=AR*J[i]
i:=i+1
r[i]:=r[1]+J[i-1]
Until(r[i]-r[i-1]<0.001)
r[0]:=r[i]
h[0]:=h[i-1]
S[0]:=S[i-1]
C[0]:=C[i-1]
rho[0]:=rho[i-1]
A[0]:=A[i-1]
J:=J[i-1]
K:=K[i-1]
END
"Nozzle throat width"
FUNCTION NOZZLETH(M[3],alpha[3],s_3pitch,rho[3],C_m3,R$,rho_ss_N,C_ss_N)
If M[3]<1 then A:=cos(alpha[3])*s_3pitch
If M[3]>1 Then A:=rho[3]*C_m3*s_3pitch/(rho_ss_N*C_ss_N)
If M[3]>1 Then CALL WARNING('Nozzle exit supersonic expansion')
B:=rho[3]*C_m3/(rho_ss_N*C_ss_N)
IF B>1 Then CALL ERROR ('Annular passage choke precludes achieving the design specifications')
NOZZLETH:=A
END
"Nozzle inlet"
PROCEDURE NOZZLEINLET(h[1,0],P[0,0],A[1],C_theta_1,m_dot,C_m3,K_volute,BK,R$:P[1,0],S[1,0],T[1,0],rho[1,0],rho[1],S[1],h[1],C[1],C_m1,T[1],P[1])
```

```
i:=1
L[i-1]:=C_m3
Q[i-1]=P[0,0]
Repeat
R[i]=ENTROPY(R$,P=Q[i-1],h=h[1,0])
W[i]=TEMPERATURE(R$,P=Q[i-1],h=h[1,0])
V[i]=DENSITY(R$,P=Q[i-1],h=h[1,0])
S[i]=R[i]
rho[i]:=m_dot/(L[i-1]*A[1]*(1-BK))
C[i]:=sqrt(L[i-1]^2+C_theta_1^2)
h[i]:=h[1,0]-(0.5*C[i]^2)
T[i]:=TEMPERATURE(R$,s=S[i],h=h[i])
P[i]:=PRESSURE(R$,h=h[i],s=S[i])
i:=i+1
rho[i]:=DENSITY(R$,s=S[i-1],h=h[i-1])
L[i-1]:=m_dot/(A[1]*rho[i]*(1-BK))
Q[i-1]=(P[0,0]+P[i-1]*K_volute)/(K_volute+1)
Until (rho[i]-rho[i-1]<0.01) AND (L[i-1]-L[i-2]<0.01) AND (Q[i-1]-Q[i-2]<0.01)
P[1,0]=Q[i-1]
S[1,0]=R[i-1]
T[1,0]=W[i-1]
rho[1,0]=V[i-1]
rho[1]:=rho[i]
S[1]=S[i-1]
h[1]:=h[i-1]
C[1]:=C[i-1]
C_m1:=L[i-1]
T[1]:=T[i-1]
P[1]:=P[i-1]
END
"Nozzle exit"
PROCEDURE
NOZZLEEXIT(S[3],h[3,0],m_dot,C_m4,BK,R$,r[4],b[3],alpha[4],C_theta_4:h[3],C[3],
C_m3,rho[3],T[3],P[3],C_theta_3,r[3],alpha[3],A[3])
i:=1
L[i-1]:=C_m4
r[i-1]:=r[4]+2*b[3]*cos(alpha[4])
Repeat
G[i]=C_theta_4*r[4]/r[i-1]
A[i]=2*pi#*r[i-1]*b[3]
rho[i]:=m_dot/(L[i-1]*A[i]*(1-BK))
C[i]:=sqrt(L[i-1]^2+G[i]^2)
h[i]:=h[3,0]-(0.5*C[i]^2)
T[i]:=TEMPERATURE(R$,s=S[3],h=h[i])
P[i]:=PRESSURE(R$,s=S[3],h=h[i])
alpha[i]=arctan(G[i]/L[i-1])
i:=i+1
rho[i]:=DENSITY(R$,s=S[3],h=h[i-1])
L[i-1]:=m_dot/(A[i-1]*rho[i]*(1-BK))
r[i-1]=r[4]+2*b[3]*cos(alpha[i-1])
```

```
Until (rho[i]-rho[i-1]<0.01) AND (L[i-1]-L[i-2]<0.01) AND (r[i-1]-r[i-2]<0.001)
rho[3]:=rho[i]
h[3]:=h[i-1]
C[3]:=C[i-1]
C_m3:=L[i-1]
T[3]:=T[i-1]
P[3]:=P[i-1]
C_theta_3:=G[i-1]
r[3]:=r[i-1]
alpha[3]:=alpha[i-1]
A[3]:=A[i-1]
END
"Number of Nozzles"
PROCEDURE NOZZLENUMBER(N_R_recom,r[3],S_N:N_N)
N_N=Ceil(2*pi#*r[3]/S_N)
if N_N<1.4*N_R_recom then N_N=1.4*N_R_recom
if N_N>30 then N_N=30
END
"Rotor throat width"
FUNCTION
ROTORTH(C_m6,W_6_rms,s_6pitch,M_6_rel_t,rho[6],R$,rho_ss_R,W_ss_R)
If M_6_rel_t<1 Then A:=C_m6*s_6pitch/W_6_rms
If M_6_rel_t>1 Then A:=rho[6]*C_m6*s_6pitch/(rho_ss_R*W_ss_R)
If M_6_rel_t>1 Then CALL WARNING('Rotor exit supersonic expansion')
B:=rho[6]*C_m6/(rho_ss_R*W_ss_R)
IF B>1 Then CALL ERROR ('Annular passage choke precludes achieving the design
specifications')
ROTORTH:=A
End
"Rotor blockage"
PROCEDURE BLOCKAGE(N_R_recom,t_b4,r[4],beta_B4:K)
K=1-(N_R_recom*t_b4)/(2*pi*r[4]*cos(beta_B4))
IF K<0.5 THEN CALL WARNING('Blockage is more than the limit',K)
END
"Rotor axial lenght"
PROCEDURE AxLen_RON (r_6t,r_6h,b[4]:DELTAz_R_RON)
A:=1.5*(r_6t-r_6h)
IF A<1.5*b[4] THEN CALL WARNING('Rotor axial length is smaller than the limit')
DELTAz_R_RON:=A
END
"Rotor exit tip radius"
FUNCTION ROTOR_TIP_RADUIS(A[6],r_6h,r[4])
a:=sqrt((A[6]/pi)+r_6h^2)
If a>0.7*r[4] then CALL WARNING('Rotor exit tip radius is out of recommended
range',a)
ROTOR_TIP_RADUIS:=a
End
"Rotor exit hub radius"
FUNCTION ROTOR_HUB_RADIUS(N_R_recom,t_b6,beta_6h,r_6h)
a:=(N_R_recom*t_b6)/(2*pi#*cos(beta_6h))
```

```
if r_6h<a  then CALL WARNING('Rotor exit hub radius is out of recommended range')
ROTOR_HUB_RADIUS:=a
END
"Rotor friction"
SUBPROGRAM TURBULANTF(Re,D_hyd:f)
RR=0.0002
1/sqrt(f)=-4*log10((RR/(D_hyd*3.7))+(1.256/(Re*sqrt(f))))
END
"Friction factor"
PROCEDURE FRICTIONFACTOR(Re,D_hyd:f)
RR=0.0002
If Re<2100 then f:=16/Re
If Re>4000 then
Call TURBULANTF(Re,D_hyd:f)
ENDIF
END
"Rotor tip clearance and back plate clearance"
PROCEDURE TIPCLEARANCE(b[6]:t_c)
t_c=0.04*b[6]
if t_c<0.0003 then t_c=0.0003
End
"Disk friction factor-Windage"
PROCEDURE DISKFRICTION (t_c,r[4],Re:k_f)
If Re<=10^5 then
k_f=3.7*(t_c/r[4])^0.1/Re^0.5
ENDIF
If Re>10^5 then
k_f=0.102*(t_c/r[4])^0.1/Re^0.2
ENDIF
END
"Reaction"
FUNCTION REACTION(h[4],h[6],h[0,0],h[6,0])
a:=(h[4]-h[6])/(h[0,0]-h[6,0])
If a<0.2 then CALL WARNING ('Reaction is out of recommended range',a)
if a>0.7 then CALL WARNING ('Reaction is out of recommended range',a)
REACTION:=a
End
"Rotor Analysis"
PROCEDURE
ROTORANALYSIS(eta_ts,P[0,0],rho[0,0],h[0,0],R$,DELTAh_s,P[6],psi,phi,xi,m_dot,
BK,i_4,alpha[6],S[0,0],radii_ratio,omega,RR:Efficiency_ts,DELTAh_0,P[4,0],h[4,0],S[
4,0],T[4,0],rho[4,0],h[6,0],C_theta_4,C[4],h[4],S[4],P[4],T[4],rho[4],alpha[4],beta_4,W
_4,M[4],M_4_rel,A[4],b[4],t_b4,beta_B4,C_theta_6,C[6],h[6],S[6],T[6],rho[6],S[6,0],P
[6,0],T[6,0],rho[6,0],h_06s,A[6],Q_6,r_6h,r_6t,r_6mean,r[6],U_6h,U_6_rms,U_6t,beta
_6h,beta_6_rms,beta_6t,W_6h,W_6_rms,W_6t,M[6],M_6_rel_rms,M_6_rel_t,DELTAz
_R_RON,N_R_recom,t_c,Re_in,Re_out,Re,L_hyd,D_hyd,f,f_curved,ff,W_bar,C_a,C_r
,rho_bar,k_f,C_m4,U_4,C_m6,r[4],DELTAh_friction_rotor,DELTAh_secondary,DELT
Ah_exit,DELTAh_clearance_Baines,DELTAh_windage,DELTAh_incidence_Rodgers,
DELTAh_nozzle_friction, DELTAh_loss_volute)
i:=1
```

```
etats[i-1]=eta_ts
Ctheta4[i-1]:=sqrt((etats[i-1]*DELTAh_s)*psi)
REPEAT
DELTAh0[i]:=DELTAh_s*etats[i-1]
U4[i]:=sqrt(DELTAh0[i]/psi)
Cm6[i]:=phi*U4[i]
Cm4[i]:=Cm6[i]*xi
r4[i]:=U4[i]/omega
r6h[i]:=r4[i]*radii_ratio
P40[i]:=P[0,0]-(rho[0,0]*DELTAh_s*(1-etats[i-1])/4)
h40[i]:=h[0,0]
S40[i]:=ENTROPY(R$,h=h40[i],P=P40[i])
T40[i]:=TEMPERATURE(R$,h=h40[i],P=P40[i])
rho40[i]:=DENSITY(R$,h=h40[i],P=P40[i])
h60[i]:=h40[i]-DELTAh0[i]
C4[i]:=sqrt(Cm4[i]^2+Ctheta4[i-1]^2)
h4[i]:=h40[i]-(0.5*C4[i]^2)
S4[i]:=S40[i]
P4[i]:=PRESSURE(R$,h=h4[i],s=S4[i])
T4[i]:=TEMPERATURE(R$,h=h4[i],s=S4[i])
rho4[i]:=DENSITY(R$,h=h4[i],s=S4[i])
alpha4[i]:=arctan(Ctheta4[i-1]/Cm4[i])
beta4[i]:=arctan((Ctheta4[i-1]-U4[i])/Cm4[i])
W4[i]:=sqrt(U4[i]^2+C4[i]^2-(2*U4[i]*Ctheta4[i-1]))
M4[i]:=C4[i]/SOUNDSPEED(R$,h=h4[i],s=S4[i])
M4rel[i]:=W4[i]/SOUNDSPEED(R$,h=h4[i],s=S4[i])
A4[i]:=m_dot/(rho4[i]*Cm4[i]*(1-BK))
b4[i]:=A4[i]/(2*pi*r4[i])
tb4[i]:=0.04*r4[i]
betaB4[i]:=beta4[i]-i_4
Ctheta6[i]:=Cm6[i]*tan(alpha[6])
C6[i]:=sqrt(Cm6[i]^2+Ctheta6[i]^2)
h6[i]:=h60[i]-(0.5*C6[i]^2)
S6[i]:=ENTROPY(R$,h=h6[i],P=P[6])
 T6[i]:=TEMPERATURE(R$,h=h6[i],P=P[6])
rho6[i]:=DENSITY(R$,h=h6[i],P=P[6])
S60[i]:=S6[i]
P60[i]:=PRESSURE(R$,h=h60[i],s=S60[i])
T60[i]:=TEMPERATURE(R$,h=h60[i],s=S60[i])
rho60[i]:=DENSITY(R$,h=h60[i],s=S60[i])
h06s[i]:=Enthalpy(R$,s=S[0,0],P=P60[i])
A6[i]:=m_dot/(rho6[i]*Cm6[i]*(1-BK))
Q6[i]:=Cm6[i]*A6[i]
r6t[i]:=sqrt((A6[i]/pi)+r6h[i]^2)
r6mean[i]:=(r6t[i]+r6h[i])/2
r6[i]:=sqrt((A6[i]/(2*pi))+r6h[i]^2)
U6h[i]:=r6h[i]*omega
U6rms[i]:=r6[i]*omega
 U6t[i]:=r6t[i]*omega
 beta6h[i]:=arctan((Ctheta6[i]-U6h[i])/Cm6[i])
```

beta6rms[i]:=arctan((Ctheta6[i]-U6rms[i])/Cm6[i])
beta6t[i]:=arctan((Ctheta6[i]-U6t[i])/Cm6[i])
W6h[i]:=sqrt(Cm6[i]^2+(U6h[i]-Ctheta6[i])^2)
W6rms[i]:=sqrt(Cm6[i]^2+(U6rms[i]-Ctheta6[i])^2)
W6t[i]:=sqrt(Cm6[i]^2+(U6t[i]-Ctheta6[i])^2)
M6[i]:=C6[i]/SOUNDSPEED(R$,T=T6[i],P=P[6])
M6relrms[i]:=W6rms[i]/SOUNDSPEED(R$,T=T6[i],P=P[6])
M6relt[i]:=W6t[i]/SOUNDSPEED(R$,T=T6[i],P=P[6])
DELTAzRRON[i]:=1.5*(r6t[i]-r6h[i])
NRrecom[i]:=round((pi/30)*(110-alpha4[i])*tan(alpha4[i]))
tc[i]:=0.04*(r6t[i]-r6h[i])
Rein[i]:=U4[i]*b4[i]/(Viscosity(R$,T=T4[i],P=P4[i])/Density(R$,T=T4[i],P=P4[i]))
Reout[i]:=U6rms[i]*(r6t[i]-
r6h[i])/(Viscosity(R$,T=T6[i],P=P[6])/Density(R$,T=T6[i],P=P[6]))
Re[i]:=Rein[i]
Lhyd[i]:=(pi#/2)*sqrt(((r4[i]-r6t[i]+(b4[i]/2))^2+((r6t[i]-r6h[i])/2)^2)/2)
Dhyd[i]:=0.5*(((4*pi#*r4[i]*b4[i])/(2*pi#*r4[i]+NRrecom[i]*b4[i]))+((2*pi#*(r6t[i]^2
-r6h[i]^2))/(pi#*(r6t[i]-r6h[i])+NRrecom[i]*(r6t[i]-r6h[i]))))
f[i]:=MoodyChart(Re[i], RR)
fcurved[i]:=f[i]*(1+0.075*Re[i]^0.25*sqrt(Dhyd[i]/(2*((r4[i]-r6t[i])+(b4[i]/2)+(r4[i]-
r6t[i])+(((r6t[i]-r6h[i])/2))))))
ff[i]:=fcurved[i]*(Re[i]*(r4[i]/((r4[i]-r6t[i])+(b4[i]/2)+(r4[i]-r6t[i])+(((r6t[i]-
r6h[i])/2))))^2)^0.05
Wbar[i]:=(W4[i]+((W6t[i]+W6h[i])/2))/2
Ca[i]:=(abs(1-(r6t[i]/r4[i])))/(Cm4[i]*b4[i])
Cr[i]:=(r6t[i]/r4[i])*(DELTAzRRON[i]-b4[i])/(Cm6[i]*r6[i]*(r6t[i]-r6h[i]))
rhobar[i]:=(rho4[i]+rho6[i])/2
kf[i]:=0.102*(tc[i]/r4[i])^0.1/Re[i]^0.2
DELTAhfrictionrotor[i]:=ff[i]*Lhyd[i]*Wbar[i]^2/Dhyd[i]
DELTAhsecondary[i]:=2*C4[i]^2*r4[i]/(NRrecom[i]*((r4[i]-r6t[i])+(b4[i]/2)+(r4[i]-
r6t[i])+(((r6t[i]-r6h[i])/2))))
DELTAhexit[i]:=0.5*C6[i]^2
DELTAhclearanceBaines[i]:=(U4[i]^3*NRrecom[i]/(8*pi#))*(0.4*tc[i]*Ca[i]+0.75*tc[i
]*Cr[i]-0.3*sqrt(tc[i]^2*Ca[i]*Cr[i]))
DELTAhwindage[i]:=kf[i]*rhobar[i]*U4[i]^3*r4[i]^2/(4*m_dot)
DELTAhincidenceRodgers[i]:=0.5*(W4[i]*cos(beta4[i]))^2
l_hyd_nozzle[i]=r[1]-r[3]
D_hyd_nozzle[i]=0.5*(((8*pi#*r[1]*b[4]*cos(alpha[1]))/(4*pi#*r[1]+(4*pi#*r[1]*b[4]/
sigma)))+((8*pi#*r[3]*b[4]*cos(alpha[3]))/(4*pi#*r[3]+(4*pi#*r[3]*b[4]/sigma))))
DELTAh_nozzle_friction[i]:=4*f*(l_hyd_nozzle[i]/D_hyd_nozzle[i])*C3[i]^2
DELTAh_loss_volute[i]:= K_volute*C1[i]^2/2
i=i+1
Ctheta4[i-1]:=(DELTAh0[i-1]+U6rms[i-1]*Ctheta6[i-1])/U4[i-1]
etats[i-1]=DELTAh0[i-1]/(DELTAh0[i-1]+DELTAhfrictionrotor[i-
1]+DELTAhsecondary[i-1]+DELTAhexit[i-1]+DELTAhclearanceBaines[i-
1]+DELTAhwindage[i-1]+DELTAhincidenceRodgers[i-1]+
DELTAh_nozzle_friction[i-1]+ DELTAh_loss_volute[i-1])
UNTIL (abs(Ctheta4[i-1]-Ctheta4[i-2])<0.1) AND (abs(etats[i-1]-etats[i-2])<0.0001)
Efficiency_ts:=etats[i-1]
DELTAh_0:=DELTAh0[i-1]

U_4:=U4[i-1]
C_m6:=Cm6[i-1]
C_m4:=Cm4[i-1]
r[4]:=r4[i-1]
P[4,0]:=P40[i-1]
h[4,0]:=h40[i-1]
S[4,0]:=S40[i-1]
T[4,0]:=T40[i-1]
rho[4,0]:=rho40[i-1]
h[6,0]:=h60[i-1]
C_theta_4:=Ctheta4[i-1]
C[4]:=C4[i-1]
h[4]:=h4[i-1]
S[4]:=S4[i-1]
P[4]:=P4[i-1]
T[4]:=T4[i-1]
rho[4]:=rho4[i-1]
alpha[4]:=alpha4[i-1]
beta_4:=beta4[i-1]
W_4:=W4[i-1]
M[4]:=M4[i-1]
M_4_rel:=M4rel[i-1]
A[4]:=A4[i-1]
b[4]:=b4[i-1]
t_b4:=tb4[i-1]
beta_B4:=betaB4[i-1]
C_theta_6:=Ctheta6[i-1]
C[6]:=C6[i-1]
h[6]:=h6[i-1]
S[6]:=S6[i-1]
T[6]:=T6[i-1]
rho[6]:=rho6[i-1]
S[6,0]:=S60[i-1]
P[6,0]:=P60[i-1]
T[6,0]:=T60[i-1]
rho[6,0]:=rho60[i-1]
h_06s:=h06s[i-1]
A[6]:=A6[i-1]
Q_6:=Q6[i-1]
r_6h:=r6h[i-1]
r_6t:=r6t[i-1]
r_6mean:=r6mean[i-1]
r[6]:=r6[i-1]
U_6h:=U6h[i-1]
U_6_rms:=U6rms[i-1]
U_6t:=U6t[i-1]
beta_6h:=beta6h[i-1]
beta_6_rms:=beta6rms[i-1]
beta_6t:=beta6t[i-1]
W_6h:=W6h[i-1]

W_6_rms:=W6rms[i-1]
W_6t:=W6t[i-1]
M[6]:=M6[i-1]
M_6_rel_rms:=M6relrms[i-1]
M_6_rel_t:=M6relt[i-1]
DELTAz_R_RON:=DELTAzRRON[i-1]
N_R_recom:=NRrecom[i-1]
t_c:=tc[i-1]
Re_in:=Rein[i-1]
Re_out:=Reout[i-1]
Re:=Re[i-1]
L_hyd:=Lhyd[i-1]
D_hyd:=Dhyd[i-1]
f:=f[i-1]
f_curved:=fcurved[i-1]
ff:=ff[i-1]
W_bar:=Wbar[i-1]
C_a:=Ca[i-1]
C_r:=Cr[i-1]
rho_bar:=rhobar[i-1]
k_f:=kf[i-1]
DELTAh_friction_rotor:=DELTAhfrictionrotor[i-1]
DELTAh_secondary:=DELTAhsecondary[i-1]
DELTAh_exit:=DELTAhexit[i-1]
DELTAh_clearance_Baines:=DELTAhclearanceBaines[i-1]
DELTAh_windage:=DELTAhwindage[i-1]
DELTAh_incidence_Rodgers:=DELTAhincidenceRodgers[i-1]
DELTAh_nozzle_friction:= DELTAh_nozzle_friction[i-1]
DELTAh_loss_volute:= DELTAh_loss_volute[i-1]
END
"User input"
"1- Operating Conditions"
T[0,0]=362.8"Inlet total temperature "
DELTAT_superheat=3.879"Degree of superheating"
ER_ts=8.225"Turbine total-to-static expansion ratio"
m_dot=0.06499"Mass flow rate"
omega=8349"Rotational speed [Rad/s]"
R$='R245fa' "Fluid selection"
"2- Design Parameters"
eta_ts=0.8"Estimate of total to static efficiency"
i_4=-20"Estimate of incidence angle"
BK=0.1"Blockage factor"
RR=0.0002"Relative roughness"
"3-Volute"
AR=1"Aspect ratio (K/J)"
SC=0.95"Swirl coefficient”
K_volute=0.05"Volute total pressure loss coefficient”
alpha[0]=90"Inlet volute angle"
"4-Nozzle"
r[1]/r[3]=radii_ratio_nozzle"Radii ratio, nozzle inlet to nozzle exit"

delta_nozzle_exit=2"Nozzle exit deviation"
Solidity=1.35"C_N/S_N"
radii_ratio_nozzle=1.204"Ratio of nozzle inlet to nozzle exit radii"
"5-Rotor"
phi=0.1887"Flow Coefficient"
psi=1.06"Loading Coefficient"
delta_rotor_exit=5"Rotor exit deviation"
alpha[6]=0"Exit absolute flow angle"
radii_ratio=0.3321"Ratio of rotor exit hub to rotor inlet radii"
xi=0.6"Rotor meridional velocity ratio"
"6- Cycle parameters"
eta_pump=0.7"Pump isentropic efficiency"
eta_mechanical=0.96"Mechanical efficiency"
eta_generator=0.96 "Generator efficiency"
"Output"
P[0,0]=P_sat(R$,T=T[0,0])
T_new=T[0,0]+DELTAT_superheat
h[0,0]=ENTHALPY(R$,T=T_new,P=P[0,0])
S[0,0]=ENTROPY(R$,T=T_new,P=P[0,0])
rho[0,0]=DENSITY(R$,T=T_new,P=P[0,0])
T[0]=TEMPERATURE(R$,h=h[0],S=S[0,0])
P[0]=PRESSURE(R$,h=h[0],S=S[0,0])
M[0]=C[0]/SOUNDSPEED(R$,h=h[0],S=S[0,0])
S_6s=S[0,0]
P[6]=P[0,0]/ER_ts
P_6s=P[6]
h_6s=ENTHALPY(R$,P=P_6s,S=S_6s)
DELTAh_s=h[0,0]-h_6s
Z_compressability=CompressibilityFactor(R$,T=T_new,P=P[0,0])
VR=Q_6/Q_1
SP=(Q_6^0.5)/(DELTAh_s)^0.25
"Rotor"
CALL
ROTORANALYSIS(eta_ts,P[0,0],rho[0,0],h[0,0],R$,DELTAh_s,P[6],psi,phi,xi,m_dot,
BK,i_4,alpha[6],S[0,0],radii_ratio,omega,RR:Efficiency_ts,DELTAh_0,P[4,0],h[4,0],S[
4,0],T[4,0],rho[4,0],h[6,0],C_theta_4,C[4],h[4],S[4],P[4],T[4],rho[4],alpha[4],beta_4,W
_4,M[4],M_4_rel,A[4],b[4],t_b4,beta_B4,C_theta_6,C[6],h[6],S[6],T[6],rho[6],S[6,0],P
[6,0],T[6,0],rho[6,0],h_06s,A[6],Q_6,r_6h,r_6t,r_6mean,r[6],U_6h,U_6_rms,U_6t,beta
_6h,beta_6_rms,beta_6t,W_6h,W_6_rms,W_6t,M[6],M_6_rel_rms,M_6_rel_t,DELTAz
_R_RON,N_R_recom,t_c,Re_in,Re_out,Re,L_hyd,D_hyd,f,f_curved,ff,W_bar,C_a,C_r
,rho_bar,k_f,C_m4,U_4,C_m6,r[4],DELTAh_friction_rotor,DELTAh_secondary,DELT
Ah_exit,DELTAh_clearance_Baines,DELTAh_windage,DELTAh_incidence_Rodgers,
DELTAh_nozzle_friction, DELTAh_loss_volute)
P=DELTAh_0*m_dot
Reaction=REACTION(h[4],h[6],h[0,0],h[6,0])
nu=U_4/sqrt(2*DELTAh_s)
N_s=(omega*sqrt(Q_6))/(DELTAh_s^(3/4))
D_s=(d[4]*DELTAh_s^0.25)/sqrt(Q_6)
ER_tt=P[0,0]/P[6,0]
eta_tt=(h[0,0]-h[6,0])/(h[0,0]-h_06s)

```
d[4]=2*r[4]
d_6h=2*r_6h
d_6t=2*r_6t
d[6]=2*r[6]
b[6]=r_6t-r_6h
Rotor_aspect_ratio=b[4]/d[4]
ExitPhaseRotor$=Phase$(R$,T=T[6],P=P[6])
relativevelocityratio=W_6t/W_4
DELTAS_rotor_check=S[6,0]-S[4,0]
beta_B6h=beta_6h+delta_rotor_exit
beta_B6_rms=beta_6_rms+delta_rotor_exit
beta_B6t=beta_6t+delta_rotor_exit
Radiiratio_Tiptoinlet=r_6t/r[4]
t_b6=0.02*r[4]
Rotor_exit_radii=r_6h/r_6t
N =omega*30/pi#
CALL BLOCKAGE(N_R_recom,t_b4,r[4],beta_B4:K_B_4)
h_6_t_rel=h[6]+0.5*W_6_rms^2
P_6_t_rel=P[6]+0.5*rho[6]*W_6_rms^2
W_ss_R=SoundSpeed(R$,h=h_6_t_rel,P=P_6_t_rel)
h_ss_R=h_6_t_rel-0.5*W_ss_R^2
P_ss_R=P_6_t_rel-0.5*rho_ss_R*W_ss_R^2
rho_ss_R=DENSITY(R$,h=h_ss_R,P=P_ss_R)
s_6pitch=2*pi*r[6]/N_R_recom
o_6=ROTORTH(C_m6,W_6_rms,s_6pitch,M_6_rel_t,rho[6],R$,rho_ss_R,W_ss_R)
sigma=1-(sqrt(cos(beta_B4_SP))/(N_R_recom^0.7))
K_B4_SP=1-(N_R_recom*t_b4)/(2*pi*r[4]*cos(beta_B4_SP))
C_theta_4=sigma*(U_4-(C_m4*tan(beta_B4_SP)/K_B4_SP))
beta_B4_RON=abs(beta_B4_SP)
"Rotor losses"
DELTAh_loss_tot=DELTAh_friction_rotor+DELTAh_secondary+DELTAh_exit+DEL
TAh_clearance_Baines+DELTAh_windage+DELTAh_incidence_Rodgers
Loss_secondary=(DELTAh_secondary/DELTAh_loss_tot)*100
Loss_friction=(DELTAh_friction_rotor/DELTAh_loss_tot)*100
Loss_exit=(DELTAh_exit/DELTAh_loss_tot)*100
Loss_clearance=(DELTAh_clearance_Baines/DELTAh_loss_tot)*100
Loss_windage=(DELTAh_windage/DELTAh_loss_tot)*100
Loss_incidence=(DELTAh_incidence_Rodgers/DELTAh_loss_tot)*100
"Nozzle"
"Outlet"
"Thermodynamic properties &Velocity triangles"
h[3,0]=h[0,0]
P[3,0]=P[4,0]
S[3,0]=ENTROPY(R$,P=P[3,0],h=h[3,0])
T[3,0]=TEMPERATURE(R$,P=P[3,0],h=h[3,0])
rho[3,0]=DENSITY(R$,P=P[3,0],h=h[3,0])
S[3]=S[3,0]
CALL
NOZZLEEXIT(S[3],h[3,0],m_dot,C_m4,BK,R$,r[4],b[3],alpha[4],C_theta_4:h[3],C[3],
C_m3,rho[3],T[3],P[3],C_theta_3,r[3],alpha[3],A[3])
```

M[3]=C[3]/SOUNDSPEED(R$,s=S[3],P=P[3])
"Geometry parameters"
d[3]=2*r[3]
b[3]=b[4]
s_3pitch=2*pi*r[3]/N_N
alpha_B3=alpha[3]+delta_nozzle_exit
C_ss_N=SoundSpeed(R$,T=T[3,0],P=P[3,0])
h_ss_N=h[3,0]-0.5*C_ss_N^2
P_ss_N=P[3,0]-0.5*rho_ss_N*C_ss_N^2
rho_ss_N=Density(R$,h=h_ss_N,P=P_ss_N)
T_ss_N=Temperature(R$,h=h_ss_N,P=P_ss_N)
o_3=NOZZLETH(M[3],alpha[3],s_3pitch,rho[3],C_m3,R$,rho_ss_N,C_ss_N)
"Inlet"
"Thermodynamic properties"
h[1,0]=h[0,0]
CALL
NOZZLEINLET(h[1,0],P[0,0],A[1],C_theta_1,m_dot,C_m3,K_volute,BK,R$:P[1,0],S[
1,0],T[1,0],rho[1,0],rho[1],S[1],h[1],C[1],C_m1,T[1],P[1])
Q_1=C_m1*A[1]
"Velocity triangles"
C_theta_1=C_theta_3*r[3]/r[1]
M[1]=C[1]/SOUNDSPEED(R$,s=S[1],h=h[1])
alpha[1]=arctan(C_theta_1/C_m1)
alpha_mean=(alpha[1]+alpha[3])/2
C_N=sqrt(abs(r[1]^2+r[3]^2-sqrt(abs((r[1]^2+r[3]^2)^2-((r[1]^2-
r[3]^2)/cos(alpha_mean))^2))))
S_N=C_N/solidity
"Geometry parameters"
b[1]=b[3]
A[1]=2*pi*r[1]*b[1]
d[1]=2*r[1]
CALL NOZZLENUMBER(N_R_recom,r[3],S_N:N_N)
"Volute"
"Velocity triangles and Geometry parameters"
CALL
VOLUTEEX(r[1],C_theta_1,SC,h[0,0],S[0,0],AR,R$,m_dot:C[0],h[0],S[0],rho[0],r[0],
A[0],J,K)
d[0]=2*r[0]
AR_Volute=A[0]/r[0]
h_3s=ENTHALPY(R$,S=S[0,0],P=P[3])
DELTAP_stator=P[0,0]-P[3,0]
K_pressureloss=(DELTAP_stator/(P[0,0]-P[6]))*100
d_max=(2*(J+r[0]))
"Cycle analysis"
P[7]=P[6]
X[7]=1
T[7]=Temperature(R$,P=P[7],x=X[7])
h[7]=ENTHALPY(R$,P=P[7],x=X[7])
rho[7]=DENSITY(R$,P=P[7],x=X[7])
S[7]=ENTROPY(R$,P=P[7],x=X[7])

```
P[8]=P[6]
X[8]=0
T[8]=Temperature(R$,P=P[8],x=X[8])
h[8]=ENTHALPY(R$,P=P[8],x=X[8])
rho[8]=DENSITY(R$,P=P[8],x=X[8])
S[8]=ENTROPY(R$,P=P[8],x=X[8])
Q_out=m_dot*(h[6]-h[8])
P[9]=P[0,0]
W_pump=m_dot*(P[9]-P[8])/(rho[8]*eta_pump)
h[9]=h[8]+(W_pump/m_dot)
rho[9]=DENSITY(R$,h=h[9],P=P[9])
T[9]=Temperature(R$,h=h[9],P=P[9])
S[9]=ENTROPY(R$,h=h[9],P=P[9])
P[10]=P[0,0]
X[10]=0
T[10]=T[0,0]
h[10]=ENTHALPY(R$,P=P[10],X=X[10])
rho[10]=DENSITY(R$,P=P[10],X=X[10])
S[10]=ENTROPY(R$,P=P[10],X=X[10])
Q_hot=m_dot*(h[0,0]-h[9])
W_net=(P*eta_generator*eta_mechanical)-W_pump
eta_thermal_cycle=W_net/Q_hot
```

B-2: RIT mean-line code with ideal-gas formulation

```
$UnitSystem SI MASS DEG PA K J
$Warnings ON
"PRELIMINARY SIZING"
"1-Station numbering convention is the same as chapter three of the axial and radial book by N.C Baines
2-All angles are WRT radial direction"
"Functions, Procedures and Modules"
PROCEDURE ROTOR_EXIT_TIP(DELTAh_0,U[4],alpha[4],T[4,0],C_p,gamma,m_dot,R,P[4,0],r[4],P[6,0],T[6,0],alpha[6],A[6],U_6t:C_theta4,C_m4,C[4],Beta[4],W_theta4,W[4],T[4],P[4],A[4],b[4],T[6],P[6],C_m6,C_theta6,C[6],beta[6],W[6],W_theta6,rho[6])
i:=1
Ctheta6[i]:=0
Ctheta4[i]:=DELTAh_0/U[4]
rho6[i]:=P[6,0]/(R*T[6,0])
Cm6[i]:=m_dot/(A[6]*rho6[i])
Repeat
Cm4[i]:=Ctheta4[i]/tan(alpha[4])
C4[i]:=sqrt(Cm4[i]^2+Ctheta4[i]^2)
beta4[i]:=arctan((Ctheta4[i]-U[4])/Cm4[i])
W4[i]:=Sign(beta4[i])*Cm4[i]/cos(beta4[i])
Wtheta4[i]:=Cm4[i]*tan(beta4[i])
T4[i]:=T[4,0]-C4[i]^2/(2*C_p)
P4[i]:=P[4,0]*(T4[i]/T[4,0])^(gamma/(gamma-1))
A4[i]:=m_dot*R*T4[i]/(P4[i]*Cm4[i])
b4[i]:=A4[i]/(2*pi*r[4])
C6[i]:=sqrt(Cm6[i]^2+Ctheta6[i]^2)
T6[i]:=T[6,0]-C6[i]^2/(2*C_p)
P6[i]:=P[6,0]*(T6[i]/T[6,0])^(gamma/(gamma-1))
beta6[i]:=arctan((Ctheta6[i]-U_6t)/Cm6[i])
W6[i]:=Sign(beta6[i])*Cm6[i]/cos(beta6[i])
Wtheta6[i]:=Cm6[i]*tan(beta6[i])
i:=i+1
rho6[i]:=P6[i-1]/(R*T6[i-1])
Cm6[i]:=m_dot/(A[6]*rho6[i])
Ctheta6[i]:=tan(alpha[6])*Cm6[i]
Ctheta4[i]:=(DELTAh_0+Ctheta6[i]*U_6t)/U[4]
Until  (Ctheta4[i]-Ctheta4[i-1]<0.001) and (Ctheta6[i]-Ctheta6[i-1]<0.001) and (rho6[i]-rho6[i-1]<0.001) and  (Cm6[i]-Cm6[i-1]<0.001)
C_theta4:=Ctheta4[i]
C_m4:=Cm4[i-1]
C[4]:=C4[i-1]
Beta[4]:=beta4[i-1]
W_theta4:=Wtheta4[i-1]
W[4]:=W4[i-1]
T[4]:=T4[i-1]
P[4]:=P4[i-1]
A[4]:=A4[i-1]
```

```
b[4]:=b4[i-1]
T[6]:=T6[i-1]
P[6]:=P6[i-1]
C_m6:=Cm6[i]
C_theta6:=Ctheta6[i]
C[6]:=C6[i-1]
beta[6]:=beta6[i-1]
W[6]:=W6[i-1]
W_theta6:=Wtheta6[i-1]
rho[6]:=rho6[i]
END
"Nozzle throat width"
FUNCTION NOZZLETH(M[3],alpha[3],S_N,rho[3],C_m3,rho_ss_N,C_ss_N)
If M[3]<1 then A:=cos(alpha[3])*S_N
If M[3]>1 Then A:=rho[3]*C_m3*S_N/(rho_ss_N*C_ss_N)
If M[3]>1 Then CALL WARNING('Nozzle exit supersonic expansion')
B:=rho[3]*C_m3/(rho_ss_N*C_ss_N)
IF B>1 Then CALL ERROR ('Annular passage choke precludes achieving the design
specifications')
NOZZLETH:=A
END
"Rotor clearance and back space clearance"
Procedure TIPCLEARANCE(b[6]:t_c)
t_c=0.04*b[6]
if t_c<0.0003 then t_c=0.0003
End
"Disk friction factor-Windage"
PROCEDURE DISKFRICTION (t_c,r[4],Re:k_f)
If Re<=10^5 then
k_f=3.7*(t_c/r[4])^0.1/Re^0.5
ENDIF
If Re>10^5 then
k_f=0.102*(t_c/r[4])^0.1/Re^0.2
ENDIF
END
"Rotor throat width"
FUNCTION ROTORTH(C_m6,W[6],s_6pitch,M_6_rel,rho[6],rho_ss_R,W_ss_R)
If M_6_rel<1 Then A:=C_m6*s_6pitch/W[6]
If M_6_rel>1 Then A:=rho[6]*C_m6*s_6pitch/(rho_ss_R*W_ss_R)
If M_6_rel>1 Then CALL WARNING('Rotor exit supersonic expansion')
B:=rho[6]*C_m6/(rho_ss_R*W_ss_R)
IF B>1 Then CALL ERROR ('Annular passage choke precludes achieving the design
specifications')
ROTORTH:=A
End
"Inputs"
"Operating conditions"
T[0,0]=323"Inlet total temperature [K]"
P[0,0]=200000"Inlet total pressure [Pa]"
ER_ts=2"Total-to-static expansion ratio [-]"
```

```
m_dot=0.09"Mass flow rate [kg/s]"
"Turbine design parameters"
nu_ts=0.68"Velocity ratio [-]"
omega=5759.586"Rotational speed [rad/sec]"
alpha[4]=78.6"Rotor inlet absolute flow angle  WRT meridional [deg]"
alpha[6]=0"Rotor exit absolute flow angle WRT meridional [deg]"
r_6t/r[4]=0.55"Rotor exit tip to inlet radii ratio []"
r_6h/r[4]=0.2"Rotor exit hub to inlet radii ratio []"
r[1]/r[3]=1.25"Nozzle radii ratio [-]"
sigma=1.35"Nozzle solidity [-]"
alpha[1]=0"Nozzle inlet angle WRT meridional [deg]"
"Estimate of efficiency"
eta_stage_ts=0.813" Total-to-static efficiency estimation [-]"
"Constant"
R=287"Air gas constant [J/kg-K]"
C_p=Cp(Air,T=T[0,0])"Specific heat capacity at constant pressure [J/kg-K]"
C_v=Cv(Air,T=T[0,0])"Specific heat capacity at constant volume [J/kg-K]"
gamma=C_p/C_v"Specific heat ratio [-]"
BK=0.1"Blockage [-]"
"Output"
C_ts=sqrt(2*C_p*T[0,0]*(1-(1/ER_ts)^((gamma-1)/gamma)))
DELTAh_ideal=C_p*T[0,0]*(1-(1/ER_ts)^((gamma-1)/gamma))
N_R_recom=round((pi/30)*(110-alpha[4])*tan(alpha[4]))
h[0,0]=Enthalpy(Air,T=T[0,0])
h[4,0]=h[0,0]
U[4]=nu_ts*C_ts
r[4]=U[4]/omega
DELTAh_0=0.5*(C_ts^2)*eta_stage_ts
Power=DELTAh_0*m_dot
T[4,0]=T[0,0]
d[4]=2*r[4]
d_6t=2*r_6t
d_6h=2*r_6h
d[6]=2*r[6]
U_6t=r_6t*omega
U_6h=r_6h*omega
U[6]=r[6]*omega
A[6]=pi*(r_6t^2-r_6h^2)*(1-BK)
r[6]=sqrt((A[6]/(2*pi))+r_6h^2)
rho[0,0]=P[0,0]/(R*T[0,0])
P[4,0]=P[0,0]-(rho[0,0]*(C_ts^2)*(1-eta_stage_ts)/8)
P[6]=P[0,0]/ER_ts
h[6]=Enthalpy(Air,T=T[6])
T[6,0]=T[0,0]*(1-eta_stage_ts*(1-(P[6]/P[0,0])^((gamma-1)/gamma)))
rho[4]=P[4,0]/(R*T[4,0])
CALL
ROTOR_EXIT_TIP(DELTAh_0,U[4],alpha[4],T[4,0],C_p,gamma,m_dot,R,P[4,0],r[4],
P[6,0],T[6,0],alpha[6],A[6],U_6t:C_theta4,C_m4,C[4],Beta[4],W_theta4,W[4],T[4],P[4
],A[4],b[4],T[6],P[6],C_m6,C_theta6,C[6],beta[6],W[6],W_theta6,rho[6])
l_rotor_x=1.5*(r_6t-r_6h)
```

```
Reaction=(T[4]-T[6])/(T[0,0]-T[6,0])
Q_6=C_m6*A[6]
N_s_ts=omega*sqrt(Q_6)/DELTAh_ideal^(0.75)
phi=C_m6/U[4]
psi=DELTAh_0/U[4]^2
eta_rotor_tt=(1-(T[6,0]/T[4,0]))/(1-(P[6,0]/P[4,0])^((gamma-1)/gamma))
eta_rotor_ts=(1-(T[6,0]/T[4,0]))/(1-(P[6]/P[4,0])^((gamma-1)/gamma))
M_4_abs=C[4]/sqrt(gamma*R*T[4])
M_4_rel=abs(W[4])/sqrt(gamma*R*T[4])
M_6_abs=C[6]/sqrt(gamma*R*T[6])
M_6_rel=abs(W[6])/sqrt(gamma*R*T[6])
beta_6t=beta[6]
beta_6h=arctan((C_theta6-U_6h)/C_m6)
W_6h=C_m6/cos(beta_6h)
b[6]=r_6t-r_6h
r[3]=r[4]+2*b[4]*cos(alpha[4])
C_theta3=(C_theta4*r[4])/r[3]
C_theta_1=(C_theta3)*r[3]/r[1]
C_m3=C_m4
C[3]=sqrt(C_theta3^2+C_m3^2)
alpha[3]=alpha[4]
alpha_mean=(alpha[1]+alpha[3])/2
C_N=sqrt(abs(r[1]^2+r[3]^2-sqrt(abs((r[1]^2+r[3]^2)^2-((r[1]^2-
r[3]^2)/cos(alpha_mean))^2))))
S_N=C_N/sigma
N_N=Ceil(2*pi#*r[3]/S_N)
O_throat=S_N*cos(alpha[3])
Athroat_total=O_throat*b[4]*N_N
M[3]=M_4_abs
rho[3]=rho[4]
C_ss_N=SoundSpeed(Air,T=T[4,0])
h_ss_N=h[4,0]-0.5*C_ss_N^2
P_ss_N=P[4,0]-0.5*rho_ss_N*C_ss_N^2
T_ss_N=Temperature(Air,h=h_ss_N)
rho_ss_N=Density(Air,T=T_ss_N, P=P_ss_N)
o_3=NOZZLETH(M[3],alpha[3],S_N,rho[3],C_m3,rho_ss_N,C_ss_N)
h_6_rel=h[6]+0.5*W[6]^2
P_6_rel=P[6]+0.5*rho[6]*W[6]^2
T_6_rel=Temperature(Air,h=h_6_rel)
W_ss_R=SoundSpeed(Air,T=T_6_rel)
h_ss_R=h_6_rel-0.5*W_ss_R^2
P_ss_R=P_6_rel-0.5*rho_ss_R*W_ss_R^2
rho_ss_R=DENSITY(Air,h=h_ss_R,P=P_ss_R)
s_6pitch=2*pi*r[6]/N_R_recom
o_6=ROTORTH(C_m6,W[6],s_6pitch,M_6_rel,rho[6],rho_ss_R,W_ss_R)
DELTAh_incidence=0.5*(W[4]*cos(beta[4]))^2
RR=0.0002
r_c=r[4]-r_6t+((b[4]+b[6])/2)
L_hyd=(pi#/2)*sqrt(((r[4]-r_6t+(b[4]/2))^2+(b[6]/2)^2)/2)
```

```
D_hyd=0.5*(((4*pi#*r[4]*b[4])/(2*pi#*r[4]+N_R_recom*b[4]))+((2*pi#*(r_6t^2-
r_6h^2))/(pi#*(r_6t-r_6h)+N_R_recom*b[6])))
Re_in=U[4]*b[4]/(Viscosity(Air_ha,T=T[4],P=P[4])/Density(Air_ha,T=T[4],P=P[4]))

Re_out=U[6]*b[6]/(Viscosity(Air_ha,T=T[6],P=P[6])/Density(Air_ha,T=T[6],P=P[6]))
Re=(Re_in+Re_out)/2
f=MoodyChart(Re, RR)
f_curved=f*(1+0.075*Re^0.25*sqrt(D_hyd/(2*r_c)))
ff=f_curved*(Re*(d[4]/(2*r_c))^2)^0.05
W_bar=(W[4]+((W[6]+W_6h)/2))/2
DELTAh_friction_rotor=ff*L_hyd*W_bar^2/D_hyd
DELTAh_secondary=2*C[4]^2*r[4]/(N_R_recom*r_c)
CALL TIPCLEARANCE(b[6]:t_c)
C_x=(abs(1-(r_6t/r[4])))/(C_m4*b[4])
C_r=(r_6t/r[4])*(l_rotor_x-b[4])/(C_m6*r[6]*(r_6t-r_6h))
DELTAh_clearance=(U[4]^3*N_R_recom/(8*pi#))*(0.4*t_c*C_x+0.75*t_c*C_r-
0.3*sqrt(t_c^2*C_x*C_r))
DELTAh_exit=0.5*C[6]^2
rho_bar=(rho[4]+rho[6])/2
CALL DISKFRICTION (t_c,r[4],Re:k_f)
DELTAh_windage=k_f*rho_bar*U[4]^3*r[4]^2/(4*m_dot)
l_hyd_nozzle=r[1]-r[3]
D_hyd_nozzle=0.5*(((8*pi#*r[1]*b[4]*cos(alpha[1]))/(4*pi#*r[1]+(4*pi#*r[1]*b[4]/sig
ma)))+((8*pi#*r[3]*b[4]*cos(alpha[3]))/(4*pi#*r[3]+(4*pi#*r[3]*b[4]/sigma))))
DELTAh_nozzle_friction=4*f*(l_hyd_nozzle/D_hyd_nozzle)*C[3]^2
eta_ts_new=DELTAh_0/(DELTAh_0+DELTAh_friction_rotor+DELTAh_secondary+
DELTAh_exit+DELTAh_clearance+DELTAh_incidence+DELTAh_windage+DELTA
h_nozzle_friction)
eta_stage_ts=eta_ts_new
```

B-3: ORC standalone code with real-gas formulation

```
$UnitSystem SI MASS DEG PA K J
$Warnings ON
"Input data"
R$='R245fa' "Fluid selection"
T[1]=360"Inlet total temperature "
DELTAT_superheat=5"Degree of superheating"
m_dot=0.04921"Working fluid mass flow rate"
ER_ts=7"Expansion ratio"
eta_pump=0.7"Pump isentropic efficiency"
eta_mechanical=0.96"Mechanical efficiency"
eta_generator=0.96"Electrical efficiency"
omega=7000"Rotational speed"
phi=0.16"Flow coefficient"
"Turbine efficiency"
{eta_turbine_ts=0.8}"Constant turbine isentropic efficiency"
DELTAh_ideal=h[1]-h5s"Isentropic enthalpy drop"
DELTAh_actual=h[1]-h[5]"Ideal enthalpy drop"
V_dot[1]=m_dot*Q[1]"Inlet volume flow rate"
V_dot[5]=m_dot*Q[5]"Exit volume flow rate"
VR=V_dot[5]/V_dot[1]"Volumetric flow rate ratio"
SF=(V_dot[5]^0.5)/(DELTAh_ideal^0.25)"Size factor"
d[4]=0.08864+(1.722*SF)-(68.56*SF^2)+(0.7159*V_dot[5])-(0.9986*V_dot[5]^2)-
(0.00001824*omega)+(1.245*(10^(-9))*(omega^2))"Rotor inlet diameter"
d_max=0.1146+(2.468*SF)+(4.411*SF^2)+(0.7707*V_dot[5])-(2.009*V_dot[5]^2)-
(0.00002232*omega)+(1.479*(10^(-9))*(omega^2))"Overall diameter"
eta_turbine_ts=0.9211-4.39146121E-01*Phi-2.96596103E-02*VR+3.47118645E-
01*V_dot[5]+1.58206622E-02*ER_ts "Optimized turbine efficiency based on
correlation obtained by linear regression"
"Calculation"
"Turbine Inlet"
T_turbine_inlet_sh=T[1]+DELTAT_superheat "Turbine superheat inlet temperature"
P[1]=P_sat(R$,T=T[1])"Inlet total saturation vapor pressure"
Z=CompressibilityFactor(R$,T=T_turbine_inlet_sh,P=P[1])"Compressibility factor"
h[1]=ENTHALPY(R$,P=P[1],T=T_turbine_inlet_sh)"Inlet total enthalpy"
S[1]=ENTROPY(R$,P=P[1],T=T_turbine_inlet_sh)"Inlet total entropy"
rho[1]=DENSITY(R$,P=P[1],T=T_turbine_inlet_sh)"Inlet total density"
Q[1]=VOLUME(R$,P=P[1],T=T_turbine_inlet_sh) "Inlet specific volume"
"Turbine outlet"
P[5]=P[1]/ER_ts"Exit pressure"
S5s=S[1]"Isentropic expansion state point at turbine
outlet"
P5s=P[5]"Isentropic expansion state point at turbine
outlet"
h5s=ENTHALPY(R$,P=P5s,S=S5s)"Isentropic enthalpy"
h[5]=h[1]-eta_turbine_ts*(h[1]-h5s)"Exit enthalpy"
T[5]=TEMPERATURE(R$,P=P[5],h=h[5])"Exit temperature"
S[5]=ENTROPY(R$,P=P[5],h=h[5])"Exit entropy"
rho[5]=DENSITY(R$,P=P[5],h=h[5])"Exit density"
```

```
Q[5]=VOLUME(R$,P=P[5],h=h[5])"Exit specific volume"
W_turbine=m_dot*(h[1]-h[5])"Turbine power output"
"Condenser mid-point"
P[5,5]=P[5]"Pressure mid-point"
X[5,5]=1"Quality mid-point"
T[5,5]=TEMPERATURE(R$,P=P[5,5],x=X[5,5])"Temperature mid-point"
h[5,5]=ENTHALPY(R$,P=P[5,5],x=X[5,5])"Enthalpy mid-point"
S[5,5]=ENTROPY(R$,P=P[5,5],x=X[5,5])"Entropy mid-point"
rho[5,5]=DENSITY(R$,P=P[5,5],x=X[5,5])"Density mid-point"
"Condenser outlet"
X[6]=0"Saturated liquid pressure at condenser exit"
P[6]=P[5]
T[6]=TEMPERATURE(R$,P=P[6],x=X[6])"Condenser exit pressure"
h[6]=ENTHALPY(R$,P=P[6],x=X[6])"Condenser exit enthalpy"
S[6]=ENTROPY(R$,P=P[6],x=X[6])"Condenser exit
entropy"
rho[6]=DENSITY(R$,P=P[6],x=X[6])"Condenser exit density"
Q_out=m_dot*(h[5]-h[6])"Condenser heat rejection"
Volume_flow_rate=m_dot/rho[6]"Liquid volume flow rate at condenser exit"
mu=VISCOSITY(R$,P=P[6],x=X[6])"Liquid viscosity at condenser exit"
SG=rho[6]/1000"Specific gravity at condenser exit"
"Pump outlet"
P[7]=P[1]"Pump exit pressure"
W_pump=m_dot*(P[7]-P[6])/(rho[6]*eta_pump)"Pump power consumption"
h[7]=h[6]+(W_pump/m_dot)"Pump exit enthalpy"
T[7]=TEMPERATURE(R$,h=h[7],P=P[7])"Pump exit temperature"
S[7]=ENTROPY(R$,h=h[7],P=P[7])"Pump exit entropy"
rho[7]=DENSITY(R$,h=h[7],P=P[7])"Pump exit density"
Q_in=m_dot*(h[1]-h[7])"Evaporator heat addition"
"Evaporator mid-point"
P[8]=P[1]"Pressure mid-point"
X[8]=0"Quality mid-point"
T[8]=TEMPERATURE(R$,P=P[8],x=X[8])"Temperature mid-point"
h[8]=ENTHALPY(R$,P=P[8],x=X[8])"Enthalpy mid-point"
S[8]=ENTROPY(R$,P=P[8],x=X[8])"Entropy mid-point"
rho[8]=DENSITY(R$,P=P[8],x=X[8])"Density mid-point"
"ORC performance"
W_net=(W_turbine*eta_generator*eta_mechanical-W_pump)"Cycle net power output"
eta_thermal_cycle=W_net/Q_in"ORC thermal efficiency”
```

Appendix C: Compressed air RIT detailed two-dimensional drawings

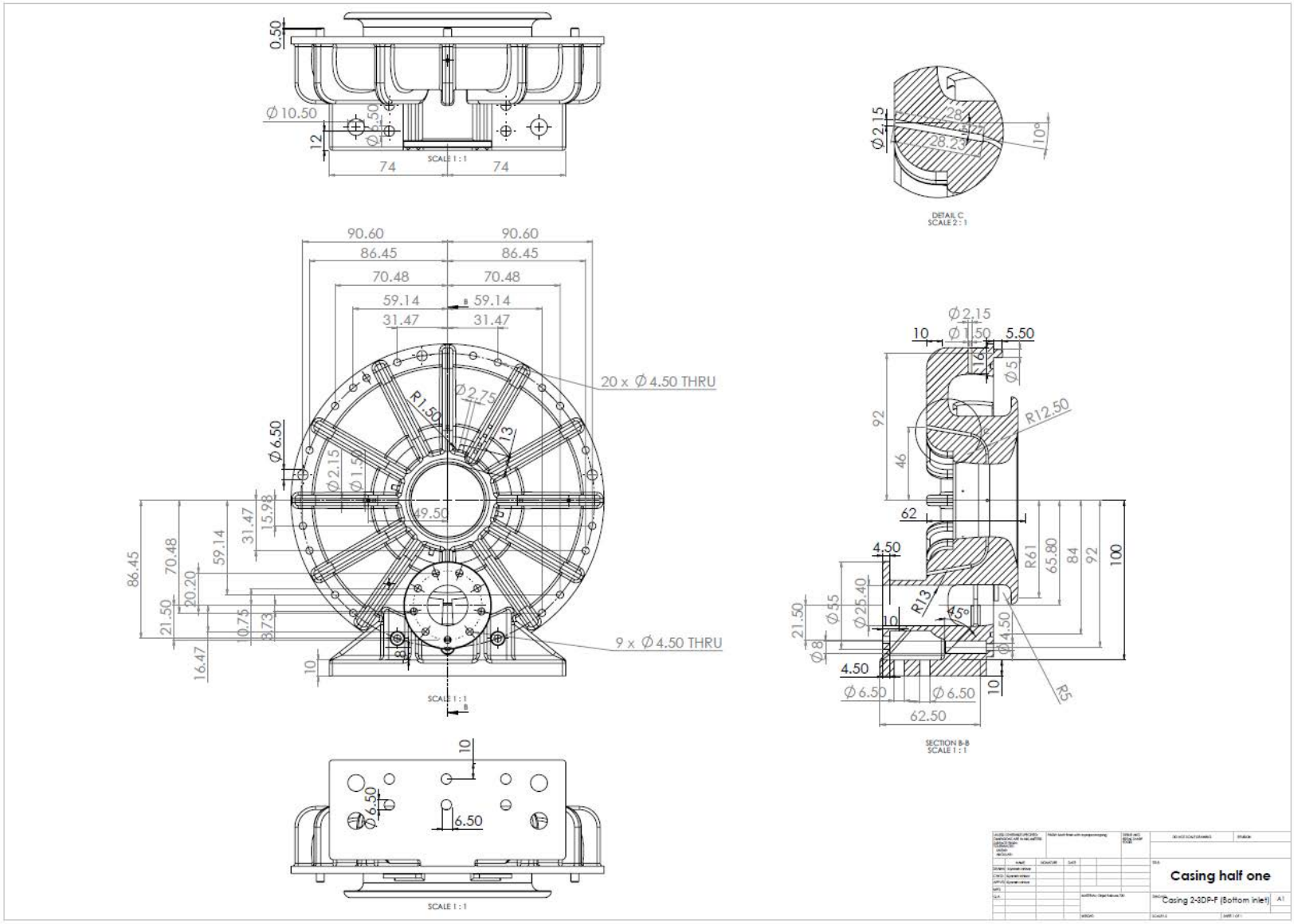

Figure C-1 Casing half one –detailed two-dimensional drawing

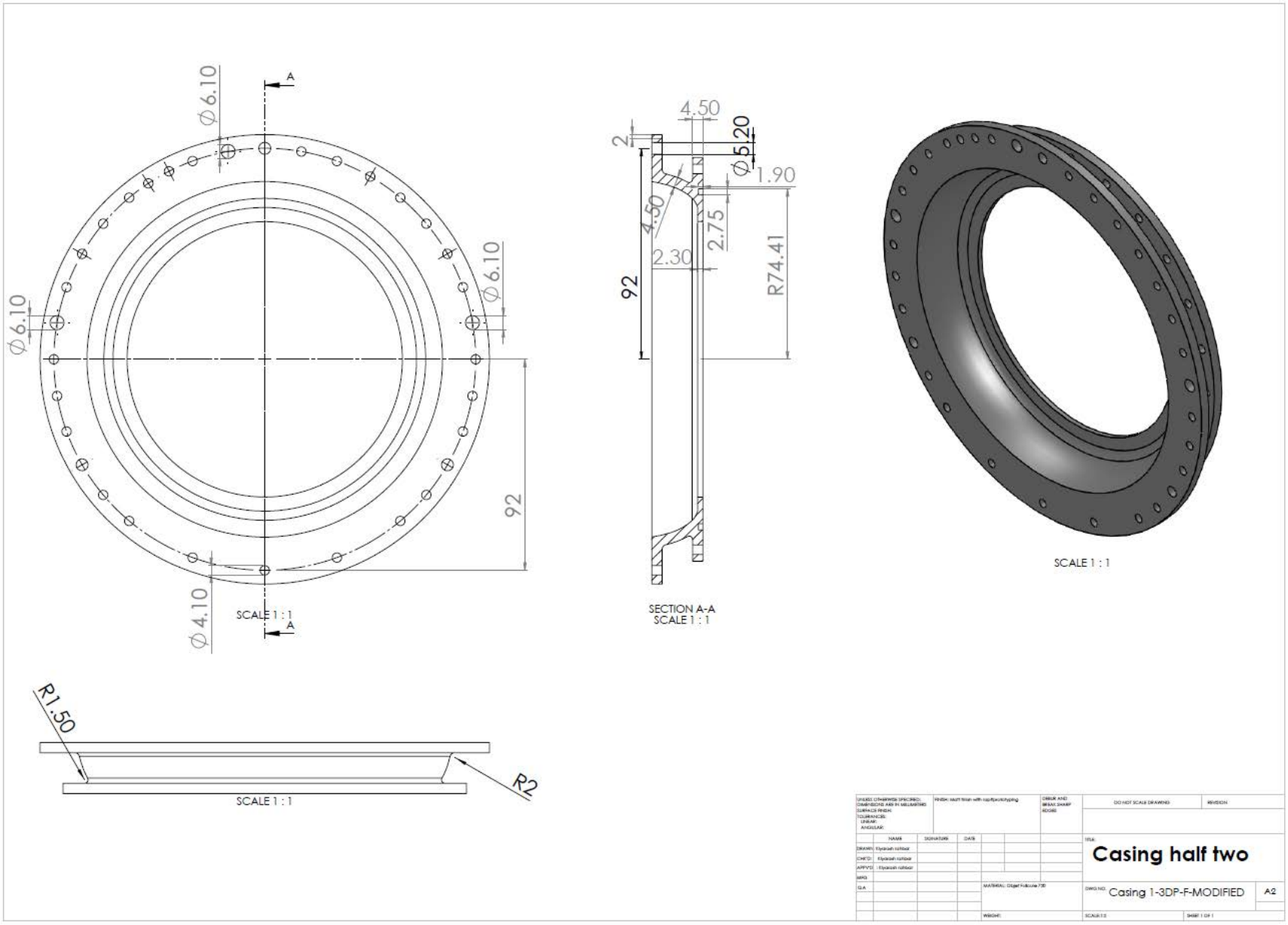

Figure C-2 Casing half two –detailed two-dimensional drawing

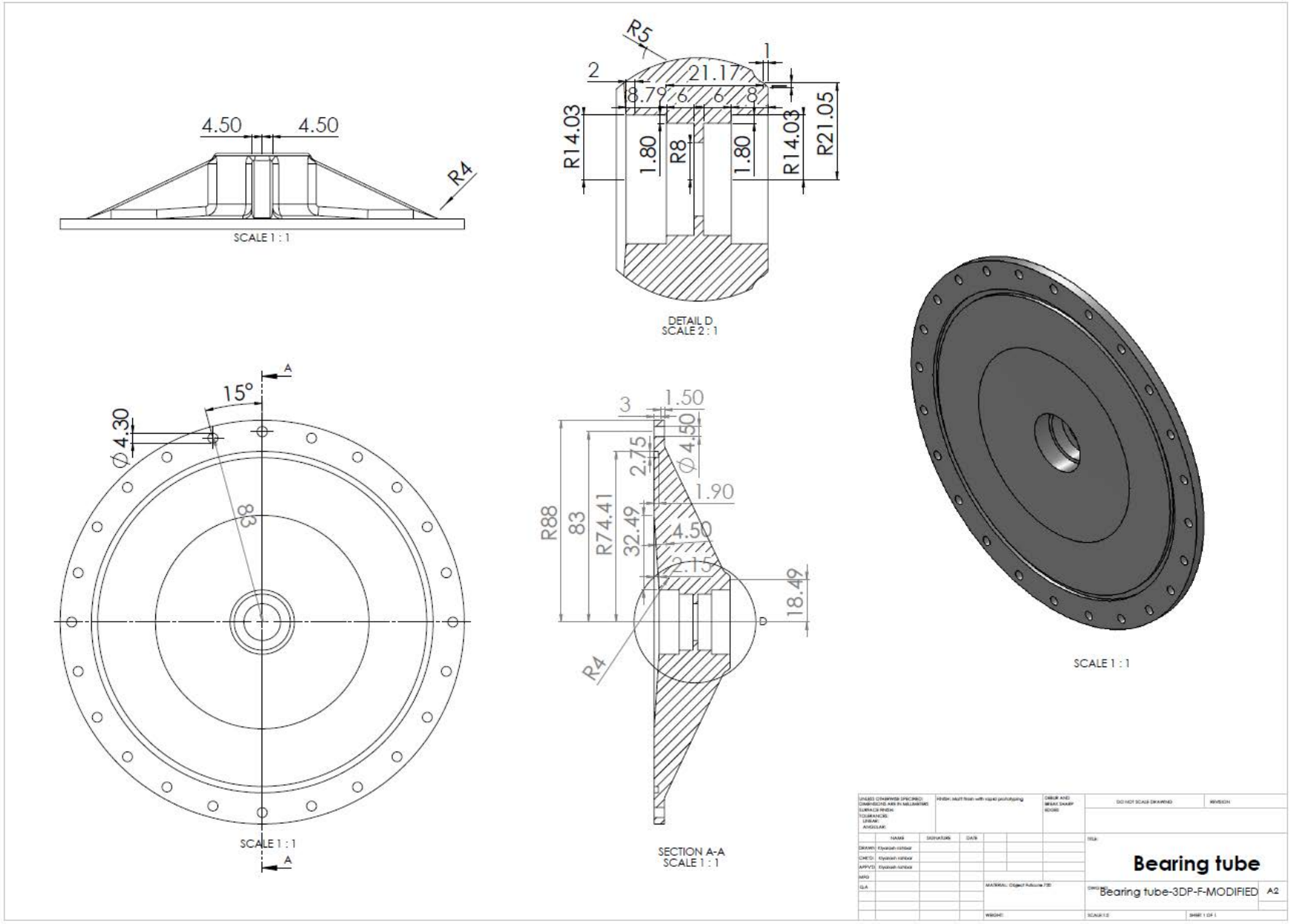

Figure C-3 Bearing tube –detailed two-dimensional drawing

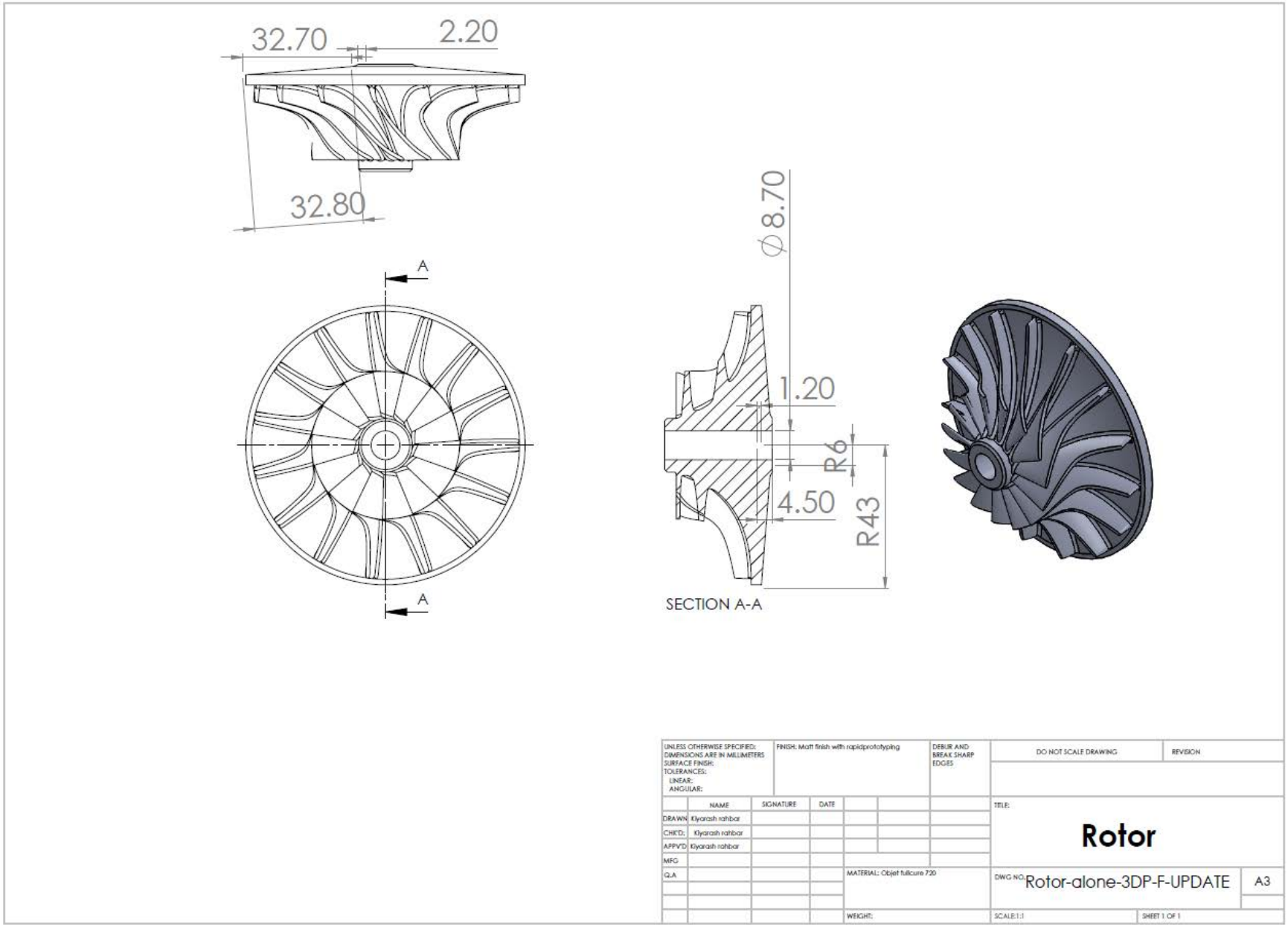

Figure C-4 Rotor –detailed two-dimensional drawing

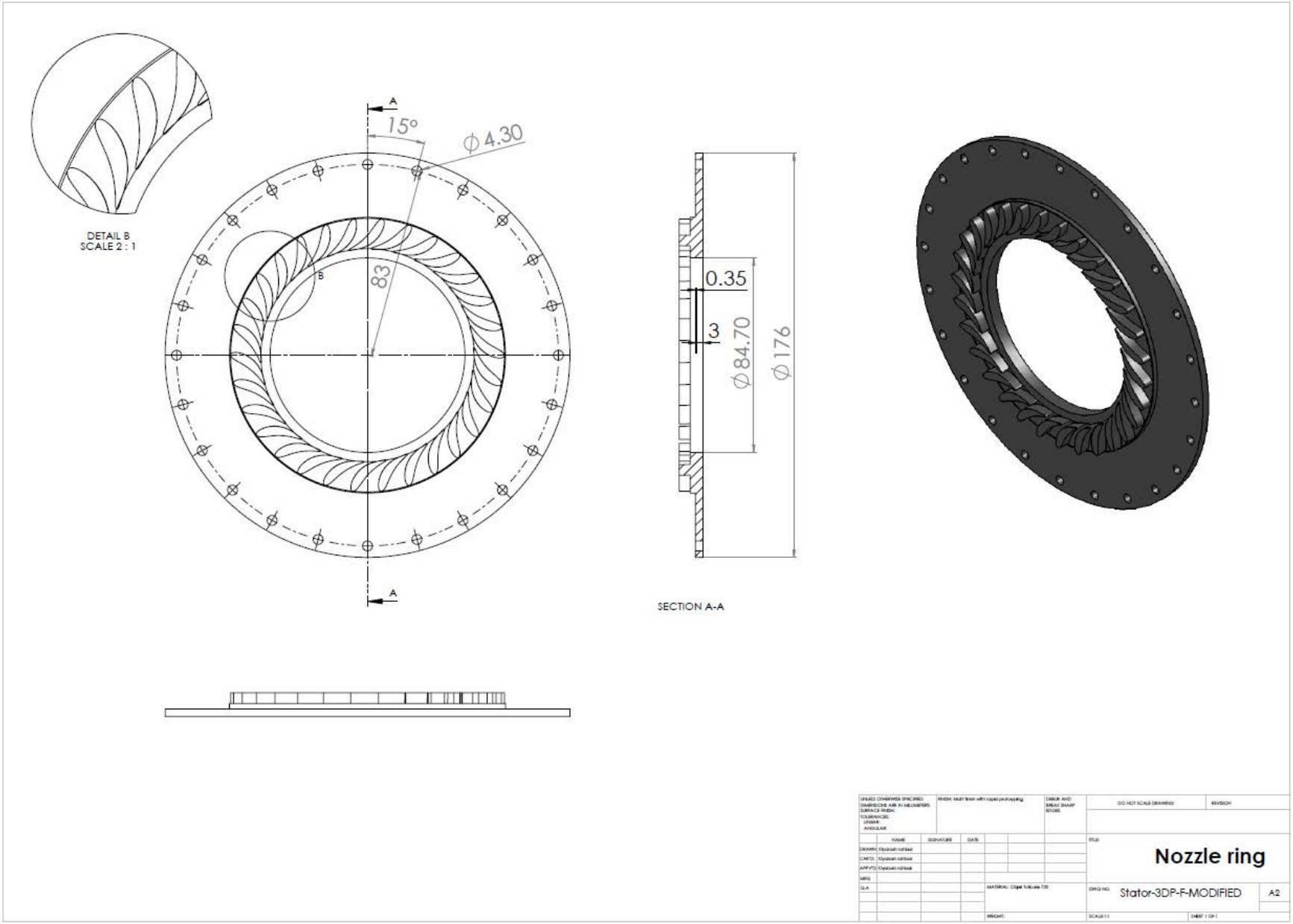

Figure C-5 Nozzle ring –detailed two-dimensional drawing

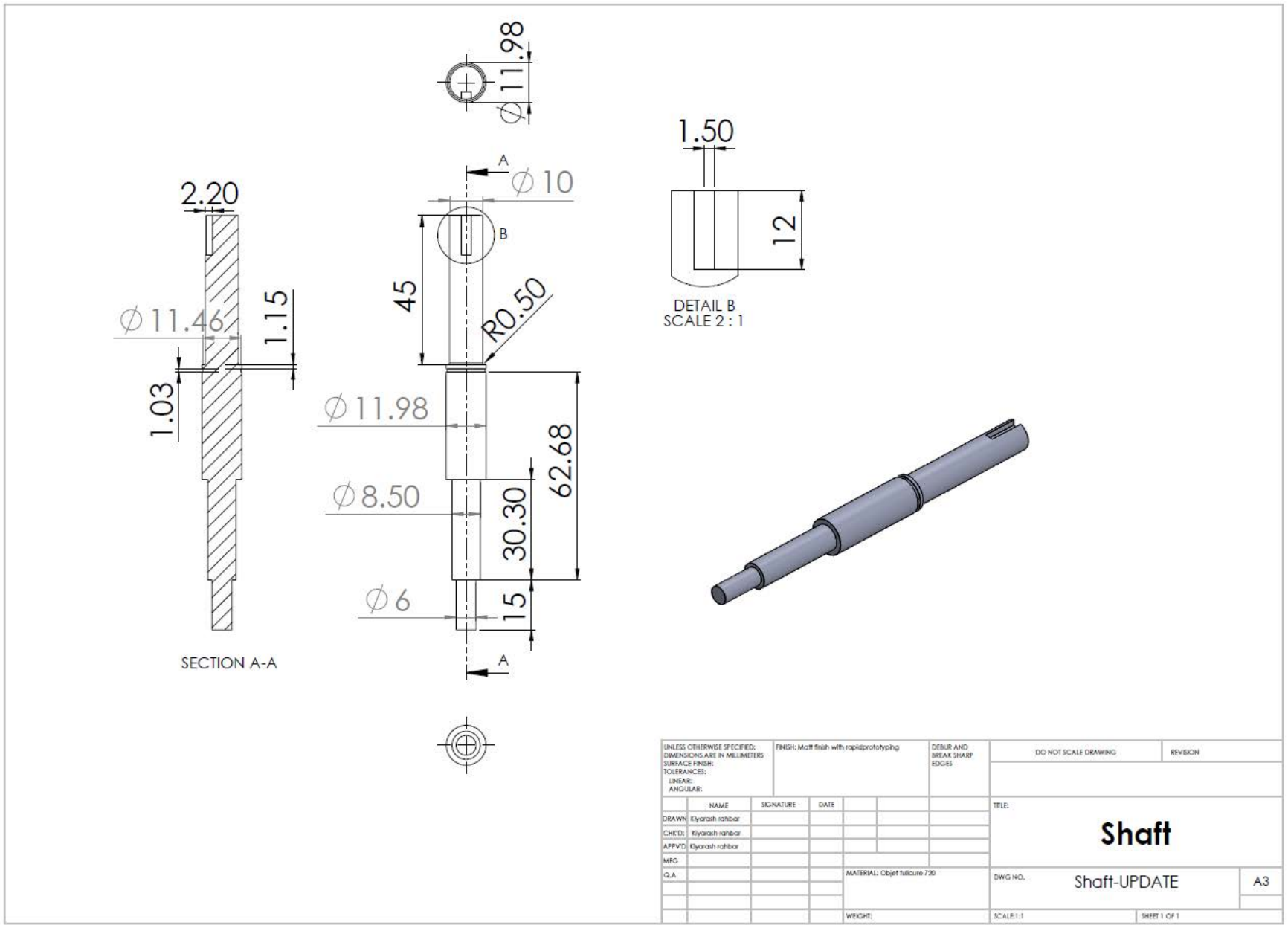

Figure C-6 Shaft –detailed two-dimensional drawing

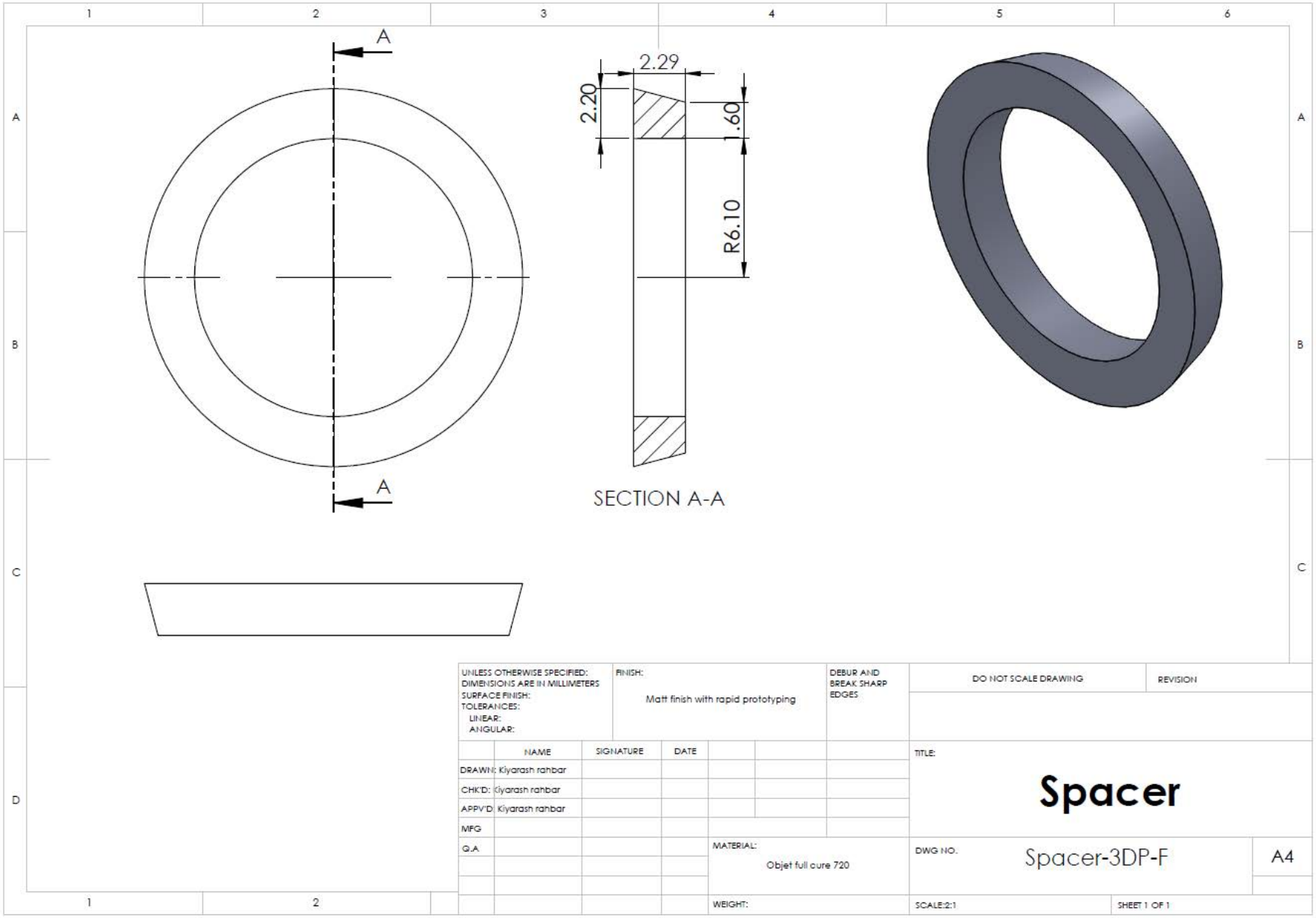

Figure C-7 Spacer –detailed two-dimensional drawing

Appendix D: Dual-stage transonic organic RIT two-dimensional and three-dimensional CAD drawings

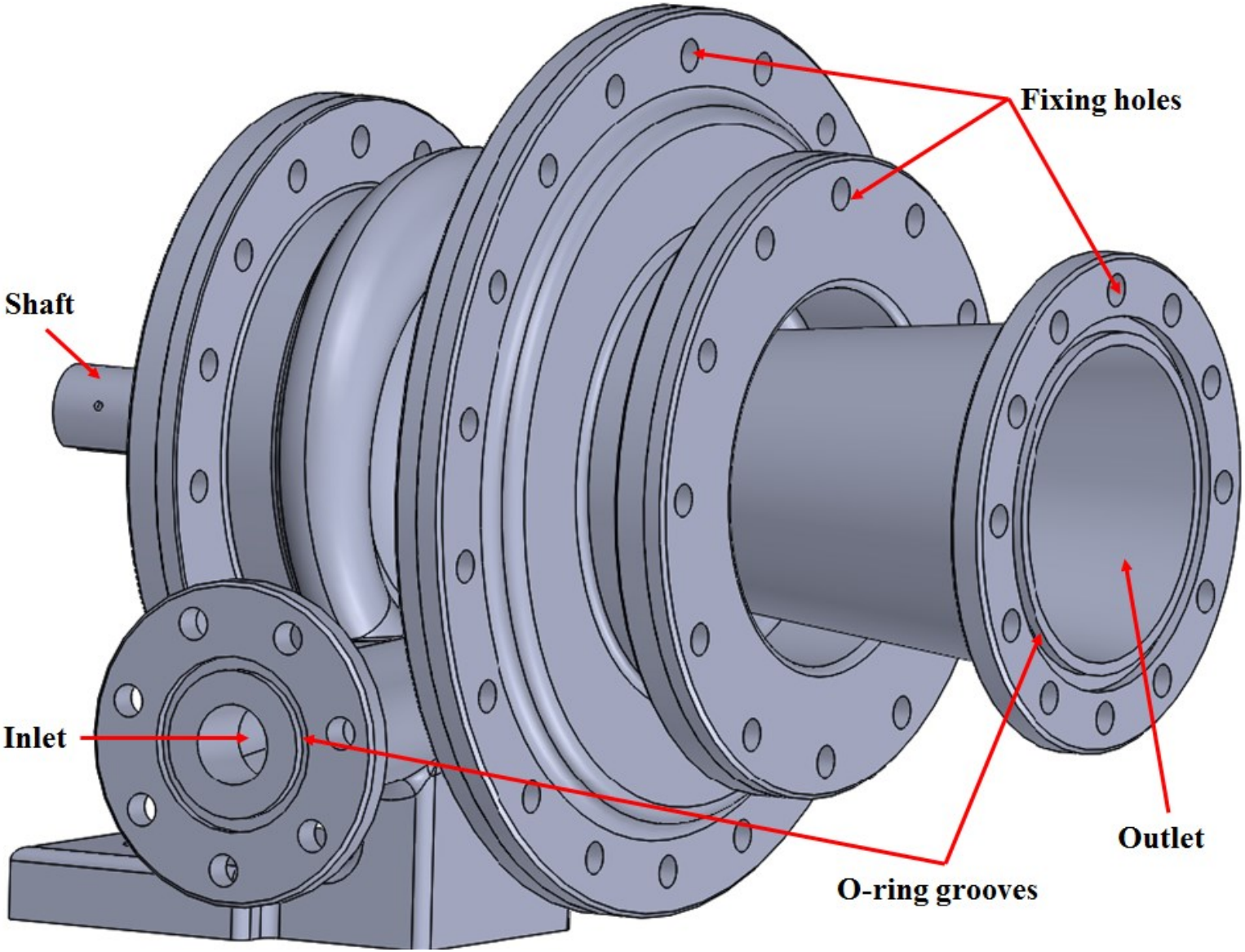

Figure D-1 CAD model of the complete dual-stage transonic organic RIT (isometric view)

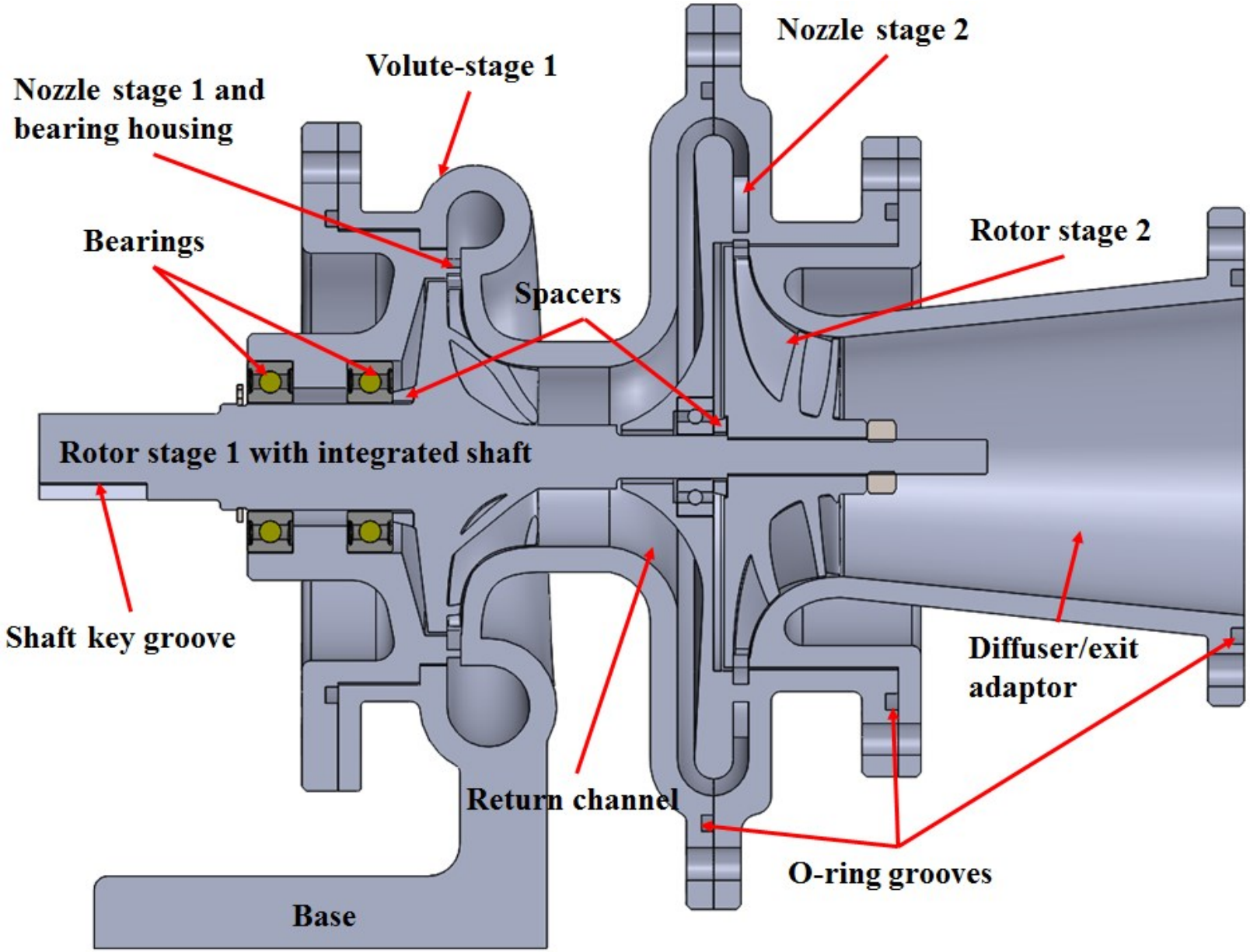

Figure D-2 CAD model of the complete dual-stage transonic organic RIT (section view)

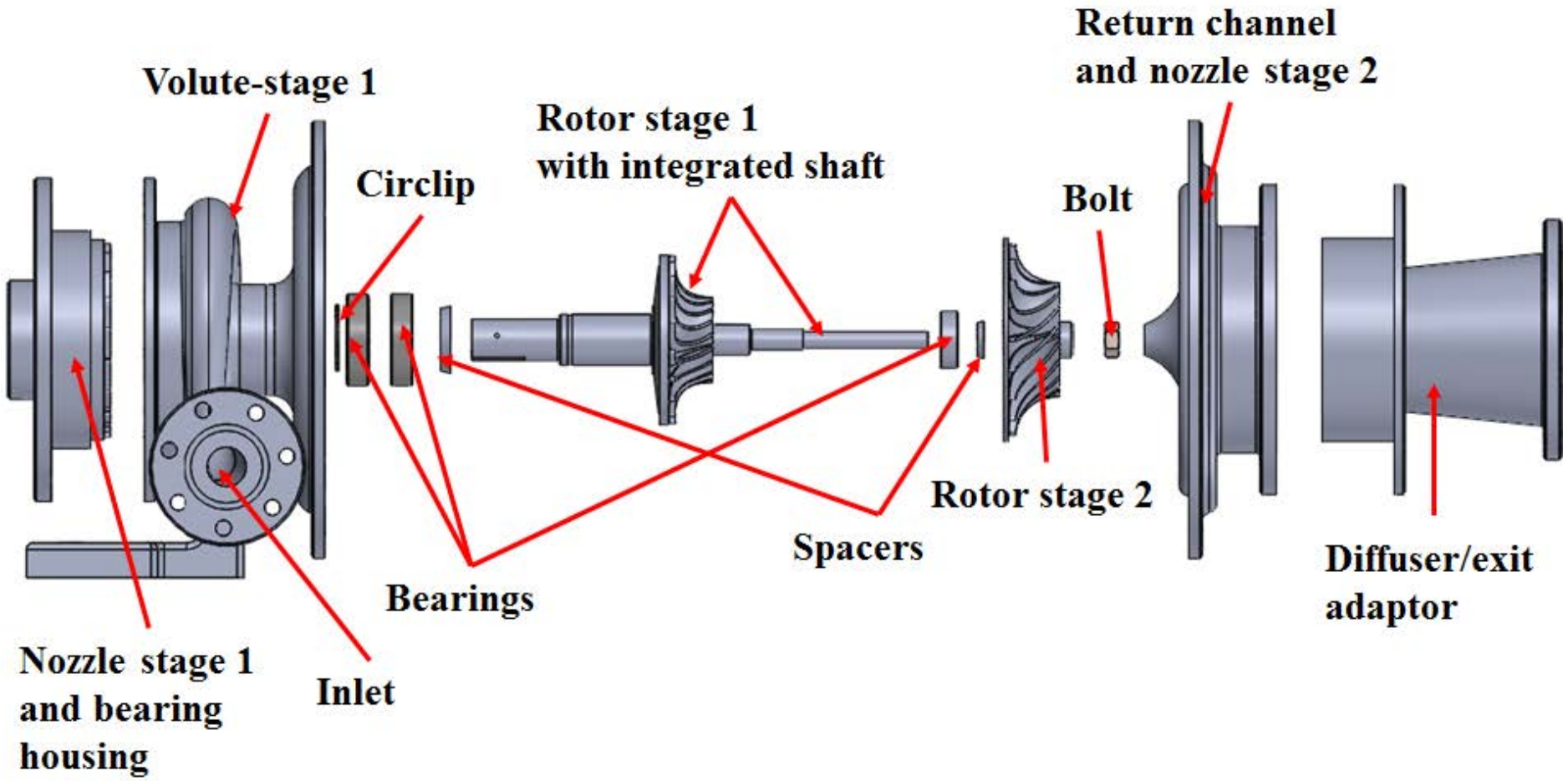

Figure D-3 CAD model of the complete dual-stage transonic organic RIT (exploded view)

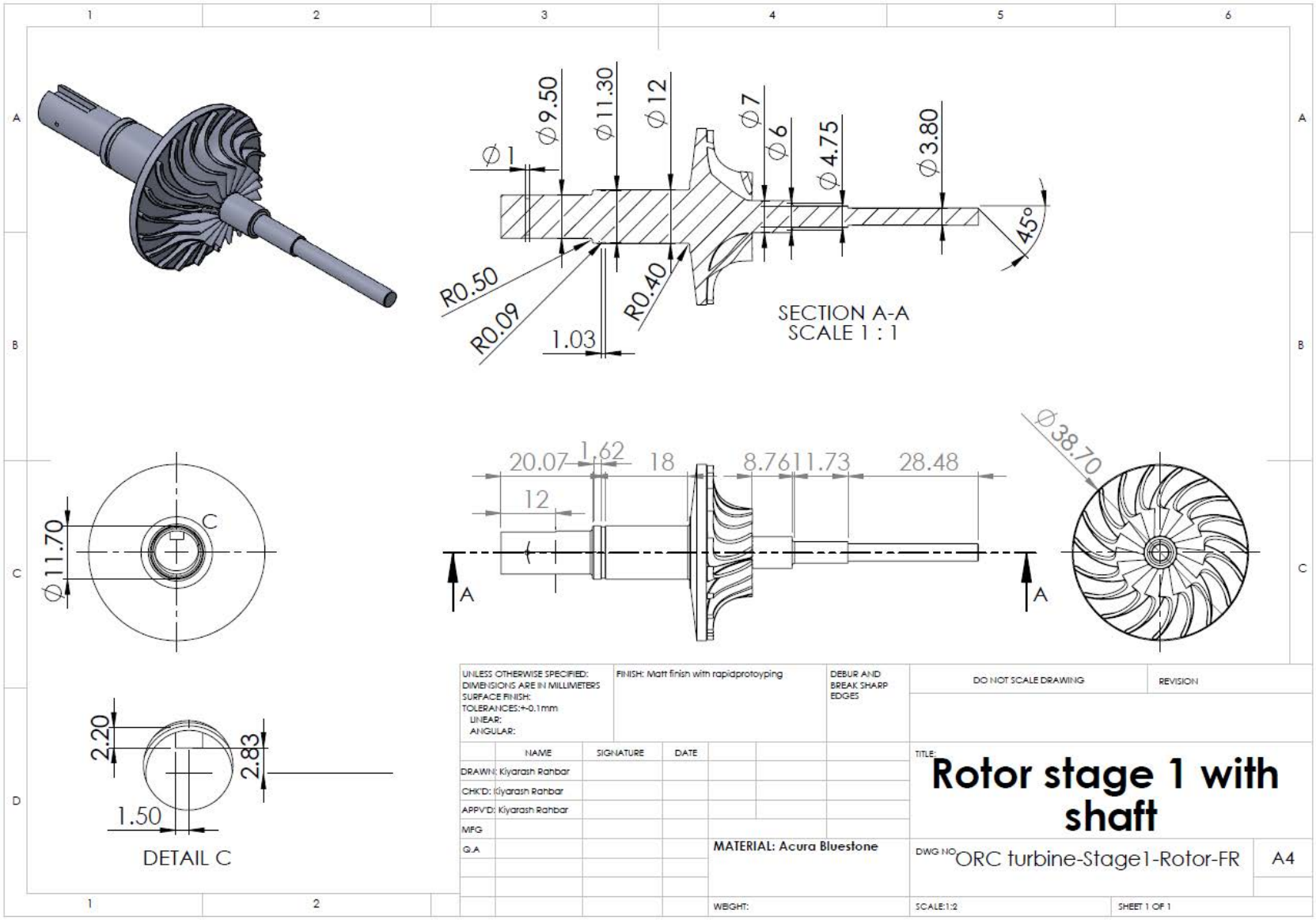

Figure D-4 Rotor stage 1 with shaft- detailed two-dimensional drawing

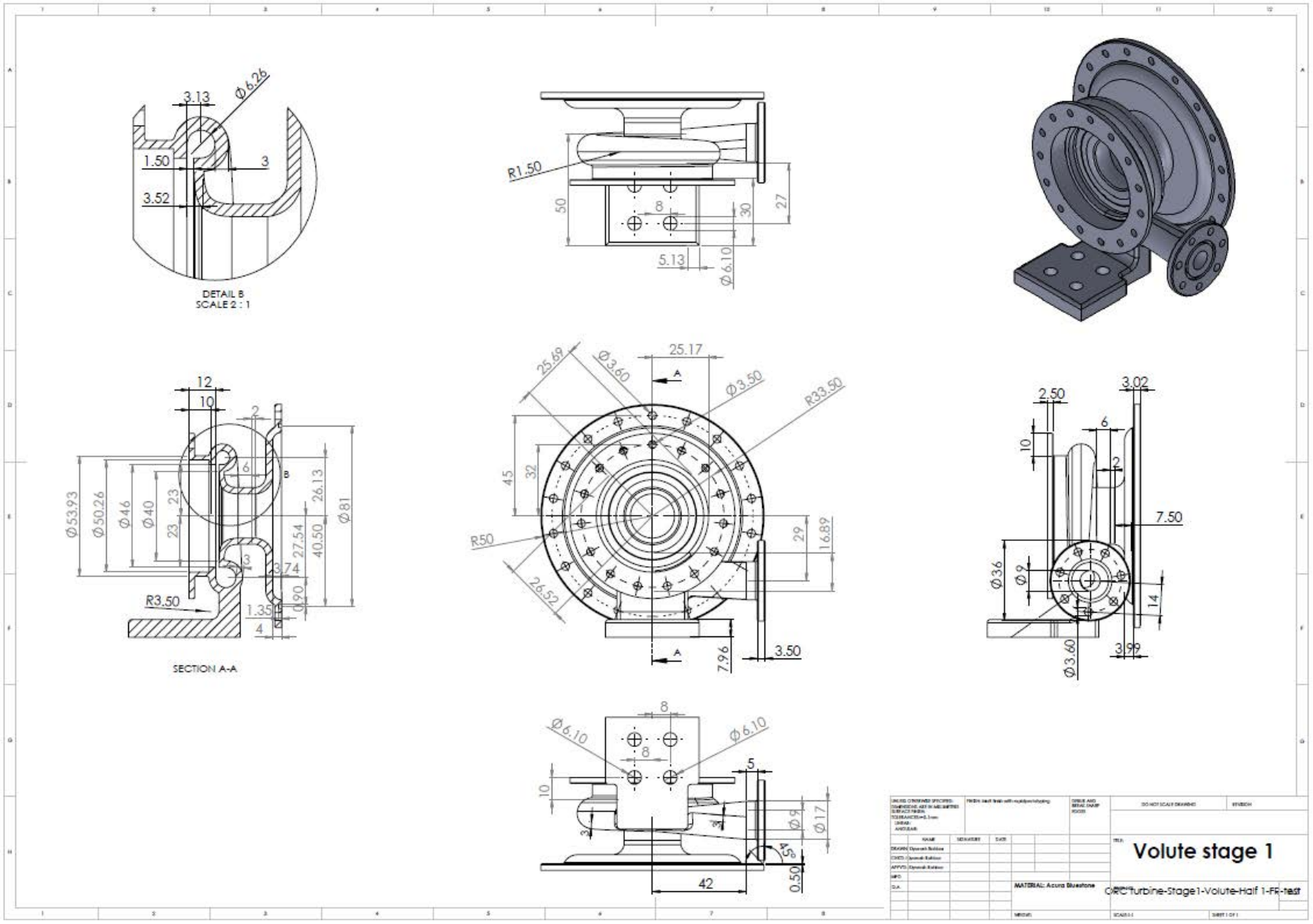

Figure D-5 Volute stage 1 - detailed two-dimensional drawing

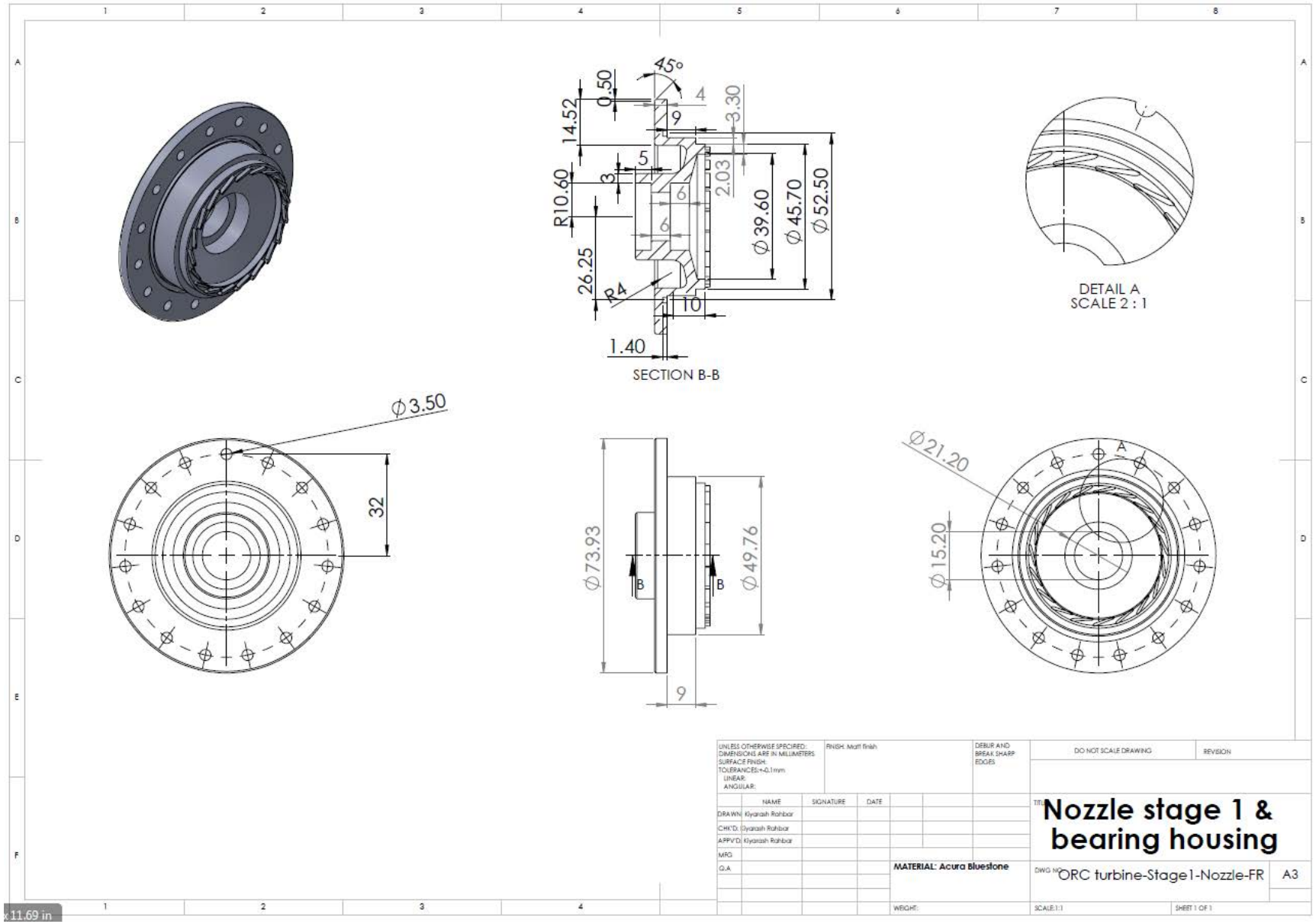

Figure D-6 Nozzle stage 1 and bearing housing - detailed two-dimensional drawing

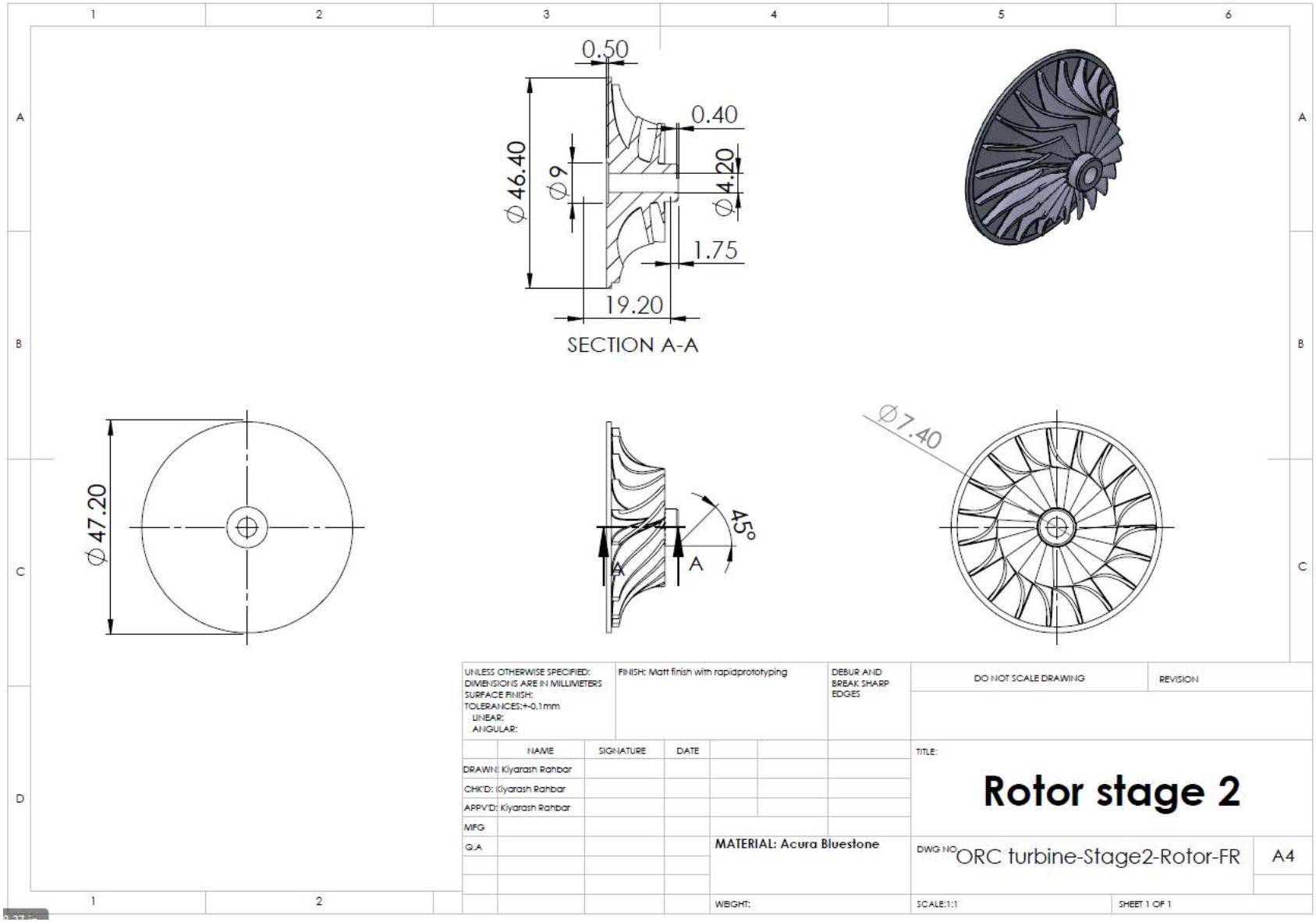

Figure D-7 Rotor stage 2- detailed two-dimensional drawing

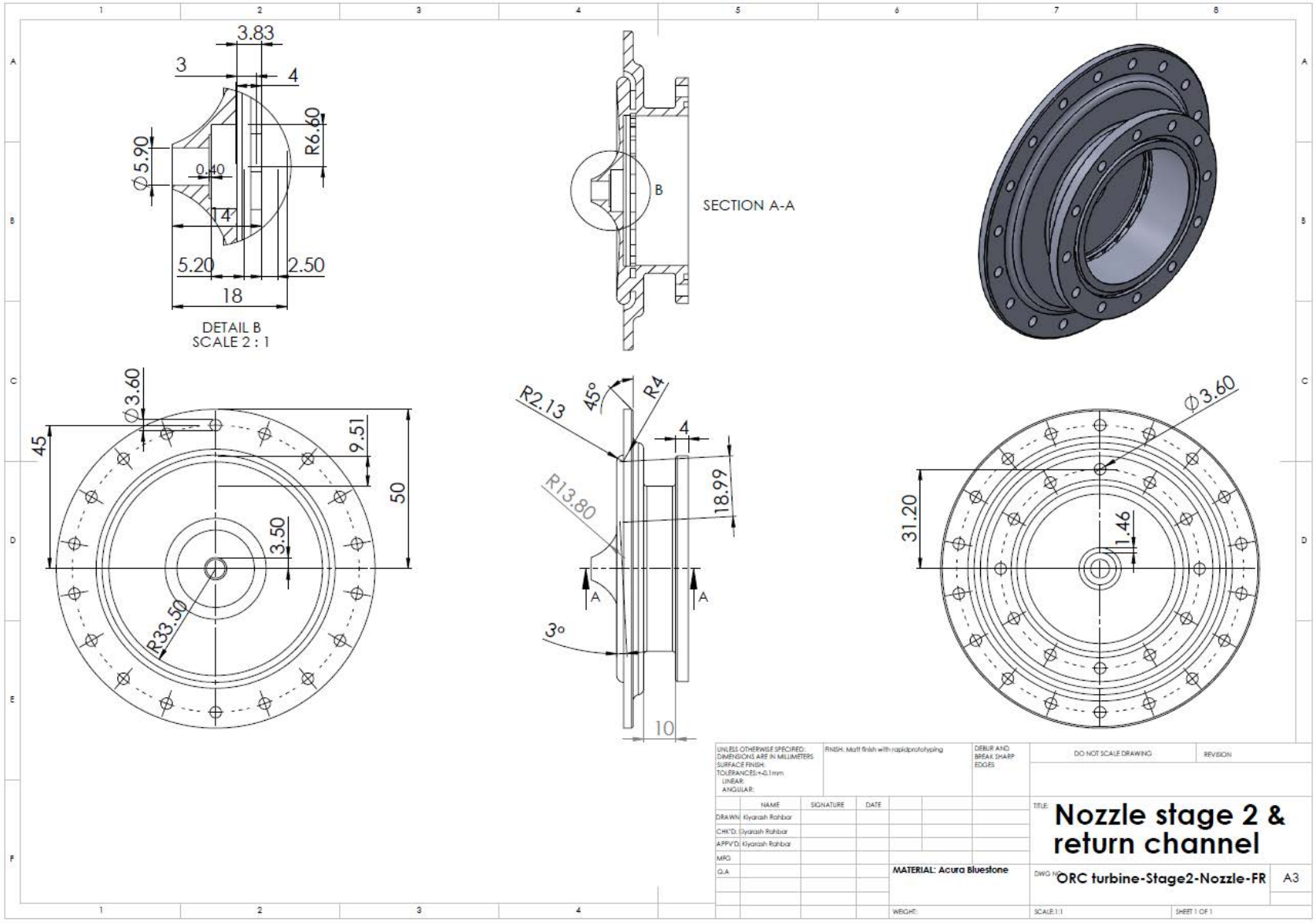

Figure D-8 Nozzle stage 2 and return channel- detailed two-dimensional drawing

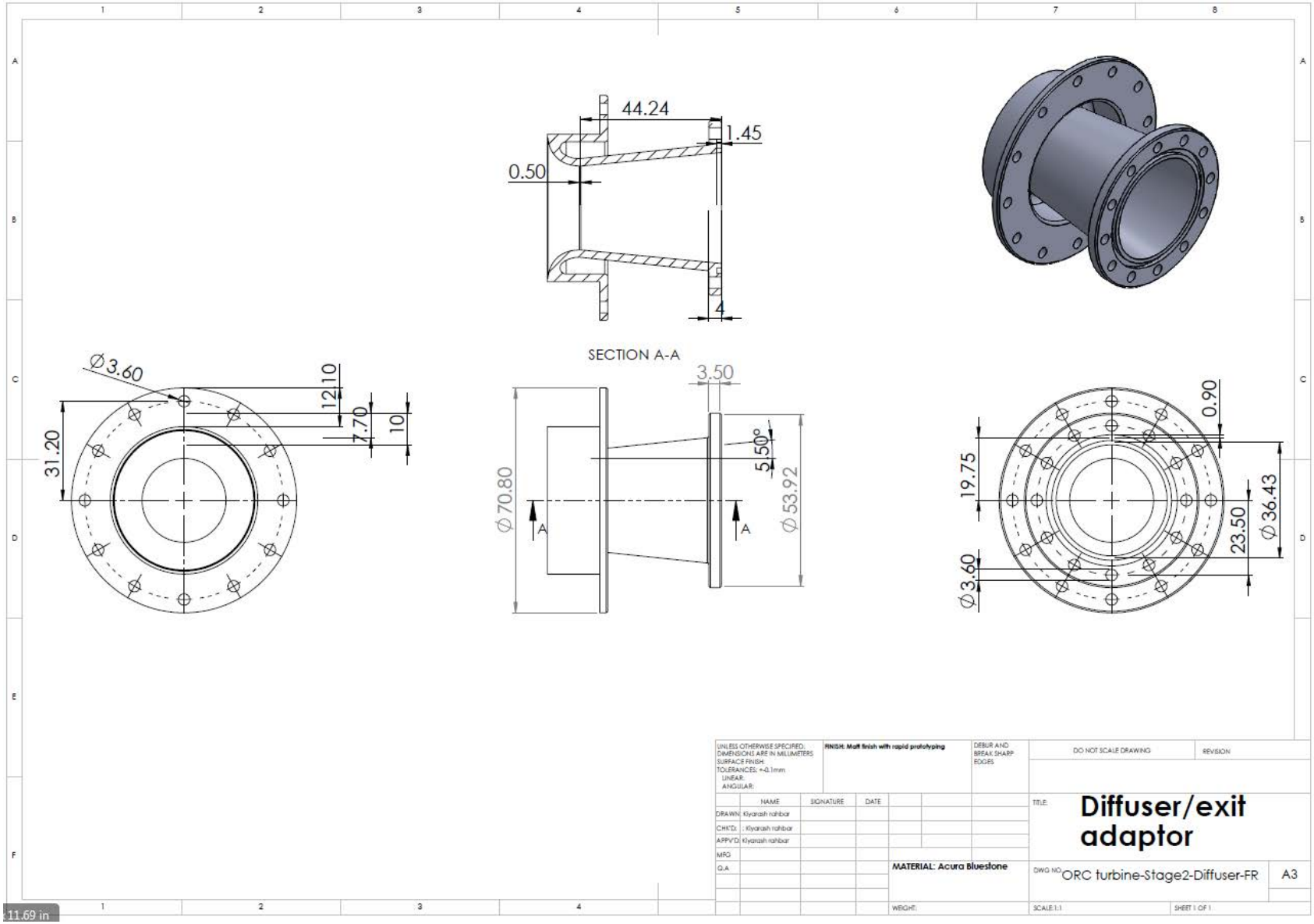

Figure D-9 Diffuser/exit adaptor- detailed two-dimensional drawing

Appendix E: Schematic of the ORC system for experimental testing

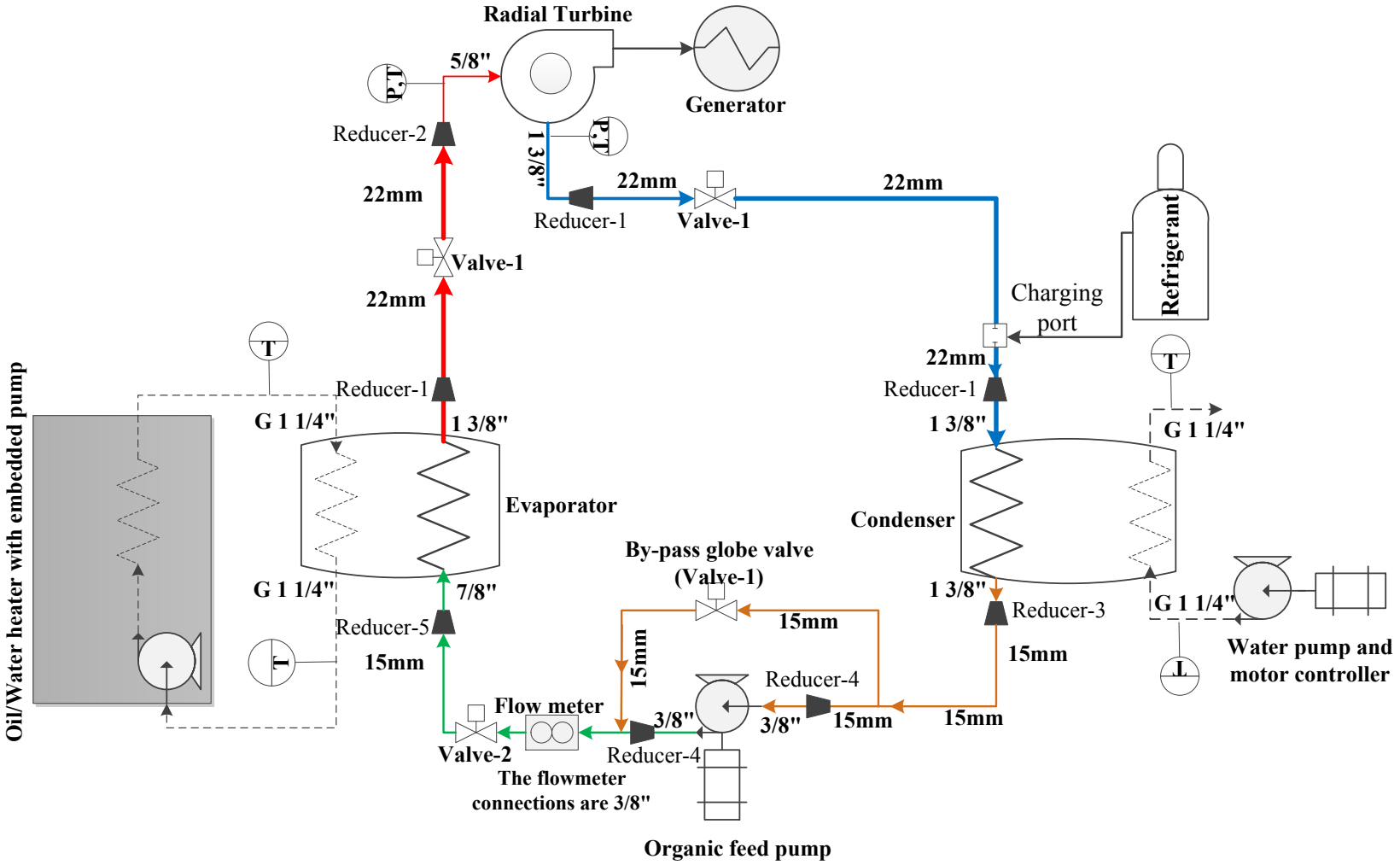

Figure E-1 Schematic of the ORC system for experimental testing